Université de la Méditerranée – Aix-Marseille II

Ph. D THESIS

Submitted to the University of Mediterranean (University of Aix-Marseille II)
In partial fulfillment of the requirements for the
Degree of Doctor of Philosophy
in Fluid Mechanics

Speciality: MECHANICS

Option: Fluid Mechanics

Numerical Study of Three Dimensional Turbulent Flows in a Habitat With Coupled Heat and Mass Transfer

by

Shengping LUO

Defended on 31st Oct. 2003 before the Examination Committee:

BEN HADID Hamda,	Prof., Université Claude Bernard, Lyon I	Referee
LAUNDER Brian,	Prof. University of Manchester (UMIST), UK	
MOJTABI Abdelkader,	Prof., Université Paul Sabatier, Toulouse III	
PAVAGEAU Michel,	Maître de Conférence, Ecole des Mines de Nantes	Referee
REY Claude,	Prof., Université d'Aix-Marseille	
ROUX Bernard,	Directeur de Recherche - CNRS, L3M, Marseille	
SANI Robert,	Prof., University of Colorado, Boulder, USA	Referee
SCHIESTEL Roland,	Directeur de Recherche - CNRS, IRPHE, Marseille	
VIGLIANO Patrick,	Prof., Université de la Méditerranée, Aix-Marseille II	

Université de la Méditerranée – Aix-Marseille II

THESE

Pour obtenir le grade de
Docteur de l'Université de la Méditerranée – Aix-Marseille II

Spécialité : MECANIQUE

Option : MECANIQUE DES FLUIDES

ETUDE NUMERIQUE D'ECOULEMENTS TURBULENTS TRIDIMENSIONNELS DANS UN HABITACLE ; COUPLAGE AVEC LES TRANSFERTS DE CHALEUR ET DE MASSE

par

Shengping LUO

Soutenue le 31 octobre 2003 à 14:30 devant la commission d'examen :

BEN HADID Hamda,	Prof., Université Claude Bernard, Lyon I	Rapporteur
LAUNDER Brian,	Prof. University of Manchester (UMIST), UK	
MOJTABI Abdelkader,	Prof., Université Paul Sabatier, Toulouse III	
PAVAGEAU Michel,	Maître de Conférence, Ecole des Mines de Nantes	Rapporteur
REY Claude,	Prof., Université d'Aix-Marseille	
ROUX Bernard,	Directeur de Recherche - CNRS, L3M, Marseille	
SANI Robert,	Prof., University of Colorado, Boulder, USA	Rapporteur
SCHIESTEL Roland,	Directeur de Recherche - CNRS, IRPHE, Marseille	
VIGLIANO Patrick,	Prof., Université de la Méditerranée, Aix-Marseille II	

獻給我的母親

To my mother

A ma mère

The person who can live in the world
without letting the world live in him
is a clever one, a free one

– A Zen saying

« Je suis à Marseille...La Méditerranée est tout entière sous le soleil, on le sent à l'unité inexprimable qui est au fond de sa beauté; Elle a une côté fauve et sévère dont les collines et les roches semblent arrondies ou taillées par Phidias; l'austérité de la rive s'accouple harmonieusement à la grâce du flot; les arbres, là où il y a des arbres, trempent leur pied dans la vague; le ciel est d'un bleu clair, la mer est d'un bleu sombre; ciel et mer sont d'un bleu profond. »

Victor Hugo

“Je voudrais que tu passes quelque temps ici, on sent autrement la couleur. Sous le ciel bleu, les fleurs prennent un éclat étonnant, et dans l'air limpide il y a je ne sais pas quoi d'heureux et d'amoureux... »

Vincent Van Gogh

« Oui, le sol, ici est toujours vibrant, il a une âpreté qui réverbère la lumière et qui fait clignoter les paupières, mais sentez comme il est toujours nuancé et moelleux"...

"Rien ici ne pétarade, tout s'intensifie dans la plus suave harmonie – il n'y aurait qu'à se laisser aller – cette terre vous porte... »

Paul Cézanne

Je suis heureux d’être parmi les amoureux de Marseille car j’en suis un.

Acknowledgements

This work was originally supported by a Ph. D study grant from the French Embassy in Beijing, China and was carried out in the Equipe Calcul Haute Performance en Mécanique (CHPM), Laboratoire de Modélisation et Simulation Numérique en Mécanique (L3M, FRE-2405-MSNM Laboratoire mixte CNRS – Universités d'Aix-Marseille).

First, I wish to express my infinite gratitude to Dr. Bernard Roux, Directeur de Recherche au CNRS, for all his efforts to make this study possible, for his taking all the troubles to supervise this thesis and for his great patience for bearing my slow progress—he never urged me to publish the immature results I got and this allows me to have a free spirit to explore the different aspects of numerical simulation of ventilation flows which I think is indispensable for doing a research work. Both of his helps in work and in life are invaluable and will be an ever-sweet souvenir in my life.

I count me as a very lucky one to have the marvelous opportunity to work in such a warm and friendly group and in such a beautiful city with its always brilliant sunshine and the blue sky. With the warm support from all the colleagues in the group and more generally in the Lab., I feel always at home even though I am far away from my family and my country. I am happy to have this chance to express my gratefulness to all my colleagues, for their warm support, both in work and in life, and for their friendly cares in many ways.

This work would not be possible without the kind help of many people. I wish to express my special thanks to J. Heikkinen of the VTT Technical Research Centre of Finland, C. Blomqvist of the National Swedish Instiute for Building Research, Prof. P. Heiselberg of University of Aalborg (Denmark), Prof. Dr.-Ing. M. Zeller of Lehrstuhl für Wärmeübertragung (Germany) for generously sharing with me their precious experimental data for the IEA Annex 20 Test Cases and to Dr. L. K. Voigt of Technical University of Denmark for kindly sending me the experimental data of the IEA Annex 20 Test Case 2D and to Dr. W. Schwarz of Fluent.Inc for kindly sending me the ASHRAE RP-1009 Report and for many inspiring discussions with him. I wish also to express my gratitude to Prof. B. E. Launder of UMIST, Prof. J. Ferziger of Stanford University, Dr. R. Schiestel of IRPHE for their help to understand turbulence modeling and the inspiring discussions with them; and to Prof. R. Sani of University of Colorado, Prof. H. Ben Hadid of Université Claude Bernard (Lyon I) and Dr. M. Pavageau of Ecole des Mines de Nantes for their many helpful suggestions on the manuscript and for acting as referees of my thesis. My thanks are also for Prof. L. Davidson of Chalmers University of Technology (Sweden), Prof. S. Kato of University of Tokyo (Japan), Dr.-Ing. M. Breuer of University of Erlangen-Nuernberg (Germany), Prof. L. Kleiser of ETH Zurich (Switherland), Prof. Dr.-Ing. G. Groetzbach of Institut fuer Reaktorsicherheit (Germany), Prof. P. Bradshaw of Stanford University, Prof. J. J. Roux and Prof. J. F. Sacadura of the Centre de Thermique de Lyon (CETHIL) and Mrs. Maggy Doolhoff, secretary to Prof. K. Hanjalic of TU Delft (The Netherlands) for sending me many helpful and hard-to-find reports and thesis. I am very grateful to Dr. S. H. Peng of Chalmers University of Technology (Sweden), Dr. C. Buchanan of University of California, Dr. J. C. Bennetsen of Dansish Institute of Agricultural Sciences, Dr. P. Schild of Norwegian University of Science and Technology (NTNU) and Dr. S. J. Rees of Oklahoma State University for kindly sending me their Ph. D thesis which have been very helpful for this study.

Finally but not lastly, I wish to express my great gratitude to my dear colleagues D. Fougère, S. Fayolle and R. Kotarba for their technical support and for keeping the computing facilities (in particular the powerful AMD-Athlon cluster, on which most of the computations have been performed) at L3M always in good order, to P. Falandry of the Centre Informatique National de l'Enseignement Supérieur (CINES) for his kind help to efficiently use their parallel machines, and to my dear friends Mrs. Sylvie Falk and Mr. Alain Poujol for their generous financial help and many warm cares in life. I am grateful for all who have helped me in one way or another and feel sorry that I cannot cite all the names here because that will be a very long list but I have always great gratitude toward them in my heart.

I send also my infinite gratitude to my family and friends in China for their loving support, especially to my mother who patiently bears my long absence at her old age and who hopes always all the best for me.

May peace and happiness be with all!

Abstract

With the ever-increasing availability of high-performance computing facilities, numerical simulation by way of Computational Fluid Dynamics (CFD) is increasingly used to predict air flow pattern and air distribution in buildings, it is now becoming an important design tool to investigate ventilation system performance, diagnose system problems and improve system designs. In this study, three kinds of 3D ventilation problems have been considered: (a) isothermal ventilation in simple rooms, (b) ventilation with coupled heat or mass transfer and (c) ventilation with simultaneous heat and mass transfer in an environmental test chamber with complicated internal configuration. They have been investigated numerically by using several turbulence models. The focus is to validate the turbulence models and modeling methods for their capability of simulating such ventilation flows with available experimental data and to evaluate their performances for the correct prediction of the above general ventilation problems often encountered in practice, especially ventilation flow in rooms with complicated internal configuration (humans, furniture, etc.) and passive or active sources (internal heat sources, CO_2 and other contaminant sources, etc.). The long-term objective is to evaluate the possibility of using CFD to investigate the ventilation flows and the associated heat and mass transfer processes inside a spacecraft cabin under microgravity. It is found that among the turbulence models tested, the two-equation SST k-ω model yields the best overall prediction for a wide range of ventilation flows, especially for the ventilation flows with complicated flow features such as impingement, recirculation and separation and with simultaneous heat and mass transfer. A preliminary study of a ventilation flow in an environmental test chamber with coupled heat and mass transfer and with complicated internal configuration (human simulators, computers, tables, lamps etc.) under normal-g and zero-g conditions shows that the microgravity environment has very strong influence on the air flow pattern and temperature and contaminant distributions inside the room, it demonstrates also that numerical simulation is capable of diagnosing possible environmental problems such as the occurrence of over-heating and over-pollution areas due to poor ventilation inside a spacecraft cabin and at the same time providing useful information for the optimization of the airflow design. Further studies are planned to also account for radiative heat transfer in the CFD predictions to more realistically represent the heat transfer process especially in a microgravity environment.

The study showed that the validation of turbulence models and near-wall treatment methods is very important for obtaining reliable prediction results of ventilation flows.

Key words: ventilation, numerical simulation, CFD, turbulence modeling, heat transfer, mass transfer, contaminant distribution, microgravity, spacecraft.

Résumé

Avec la disponibilité toujours croissante d'équipements de calcul très performants, la simulation numérique CFD est de plus en plus employée pour prévoir les modèles d'écoulements de ventilation et la distribution d'air dans les bâtiments. La CFD devient maintenant un outil de conception important pour examiner la performance de systèmes de ventilation, diagnostiquer des problèmes et améliorer les conceptions de systèmes. Dans la présente étude, trois sortes de problèmes de ventilation tri-dimensionnels ont été considérées: (a) ventilation isotherme dans des pièces simples, (b) ventilation et couplage avec le transfert de chaleur ou de masse, et (c) ventilation et couplage simultané avec les transferts de chaleur et de masse dans une salle de test d'environnement ayant une configuration interne compliquée. Ces problèmes ont été étudiés numériquement en employant plusieurs modèles de turbulence. L'un des buts est de valider les modèles de turbulence et les méthodes de modélisation pour leur capacité à simuler de tels écoulements de ventilation avec des données expérimentales disponibles, et d'évaluer la fiabilité de ces modèles pour la prédiction correcte des problèmes de ventilation généraux souvent rencontrés en pratique, c'est-à-dire, la prédiction d'écoulements de ventilation dans des pièces ayant une configuration interne compliquée (avec des personnes, des meubles, etc.) et comportant des sources passives ou actives (sources de chaleur internes, sources de CO_2 et de polluants, etc.). L'objectif à long terme est d'évaluer la possibilité d'employer efficacement la CFD pour prédire les écoulements de ventilation, les transferts de chaleur associés, ainsi que les processus de transfert de masse à l'intérieur d'une cabine d'un vaisseau spatial dans les conditions d'apesanteur. Un grand nombre de modèles ont été testés au préalable dans les conditions terrestres par comparaison avec les résultats expérimentaux disponibles dans la littérature, notamment ceux produits lors du vaste projet de recherche international réalisé sous l'égide de l'Agence Internationale de l'Energie (Annex 20: "Air Flow Patterns within Buildings"). Parmi les modèles de turbulence testés, on a trouvé que c'est le modèle SST k-ω qui peut apporter la meilleure prédiction complète pour un grand choix d'écoulements de ventilation, particulièrement pour les écoulements de ventilation avec des particularités compliquées comme l'impact (sur les parois) de jets ou de panaches thermiques, la recirculation et la séparation, et avec transfert couplé de chaleur et de masse. Une étude préliminaire d'un écoulement de ventilation dans un habitacle de test d'environnement avec transfert de chaleur et masse, et avec une configuration interne complexe comportant des simulateurs humains, des ordinateurs, des tables, des lampes, a été réalisée dans des conditions de gravité normale et de gravité nulle (g=0). Elle montre que l'environnement de microgravité a une influence très importante sur l'écoulement de l'air et sur la distribution de température et de polluant à l'intérieur de l'habitacle. L'étude montre que les modèles de turbulence et la simulation numérique, avec maillage très fin, permettent de diagnostiquer de possibles problèmes environnementaux à l'intérieur d'une cabine spatiale, comme l'existence de zones surchauffées ou sur-polluées résultant d'une mauvaise ventilation, et fournissent les informations utiles pour corriger ces défauts et optimiser le système de ventilation. Des études complémentaires sont prévues ultérieurement pour prendre en compte également le transfert de chaleur radiatif dans les prédictions CFD pour représenter avec plus de réalisme les processus de transfert de chaleur particulièrement dans un environnement de microgravité.

L'étude a montré que la validation de modèles de turbulence et des méthodes de traitement de proche paroi est très importante pour l'obtention des résultats de prédiction fiables d'écoulements de ventilation.

Mots clefs : ventilation, simulation numérique, CFD, modélisation de turbulence, transfert de chaleur, transfert de masse, polluant, microgravité, cabine spatiale.

Table of contents

Introduction

Motivation and outline of the thesis.

The present work is motivated by the problem of ventilation and its influence on the distribution of oxygen, carbon dioxide and temperature etc. inside a manned spacecraft cabin. In space, because of the microgravity environment, the natural convection due to the buoyancy of warm or cold air in a gravity field is eliminated or greatly reduced, many heat and mass transfer processes such as the mixing of the atmosphere constituents (O_2, N_2, CO_2, water vapour etc.) and the cooling of electric equipment etc. by natural convection which happen naturally on Earth must be accomplished by forced convection (ventilation), therefore an appropriate ventilation system is very important because forced ventilation is the primary means to promote the well mixing of atmosphere constituents and to remove the excessive heat produced by onboard equipment and the crew — both of the processes are very important to assure a comfortable thermal condition and a good air quality inside the cabin for the well-being of the crew and to promote their productivity.

The environmental condition inside a manned spacecraft cabin is maintained by the Environmental Control and Life Support System (ECLSS) which is a very complicated system consisting of many subsystems such as atmosphere control and supply (ACS) subsystem, temperature and humidity control (THC) subsystem, air revitalization (AR) subsystem etc. Its environmental control part is responsible for the control of the cabin total pressure, cabin air temperature and humidity, cabin ventilation, and also for the control of the concentrations of oxygen, carbon dioxide, and many other trace contaminants emitted by the crew and by various onboard equipment and construction materials. The main task of the cabin ventilation system is to distribute the freshly supplied oxygen to the cabin, to dissipate the heat produced by the onboard electric equipment and to diffuse the carbon dioxide exhaled by the crew to the cabin air by forced convection. The aim is to maintain a uniform distribution of oxygen, carbon dioxide, humidity and temperature in the cabin air to provide comfortable and productive living conditions for the crew. For this purpose, air ventilation and circulation has to be carefully optimized to allow the maximum mixing of oxygen with cabin air, efficient removal of carbon dioxide and other trace contaminants and for heat and humidity control. Unfortunately it is almost impossible to optimize the ventilation system design by means of experiments conducted on Earth because the influence of natural convection cannot be eliminated which may be responsible for an important part of the heat and mass transferred in the experiments. It is thus decided to investigate this problem with the help of Computational Fluid Dynamics (CFD) which, due to the ever-increasing availability of high-performance computation facilities and the rapid development of numerical techniques, is now increasingly employed to investigate building ventilation problems and has become one of the most generally used methods to study air flow pattern and air distribution in buildings.

Due to the presence of turbulence in ventilation flows and uncertainties in turbulence modelling and in specifying appropriate boundary conditions for air supply diffusers, ventilation fans, internal heat and mass sources etc., the numerical models and modelling methods used in CFD simulations must be validated against experimental data before they can be trusted to use for practical purposes, which is an important and necessary step of the simulation process.

In order to validate modelling and simulation methods for such airflow problems, it is necessary to compare simulation results with experimental data from carefully designed and well instrumented experiments. Up to now, such experiment data are only available for ground-based systems in open literature, and they are mainly for the room airflow problems in buildings. It was thus decided to limit the objectives of the present thesis to study some basic ventilation problems and the associated heat and mass transfer processes, which allow us to investigate separately the main classes of environmental problems encountered in a spacecraft cabin. Namely, we consider the following problems:

- ventilation under isothermal and homogeneous condition;

- ventilation with internal mass sources (heterogeneous, isothermal) or heat sources (homogeneous, non-isothermal);
- ventilation with internal heat and mass sources (heterogeneous and non-isothermal).

The last two problems involve a strong coupling between natural and forced convections. In fact the forced convection (ventilation) in an indoor environment or in a spacecraft cabin cannot be too strong due to the consideration of thermal comfort and energy saving, thus the airflow in such an environment is often of the character of turbulent mixed convection which is at present still a very challenging problem to solve by numerical simulations, and in some sense the problem is more difficult to solve for ground-based condition than for microgravity condition because in the latter case the influence of gravity and thus the influence of natural convection is greatly reduced. Once the solution method is validated for ground-based condition, we can expect that it can be safely used for microgravity condition.

The perspective of this study is: through such a study, we should eventually be able to answer the following important questions:

- For a given ventilation configuration, what will be the air flow pattern and air distribution in the cabin?
- For a desired air flow pattern, how and where the air supply diffusers and return openings should be placed and how many of them should be used?
- How well the ventilation experiments conducted on Earth represent the real cases in space?

The thesis' manuscript is organized as follows:

A brief introduction to the basic concepts of Environmental Control and Life Support System (ECLSS) and its functions is first given in Chapter 1 which is the background of the present study.

A general review on ventilation methods and their numerical simulations is presented in Chapter 2. The main issues and problems related to the modeling and simulation of ventilation flows are highlighted and analyzed.

The basic concepts of turbulence modeling and some commonly used turbulence models are introduced in Chapter 3. Some turbulence modeling problems pertaining to ventilation flow simulation are highlighted.

Chapter 4 presents the results of validation studies on isothermal 2D/3D ventilation flow simulation: validation of simulations on a 2D baseline test case (IEA Annex 20 benchmark Test Case 2D), ventilation in a 3D partitioned room featuring jet impingement, strong recirculation and flow separation and 3D ventilation with complicated boundary conditions (IEA Annex 20 Test Case B).

Validation studies on 3D ventilation flow with heat or mass transfer are presented in Chapter 5. Two test cases were considered: IEA Annex 20 Test Case E (Mixed convection, summer cooling) and IEA Annex 20 Test Case F (Forced convection, isothermal with contaminants).

Chapter 6 presents the results of validation studies on two test cases with complicated flow configuration and simultaneous heat and mass transfer: displacement ventilation (buoyancy-driven) in a complicated 3D room (PCs, human simulators, cabinets and lamps) with pollutant transport (SF_6) and forced ventilation with ceiling slot diffuser under the same configuration. For the latter case which is similar to the ventilation system in a spacecraft cabin (forced convection), simulations were carried out under normal g and zero g conditions. The results are compared in terms of velocity, temperature, SF_6 distribution and also thermal comfort to show the differences of heat and mass transfer processes under these two conditions and their influences on the thermal comfort.

Finally the general conclusions and the perspective for future study are presented in Chapter 7.

Chapter 1

Introduction to Environmental Control and Life Support System

In this chapter, a brief introduction is given to the basic concepts of Environmental Control and Life Support System (ECLSS) and its functions which is the background of the present study.

1.1 ECLS functions

The Environmental Control and Life Support (ECLS) System is a vital part of a manned spacecraft; it provides a habitat in which the crew can live and work in a safe and habitable environment. Generally an ECLS system is responsible for the following functions (NASA 2002):

- Provides oxygen and food for metabolic consumption;
- Provides potable water for consumption, food preparation, and hygiene uses;
- Removes carbon dioxide from the cabin air;
- Filters particulates and microorganisms from the cabin air;
- Removes volatile organic trace gases from the cabin air;
- Monitors and controls cabin air partial pressures of nitrogen, oxygen, carbon dioxide, methane, hydrogen and water vapor;
- Maintains cabin temperature and humidity levels;
- Maintains total cabin pressure;
- Distributes cabin air between connected modules.

1.1.1 ECLS subsystems and interfaces

There are many different approaches to perform the above ECLS functions. The choice depends on many factors such as mission requirements, cost and safety considerations and man-machine interactions etc. In general, an ECLS system consists of the following subsystems (Wieland 1994):

- Atmosphere revitalization (AR)
    - CO_2 removal/reduction
    - O_2 supply/regeneration
    - Trace contaminant monitoring and control
    - Microorganism control
- Atmosphere control and supply (ACS)
    - Monitoring major constituents
    - Atmosphere constituents (N_2, O_2) storage
    - Atmosphere components control
    - Total pressure control
- Temperature and humidity control (THC)
    - Temperature control
    - Humidity control
    - Ventilation
    - Equipment cooling
- Water recovery and management (WRM)
    - Water storage and distribution

- o Water recovery
- o Water quality monitoring

- Waste management (WM)

  - o Metabolic waste (urine, feces etc.) management
  - o Liquid wastes management
  - o Other solid wastes management

- Fire detection and suppression (FDS)

  - o Detection of incipient fire
  - o Suppression of fires
  - o Clean up after fires (smoke, debris, etc.)

- Other

  - o Food storage and preparation
  - o Thermally conditioned storage
  - o Personal hygiene

As an example, Fig. 1.1 gives a functional overview of the planned ECLS system for the International Space Station (ISS).

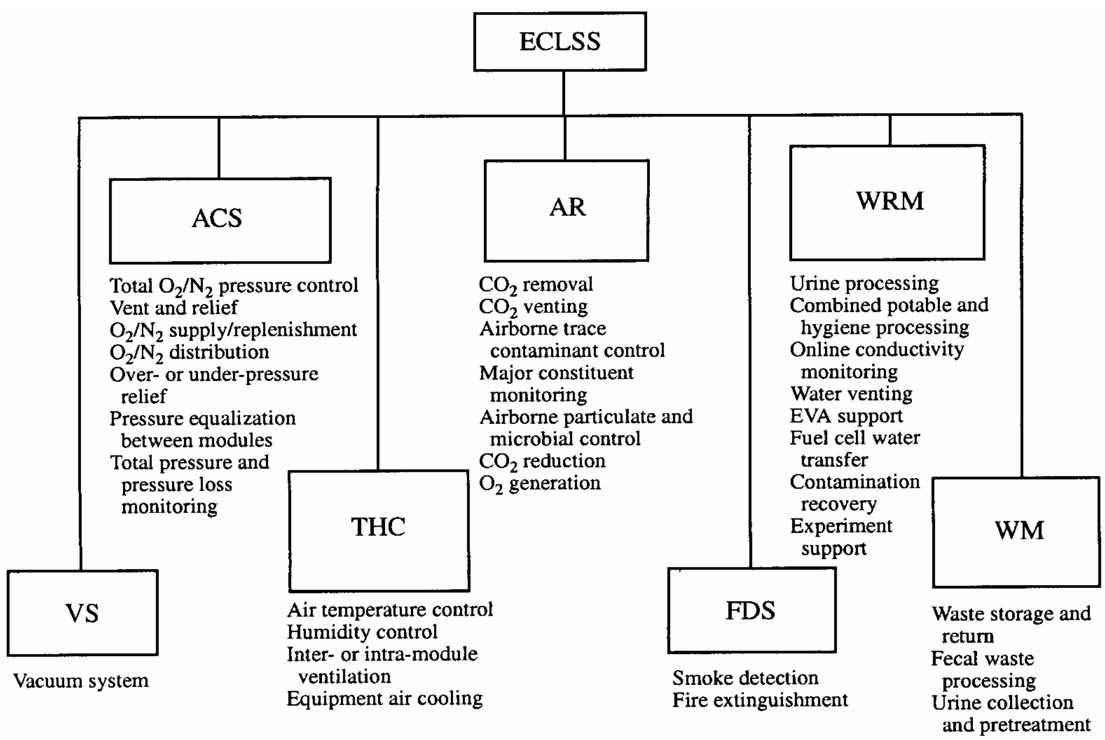

Fig.1.1 Overview of the ISS ECLSS functions (Jorgensen 2000)

The ECLS subsystems have complicated interactions. A simplified schematic of the interfaces between these subsystems for the ISS ECLSS is shown in Fig. 1.2.

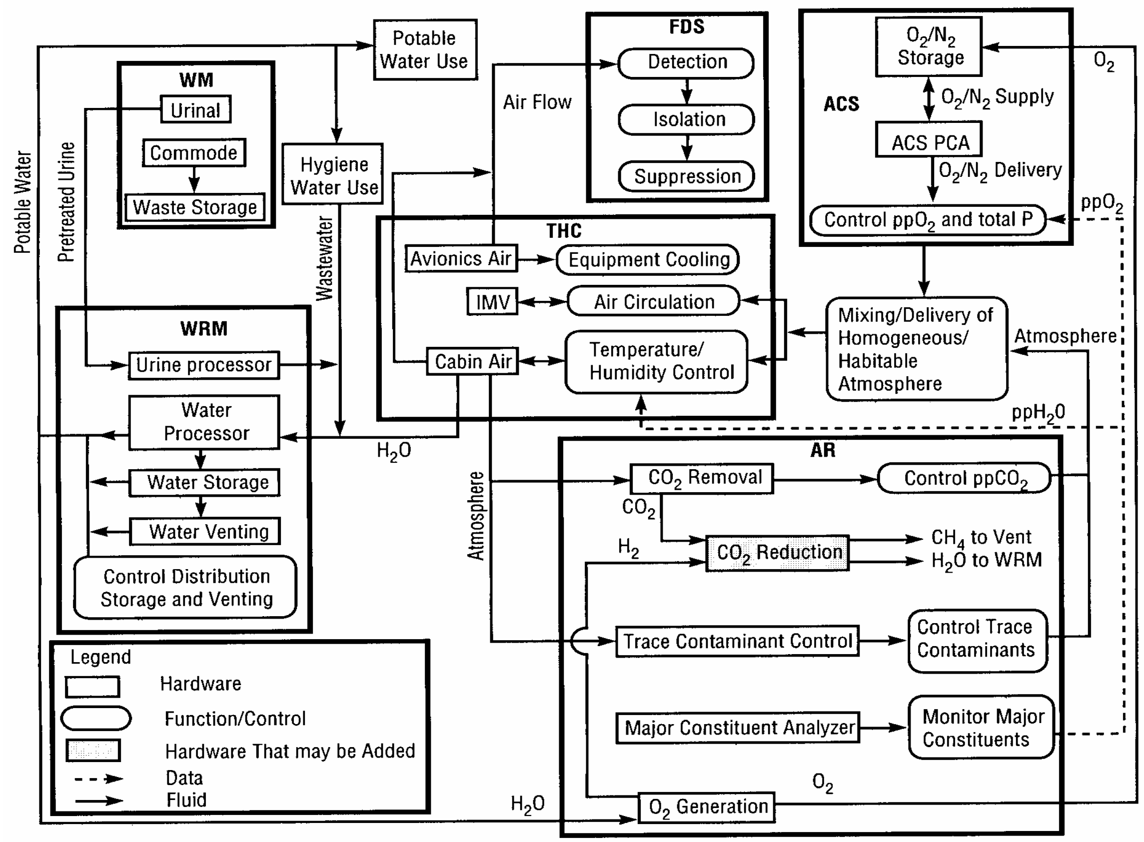

PCA: Pressure Control Assembly   IMV: Inter-Module Ventilation

Fig. 1.2 ECLSS subsystem interfaces (Wieland 1998)

1.2 General environmental control requirements

Among the above subsystems, the atmosphere control and supply (ACS) subsystem and the air temperature and humidity control (THC) subsystem are responsible for maintaining a healthy environmental condition i.e. appropriate atmosphere composition (O_2, N_2, CO_2 etc.) and total pressure, appropriate air temperature and humidity etc. inside the cabin, thus they are often referred to as Environmental Control System (ECS). The ECS requirements may differ for different missions. For the International Space Station, the general ECS requirements are shown in Table 1.1. Because ECS is an indispensable part for sustaining life in space, often an environmental control and life support system is simply referred to as a Life Support System (LSS).

Table 1.1 General ECS requirements for the International Space Station (Wieland 1998)

Parameter	US ECS Requirements Range	Russian ECS Requirements Range
Total pressure (kPa)	97.9 ~ 102.7	79.9 ~ 114.4
CO_2 partial pressure (kPa)	0.705 ~ 1.011	0.707 ~ 1.013
O_2 partial pressure (kPa)	19.5 ~ 23.1	19.5 ~ 23.1
N_2 partial pressure (kPa)	< 80kPa	< 80kPa
Atmosphere temperature (°C)	17.8 ~ 26.7	18 ~ 28
Relative humidity (%)	25 ~ 70	30 ~ 70
Dew point (°C)	4.4 ~15.6	4.4 ~ 15.6
Intramodule ventilation (m/s)	0.051 ~ 0.2	0.05 ~ 0.2
Intermodule ventilation (L/s)	66 ± 2.4	60 ~ 70

In an actual flight system, an ECLS system may contain all or only part of the above subsystems, which is determined by the mission requirements. There are complicated energy and mass flows inside/through the ECLS system. The energy (heat) flow is mainly from the onboard equipment and the crew to the THC subsystem, and then the excessive heat is rejected into space by radiating through space radiator or by evaporating a liquid through evaporating heat exchanger. The mass flow is mainly from the ACS, AR, and WRM subsystems to the crew and then to the WM subsystem. Fig. 1.3 shows the daily mass flows which should be managed by the ECLS system for an average sized person under moderate activity in space.

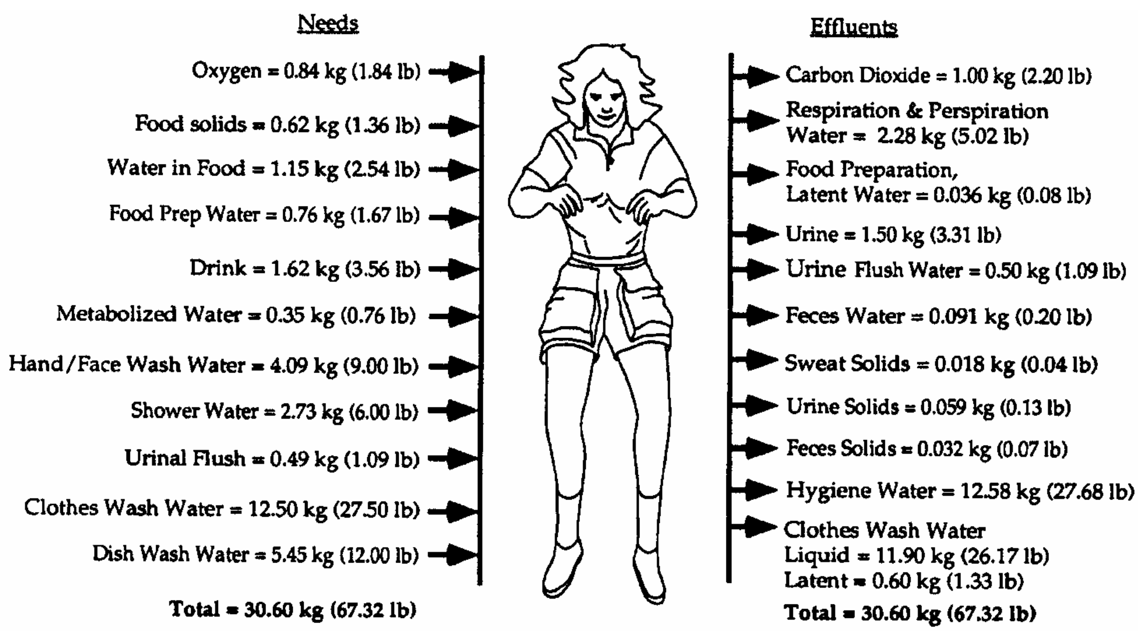

Fig. 1.3 Human needs and effluents mass balance (per person per day) (Wieland 1994)

The above values are based on an average metabolic rate of 136.7 W/person and a respiration quotient of 0.87. The values will be higher when activity levels are greater and for larger than average people. The respiration quotient is the molar ratio of CO_2 generated to O_2 consumed.

1.3 "Open-loop" vs. "closed-loop" ECLSS

A life support system can be described as "open-loop" or "closed-loop", depending on the flow of material resources through, or within, the system. Open-loop life support systems provide all required resources, such as water, oxygen, and food, from storage or resupply, and store waste materials for disposal or return to earth. In an open-loop system, the resources required increase proportionally as mission duration and crew size increase. Closed-loop life systems require an initial supply of resources but then process waste products, such as carbon dioxide, urine, and waste water, to recover useful resources, such as oxygen or water for reuse, thus reduce dependence on resupply. Both open-loop and closed-loop systems require energy from outside the system. The ultimate combination of technologies will be chosen based on results of system trade-offs to determine the optimal degree of closure, which is defined as the percentage of the total required resources provided by recycling, i.e., zero percent closure indicates that no resources are provided by recycling, and 100 percent implies that all resources are provided by recycling. (Wieland 1994)

Almost all of the ECLS systems onboard a manned spacecraft so far, except for the permanent spacecrafts like the Russian MIR station and ISS, were open-loop, i.e., no material was recovered or recycled. On the

Mir station, since 1989, the oxygen has been recovered by electrolyzing recovered waste water into O_2 and H_2; this has greatly decreased the resupply needs for oxygen and made it possible for a longer duration stay in space. The by-product H_2 from the electrolyzing process was vented into space. The ISS ECLSS has been planned to be a partially closed-loop system: the first step is to close the loop for the oxygen supply, which will be accomplished by electrolyzing the recovered water as has been done on the Mir station. The resulted H_2 will be vented into space at the beginning and eventually it will be used for the reduction of CO_2 by the Sabatier reaction (Wieland 1998):

$$CO_2 + 4H_2 \rightarrow 2H_2O + CH_4$$

The H_2O obtained from CO_2 reduction will be used as potable water or reused for producing O_2, thus further close the loop for oxygen supply. Also, the water loop will be eventually closed by processing the waste water into potable and hygiene water. The schematic of the planned ISS ECLS functions are shown in Fig. 1.4 to Fig. 1.9.

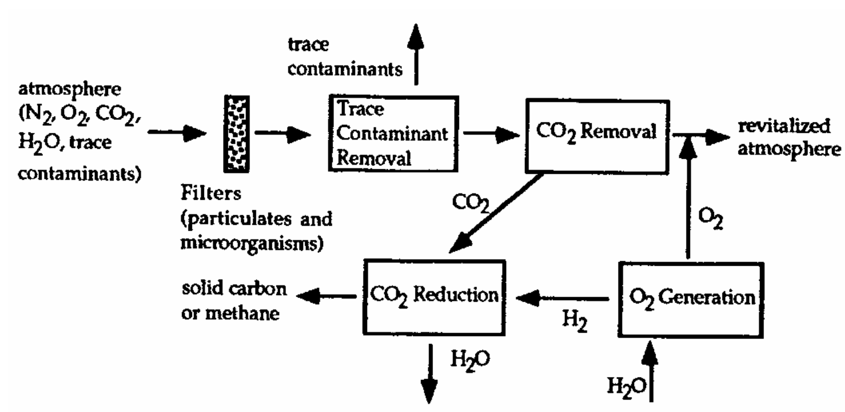

Fig. 1.4 Schematic of Air Revitalization (AR) on the ISS (Wieland 1994)

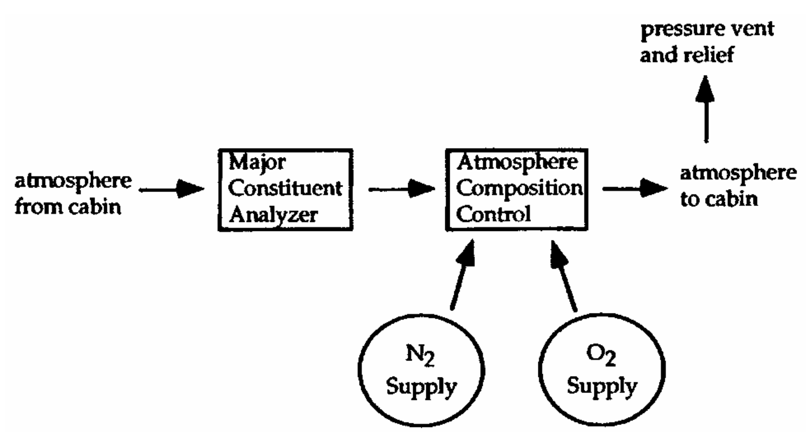

Fig. 1.5 Schematic of Atmosphere Control and Supply (ACS) on the ISS (Wieland 1994)

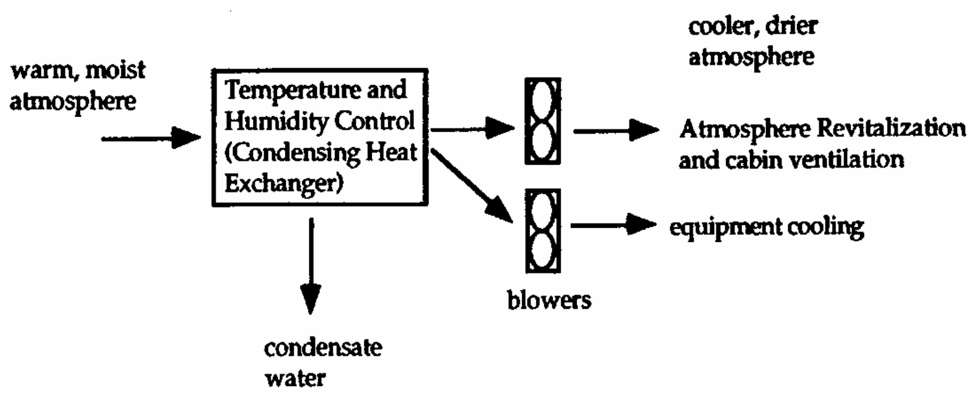

Fig. 1.6 Schematic of Air Temperature and Humidity Control (ATHS) on the ISS (Wieland 1994)

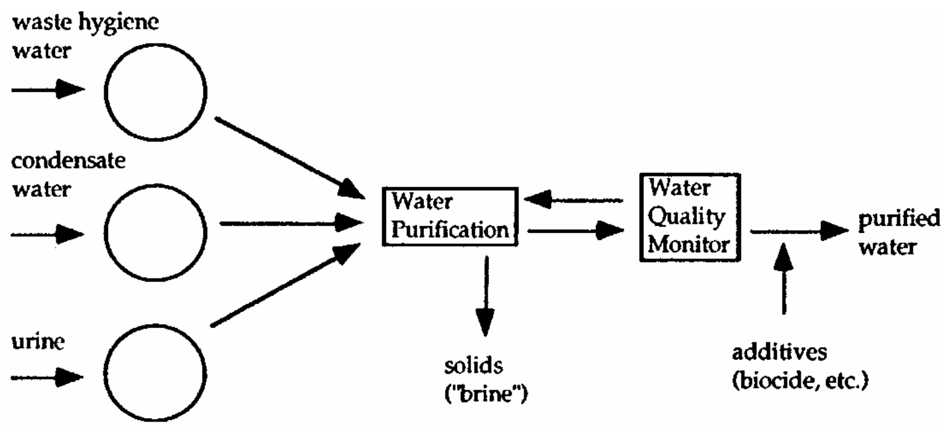

Fig. 1.7 Schematic of Water Recovery and Management (WRM) on the ISS (Wieland 1994)

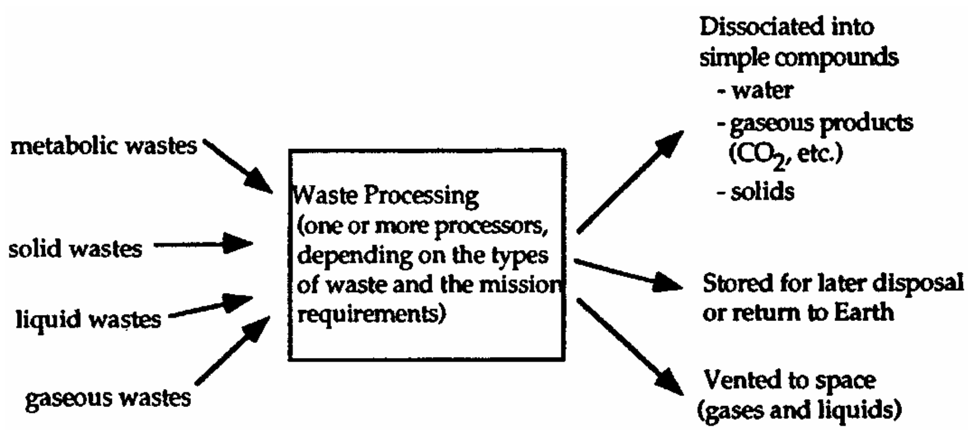

Fig. 1.8 Schematic of Waste Management (WM) on the ISS (Wieland 1994)

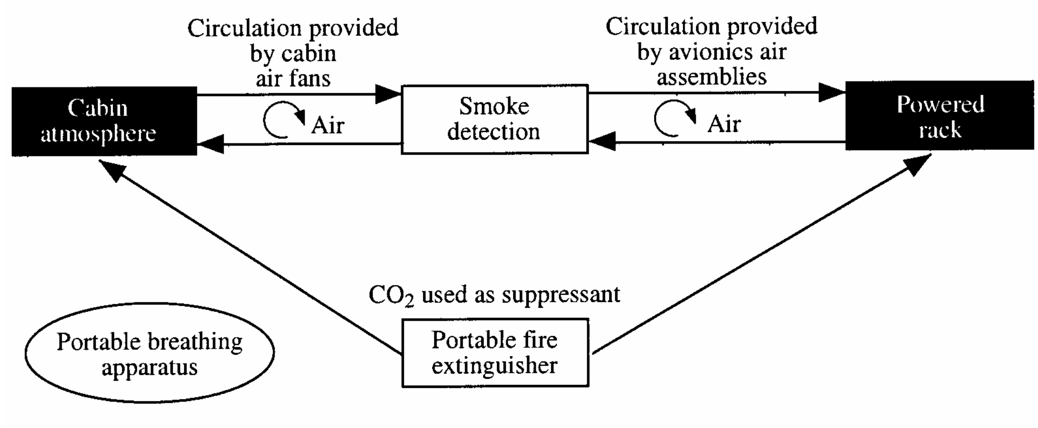

Fig. 1.9 Schematic of Fire Detection and Suppression (FDS) on the ISS (Jorgensen 2000)

1.4 Hierarchy of ECLS systems

There can be three levels of ECLSS:

- ECLSS depending on expendables
  Most of the ECLS systems used so far are at this level, i.e., all the required materials are brought from earth at launch or resupplied by resupply vehicles, and no waste is recycled or recovered, thus they are completely open-loop.

- Regenerative ECLSS (physical-chemical regenerative life support system)
  In a regenerative ECLSS, part of the required materials such as water, oxygen is recovered from wastes by physical-chemical processes. The loops for these materials can be partially closed or completely closed depending on the mission requirements and technological maturity. The ECLS system on the Mir station has been the first regenerative ECLSS in flight, in which the oxygen has been recovered from waste water since 1989. The ECLS system on the ISS is the second regenerative ECLSS in flight in which the loop for oxygen will be first closed by recovering it from the waste water and then the loop for water will be eventually closed by adding the CO_2 reduction assembly, thus reach the maximum closure (water and oxygen) at this level. A simplified schematic of the regenerative ECLSS is shown in Fig. 1.10.

- Controlled Ecological Life Support System (CELSS) or Biological (Bioregenerative) Life Support System (BLSS).
  As the mission duration becomes longer such as a mission to the Mars or the permanent stay on Lunar Bases, the cost for resupplying food and other necessary materials will become prohibitively high or resupply is simply impossible, it is necessary to recycle food, water, oxygen and carbon dioxide etc. by chained biological processes similar to those happening in Earth's biosphere—that's the aim of the Controlled Ecological Life Support System (CELSS) or Biological (Bioregenerative) Life Support System (BLSS). In a CELSS, photosynthetic organisms such as plants or algae are used to produce food, oxygen and potable water, and to remove carbon dioxide exhaled by the crew through photosynthesis process. Physical subsystems are required to support these biological processes, including a temperature and humidity control subsystem, a food processing subsystem to convert biomass (plants or algae) into edible food and a waste processing subsystem to convert waste products including waste water, into useful resources. Fig. 1.11 shows the basic elements of a CELSS.

The common feature for all the three levels of ECLS system is that an Environmental Control Systems (ECS), i.e., an atmosphere control and supply (ACS) subsystem and an air temperature and humidity control (TCH) subsystem, is indispensable. An ACS subsystem is necessary for the makeup of N_2 due to leakage to maintain the total cabin pressure; a TCH subsystem is indispensable for maintaining an optimum temperature and humidity level for both the human comfort and the plant growth, and for the mixing of atmosphere constituents (O_2, N_2, water vapor etc.) and equipment cooling by forced ventilation.

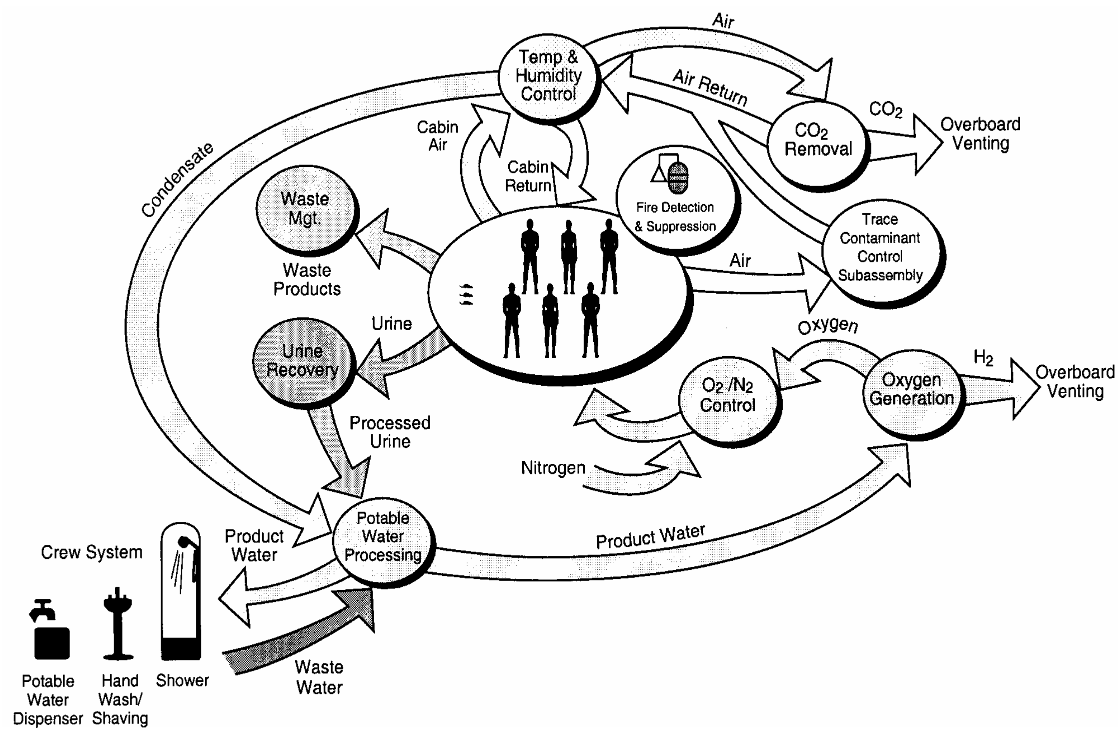

Fig. 1.10 Schematic of Regenerative Environmental Control and Life Support System (NASA 2002)

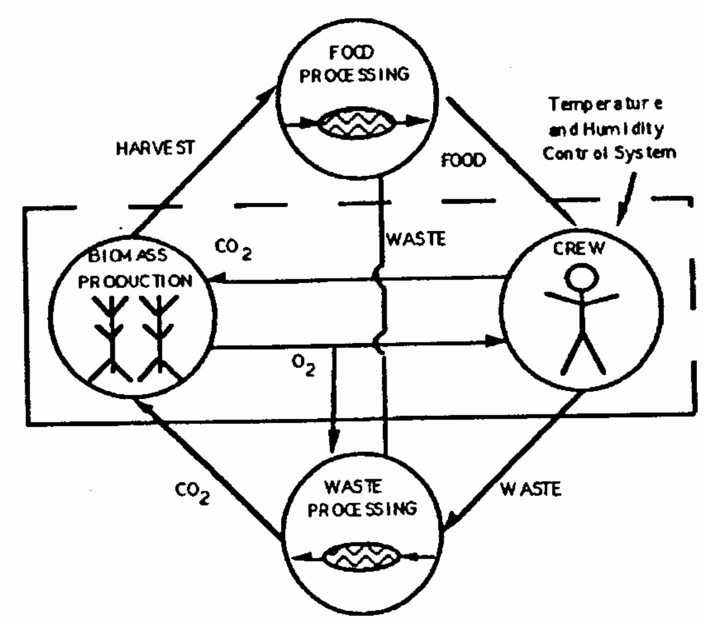

Fig. 1.11 Basic elements of a Controlled Ecological Life Support System (CELSS) (Wieland 1994)

1.5 Significance of forced ventilation in space

Forced ventilation is essential in order to ensure good mixing and circulation of the atmosphere constituents for adequate removal of CO_2, water, and trace contaminants and to provide sufficient O_2 for metabolic requirements. Ventilation is also the primary method of removing heat. The cooling of payloads is a special thermal control problem due to the need for forced convection. The natural convection of air on Earth due to the buoyancy of warm air in a gravity field is eliminated or reduced in space where microgravity (low earth orbit or transfer missions) or reduced gravity (Lunar and Martian missions) environments are encountered. The heat generated by electrical equipments must be removed and one of two methods is generally used to do this: forced convection or “cold plates”. Forced convection of the atmosphere over or through the equipment is an effective way to remove excess heat, provided the flow rates and temperatures are appropriate. For situations where forced convection may not be suitable or not enough, heat can be removed by conduction to liquid- or atmosphere-cooled cold plates to which the equipment is fastened. After the heat is removed from the equipment it must then be removed from the cooling fluid. For forced convection the heat must be removed by the Temperature and Humidity Control Subsystem (THCS), typically by a liquid-atmosphere heat exchanger. For liquid cooled cold plates (and for the liquid coolant in the THCS) the heat must then be removed by radiating it to space or conducting it to the external environment on the Moon, Mars, etc. (Wieland 1994)

Ventilation flow rates in the cabin are determined by medical requirements to avoid stagnant regions where the O_2 level may get too low or the CO_2 level too high, and by the requirements for heat rejection to accommodate the expected amount of waste heat generated by people, animals, equipment, and experiments. Another factor in selecting the ventilation rate is the total pressure. Lower total pressures require higher ventilation rates for the same amount of cooling capacity (Wieland 1994).

The air flow patterns inside the cabin are a function of the diffuser characteristics and location. Appropriate ventilation, especially in a microgravity environment, is essential to assure that no stagnant regions exist which could lead to the buildup of carbon dioxide, particulate, and trace contaminant levels in the habitat. To avoid the risk of draft, the maximum allowable air flow velocity inside the cabins is 0.2 m/s for the ISS. The air distribution system must be designed to ensure adequate flow across habitable volumes (“modules”) and the diffusers and return ducts must be positioned to avoid “short circuiting” of the flows (Wieland 1994).

Chapter 2

CFD Simulation of Ventilation Flows – A Review

In this chapter a general review on the ventilation methods and their numerical simulations is given. The main issues and problems related to the modeling and simulation of ventilation flows are highlighted and analyzed.

Ventilation is a process of introducing fresh air into a space of interest to dilute contamination and to remove excess heating or cooling loads. For building ventilation, the fresh air comes from outdoor or from HVAC (heating, ventilation and air conditioning) systems. In a manned spacecraft, the fresh air comes from Air Revitalization (AR) Subsystem (CO_2 and trace contaminants removal), Temperature and Humidity Control (THC) Subsystem (heat and water vapor removal) and Atmosphere Control and Supply (ACS) Subsystem (O_2 supply) as shown in Fig. 2.1. In space, because of the absence of natural convection, ventilation is also the primary means to remove the heat produced by onboard equipment and the crew and to promote the well mixing of the atmosphere constituents (O_2, N_2, CO_2, etc.) inside the cabin.

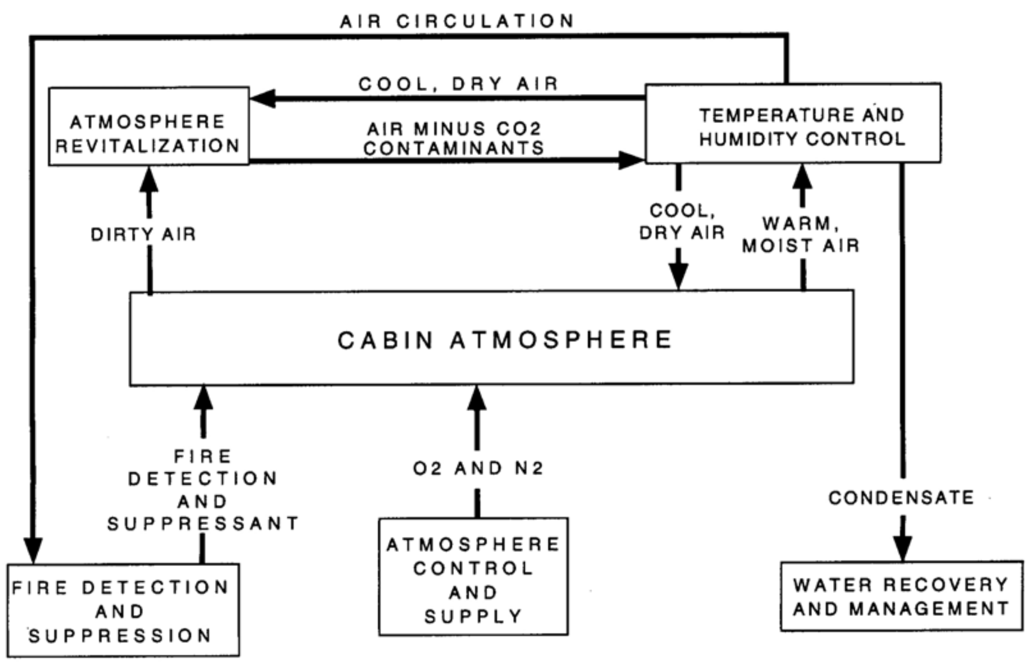

Fig. 2.1 Schematic of the cabin ventilation system of a manned spacecraft (NASA 1998)

In general, the objective of ventilation is to provide a habitat with good air quality and thermal condition that are more suitable for people and processes than what naturally occurs in an unventilated space with lowest possible energy consumption. Therefore, the value of ventilation lies in how well these basic needs are fulfilled. A good ventilation system can thus be defined as the one which can provide a habitat with healthy indoor air quality and comfortable indoor thermal condition with as low as possible energy consumption (Peng 1998).

2.1 Ventilation methods

There are several different methods for building ventilation. According to the approach of withdrawing air from a space, ventilation systems can be classified in two types: *local ventilation* and *general ventilation*. The former, which is widely used in industrial ventilation, exhausts air and contaminants from a limited region where pollution sources are located. Some local equipment such as a laboratory fume hood, glove box and canopy hood, etc. are often used. With the latter type, the air is extracted from the entire space and replaced with the make-up fresh air.

According to the approach of supplying air to a space, general ventilation can be further classified into *natural ventilation*, *mixing ventilation*, *displacement ventilation* and *plug-flow ventilation*. Natural ventilation does not rely on any mechanical system. Instead, room air motion is created by indoor and outdoor temperature and/or pressure differences through infiltration and ex-filtration. Natural ventilation has the advantage of zero energy consumption, but it relies heavily on the indoor and outdoor air conditions and is thus less controllable. It can be used in regions where the climate doesn't change much and is not often used in modern buildings. Mixing and displacement ventilation system are the most used types, which rely on mechanically driven systems built with fans, ducts, filters and air diffusers etc. (Peng 1994, 1998)

2.1.1 Mixing ventilation

In mixing ventilation, fresh air is supplied at a high momentum to induce overall recirculation and promote sufficient mixture of contaminants and fresh air. It is thus aimed at diluting the contamination level down to an acceptable level. To avoid sensible air draught in the occupied zone, the supply opening (usually a slot or a diffuser) is often installed at the ceiling level. In most of the cases the inflow forms a wall jet. As the initial momentum is large enough, the wall jet is able to reach the opposite wall and consequently becomes an impinging jet, see Fig. 2.2a (Peng 1998).

Although the wall jet is generally characterised by fully developed turbulence, the air motion in the occupied zone is often characterised by low velocities induced as a result of jet entrainment and air recirculation. Nielsen (1989) showed that the maximum velocity in the occupied zone is linearly proportional to supply air flow rate for isothermal mixing ventilation flows. If the ventilation air flow rate is lower than 4 ACH (air change per hour), however, this proportionality no longer holds and the velocity decays more sharply.

2.1.2 Displacement ventilation

In displacement ventilation, cooled fresh air is supplied at floor level with low momentum. Upward buoyant convection created by indoor heat sources carries contaminants into the upper zone, where recirculation and mixture occur and contaminated air and/or excess heat are exhausted (Fig. 2.2b). This system thus aims at directly delivering fresh air into the occupied zone without inducing significant mixture with contaminants. Therefore the buoyancy is the virtual origin of the air motion. Displacement ventilation can be used in cooling conditions only.

In displacement ventilation, the mechanism of inducing buoyancy relies on the behaviour of both air supply and heat sources. To investigate the performance of such a system, special attention must be paid to the air supply, buoyant convection, and their interaction. Since the air is supplied at a low velocity and at a temperature of usually 2~4 °C lower than the mean room air temperature, the inflow forms a gravity current due to buoyancy and spreads over the floor surface. On the other hand, heat sources (e. g. people, lamps and computers, etc.) create upward thermal plumes which then entrain surrounding ambient air and rise to the upper zone. The flow is thus characterised by stable thermal stratification with linear vertical temperature distribution in the room. Nevertheless, recirculating and mixing air motion often occurs locally, owing to the entrainment of thermal plumes and the downwards natural convection along non-adiabatic cold wall surfaces. Furthermore, the plumes created by heat sources may entail local turbulence damping in the vertical direction and trigger locally anisotropic turbulence. In the lower zone, weak turbulence often tends to be relaminarized. In numerical simulations, displacement ventilation flows are generally more difficult to handle than mixing ventilation flows (Peng, 1998).

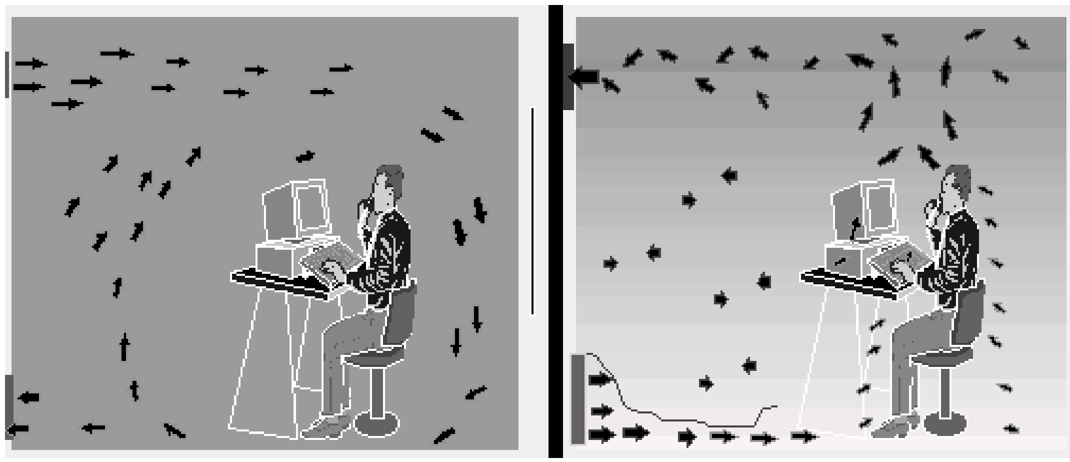

(a) Mixing ventilation (b) Displacement ventilation

Fig. 2.2 Illustration of mixing ventilation and displacement ventilation (http://www.glam.ac.uk/sot/envgeog/research/vent.php)

2.1.3 Plug-flow ventilation

In case of plug-flow ventilation which is used only in cleanrooms, a low turbulence and relatively low-velocity air flow is supplied across the entire cross-section of the room (usually from the ceiling), pushing forward the entire air volume to an exhaust which is also cross-section-wide. To keep contaminant concentrations at an acceptable level, this method is by far the best. However, due to the very large volume of air supply required, the costs are very high, even irrespective of the stringent air quality requirements in rooms (Roos 1998).

In space, because of the microgravity environment, the only viable ventilation method is mixing ventilation, i.e. forced convection entailed by ventilation fans, air supply diffusers etc., thus in the present study the emphasis is on the mixing ventilation and its numerical simulation.

2.2 The characteristics of ventilation flows

To correctly simulate ventilation flow, it is necessary to understand first the characteristics of ventilation flows.

Numerous experimental measurements have been carried out to study the characteristics of ventilation flows, such as the work of Melikov et al. (1988, 1990, 1997), Sandberg et al. (1987) and Kovanen et al. (1987). Most ventilation flows encountered in practice can be characterized as being incompressible, non-isothermal, turbulent, three-dimensional and unsteady (Loomans 1998; Peng 1998). In the main body of a ventilated room, measurements of air movement demonstrate high amplitude, low frequency fluctuations which is characteristic of transitional flows (Jones et al. 1992). Measurements carried out by Sandberg et al (1987), Hanzawa et al (1987) and Kovanen et al (1987) showed the turbulence intensity in rooms with mixing ventilation ranged about 20~30%.

In addition to the above general flow features, ventilation flows can often exhibit other local features in different regions of a ventilated space. Typical flow characteristics include wakes and vortex shedding behind obstacles, potential flow near exhaust openings, thermal jets or plumes arising above heat sources, and laminar and transitional flows in near wall boundary layers and in regions far from walls due to dampened turbulence with thermal stratification. These and other flow phenomena are associated with the ventilation system used: they may appear with one ventilation system and may not with another (Peng 1998).

In general, the physical process of turbulence in ventilation flows enhances mixing and entrainment which is necessary for the proper operation of air distribution systems (Jones et al. 1992). But too high a turbulence intensity should be avoided because it may cause local thermal discomfort (Fanger et al. 1988).

2.3 Numerical simulation of ventilation flows

There are two numerical approaches to study indoor airflow and contaminant transport in buildings — multizone modeling and CFD modeling. Multizone modeling takes a macroscopic view of Indoor Air Quality (IAQ) by evaluating average pollutant concentrations in the different zones of a building as contaminants are transported through the building and its HVAC system. CFD modeling takes a microscopic view of IAQ by examining the detailed flow fields and pollutant concentration distributions within a room or rooms (Emmerich 1997). The study of these two techniques has been the objective of a large international research project IEA Annex 20 "Air Flow Patten within Buildings" organized by the International Energy Agency (IEA). Each approach has strengths and limitations for studying different building ventilation and IAQ problems.

The study on indoor airflow has traditionally been an area of experimental and empirical research and for the most part has been limited to very simplified models of the physical indoor environment, due to the complicated flow characteristics of practical ventilation flows. CFD opened a new era to numerically predict the indoor climate on a detailed level with high flexibility in terms of configurations and boundary conditions. Information on thermal comfort and the effectiveness of the proposed ventilations system can be derived from the calculated indoor air flow pattern, temperature and contaminant distributions. According to Peng (1994), the unique advantages of using CFD can be summarized as:

- Substantial reduction in the cost of new designs;
- The ability to study systems where controlled experiments are difficult to carry out;
- The ability to study hazardous systems at and beyond their normal performance levels; and
- The unlimited detail of results and analysis options.

A special advantage of CFD for the ventilation system design is that various technical parameters of a ventilation system can be easily changed in a CFD simulation. It is thus possible to optimize in the design stage the performance of a ventilation system by specifying different sizes, locations and types for diffusers, enclosure layout and heat sources etc. If measurements were to be used for optimization, the process would be very costly and time consuming (Peng 1994).

With the ever-increasing availability of high-performance computing facilities, the above advantages have made the CFD prediction of ventilation flows increasingly attractive, especially when compared to the difficulties of experimental methods. A significant problem with experiment methods is that apart from being costly and time consuming, experimental measurements are often not possible to be carried out at full scale. Air distribution studies for the design of atria, theatres, indoor stadiums etc. can only be feasibly conducted with reduced scale models. However, tests carried out in a model should be made with dynamic and thermal similarity if they are to be directly applied to the full scale. This normally requires the simultaneous equality of the Reynolds number (Re) and the Archimedes number (Ar) between the model and the full scale, which is impossible to achieve in the model concurrently (Awbi 1989). On the other hand, CFD prediction is capable of providing detailed velocity and temperature distributions from which interpretations relating thermal comfort and energy use can be made. It is also possible to predict the spatially and temporally varying distribution of indoor air pollution within the space and hence evaluate ventilation efficiency. The effectiveness of a ventilation system is mainly determined by: (a) the removal of internally produced contaminants from the room; and (b) the supply of fresh air of acceptable quality in the room, in particular to the inhabited zone. It depends on the entire air flow pattern in a room (Peng 1998). The availability of CFD prediction has significantly enlarged the scopes and possibilities in ventilation research, it is now becoming one of the most generally used methods to study indoor air flow and air distributions.

The major requirements of air flow modeling in buildings are to predict and provide information on the following topics (Jones et al. 1992):

- Thermal comfort, which is important for the well-being and productivity of occupants. It can be defined in terms of a range of environmental and physiological factors which include air velocity and temperature, turbulence intensity, mean radiant temperature, vector radiant temperature, humidity, clothing level, metabolic rate and external activity level;
- The effectiveness of the ventilation system in removing or controlling contaminants and providing specified standards of air cleanness for example, in a process environment or operating theatre;
- The effectiveness and efficiency of energy distribution in the space, including heat transfer processes within the main body of the room and at surfaces.

In short, these requirements are about the *thermal comfort*, *indoor air quality* and *energy efficiency* that a given ventilation system can provide. They form the basic requirements for assessing the performance of a ventilation system and should be considered in the ventilation system design. These aspects can be explored in detail with the aid of numerical simulations. In ventilation practice, CFD is now becoming a powerful tool to investigate system performance, diagnose system problems and improve system designs. The development of CFD as a reliable alternative and complement to conventional experimental measurements is thus of great practical importance in building research to realize the above basic requirements on building ventilation (Peng 1998).

2.4 General Problems in Modelling Ventilation Flows

2.4.1 The need of validation

Despite all the above advantages, there are still many uncertainties in turbulence modeling and in specifying appropriate boundary conditions for air supply devices, internal heat and mass sources etc. in CFD predictions, thus experimental validation of the models and modeling methods remains as an important and necessary step for a quantitative credibility of the simulation results. Loomans (1998) stated that validation of CFD-simulations and the quality of the model is an "intrinsic" part of the simulation process. Once the model and modeling methods are validated, they can be used for conducting parameter studies by changing, for example, the position, the type, the number of the air supply diffusers or by changing the ventilation rate, room layout etc. – this is one of the most attractive features of CFD: it can easily simulate a ventilation flow under a wide range of alternate configurations and parameters.

There are very few well-documented full-scale three-dimensional validation studies on indoor air flows in open literature, possibly due to the high investment involved for carrying out full-scale experimental measurements and the limitation of currently available measuring methods. The characteristics of indoor air flow (low velocity and high turbulence intensity) and the level of measuring accuracy required for validation purpose place high demands on measurement techniques (Loomans 1998).

2.4.2 Air flow velocity measuring problems

Loomans et al. (1995) surveyed the currently available measuring techniques for indoor air flow studies and grouped them in five categories:

- Visualisation techniques
  These techniques make the whole flow pattern visible (for the human eye). From recorded images of the visualised flow pattern it is eventually possible to retrieve quantitative information.
  Examples: smoke and helium-filled soap bubbles.
- Heat transfer techniques
  These techniques are based on the transfer of thermal energy from a heat source to the fluid flow. The quantity of transferred energy is a measure for the flow velocity.
  Example: hot wire anemometry.
- Time-of-flight techniques
  In these techniques, the time interval between the upstream injection of the tracer and its downstream detection is measured; or the displacement of a tracer during a time interval is measured. Sonic pulses, ions or particles can be used as tracer.
  Examples: sonic anemometry and particle tracking velocimetry.
- Kinetic energy techniques
  The kinetic energy is transformed into a pressure difference, which is a measure for the velocity of the fluid.
  Examples: Pitot tube and cup anemometry.
- Doppler effect techniques
  Velocities are determined from changes in propagation of light waves through the fluid. The waves are scattered by particles in fluid, causing a frequency shift (Doppler shift) of the emitted wave.
  Example: laser-Doppler anemometry (LDA).

After a detailed review and evaluation of the above methods, he concluded that the currently most practical and most applied technique — the hot-sphere anemometer and the most promising technique for indoor air flow velocity registration — Particle Tracking Velocimetry (PTV), both have their limitations when applied to indoor air flow studies. The accuracy that can be obtained with hot-sphere anemometer is very restricted because this anemometer derives the velocity from the heat transfer between the probe and the surrounding air. Such a measurement technique requires an accurate ***conformity*** between calibration and application conditions to attain the expected measurement accuracy. In the case of ventilation flows where the air flow speed is often very slow, the measurement accuracy is further restricted by the self-heating of the probe. Furthermore, it can only give the velocity magnitude but can not give velocity direction because it is omni-directional, thus strictly speaking, the measured air flow velocity obtained with hot-sphere anemometer is not directly comparable with that obtained by CFD predictions because it is the mean air speed while the latter is the magnitude of the mean velocity vector. Nevertheless, he concluded that this technique is still the currently most readily applicable measuring method for indoor air flow studies. The application of PTV is very much hampered by the sufficient and homogeneous production of the applied tracer particle—a helium-filled soap bubble, which is required to visualise the flow pattern. Furthermore, it requires a very high investment and technical skills, and thus is not widely available.

The above review of Loomans et al. (1995) can explain why there are so few full-scale or even model-scale validation studies on 3D ventilation flows in the literature. As was emphasized by Loomans (1998), effort to improve the reliability of the CFD technique is only possible through comparison with accurate full-scale experiment measurements. In the past, empty rooms have been the most commonly used subjects of investigation and relatively good results have been reported, but more realistic flow problems are often those that have multiple heat/mass sources and obstacles in rooms, these problems put much higher demands on the simulation process; but if CFD is to be used as a design tool for practical ventilation system design, more validation studies and experiment data are needed for such practical cases which are at present still very scarce in the literature.

2.4.3 Main problems for indoor airflow simulation

At present, there are still many problems which need to be resolved for the accurate prediction of air flow pattern and air distribution in rooms. The following problems have been identified by many authors (Moser 1991; Chen et al. 1992; Lemaire 1993):

- Appropriate turbulence models at the Reynolds-number range of ventilation flows.

  Most of the turbulence models were developed from some basic flows of high Reynolds numbers. Their suitability for the prediction of indoor airflows for which the Reynolds number is considerably low and their ability to handle the complicated flow features such as those found in ventilation flows need to be evaluated and verified against experiment data. Chen (1988) indicated that airflows in rooms in many cases include natural or mixed convection, and the overall turbulence Reynolds numbers are rather small. The commonly used turbulence models together with logarithmic wall functions may not be suitable for regions both near the wall and far away from it. Chen (1995, 1996) tested eight popular eddy-viscosity and Reynolds-stress models for predicting natural convection, forced and mixed convection, and impinging jet flows in rooms, he found that none of the models produces satisfactory results. The difference between the computed turbulence level and the measured one can be more than 100%. A model may perform well in one case and poorly in another. Therefore, for each type of flow, an experimental validation is always required to ensure the suitability of the model used (Chen 1997).

- Appropriate near-wall treatment.

  The commonly used standard wall-function was developed from forced convection flows, its validity for natural convection or mixed convection boundary layer flows often found in ventilation flows is questionable. Loomans (1998) found that the available wall functions are not valid for developing boundary layer flows, free convection flows and impinging plumes as appear indoors and will lead to grid dependent solutions. Peng (1998) indicated that using the conventional wall function might be an inappropriate approach for near-wall treatment, particularly when the flow is not fully developed turbulence (e.g. with low supply air flow rate) and when the flow is characterized by separation and affected by thermal buoyancy forces. Gosman (1999) indicated that buoyancy and low-Reynolds number effects in both the near-wall and bulk flow regions have proved to be particularly difficult to capture correctly by turbulence models, and in case of near-wall flows these often require direct calculation of boundary layers rather than the use of wall functions, which can be excessively expensive for indoor airflow simulation because there are often lots of flow obstacles in the flow regions and thus many walls.

  Another problem related to the near wall treatment is the calculation of convective heat transfer at walls. Many investigators have reported that the heat transfer calculated by wall functions is very sensitive to the near-wall grid spacing. A coarse grid results in the underestimation of the convective heat transfer coefficient, and vice versa. The main reason for the grid dependency of traditional wall functions is that they are based on the logarithmic velocity profile of boundary layer flow with zero pressure gradient, so strictly speaking, they cannot model boundary layers which have a different velocity or temperature profile, such as mixed or natural convection, or wall jet flow. As a result, if a coarse grid is used, the traditional wall functions will underestimate the convective heat transfer coefficient because the first grid point is further from the wall than the locus of maximum convection velocity. Conversely, if a fine grid is used, the convective heat transfer coefficient is overestimated, because the first grid cell is located within laminar region of the boundary layer, and so the chosen high-Reynolds number turbulence model incorrectly enforces turbulent flow in the grid cells lying within the inner region of the boundary layer. That will result in an unnaturally high convective heat transfer coefficient due to an artificial increase in the temperature gradient at the wall. Another weakness of the traditional log-law wall functions is that they fit the experimental data poorly for values of local Reynolds-number in the range $8<y^+<40$, while fit good for $y^+<8$ and $y^+>40$ (Schild 1997). Murakami et al. (1995) indicated that the use of wall function approach is particularly limited in the analysis of the heat transfer mechanism at a wall. For analyzing the heat transfer accurately, the Low-Reynolds Number (LRN) models with no-slip boundary condition should be used. But application of these models to ventilation flows remains difficult because very fine mesh grids are needed in the near wall regions which is limited by the available CPU capacity and computer memory.

- Boundary conditions of air supply devices

  Chen et al. (1992) indicated that the air diffusion in a room is dominated by diffuser type and the air supply parameters of the diffuser, but it is difficult to compute the airflow around a diffuser because of the complex geometric configurations of diffusers used in practice. Without a correct description of the airflow around a diffuser, the simulations of air diffusion in rooms are not reliable. Hence, an appropriate method suitable for simulating diffusers is essential in predicting room air motion. Murakami et al. (1995) indicated that the most important regions for simulation of a flow field in an enclosure are the areas around the supply jet and the exhaust opening, since the velocity gradient is very steep in these areas. Most energy production and dissipation occurs here. We should therefore be very careful in setting the grid discretization in these areas. However, when analyzing room airflows, it is usually impossible to arrange sufficiently fine grids at the supply and exhaust openings, so the simulation results will inevitably have significant errors in these regions.

- Grid-dependence

  Ventilation flows are often three-dimensional. It was found that a grid-independent result is very difficult to achieve in three dimensional cases especially when buoyancy effects exist.

- Convergence

  When calculating flow fields with buoyancy effects which is often the case for room air flows, the convergence is generally poor. Improved speed and stability of the numerical procedures to reach the solution are needed for the prediction of practical ventilation flows.

- Grid generation.

  Mesh generation is very time consuming, and accounts for typically 80% of the total time needed for case preparation (Schild 1997). More efficient and easy-to-use grid generation methods are needed to account for the complicated flow configurations often found in an indoor environment.

In a more recent review, Gosman (1999) highlighted the following problems for the simulation of indoor air flows:

- Convective heat and mass transfer requires consideration and modeling of turbulence effects, accurate prediction of the relevant flow field features is a prerequisite to good heat/mass transfer modeling. Surface heat transfer is particularly sensitive to details of the wall boundary layers, including their turbulence structure—ironically often more than the flow itself. Thus, predictions of heat transfer coefficients may be less accurate than friction factors. This is sometimes compensated for pragmatically, by employing empirical heat transfer coefficient correlations in the CFD model.

- Buoyancy-induced flows are particularly challenging to model due to the strong interactions between the flow and density fields, which can either augment or diminish the turbulence, according to whether the flow is unstably or stably stratified, respectively. Stable stratification can lead to locally low Reynolds numbers and additional associated modeling difficulties.

- Pollutant dispersion modeling from localized sources involves similar issues as heat transfer, including sensitivity to turbulence anisotropy, even in simple boundary layer flows.

Despite the problems listed above, the consensus among investigators is that conventional CFD codes can predict room air movement with sufficient realism to be useful in most design practices, provided that sound engineering judgment is exercised in its use (Lemaire 1993)

2.5 Review of the validation data used in the present study

2.5.1 The IEA Annex 20 Project

As stated above, the validation of numerical models and modeling methods is a necessary step for a quantitative credibility of CFD predictions. Buchanan (1997) and Loomans (1998) have reviewed the validation studies conducted so far in the field of room air flow simulations. Both of them have emphasized that the lack of carefully designed and well-documented validation data for ventilation flows in realistic three-dimensional configurations is one of the important limiting factors for the development of new modeling techniques for room airflow simulations.

For providing realistic benchmark data in a three-dimensional configuration with practical relevance to validate numerical models for room airflow simulation, the International Energy Agency (IEA) has organized a large-scale international research project: "Energy Conservation in Buildings and Community Systems—Annex 20: Air Flow Patterns within Buildings". The aim of its subtask-1 "Room Air and Contaminant Flow" is to evaluate the performance of numerical methods for the prediction of air flow patterns in buildings. The main objectives were (Lemaire 1993):

- To evaluate the performance of three-dimensional complex and simplified air flow models in predicting air flow patterns, energy transport and indoor air quality (IAQ);
- To show how to improve air flow models;
- To evaluate their applicability as design tools;
- To produce guidelines for selection and use of models;
- To acquire experimental data for evaluation of models.

Researchers from thirteen countries have participated in this project. Within a research period of three years and a half (May 1, 1988 ~ Nov. 1, 1991), many full scale experiments on forced convection, mixed convection and natural convection have been conducted by different research groups in an identical three-dimensional experiment configuration (IEA Annex 20 Standard Test Room) on different sites and many useful experiment data acquired and compiled and relevant numerical simulations carried out. It remains as the most important and most complete validation study on indoor air flow simulation carried out so far. The main conclusions concerning the performance of numerical models in predicting air flow parameters are as follows (Lemaire 1993):

- For isothermal air flow, almost all the CFD models and modeling approaches can predict the flow pattern and velocity decay with an acceptable degree of realism. In some cases velocities are under-predicted, but the reason is not clear. The 2D test results showed very good agreement for velocity decay and for the general trend of the turbulence kinetic energy, although the latter was generally under-predicted.
- For buoyancy-flow, the CFD models can predict flow pattern, velocity and temperature distribution, but with a reduced reliability compared with that demonstrated for isothermal flow. It was hard to obtain converged and grid independent results.

Main problem areas were also identified through this project, among them the two most important problems are the appropriate modeling of turbulence in room air flows and the correct modeling of air supply devices (Lemaire 1993).

Full-scale experiment measurements on five types of ventilation flows typically encountered in practice were carried out in this project, including (Lemaire 1993):

- Test Case B: Forced convection, isothermal;
- Test Case D: Free convection with a radiator, winter heating;
- Test Case E: Mixed convection, summer cooling;
- Test Case F: Forced convection, isothermal with contaminants;
- Test Case G: Displacement ventilation.

Also for the purpose of evaluating numerical simulation methods (CFD) as a practical design tool and to provide realistic benchmark data to validate CFD codes, a complicated nozzle diffuser was purposely chosen as the air supply device in the IEA Annex 20 project which was proved to be particularly difficult to model later (Nielsen 1992, Lemaire 1993). In the present study, the IEA Annex 20 experimental data are extensively used to validate numerical models and simulation results for forced convection (ventilation) flows similar to those likely encountered in a spacecraft cabin. More specifically, studies are carried out on the following Test Cases:

- Test Case B: B2 (3 ACH) and B3 (6 ACH)
- Test Case E: E2 (3 ACH) and E3 (6 ACH)
- Test Case F: F1, F2 and F3 (1.5 ACH)

The experimental data of Heikkinen (1991b, Test Cases B2, B3 and Test Cases E2 and E3), Blomqvist (1991b, Test Cases E2 and E3) and Heiselberg (Test Cases F1, F2 and F3) are used to validate the simulation results.

2.5.2 ASHRAE-1009

As has been identified in the IEA Annex 20 project and also been pointed out by many authors (Chen et al. 1992, 2001; Moser 1991; Nielsen 1992; Lemaire 1993; Murakami et al. 1995) the modeling of the air supply devices is one of the most important problems for the correct prediction of air flow pattern in rooms. To provide guidelines for the correct modeling of some most often used air supply devices in modern buildings, the ASHRAE (American Society of Heating, Refrigerating and Air-Conditioning Engineers) has sponsored a research program "Simplified Diffuser Boundary Conditions for Numerical Room Airflow Models" which was carried out by Chen et al. (2001). In this program, the modeling methods for eight commonly used air supply devices including nozzle diffuser, valve diffuser, displacement diffuser, grille diffuser, slot diffuser, square and round ceiling diffuser and vortex diffuser were studied and validated against experiment measurements carried out in a environment test chamber with complicated internal configuration: two human simulators, two computers, two tables, two cabinets and four lamps. A tracer gas SF6 was used to simulate the transport of CO_2 exhaled by the persons. Measured data include mean air speed, temperature and SF6 concentration at chosen points inside the test chamber. Two experimental measurements from this program are chosen to validate the modeling methods and simulation results in a complicated practical configuration with simultaneous heat and mass transfer in the present study: the case with the displacement diffuser and the case with ceiling slot diffuser. The former is used to validate the numerical models for the simulation of buoyancy-driven flows which is well-known to be very difficult to handle by the turbulence models and the latter is used to validate the numerical models for the simulation of forced convection flows with simultaneous heat and mass transfer, which is similar to what happens in the ventilation system of a spacecraft cabin.

2.6 Review of CFD simulation of ventilation flows for space application

There have been very few reports about CFD simulation of ventilation flows for space application in the literature. Earlier reports include that of Embacher et al. (1991) about the application of CFD tools in space projects, an example of CFD analysis of ventilation for electronic cooling under microgravity environment is given. Markus et al. (1992) has reported a 3D CFD analysis of CO_2 distribution in the COLUMBUS Attached Pressurized Module (APM) for the purpose of fire suppression: it was foreseen that in case of fire in APM, a CO_2 stream will be injected into the module to extinguish the fire. In their CFD analysis the complex inlet conditions were examined in detail to investigate a proper method for implementation in the model, and several runs with different nozzle positions and mass flow rates were carried out. Their results showed that a fire in the COLUMBUS APM sub-floor area can be extinguished by blowing CO2 into the volume. McConnaughey (1992) has conducted a CFD analysis of the air distribution system aboard the Space Station Freedom (the later International Space Station) using the INS3D code. An algebraic turbulence model specially calibrated for internal ventilation flows was used to account for the effect of turbulence on the airflow. Through such an analysis, several regions with too low air speed and short-circuit ventilation were identified.

In recent years, more reports about the CFD simulation of ventilation flows emerged in the literature, this is likely due to the availability of ever-increasing computation power and the more efficient numerical techniques and simulation codes. Examples include the work of Burgio et al. (1997), who reported a CFD application to analyze the Fire Detection and Suppression (FDS) system of the COLUMBUS APM for the well positioning of fire and smoke detectors and also CO_2 injectors for the effective detecting and distinguishing of fire, the commercial CFD codes PHOENICS and FLUENT were used for the CFD analysis and the standard k-ε model and the RNG k-ε model were used for the modeling of turbulence. Lin et al. (2000) reported a CFD study on the ECLSS airflow and CO_2 accumulation in the International Space Station because during a flight on ISS, the astronauts reported improper ventilation and stuffiness of air. To diagnose the problem, a CFD model of the air distribution system was built to characterize air flow between the ISS elements, the study of CO_2 accumulation was accomplished by simulating the generation and the transport of CO_2 due to the metabolic sources of the crew and the blockage or disruption of the air path inside the ISS. The study showed that poor air exchange occurs between several ISS elements and some measures to improve the air flow and exchange were predicted based on the CFD analysis. Steelant et al. (2001) reported an application of CFD simulation of ventilation flow inside the Automatic Transfer Vehicle (ATV) and the simulation of the venting of the payload chambers of the COLUMBUS module, both of them are parts of the International Space Station. The CFD code CFX was used for the CFD simulation. Eckhardt et al. (2003) reported a CFD analysis of the ventilation system in X-38, the "life boat" of the ISS which serves as an emergency return vehicle for the crew. The complicated interior geometry of X-38 was represented in the CFD model through the use of an unstructured mesh and a CFD code FLUENT was used to carried out the simulation. It was claimed that partly due to the use of CFD, the estimated costs of building the X-38 are less than one-tenth the cost of previous space vehicles.

It can be foreseen that with the easy access to the ever-increasing high-performance computation resources and with the efficient numerical techniques and enhanced numerical models now available, CFD will be increasingly used to analyze air flow and air distribution problems in manned spacecraft due to the special microgravity environment of spaceflight which cannot be reproduced on Earth, but can be more easily considered (with considerably reduced buoyancy convection) in CFD simulations—which is a very attractive and unique feature of CFD for the analysis of ventilation flows in space.

Chapter 3

Turbulence Modeling

In this chapter the basic concepts of turbulence modeling and some commonly used turbulence models employed in this study are presented. Special problems related to ventilation flow modeling are highlighted.

The description of turbulence modeling is the subject of very abundant literature, and textbooks among which we can recommend: Launder et al. (1972), Rodi (1980), Schiestel (1998), Celik (1999) and Wilcox (2000) etc. In this chapter, the basic concepts of turbulence modeling and some commonly used turbulence models used in this study are presented for easy reference. Interested readers are referred to the above textbooks or Fluent Inc. (2001) for more details of the models. A good recent review can be found in Jaw et al. (1998a, 1998b) or in Rodi (2000).

A fluid motion is described as turbulent if it is rotational, intermittent, highly disordered, diffusive and dissipative. The general characteristics of turbulent flows can be summarized as:

- Irregular (disorderly or random)
- Transient (always unsteady)
- Three-dimensional (spatially varying in 3D)
- Diffusive: enhances mixing and entrainment
- Dissipative: dissipates kinetic energy into heat
- Occurring at large enough Reynolds numbers

The mechanism of turbulence is often described in terms of *eddies* and *energy cascade*. A turbulence eddy can be thought as a local swirling motion whose characteristic dimension is on the order of the local turbulence length scale. Because turbulence is a continuum phenomenon that exists on a large range of length and time scales, the turbulent eddies also overlap in space, where larger eddies carry smaller ones. Through the interaction of turbulent eddies of different scales (or turbulent eddy sizes), energy is transferred from larger scales to smaller scales, and eventually to the smallest scales where the energy is finally dissipated into heat by molecular viscosity. This process of energy transfer is referred to as *energy cascade*. Thus turbulent flows are always dissipative (Celik 1999; Wilcox 2000).

It is generally accepted that turbulence can be described by the Navier-Stokes momentum-transport equations, which express the conservation of momentum for a continuum fluid with viscous stress directly proportional to the rate of strain (Celik 1999). The Navier-Stokes equations together with the conservation equations for mass and energy form the basic equations describing fluid flow and the associated heat and mass transfer processes in the flow.

3.1 The characteristics of turbulence

The characteristic feature of a turbulent flow is its random, disorderly, three-dimensional fluctuations which are self-sustaining and have the effect of enhanced mixing, diffusion, entrainment and dissipation. In general, turbulence can be characterized by a number of length and velocity scales. There is at least one scale for the large-scale eddies, known as energy containing range, which is proportional to the dimensions of the flow field, and one for the smallest scale eddies containing a minimum kinetic energy, known as the dissipative range. Similarly there is at least one velocity scale for both the energy containing and dissipative eddies. The number of scales that are needed to describe a turbulent flow depends on its level of complexity. Several circumstances may cause a turbulent flow to have multiple length and velocity scales, and thus exhibit complex turbulence. For example, more than one production mechanism (shear and buoyancy, for example) or a spatially varying strain rate field can result in a turbulent flow with several length scales. Although many flows of practical interest have more than one scale of length and velocity, most turbulence models developed thus far are obtained by assuming that the flows of interest have only one length scale and one velocity scale.

In general, it is the generation mechanisms that determine the characteristic of a turbulent flow. Inertial forces then come into action to transfer energy from large-scales to smaller-scales and eventually to the dissipation range where energy is finally converted into heat by viscous action. This transfer of energy from the large scales to small scales is known as energy cascade. Physically, this process occurs by vortex stretching.

In the 1940's, Kolmogorov has suggested that turbulence energy loses information about its mechanism of production as it flows through the energy cascade. With an infinite number of steps in the cascade (infinite Reynolds number), the dissipative scales would lost all the information about the energy containing scales and would only be influenced by the amount of energy that they receive. An important implication of this theory is that the anisotropy of the large-scales is lost, leaving the small-scales in a state of isotropy. Anisotropy exists in the large-scale because the production mechanisms generally feed energy unevenly into different components of the turbulent velocity field. With time, the energy is redistributed to the other components and the degree of anisotropy decreases. In real flows, at finite Reynolds numbers, there is not enough time for the redistribution process to occur completely, thus a true state of isotropy does not exist at the small scales. However, at high Reynolds numbers isotropy of the small scales is often a good approximation and this is a fundamental assumption for most theories of turbulence modeling (Buchanan 1997, Celik 1999).

3.2 Approaches in turbulence modeling and simulation

A turbulence model is defined as a set of equations which determine the turbulent transport terms in the mean flow equation. Turbulence models are based on the hypothesis about the turbulence processes and require input in the form of model constants or functions; they do not simulate the details of the turbulent motion, but only the effect of turbulence on the mean flow behaviour. The concept of Reynolds averaging and the averaged conservation equations are the main concepts that form the basis of turbulence modeling (Celik 1999).

Since turbulent flows are transient and three-dimensional, it is necessary to develop some methods for getting averaged quantities to extract any useful information. The most popular method for dealing with turbulent flows is Reynolds averaging which provides information about the overall mean flow properties. The main idea behind Reynolds averaging is to express any variable $\varphi(x, t)$, which is a function of space and time, as the sum of a mean and a fluctuating component as given by:

$$\varphi(x, t) = \Phi(x, t) + \varphi'(x, t) \tag{3.1}$$

where Φ is the mean and φ' is the fluctuating component.

There are three main averaging forms which are pertinent in turbulence modeling research: *time average*, *spatial average* and *ensemble average*, the general term used to describe these averaging processes is "mean".

Time average is appropriate for stationary turbulence, i.e., a turbulent flow that, on the average, does not vary with time. For such a flow, the time average of an instantaneous flow variable $f(\vec{x},t)$ is defined by

$$F_T(\vec{x}) = \lim_{T\to\infty}\frac{1}{T}\int_t^{t+T} f(\vec{x},t)dt \tag{3.2}$$

Spatial averaging can be used for homogeneous turbulence, which is a turbulent flow that, on the average, is uniform in all directions. The spatial average of the flow variable $f(\vec{x},t)$ can be obtained by doing a volume integral:

$$F_V(t) = \lim_{V\to\infty} \iiint_V f(\vec{x},t)dV \tag{3.3}$$

Ensemble averaging is the most general type of Reynolds averaging suitable for e.g., flows that decay in time. As an idealized example, in terms of measurements from N identical experiments (with initial and boundary conditions that differ by random infinitesimal perturbations) where $f(\vec{x},t) = f_n(\vec{x},t)$ in the nth experiment, the average is defined by:

$$F_E(\vec{x},t) = \lim_{N\to\infty} \frac{1}{N}\sum_{n=1}^{N} f_n(\vec{x},t) \tag{3.4}$$

For turbulence that is both stationary and homogeneous, it is assumed that these three averages are equal. This assumption is known as the *Ergodic Hypothesis* (Wilcox 2000).

3.2.1 Fundamental equations of viscous fluid motion

Fluid flow and the associated heat and mass transfer in the flow are governed by the conservation laws of mass, momentum, energy and species. When applied to a fluid continuum, these laws have the following general forms:

- Mass conservation (continuity equation)

$$\frac{\partial \rho}{\partial t} + \frac{\partial(\rho U_i)}{\partial x_i} = 0 \tag{3.5}$$

- Momentum conservation (Navier-Stokes equation)

$$\frac{\partial}{\partial t}(\rho U_i) + \frac{\partial}{\partial x_j}(\rho U_i U_j) = -\frac{\partial p}{\partial x_i} + \frac{\partial}{\partial x_j}\left[\mu(\frac{\partial U_i}{\partial x_j} + \frac{\partial U_j}{\partial x_i})\right] + f_i \tag{3.6}$$

- Energy conservation

$$\frac{\partial}{\partial t}(\rho T) + \frac{\partial}{\partial x_j}(\rho U_j T) = \frac{\partial}{\partial x_j}(\Gamma_T \frac{\partial T}{\partial x_j}) + S_T \tag{3.7}$$

- Species conservation

$$\frac{\partial}{\partial t}(\rho \Phi) + \frac{\partial}{\partial x_j}(\rho U_j \Phi) = \frac{\partial}{\partial x_j}(\Gamma_\Phi \frac{\partial \Phi}{\partial x_j}) + S_\Phi \tag{3.8}$$

where

U_i, U_j — instantaneous velocity
p — pressure
f_i — total body force acting on the fluid
T — temperature
Φ — species concentration

S_T and S_Φ — energy source and species source, respectively

Γ_T and Γ_Φ — diffusion coefficients for energy and species, respectively

Because of the nonlinear terms and strong coupling, the above equations can hardly be solved analytically except in very few special cases. It is a common practice to take the time-average or ensemble-average of the above equations using Reynolds averaging method and to solve numerically the averaged equations (often referred to as Reynolds equations) to obtain the mean flow quantities (e.g. velocity, temperature, etc.) for practical engineering purposes. The Reynolds equations have similar forms as equations 3.5 ~ 3.8, except that an additional term is added to equations 3.6 ~ 3.8 which arises from the averaging process:

$$\frac{\partial \rho}{\partial t} + \frac{\partial (\rho U_i)}{\partial x_i} = 0 \tag{3.9}$$

$$\frac{\partial}{\partial t}(\rho U_i) + \frac{\partial}{\partial x_j}(\rho U_i U_j) = -\frac{\partial P}{\partial x_i} + \frac{\partial}{\partial x_j}\left[\mu\left(\frac{\partial U_i}{\partial x_j} + \frac{\partial U_j}{\partial x_i}\right)\right] + \frac{\partial}{\partial x_j}(-\rho\overline{u_i u_j}) + f_i \tag{3.10}$$

$$\frac{\partial}{\partial t}(\rho T) + \frac{\partial}{\partial x_j}(\rho U_j T) = \frac{\partial}{\partial x_j}\left(\Gamma_T \frac{\partial T}{\partial x_j} - \rho\overline{u_j T'}\right) + S_T \tag{3.11}$$

$$\frac{\partial}{\partial t}(\rho \Phi) + \frac{\partial}{\partial x_j}(\rho U_j \Phi) = \frac{\partial}{\partial x_j}\left(\Gamma_\Phi \frac{\partial \Phi}{\partial x_j} - \rho\overline{u_j \Phi'}\right) + S_\Phi \tag{3.12}$$

where

U_i, U_j — mean velocity

u_i, u_j — velocity fluctuation

f_i — total body force acting on the fluid

T — mean temperature

Φ — mean species concentration

P — mean pressure

S_T and S_Φ — source terms for energy and species

Γ_T and Γ_Φ — diffusion coefficients for energy and species

T' — temperature fluctuation

Φ' — concentration fluctuation

for the sake of simplicity, the conventional upper bar denoting the averaged mean quantities is omitted in the above equations. The additional terms $-\rho\overline{u_i u_j}$, $-\rho\overline{u_j T'}$ and $-\rho\overline{u_j \phi'}$ represent the convective transport of momentum, heat and species due to turbulent fluctuations, which are generally referred to as Reynolds fluxes, or more specifically, Reynolds stresses, turbulent (Reynolds) heat flux and turbulent (Reynolds) mass flux, respectively (Celik 1999). These extra terms involve correlations between fluctuating velocity components, and are not known *a priori*. The solution of the above conservation equations requires some empirical input to formulate mathematical models for these additional terms, and thus close the set of equations. This is the purpose of turbulence modeling.

The above equations 3.9 ~ 3.12 are often referred to as Reynolds Averaged Navier-Stokes (RANS) equations and the turbulence models developed in this framework are known as RANS turbulence models.

3.2.2 Basic concepts in turbulence modeling

Currently there are three major approaches available for modelling turbulence: Direct Numerical Simulation (DNS), Large-Eddy Simulation (LES) and turbulence transport modelling, i.e. Reynolds-Averaged Navier-Stokes (RANS) modelling.

3.2.2.1 Direct Numerical Simulation (DNS)

A Direct Numerical Simulation (DNS) solves directly the discretized Navier-Stokes and continuity equations. In order to obtain accurate solutions all relevant time and length scales present have to be resolved. For turbulent flows, a “true” DNS resolves all scales down to the Kolmogorov scales. This requirement results in the need for highly accurate codes (high-order compact differences or spectral methods) and very fine computational grids. Therefore, the computational costs involved are extremely high (proportional to Re^3, Piomelli 1999), thus for practical engineering applications it is not feasible. In principle, a fully resolved DNS delivers numerically accurate solutions of the exact equations of motions. No modelling assumptions are required. Consequently, DNS can be regarded as an experiment - taken without obtrusive measuring techniques (Terzi 1996). This alone ensures its usefulness as a research tool. Xu (1998) indicated that for room airflows, DNS goes far beyond the available computational resources and the practical interests of design engineers who concern mainly on the average quantities of velocity, temperature and turbulence intensity etc. Since DNS solves directly the Navier-Stokes equations without making any artificial assumptions about turbulence, it gives complete information about the flow in great spatial and temporal detail, thus results from DNS are very useful to be used as calibration data to develop new turbulence models (Xu 1998).

3.2.2.2 Large Eddy Simulation (LES)

Large Eddy Simulation(LES) is an alternate approach for turbulence modeling which differs from the conventional turbulence transport modeling approach by assuming that turbulent motions can be divided into “large eddies” and “small eddies” and explicitly solving the large eddies in a three-dimensional, time-dependent manner and modeling only the unresolved small eddies. In LES the low-pass-filtered Navier-Stokes and continuity equations are solved. Therefore, by filtering operation, the need arises to model the effects of the unresolved scales, i.e., the so-called subgrid-scale (SGS) on the resolved flow. Similar to DNS, LES produces a three-dimensional, time-dependent solution. By computing only the largest, most energy containing scales of motion explicitly while modelling the small scales, LES computations can be substantially less expensive than those of DNS at a given Reynolds number. This makes LES a useful tool for calculating turbulent flows at Reynolds numbers beyond the reach of DNS. Two classes of large-eddy simulations can be distinguished. The first resolves well all eddies contributing to the turbulence kinetic energy production mechanism and the role of the SGS model is restricted to dissipate the proper amount of energy from the resolved flow field. In this case the SGS effects are small. Computations are costly, but still less expensive than DNS since resolving scales within the inertial subrange might be sufficient. This class of LES has already its place in scientific research but still far beyond the scope of engineering applications. The second class, sometimes called VLES (Very Large Eddy Simulation), does not fully resolve the turbulence kinetic energy production. Consequently, the SGS model has to account for large amounts of energy transfer and the role of the SGS component might even dominate that of the resolved field. VLES depends very much on the quality of the SGS model. Once this is established for a given flow family, it might be used for engineering-like parameter studies (Terzi 1996).

3.2.2.3 Reynolds Averaged Navier-Stokes models (RANS)

In the RANS framework, there are two types of models to account for the influence of turbulence on the mean flow: the eddy-viscosity models (EVM) which are based on the eddy-viscosity concept and the Reynolds-stress models which solve directly the Reynolds stresses using transport equations.

Eddy-viscosity models

Eddy-viscosity models are the mostly widely used models in practice. The main idea behind these models is Boussinesq's eddy-viscosity concept, which assumes that, in analogy to the viscous stresses in laminar flows, the turbulent stresses are proportional to the mean velocity gradient. This approach stems from treating turbulent eddies in a similar way that molecules are treated and analyzed in kinetic theory. Here eddies replace molecules as carriers of thermal energy and momentum. The primary goal of many turbulence models is thus to provide some prescription for the eddy viscosity to model the Reynolds stresses. These may range from relatively simple algebraic models, to the more complex two-equation models, such as the k-ε model, where two additional transport equations are solved in addition to the mean flow equations.

For a general flow situation, the eddy-viscosity model may be written as

$$-\overline{u_i u_j} = \nu_t \left(\frac{\partial U_i}{\partial x_j} + \frac{\partial U_j}{\partial x_i}\right) - \frac{2}{3} k\delta_{ij} \tag{3.13}$$

where ν_t is the turbulent or eddy viscosity, and k is the turbulent kinetic energy which is defined as:

$$k = \frac{1}{2}\overline{u_i u_i} \tag{3.14}$$

δ_{ij} is the Kronecker symbol:

$$\delta_{ij} = \begin{cases} 1 (i = j) \\ 0 (i \neq j) \end{cases} \tag{3.15}$$

In contrast to the molecular viscosity, the turbulent viscosity is not a fluid property but depends strongly on the state of turbulence; ν_t may vary significantly from one point to another and also from flow to flow. The main problem of turbulence modeling is thus to determine the distribution of ν_t.

Inclusion of the second part of eddy viscosity expression in equation 3.13 assures that the sum of the normal stresses is equal to 2k, which is required by the definition of k (equation 3.14). The normal stresses act like pressure forces, and thus the second part constitutes pressure. The above equation 3.13 is used to eliminate $\overline{u_i u_j}$ in the momentum equation. The second part can be absorbed into the pressure-gradient term so that, in effect, the static pressure is replaced as an unknown quantity by the modified pressure given by

$$p^* = p + \frac{2}{3}\rho k \tag{3.16}$$

The main objective is then to determine the eddy-viscosity.

In direct analogy to the turbulent momentum transport, the turbulent heat or mass transport is often assumed to be related to the gradient of the transported quantity, with eddies again replacing molecules as the carrier. With this concept, the turbulent heat flux and the turbulent mass flux may be represented as the products of the turbulent diffusivity of heat (Γ_{Tt}) or mass ($\Gamma_{\Phi t}$), and the mean temperature gradient or concentration gradient, respectively:

$$-\overline{u_j T'} = \Gamma_{Tt} \frac{\partial T}{\partial x_j} \tag{3.17}$$

$$-\overline{u_j C'} = \Gamma_{\Phi t} \frac{\partial C}{\partial x_j} \tag{3.18}$$

The turbulent diffusivity Γ_{Tt} or $\Gamma_{\Phi t}$ has unit equivalent to the thermal diffusivity of m^2/s. Like the eddy-viscosity, the eddy-diffusivity is not a fluid property but depends on the state of the turbulence. The eddy diffusivity is usually related to the turbulent eddy viscosity via

$$\Gamma_{Tt} = \nu_t / \sigma_t \tag{3.19}$$

$$\Gamma_{\Phi t} = \nu_t / Sc_t \tag{3.20}$$

where σ_t is the turbulent Prandtl number and Sc_t is the turbulent Schmidt number, both of them are constant approximately equal to one. The main goal of turbulence modeling is thus to find some prescription for the eddy viscosity to model the Reynolds stresses (Celik 1999).

Reynolds-stress models

The eddy-viscosity approximation for determining the Reynolds stresses is not a good model for flows with sudden change in mean strain rate, curved surfaces, secondary motions, rotating and stratified flows, and flows with separation. The main reason that the eddy-viscosity models don't work well for such kind of flows is the local isotropy and local equilibrium assumptions contained in these models. Inherent in these assumptions is that the normal Reynolds stresses are equal and that the flow history effects of the Reynolds stresses are negligible (Celik 1999). The Reynolds-stress models (RSM) do not employ the eddy-viscosity concept but solve directly the modeled transport equations for the individual Reynolds stresses, thus they automatically account for certain extra effects on turbulence such as those due to streamline curvature, rotation, buoyancy and flow dilatation and are better suited for complex strain fields as well as for simulating transport and history effects and the anisotropy of turbulence (Rodi 2000). However, a major problem is that for a three-dimensional flow, six additional transport equations for the Reynolds-stresses must be solved in addition to the Navier-Stokes and continuity equations, and in most cases, the k and ε equations must also be solved, thus it is computational expensive for practical flow simulations (Celik 1999). Also, the numerical solution of these equations is more difficult and can cause convergence problems, and these models are more demanding with respect to the specification of boundary conditions (Rodi 2000), therefore they are not widely used in ventilation flow simulations at present.

Piomelli (1996) sketched out a brief comparison of the above three turbulence modelling approaches, the main points are as follows:

DNS

- Yields mean and turbulent quantities
- All the turbulent motions are calculated
- Requires massive amounts of CPU time
- The application to flows of engineering interest is difficult

LES

- Yields mean and turbulent quantities
- Only the largest turbulent motions are calculated
- Subgrid-scale models are more universal than models for RANS
- Requires substantially less CPU time than DNS, although substantially more than RANS
- More accurate than RANS in unsteady or 3D flows
- More expensive than RANS, less than DNS

- Initially begins to be used in engineering flow problems

RANS (turbulence transport models)

- Yields mean quantities
- All the turbulent motions are modelled
- The models require *ad hoc* adjustment of the coefficients
- The model has difficulty in predicting unsteady or 3D flows

For simulating ventilation flows in buildings, the RANS approach, or more specifically, the k-ε type of turbulence models and its low-Reynolds number (LRN) variants (i.e., LRN k-ε models) are the most widely used turbulence models (Chen 1997) at present.

3.3 Statistical turbulence models

3.3.1 Classification of turbulence closures

Turbulence models developed within the framework of Reynolds averaging approach are generally classified by the number of additional differential equations to be solved with respect to the RANS equations 3.9 ~ 3.12.

3.3.2 Algebraic turbulence models: zero-equation models

The simplest turbulence models, also referred to as zero equation models, use a Boussinesq eddy viscosity approach to calculate the Reynolds stress. In direct analogy to the molecular transport of momentum, Prandtl's mixing length model assumes that the turbulent eddies cling together and maintain their momentum for a distance l_{mix} , and are propelled by some turbulent velocity v_{mix} . With these assumptions, the Reynolds stress terms can be modeled by

$$-\rho\overline{uv} = \rho v_{mix} l_{mix} \frac{\partial U}{\partial y} \qquad (3.21)$$

for a two-dimensional shear flow. This model further postulates that the mixing velocity, v_{mix} , is of the same order of magnitude as the (horizontal) fluctuating velocities of the eddies, which can be supported through experimental results for a wide range of turbulent flows. With this assumption

$$v_{mix} \approx |u| \approx |v| \approx |w| \approx l_{mix}\left|\frac{\partial U}{\partial y}\right| \qquad (3.22)$$

or, in terms of the eddy (turbulent) viscosity for a shear flow:

$$\mu_t = \rho (l_{mix})^2 \left|\frac{\partial U}{\partial y}\right| \qquad (3.23)$$

This definition can also be implied on dimensional grounds. With these definitions in mind, the objective of most algebraic models is to find some prescription for turbulent mixing length, in order to provide closure to the above equations for Reynolds stress or eddy viscosity (Celik 1999).

3.3.3 One-equation turbulence models

As an attempt to improve the prediction of algebraic or mixing length models, one-equation models have been developed by solving one addition transport equation for some turbulent quantities. There are several different turbulent scales which have been used as the variable in the additional transport equation, the most popular method is to solve for the characteristic turbulent velocity scale proportional to the square root of the specific kinetic energy of the turbulent fluctuations which is usually referred to as the turbulent kinetic energy and is defined in equation 3.14. The Reynolds stresses are then related to the characteristic turbulent velocity scale in a similar manner in which $-\rho\overline{uv}$ was related to v_{mix} and l_{mix} in algebraic models as shown in equation 3.21.

As in the algebraic models, there is still a requirement to determine the length scale l in one-equation models which can only be prescribed from experimental information. While such information exists for some simple flows, for most practical engineering flows, no such information exists. This is a definite limitation for one-equation models. For this reason, most researchers have abandoned these models in favor of two or even more equation models (Celik 1999).

3.3.4 Two-equation turbulence models

Two-equation turbulence models have been the most popular models for a wide range of engineering analysis and research. These models provide independent transport equations for both the turbulence length scale, or some equivalent parameter, and the turbulent kinetic energy. With the specification of these two variables, two-equation models are complete; no additional information about the turbulence is necessary to use the model for a given scenario. While complete in that no new information is needed, the two-equation model is to some degree limited to flows in which its fundamental assumptions are not grossly violated. Specifically, most two-equation models make the same fundamental assumption of local equilibrium, where the turbulent production and dissipation balance. This assumption further implies that the scales of the turbulence are locally proportional to the scales of the mean flow, therefore, most two equation models will be in error when applied to non-equilibrium flows. Though somewhat restricted, two-equation models are still very popular and can be used to give results well within engineering accuracy when applied to appropriate cases (Celik 1999).

In two-equation models, the turbulence length-scale L_k is usually not chosen as a proper dependent variable for the L_k -equation. Instead, a combination of k and L_k having the form:

$$Z = k^m L_k^n \tag{3.24}$$

is chosen as the dependent variable, such that it can be interpreted physically. The commonly used forms of Z are (Markatos 1987):

$Z = k^{1/2} / L_k \equiv \omega$	(turbulence frequency of energy containing eddies)
$Z = k / L_k^2 \equiv w$	(time-average square of the vorticity fluctuations)
$Z = k^{3/2} / L_k \equiv \varepsilon$	(dissipation rate of turbulence energy)
$Z = kL_k$	(energy ~ length-scale product)

It has been shown that the various modeled transport equations for Z differ mainly in diffusion and "secondary" source (as a near-wall correction term which is zero for free flows) term. The variable Z=ε is the most preferred one because it does not require a secondary source term and a simple gradient diffusion hypothesis is fairly good for the diffusion term. An explicit transport equation for ε also eliminates the use of any empirical expression (Markatos 1987). Z=ω is another popular choice for the second variable.

The two-equation k-ε and k-ω models are extensively used in this study. All of the simulations are carried out using a flow solver FLUENT 6. For easy reference, the transport equations of two k-ε models, i.e. the standard k-ε model and the ReNormalization Group (RNG) k-ε model are presented here. For more details of the turbulence models used in this study, the interested readers are referred to the textbooks recommended at the beginning of this chapter or to Fluent Inc. (2001).

3.3.4.1 The standard k-ε model

The two-equation k-ε turbulence model was first developed by Launder and Spalding (1974), which remains as the most widely used turbulence model for a range of engineering flows and is often referred to as the standard k-ε model.

For incompressible flows, the model has the following form (Fluent Inc. 2001):

$$\frac{\partial}{\partial t}(\rho k)+\frac{\partial}{\partial x_j}(\rho k U_j)=\frac{\partial}{\partial x_j}\left[(\mu+\frac{\mu_t}{\sigma_k})\frac{\partial k}{\partial x_j}\right]+G_k+G_b-\rho\varepsilon+S_k \qquad (3.25)$$

$$\frac{\partial}{\partial t}(\rho \varepsilon)+\frac{\partial}{\partial x_j}(\rho \varepsilon U_j)=\frac{\partial}{\partial x_j}\left[(\mu+\frac{\mu_t}{\sigma_\varepsilon})\frac{\partial \varepsilon}{\partial x_j}\right]+C_{1\varepsilon}\frac{k}{\varepsilon}(G_k+C_{3\varepsilon}G_b)-C_{2\varepsilon}\rho\frac{\varepsilon^2}{k}+S_\varepsilon \qquad (3.26)$$

where

σ_k and σ_ε are turbulent Prandtl numbers for k and ε, respectively; S_k and S_ε are the source terms

G_k represents the generation of turbulent kinetic energy due to the mean velocity gradients:

$$G_k=-\rho\overline{u_i u_j}\frac{\partial U_j}{\partial x_i}=\mu_t(\frac{\partial U_i}{\partial x_j}+\frac{\partial U_j}{\partial x_i})\frac{\partial U_j}{\partial x_i} \qquad (3.27)$$

G_b represents the production of turbulent kinetic energy due to buoyancy:

$$G_b=\beta g_i\frac{\mu_t}{\sigma_t}\frac{\partial T}{\partial x_i} \qquad (3.28)$$

g_i is the component of the gravitational vector in i-direction, β is the thermal expansion coefficient and is defined as:

$$\beta=-\frac{1}{\rho}(\frac{\partial \rho}{\partial T})_p \qquad (3.29)$$

For ideal gas, equation 3.28 reduces to:

$$G_b=-g_i\frac{\mu_t}{\rho\sigma_t}\frac{\partial \rho}{\partial x_i} \qquad (3.30)$$

The turbulent (eddy) viscosity μ_t is obtained by combining k and ε as follows:

$$\mu_t=\rho C_\mu\frac{k^2}{\varepsilon} \qquad (3.31)$$

C_μ, $C_{1\varepsilon}$, $C_{2\varepsilon}$, $C_{3\varepsilon}$ are model coefficients. C_μ, $C_{1\varepsilon}$, $C_{2\varepsilon}$, σ_k and σ_ε are constants and have the following values as originally proposed by Launder and Spalding (1974):

$$C_\mu=0.09,\ C_{1\varepsilon}=1.44,\ C_{2\varepsilon}=1.92,\ \sigma_k=1.0,\ \sigma_\varepsilon=1.3$$

$C_{3\varepsilon}$ is determined from the equation:

$$C_{3\varepsilon} = \tanh\left|\frac{v}{u}\right| \tag{3.32}$$

where v is the component of the flow velocity parallel to the gravitational vector and u is the component of the flow velocity perpendicular to the gravitational vector.

3.3.4.2 The RNG k-ε model

The RNG k-ε turbulence model is derived from the instantaneous Navier-Stokes equations by using a mathematical technique called "ReNormalization Group" (RNG) method. The analytical derivation results in a model with constants different from those in the standard k- model, and additional terms and functions in the transport equations for k and ε. The RNG k-ε model is very similar in form to the standard k-ε model. For incompressible flows, the transport equations for k and ε are as follows (Fluent Inc. 2001):

$$\frac{\partial}{\partial t}(\rho k) + \frac{\partial}{\partial x_j}(\rho k U_j) = \frac{\partial}{\partial x_j}(\alpha_k \mu_{eff} \frac{\partial k}{\partial x_j}) + G_k + G_b - \rho\varepsilon + S_k \tag{3.33}$$

$$\frac{\partial}{\partial}(\rho\varepsilon) + \frac{\partial}{\partial x_j}(\rho\varepsilon U_j) = \frac{\partial}{\partial x_j}(\alpha_\varepsilon \mu_{eff} \frac{\partial \varepsilon}{\partial x_j}) + C_{1\varepsilon}\frac{\varepsilon}{k}(G_k + C_{3\varepsilon} G_b) - C_{2\varepsilon}\rho\frac{\varepsilon^2}{k} - R_\varepsilon + S_\varepsilon \tag{3.34}$$

As with the standard k-ε model, the G_k and G_b terms in the above equations represent the generation of turbulence kinetic energy due to the mean velocity gradients and due to buoyancy, respectively, they are calculated using the same equations 3.27 and 3.28 as in the standard k-ε model. The quantities of α_k and α_ε are the inverse effective Prandtl numbers for k and ε, respectively; S_k and S_ε are the source terms for k and ε, respectively.

The scale elimination procedure in RNG theory results in a differential equation for turbulent viscosity:

$$d(\frac{\rho^2 k}{\sqrt{\varepsilon\mu}}) = 1.72\frac{\hat{v}}{\sqrt{\hat{v}^3} - 1 + C_v} d\hat{v} \tag{3.35}$$

where $\hat{v} = \mu_{eff} / \mu$, $C_v \approx 100$.

By integration equation 3.35, an accurate description of how the effective turbulence transport varies with the effective Reynolds number (or eddy scale) can be obtained, which allows the model to better handle low-Reynolds number and near-wall flows. In high-Reynolds number limit, the equation 3.35 gives the same form for computing the turbulent viscosity as equation 3.31 but with a slightly different coefficient C_μ=0.0845, which was derived by using RNG theory.

The inverse effective Prandtl numbers α_k and α_ε are computed using the following formula derived by the RNG theory:

$$\left|\frac{\alpha - 1.3929}{\alpha_0 - 1.3929}\right|^{0.6321} \left|\frac{\alpha + 2.3929}{\alpha_0 = 2.3929}\right|^{0.3679} = \frac{\mu_{mol}}{\mu_{eff}} \tag{3.36}$$

where α_0=1.0. In the high-Reynolds number limit (μ_{mol}/μ_{eff} <<1), $\alpha_k = \alpha_\varepsilon \approx 1.393$, that means the effective Prandtl numbers for k and ε are about 0.7178.

The main difference between the RNG and standard k-ε models lies in the additional term in the ε equation given by

$$R_\varepsilon = \frac{C_\mu \rho \eta^3 (1-\eta/\eta_0)}{1+\beta\eta^3}\frac{\varepsilon^2}{k} \tag{3.37}$$

where $\eta \equiv Sk/\varepsilon$, η_0=4.38, β=0.012.

The effects of this term in the RNG equation can be seen more clearly by rearranging equation 3.33. Using equation 3.37, the third and fourth terms on the right-hand side of equation 3.33 can be merged and the resulting equation can be rewritten as:

$$\frac{\partial}{\partial}(\rho\varepsilon) + \frac{\partial}{\partial x_j}(\rho\varepsilon U_j) = \frac{\partial}{\partial x_j}(\alpha_\varepsilon \mu_{eff}\frac{\partial \varepsilon}{\partial x_j}) + C_{1\varepsilon}\frac{\varepsilon}{k}(G_k + C_{3\varepsilon}G_b) - C^*_{2\varepsilon}\rho\frac{\varepsilon^2}{k} + S_\varepsilon \tag{3.38}$$

where $C^*_{2\varepsilon}$ is given by

$$C^*_{2\varepsilon} = C_{2\varepsilon} + \frac{C_\mu \rho \eta^3 (1-\eta/\eta_0)}{1+\beta\eta^3} \tag{3.39}$$

In regions where $\eta<\eta_0$, the R term makes a positive contribution, and $C^*_{2\varepsilon}$ becomes larger than $C_{2\varepsilon}$. In the logarithmic layer, for instance, it can be shown that $\eta\approx3.0$, giving $C^*_{2\varepsilon} \approx 2$, which is close in magnitude to the value of in the standard k-ε model (1.92). As a result, for weakly to moderately strained flows, the RNG model tends to give results largely comparable to the standard k-ε model. In regions of large strain rate ($\eta>\eta_0$), however, the R term makes a negative contribution, making the value of $C^*_{2\varepsilon}$ less than $C_{2\varepsilon}$. In comparison with the standard k-ε model, the smaller destruction of ε augments ε, reducing k and, eventually, the effective viscosity. As a result, in rapidly strained flows, the RNG model yields a lower turbulent viscosity than the standard k-ε model. Thus, the RNG model is more responsive to the effects of rapid strain and streamline curvature than the standard k-ε model, which explains the superior performance of the RNG model for certain classes of flows (Fluent Inc. 2001).

The model constants in equation 3.33 are derived from the RNG theory and have the following values:

$C_{1\varepsilon}$=1.42 and $C_{2\varepsilon}$=1.68

The coefficient $C_{3\varepsilon}$ is determined by equation 3.32.

3.4 Turbulence modeling for ventilation flows

Many authors have commented on the use of the conventional turbulence models for the simulation of indoor ventilation flows. These discussions focused mainly on the problem of appropriate turbulence models for simulating indoor airflows, and of using high-Reynolds number turbulence models to predict the low-Reynolds number flows often found in ventilation flows and on the use of wall function approach to predict convective heat transfer in rooms. Peng (1998) emphasized that due to the complex flow characteristics in a ventilated space, three principal and problematic aspects must be well accounted for when carrying out numerical simulations with a two-equation model to achieve reliable predictions:

- Using the conventional wall function might be an inappropriate approach for near-wall treatment, particularly when the flow is not fully developed turbulence (e.g. with low supply air flow rate) and when the flow is characterized by separation and affected by thermal buoyancy forces.
- Using turbulence models without incorporating LRN formulation, for example the standard high-Reynolds number k-ε turbulence model, might be one of the main sources of error in predictions since most ventilation flows are characterized by LRN turbulence.

- Using LRN turbulence models that cannot accommodate well near-wall turbulence behavior associated with buoyancy effects and laminar-turbulence transition might result in predictions deviating far from reality in air-to-wall convective heat transfer and in computed mean flow field.

By far systematic evaluation on the performance of turbulence models for indoor airflow simulation is rare in the literature, possibly due to the lack of quality validation data. The few evaluation works having been done thus far were mainly for 2D ventilation cases and with very simple configurations, thus the conclusions obtained from these works are only of limited value for the correct evaluation of turbulence models on their capability to predict practical ventilations flows, which are, in most cases, three dimensional with complicated flow features and internal configurations. Chen (1995, 1996) tested eight popular eddy-viscosity and Reynolds-stress models for 2D natural convection, forced and mixed convection, and impinging jet flows in rooms, he found that none of these models produces satisfactory results. Among them the performance of the RNG k-ε model is slightly better than that of the standard k-ε model, he thus recommended using the RNG k-ε model for indoor air flow simulations. Gan (1998) systematically evaluated the different terms in the RNG k-ε model, by comparison with available experimental data, he found that the RNG k-ε model predicts better the buoyancy-induced flow in a differentially heated tall cavity than does the standard k-ε model, he thus recommended using this model to predict buoyancy-induced flows often found in an indoor environment. He further concluded that the improvement comes mainly from the rate-of-strain term R_ε in the ε equation 3.34 and in equation 3.37. Murakami et al. (1994) examined the performances of the standard k-ε model, an algebraic stress model (ASM) and a Reynolds stress model for predicting a nonisothermal horizontal jet flow in a room, they concluded that the RSM model clearly manifest the turbulence structures of the flow field, and thus is more accurate than the standard k-ε model. In an earlier review, Chen et al. (1992) concluded that the standard k-ε model is the most appropriate turbulence model in computing room airflows. In a more recent report, Chen et al. (2001) still confirmed that no turbulence models performed superior to the standard k-ε model for indoor airflow simulations. It can be seen that there is no a common consensus about which model performs best for the indoor air flow simulation, perhaps such a model doesn't exist; but in practice, the k-ε type turbulence models remain as the most widely used models for indoor air flow simulation at present.

As discussed in Chapter 2, ventilation flows are often low-Reynolds number flows due to the consideration of thermal comfort and energy saving, and there are often transitional flow and/or relaminarization flow in some regions of a ventilated space. Buchanan (1997) indicated that one important problem with current CFD models that are commonly used to simulate indoor air flows, and the complex phenomena which they possess, is that these models have been developed from information pertaining to very simple flows. They were not developed to simulate complex geometries and the complicated mechanisms that indoor airflows often have. Also, these models were developed assuming the flow is at a high Reynolds number, but it is not the case for the air flows in most modern buildings. Thus, it is of vital importance that more complicated, realistic environments be examined and comparisons be made with experimental data to determine the limits of current models. He emphasized that model validation is necessary because a model may work well in one situation but poorly when conditions are slightly different. Chen (1997) also commented that in many room airflows such as natural convection flows the Reynolds numbers are rather low. Most of the turbulence models were developed from some basic flows of high Reynolds numbers. They are not suitable for the prediction of indoor airflows for which the Reynolds number is considerably low. Therefore, excellent agreement is impossible between computed results and measured data.

Many authors have commented the importance of the appropriate near-wall treatment for the correct prediction of ventilation flows especially for the accurate prediction of convective heat transfer at walls. Loomans (1998) indicated that the prediction of surface convection remains problematic for CFD, principally because of the nature of turbulence in room air flows and the related treatment of near-wall regions. The standard k-ε turbulence model with log-law wall functions remains by far the most commonly employed approach in the CFD modeling of room air flows, although it has been well demonstrated that this can lead to significant errors in surface convection predictions. Gan (1998) indicated that the grid distribution near the wall surface is important for the correct prediction of heat transfer near walls. When the air temperature gradient is evaluated at the wall for calculating wall heat transfer, at least the first grid point should lie in the viscous region. However, if the grid points rather than the first are too close to the wall, the equations for turbulent flow, unless incorporating a low-Re model, may inappropriately be applied to the viscous region. On the other hand, if the first grid point is place outside the buoyancy-induced boundary layer, using wall functions will result in unreliable flow predictions. The optimum position of the inner grid point for predicting buoyant flow using k-ε models is thus near the outer edge of the viscous region ($y^+ = 3 \sim 5$) so that the next computational grid point is just beyond the region. For the accurate prediction of the wall heat transfer, the common consensus is that a low-Reynolds number (LRN) turbulence model should be used which allows the direct integration to the walls. Another advantage of LRN turbulence models is that the laminar and turbulent flow regimes need not be specified a priori but may be computed within the framework of the model. LRN k-ε models have been applied to natural convection flows by various investigators, they all concluded that the Jones and Launder model or its variations should be used when modeling turbulent natural convection (Heindel et al. 1994). However, the option to abandon the wall functions by solving the near-wall flow characteristics via low-Reynolds number modified turbulence models is restricted in practice by fine grid requirements and the necessary computing power. Thus the application of empirical relations currently presents a more realistic alternative when the relation and the position of the reference temperature are strictly defined (Loomans 1998; Gosman 1999).

3.5 Remarks

Turbulence modeling still remains as one of the most important problems for the correct prediction of indoor air flows. Due to the complicated flow features and pervasive low-Reynolds number effects that often exist in ventilation flows, it seems that an universal model which can account well for all such flow features in ventilation flows doesn't exist, thus model validation is always an important and necessary step in conducting numerical simulation of ventilation flows—which forms the main part of the present study.

Chapter 4

Numerical Simulation for 2D and 3D Isothermal Ventilation Flows

In this chapter, validation studies of numerical simulation on 2D/3D isothermal ventilation flows are presented.

In this chapter, three isothermal ventilation test cases, i.e., a baseline 2D test case, a case for 3D ventilation in a partitioned model room and a case for 3D ventilation with complicated boundary conditions are studied to validate the numerical models and simulation results.

4.1 Validation study: IEA Annex 20 Test Case 2D (Force convection in a 2D room)

In the IEA Annex 20 project, a simple 2D test case (Test Case 2D) for forced convection was used as a baseline test case to benchmark the CFD codes and turbulence models. The configuration of this test case is shown in Fig. 4.1 with L/H=3.0, h/H=0.056 and t/H=0.16, where H=3.0m, L=9.0m, h=0.168m and t=0.48m (Nielsen 1990; Lemaire 1993).

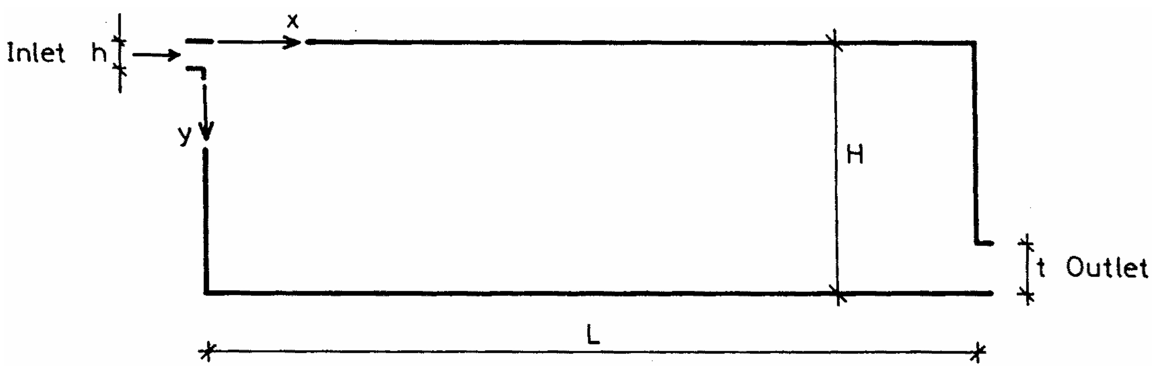

Fig. 4.1 Configuration of the IEA Annex 20 2D Test Room (Nielsen 1990)

Experimental data for this test case were obtained from a scale model room using LDA (Restivo 1979). The data include measured horizontal velocity component U and turbulence intensity at two vertical lines of x=H (x=3m) and x=2H (x=6m) and two horizontal lines of y=h/2 (y=0.084m) and y=H-h/2 (y=2.916m). The experimental data are expressed in terms of dimensionless horizontal velocity U/Uo and horizontal turbulent velocity U'/Uo, where Uo is the supply air velocity at the inlet, U is the horizontal velocity component and U' is the horizontal turbulence velocity component.

To obtain U' from simulation results, Nielsen (1990) gave the following relations for the turbulence velocities in the other two directions:

$$V'^2 \sim 0.6\ U'^2 \quad \text{(Y direction)}$$
$$W'^2 \sim 0.8\ U'^2 \quad \text{(Z direction)}$$

From the definition of turbulent kinetic energy k= $(U'^2+V'^2+W'^2)/2$, the horizontal turbulence velocity component U' (X direction) can be obtained as:

$$U' = \frac{\sqrt{k}}{1.1} \tag{4.1}$$

Test condition

The Reynolds number based on the inlet height (h) is about 5000, which corresponds to an inlet velocity Uo of 0.455m/s. The turbulent kinetic energy *k* and dissipation rate *ε* at the inlet are given by Nielsen (1990) as the following:

$$k_o = 1.5(0.04 \cdot U_o)^2 \qquad (4.2)$$

$$\varepsilon_o = k_0^{1.5} / l_o \qquad (4.3)$$

where l_o is the length scale of the inlet, l_o = h/10. The above inlet conditions correspond to a turbulence intensity of 4% (Nielsen 1990).

Boundary conditions

The boundary conditions for this test case can be summarized as:

Inlet:

velocity inlet

Uo = 0.455 m/s, Vo=0 m/s

k_o, ε_o as defined in equations 4.2~4.3.

Outlet:

outflow, i.e. *dp/dx*=0

where Vo is the vertical velocity component at the inlet and *p* is pressure.

4.1.1 Numerical simulation with different k-ε turbulence models

4.1.1.1 Prediction with standard k-ε turbulence model

The most widely used standard k-ε model is used as a baseline model for this test case. The predicted flow pattern using the standard k-ε model and a mesh grid of 50x28 is shown in Fig. 4.2; a comparison with experimental data of the prediction results using standard k-ε model and three different near-wall treatments: standard wall-function (SWF), non-equilibrium wall function (NEWF) and enhanced wall treatment (EWF) is given in Fig. 4.3. It can be seen that the predicted results from these three different near-wall treatments are nearly the same. The X velocities in the wall jet (Y=0.084m) and near the floor (Y=2.916m) are slightly under-predicted, but in total the predicted velocity profiles correspond very well to the measured data. The prediction using enhanced wall treatment under-predicts more of the jet velocity in the upper right corner than using the other two near-wall treatments, but the predicted turbulent velocity in that region is closer to the measurement. Only with EWF the small recirculation flow at the upper right corner can be predicted but it is much weaker than that observed. The turbulent velocity is under-predicted in most part of the test room, but near the outlet, the turbulence velocity is largely over-predicted.

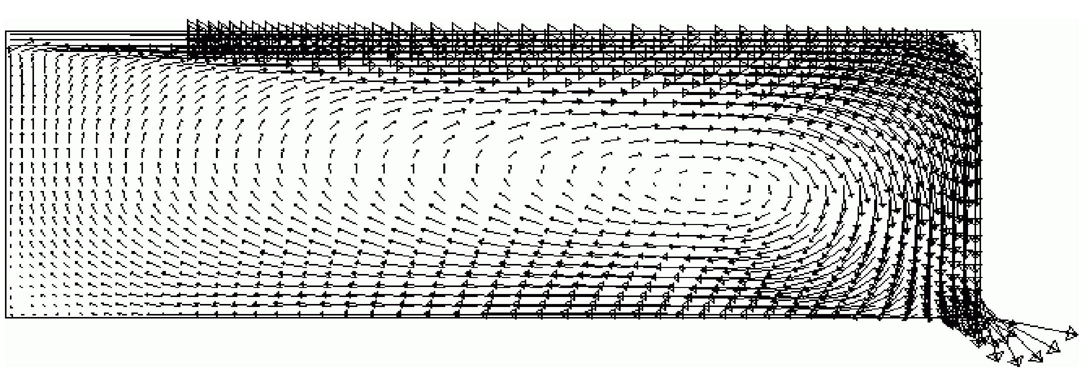

Fig. 4.2 Predicted flow pattern using standard k-ε model and standard wall function

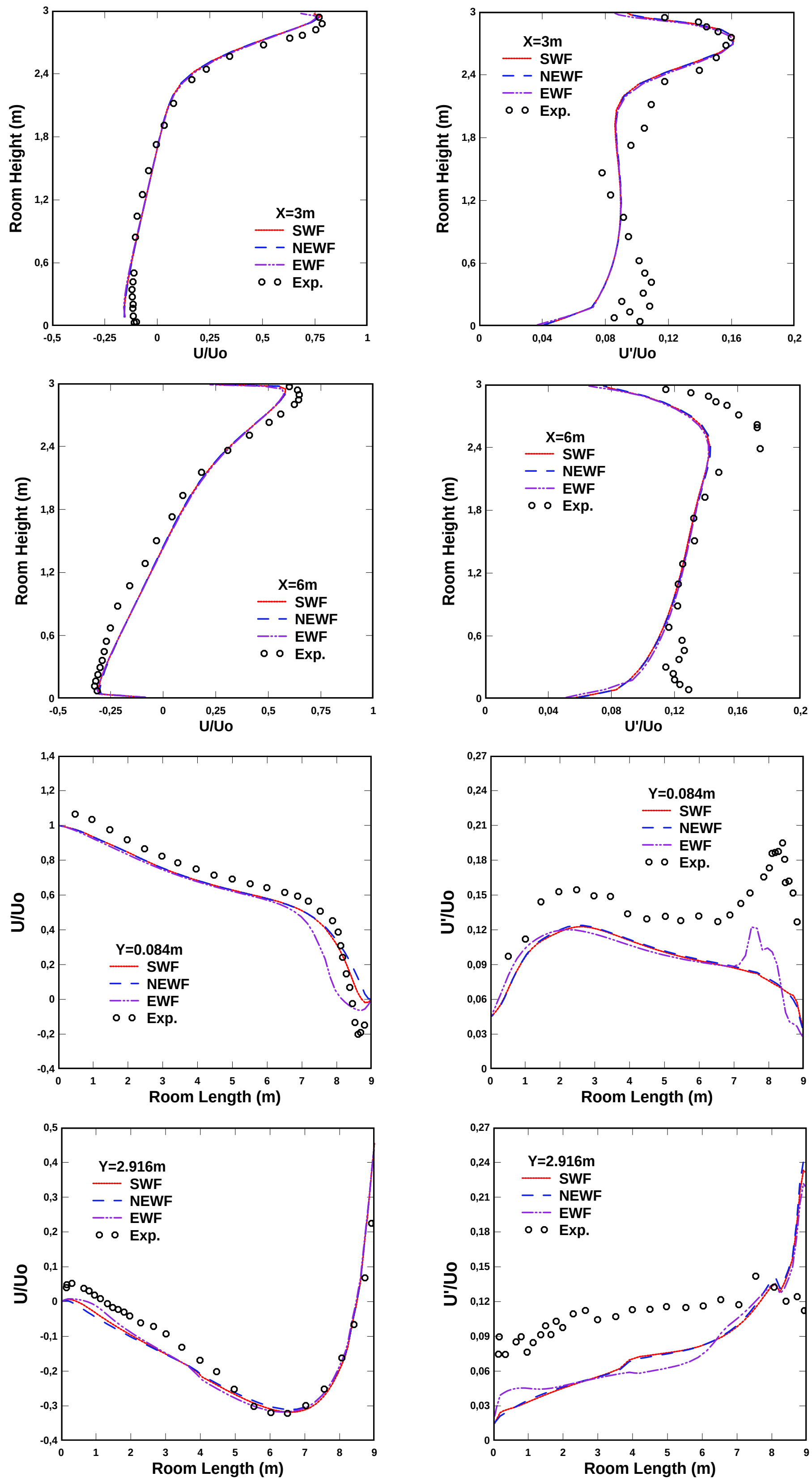

Fig. 4.3 Comparison of the predicted results with experimental data using standard k-ε model

4.1.1.2 Prediction with RNG k-ε model and Realizable k-ε model

The predictions using RNG k-ε model and Realizable k-ε model together with SWF are shown in Fig. 4.4. The mesh grid used is again 50 x 28. As a baseline result, the prediction using standard k-ε model and SWF is also shown in Fig. 4.4. It can be seen that the predictions from the standard k-ε model and the RNG k-ε have very little difference, the Realizable k-ε predicts better the jet flow at X=6m but under-predicts the X velocity near the floor, it under-predicts also more of the turbulent velocity than do the other two k-ε models. The turbulent velocity near the outlet is again greatly over-predicted.

4.1.1.3 Prediction with low-Reynolds number (LRN) k-ε turbulence models

In Fig. 4.5, the predictions using six low-Reynolds number k-ε models, i.e., the Abid, Lam-Bremhorst (LB), Launder-Sharma (LS), Yang-Shih (YS), Abe-Kondoh-Nagano (AKN) and Chang-Ksien-Chen (CKC) models are compared, the computation mesh used is 80x41. A finer mesh of 100x52 was also tested, no appreciable difference was found between the predictions from these two meshes. The prediction from the standard k-ε model (Std k-e) with a mesh size of 50x28 is also shown in Fig. 4.5. It can be seen that the predictions between the LRN k-ε models and also the standard k-ε model show very little difference for the four X velocity profiles, except near the floor (Y=2.916m) where the predicted X velocity profiles using LRN k-ε models are slightly better than that predicted using the standard k-ε model. The LB model and the Abid model predict better the four turbulent velocity profiles, the prediction from the YS model is the worst. None of these models is able to predict the small recirculation flow at the upper right corner, which is indicated by the negative X velocity near the right wall at Y=0.084m.

4.1.2 Prediction with k-ω turbulence models

The predictions using standard k-ω (Std k-O) model and the shear-stress transport (SST) k-ω (SST k-O) model are shown in Fig. 4.6. While the standard k-ω model can give comparable prediction results for the four X-velocity profiles compared with those obtained from the standard k-ε model, the prediction from the SST k-ω model is amazingly bad for both the X-velocity profiles and the turbulent velocity profiles. It is not known what the reason is for such a result, it was repeatedly observed when working with different mesh sizes. Attention has been paid to assure that the dimensionless distance of the first cell center to the nearest wall Y^+ is about 30, but the same result was always observed.

In Fig. 4.6 the predictions from the two k-ω models with transitional flow correction (the LRN version of the two models) are also compared with experimental data. The strange behavior of the SST model especially in the region near the floor (Y=2.916m) is again observed. The standard k-ω model yields reasonable prediction in this region but its LRN version shows the same strange behavior as does the SST model. The LRN version of the two k-ω models do capture the small recirculation flow at the upper right corner of the model room, but the prediction for the turbulent velocity profiles is far from the measured data.

4.1.3 Prediction with the RSM model

The predictions using the RSM model with different near-wall approaches are compared in Fig. 4.7. It can be seen that the predicted results are less good than those obtained using standard k-ε model, especially when the wall-reflection (WR) term is included in the RSM model. It's rather amazing to see that the RSM model only predict a very weak recirculation flow at the upper right corner of the model room, and it over-predicts the turbulent velocity in the jet flow but under-predicts the turbulence level in other regions of the model room.

4.1.4 Remarks

It seems that for 2D ventilation flows, the k-ε models and their LRN variants perform better than the k-ω models and the RSM model. The calculation converges very smoothly and quickly, good results can be obtained even with rather coarser meshes. The recirculation flow at the upper right corner is best predicted by the k-ω models, the RSM model predicts only a very weak recirculation flow.

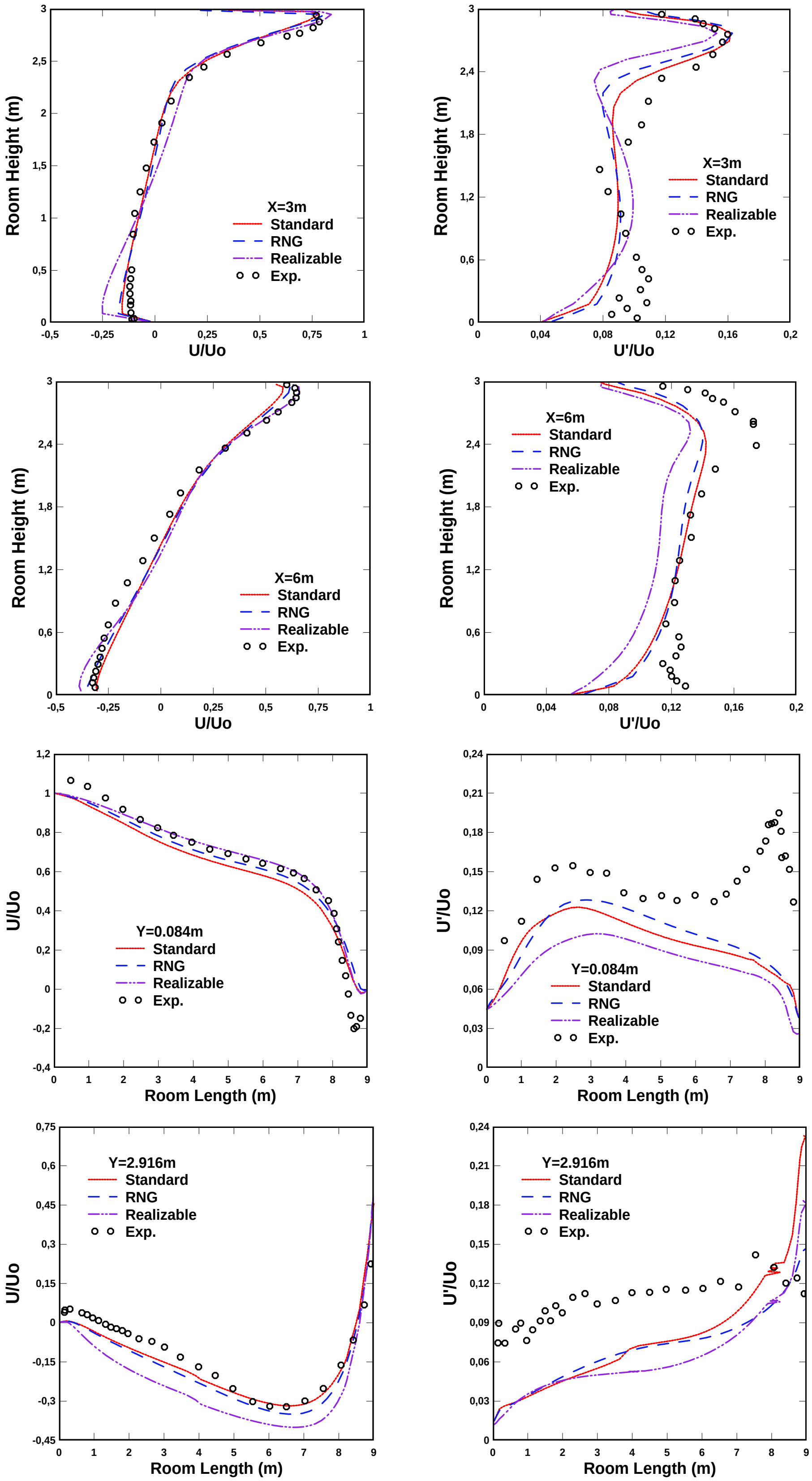

Fig. 4.4 Comparison of predicted results using different k-ε models with experimental data

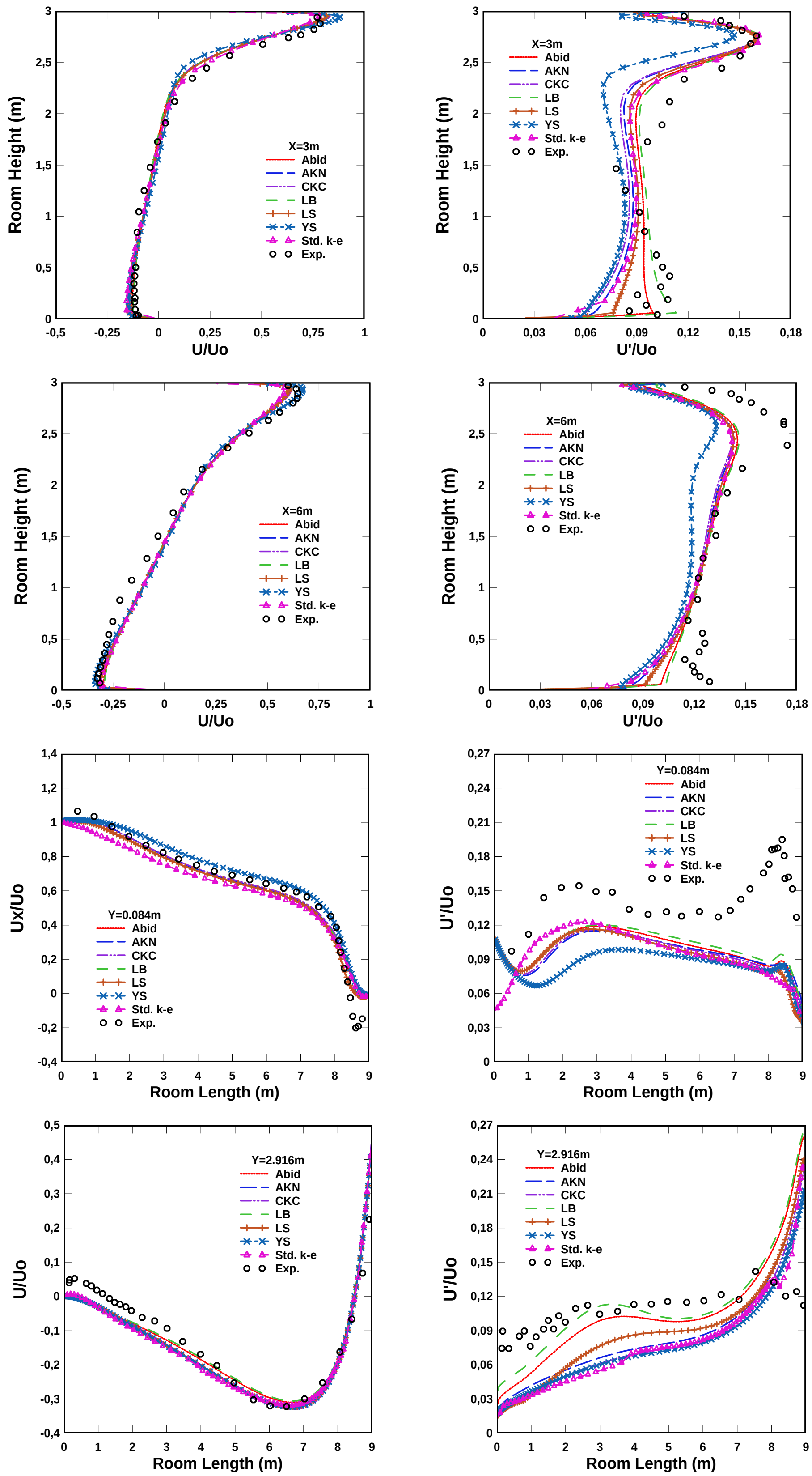

Fig. 4.5 Comparison of the predictions using different LRN k-ε models

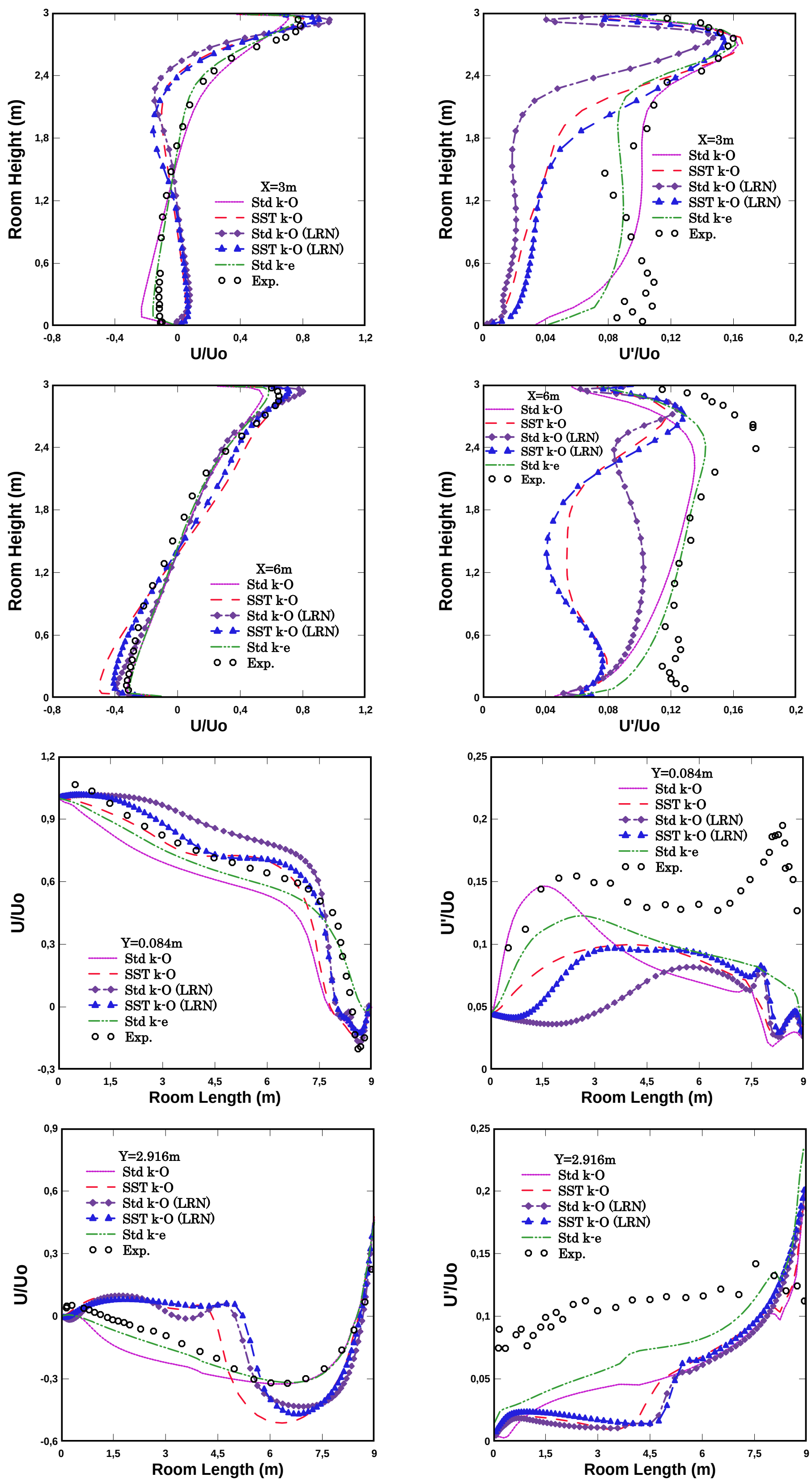

Fig. 4.6 Comparison of the predictions using the Standard and SST k-Ω models and their LRN versions

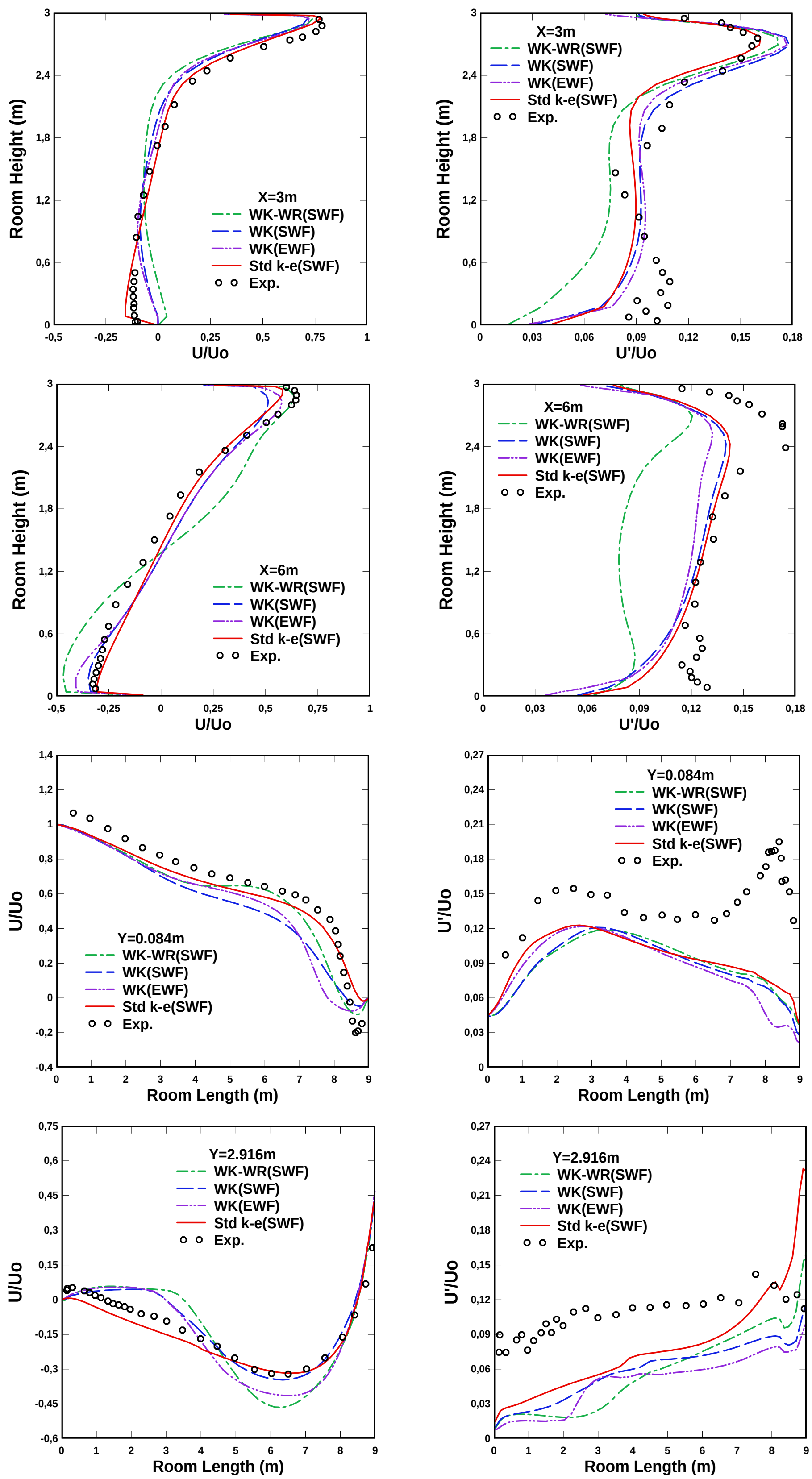

Fig. 4.7 Comparison of the predicted results using the RSM model and different near-wall treatments

4.2 Validation study: Forced convection in a partitioned 3D room

To further evaluate the performance of different turbulence models for the prediction of 3D ventilation flows, an isothermal ventilation flow in a 3D partitioned room as reported in Buchanan (1997) was chosen as the test case. The experiment was carried out in a model room which has the dimensions of 0.915m x 0.46m x 0.3m. The model room is about 1/10 scale of a typical modern office room, it has one inlet and one outlet, both of them are of 0.1m x 0.1m size and located on the room ceiling. At the middle of the room, a partition wall which is of half of the room height (0.15m) is located. The configuration of the model room is shown in Fig. 4.8a.

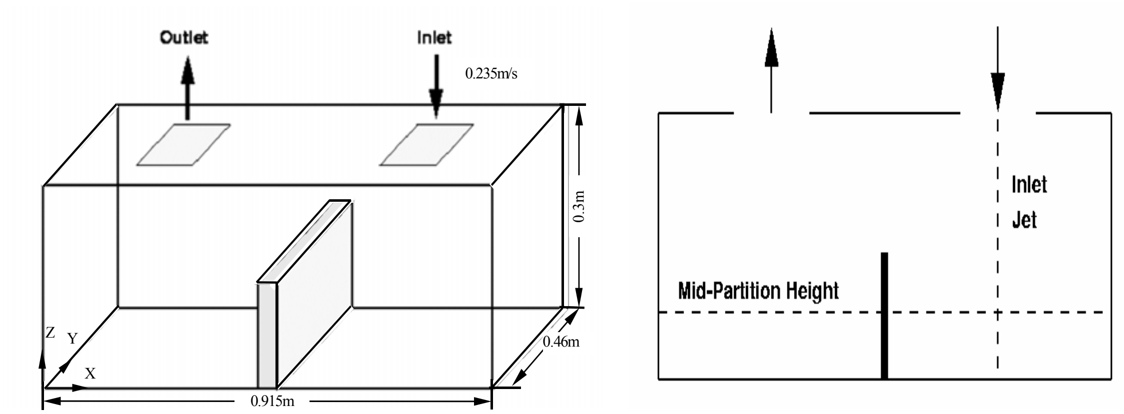

a. Model room configuration b. Locations of velocity measurement

Fig. 4.8 Model room configuration and velocity measurement locations

Test Conditions

The air supply velocity at the inlet is 0.235m/s, which gives a Reynolds number of about 1600 based on the inlet size. The partition wall is very thin; its thickness is only of 0.01m. Measurements were carried out using LDA along the inlet jet center-line and along a line on the symmetry plane at half the height of the partition wall (Z=0.075m, Fig. 4.8b). Only the vertical velocity components (Z-velocities) at different locations were measured.

Boundary conditions

According to Buchanan (1997), the following boundary conditions are used in the numerical simulations:

Inlet:

Velocity inlet, Vz=−0.235m/s.

Turbulence quantities at the inlet:

Turbulence intensity TI=4.4%, hydraulic diameter D=0.1m.

For k-ε models and the RSM model, the turbulent kinetic energy (TKE, k) and its dissipation rate (ε) at the inlet are calculated using the following equations:

$$k_{inlet} = 1.5TI^2 U_{inlet}^2 \quad (4.4)$$

$$\varepsilon_{inlet} = C_\mu^{3/4} k_{inlet}^{3/2} / l \quad (4.5)$$

where

l is the length scale of the inlet, $l = 0.07D$ (Fluent Inc. 2001, Versteeg et al. 1995); C_μ is a constant which is 0.09.

For k-ω models, the TKE at the inlet is calculated using equation 4.4 and the specific dissipation rate ω is calculated using the following equation (Fluent Inc. 2001):

$$\omega = C_\mu^{-1/4} k^{1/2} / l \qquad (4.6)$$

Outlet:

Pressure outlet, i.e., the gauge pressure at the outlet equals zero.

4.2.1 Prediction with two-equation models

Three two-equation k-ε models, i.e., the standard k-ε model, the RNG k-ε model and the Realizable k-ε model and two k-ω models, i.e., the standard and the SST k-ω models were tested. Although the configuration is rather simple, the air flow in the room has rather complicated features including impingement, recirculation and separation, which have been proven to be a non-trivial test for the turbulence models. Also the flow in most part of the room is rather slow, which poses another challenge for the turbulence models and the near-wall treatment methods.

4.2.1.1 Prediction with k-ε models

As was anticipated, the flow in the room has rather complicated flow features and all the k-ε models fail to reasonably predict the measured velocity profiles along the line at half of the height of the partition wall on the symmetry plane (i.e., Y=0.23m and Z=0.075m, referred to as mid-height line hereafter). Fig. 4.9 shows the general flow pattern at the symmetry plane of the model room predicted using RNG k-ε model. It can be seen that around the inlet jet, there are strong recirculation flows in the room; near the top of the partition wall, flow separation takes place.

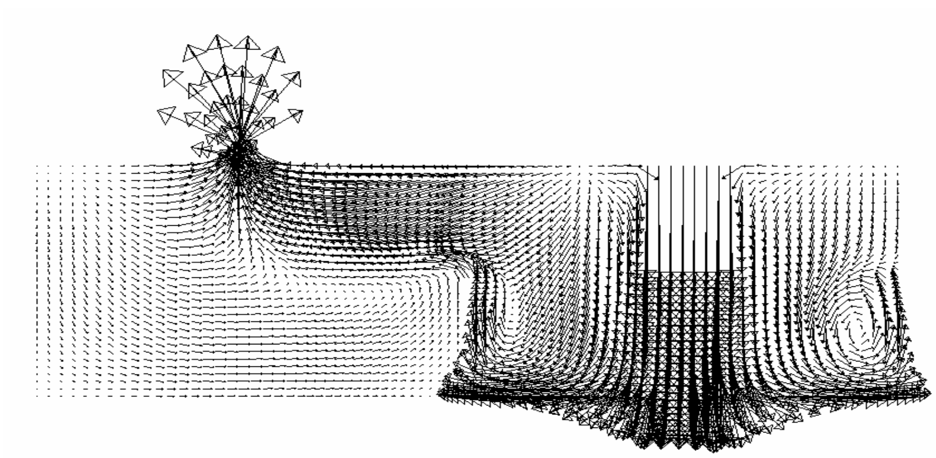

Fig. 4.9 Predicted flow pattern at the symmetry plane of the model room

In Fig. 4.10, the predictions using standard k-ε model and three different near-wall treatments (standard wall function, non-equilibrium wall function and enhanced wall treatment) are compared with experimental data. It can be seen that the recirculation flows at both sides of the inlet jet are not correctly predicted, the Z-velocities in the two recirculation regions are over-predicted and in the impinging region under-predicted. Among the three near-wall treatment methods, the non-equilibrium wall function gives slightly better prediction for the Z-velocity in the recirculation regions, but the two velocity peaks near the partition wall and the right-wall is greatly under-predicted. The standard wall function predicts better the peak velocities near these two walls, but the prediction for the recirculation regions especially the recirculation near the right wall is less good. Among the three near-wall treatments, the enhanced wall treatments has the worst performance, it under-predicts the Z-velocities in both the impinging region and along the inlet jet center-line much more than the other two near-wall treatment methods. It's an amazing result because the enhanced wall treatment is said to be valid throughout the whole near-wall region (i.e., laminar sublayer, buffer region, and fully-turbulent outer region) (Fluent Inc. 2001). Further tests using RNG k-ε model and Realizable k-ε model together with the enhanced near-wall treatment show the similar results.

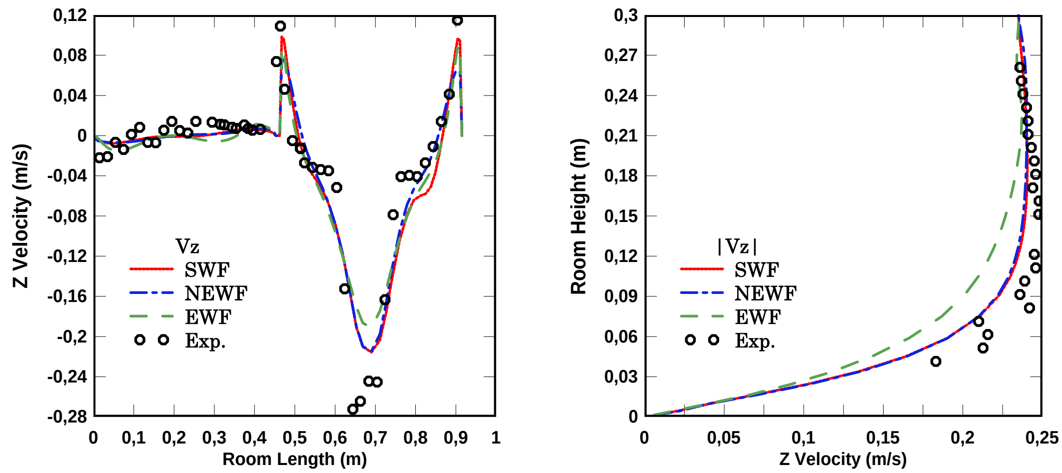

(a) Mid-height line

(b) Jet center-line

Fig. 4.10 Comparison of the predicted velocity profiles with measurements using standard k-ε model and different near-wall treatments (Mesh size: 74x34x32)

It should be noted that the flow in most part of the model room is rather slow, the mesh used in the above calculations is already too fine for working with a wall-function approach because the maximum dimensionless distance of the first grid cell to the nearest wall Y^+ is only about 7, which is much lower than the recommended value (about 30) and violates the minimum requirement of $Y^+ \geq 11.5$ for the standard wall function and non-equilibrium function approaches. If a Y^+ value of about 30 is to be used, a rather coarse mesh should be used which is obviously not capable of resolving the strong recirculation flows in the room. Fig. 4.11 shows the effect of the mesh resolution on the prediction results.

It can be seen from Fig. 4.11 that when a coarse mesh of 43x16x16 is used which conforms to the requirement of $Y^+ \approx 30$ of the standard wall function and non-equilibrium wall function, the Z-velocities in the recirculation region near the right wall are greatly over-predicted and in the impinging region under-predicted; increasing the mesh resolution improves the prediction of the Z-velocity in these two regions and along the jet center-line, but when the mesh size in the X-direction is increased to 82 and above, the predicted results along the mid-height line and the jet center-line have practically no change. In the predictions shown in Fig. 4.11, the non-equilibrium wall function is employed, again the last three mesh grids used are too fine for this wall function approach but they are still not enough to resolve the recirculation flows in the room.

In Fig. 4.12 a comparison of the predicted results with measurements using the three k-ε models and the same mesh as shown in Fig. 4.10 (74x34x32) is given. It can been seen that the prediction using these three models doesn't differ much**;** the standard k-ε under-predicts most seriously the peak of Z-velocities near the partition wall and the right wall, the realizable k-ε predicts best the peak of Z-velocities at these two places but over-predicts most seriously the Z-velocities in the recirculation region near the right wall. In total, the RNG k-ε model has the best overall performance which is only marginally better than that of the standard k-ε model. The predicted Z-velocity profiles from all the three k-ε models are far from the measured one which means that the k-ε models are not capable of correctly predicting the recirculation flows in the room. The prevailing low-Reynolds number (LRN) flow in the room also needs other better near-wall treatments.

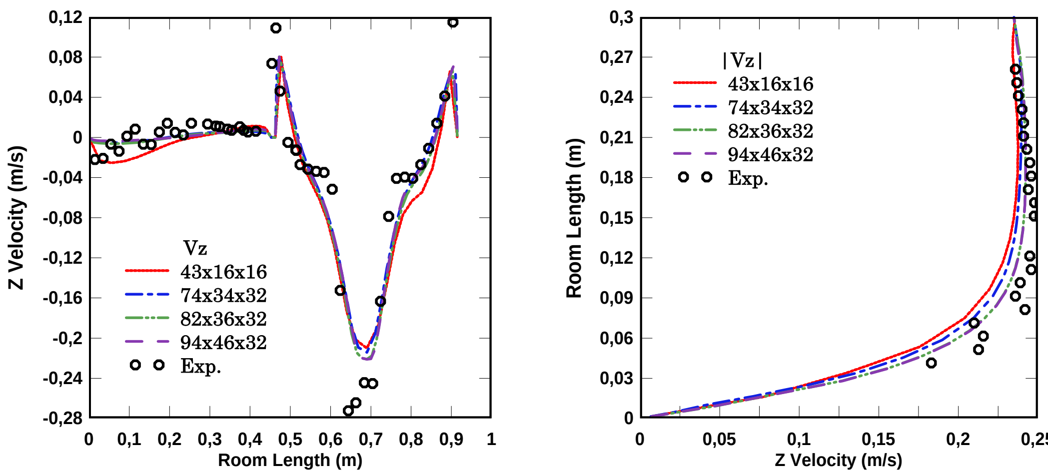

(a) Mid-height line (b) Jet center-line

Fig. 4.11 Influence of mesh resolution on the predicted results

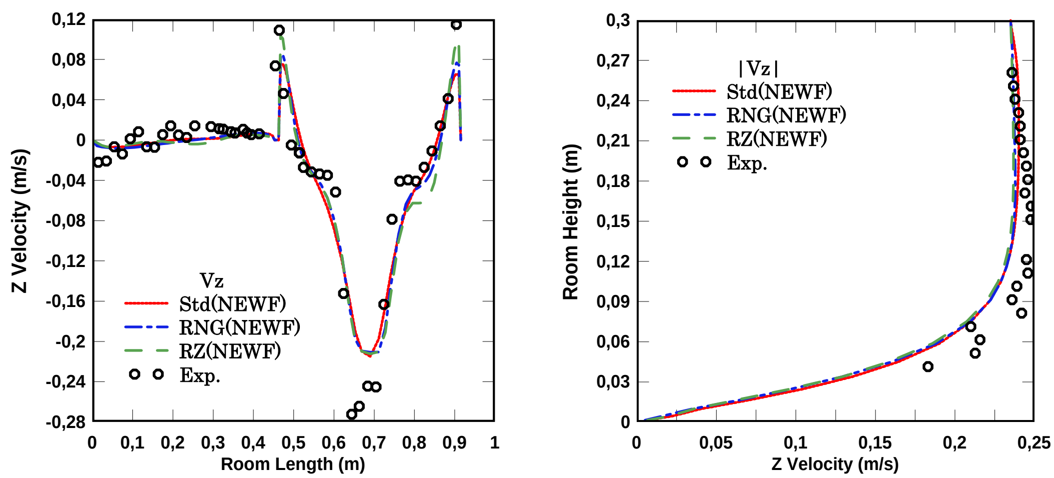

(a) Mid-height line (b) Jet center-line

Fig. 4.12 Comparison of the predictions from different k-ε models

4.2.1.2 Prediction with low-Reynolds number (LRN) k-ε models

Because of the prevailing LRN effect in the test room, it may not be appropriate to use the wall function approach to simulate such a kind of flows, the k-ε model with low-Reynolds number modification may represent a better approach.

Fig. 4.13 is a comparison of predicted Z-velocity profiles with experiment data using three LRN k-ε models and a mesh grid of 83x36x32.

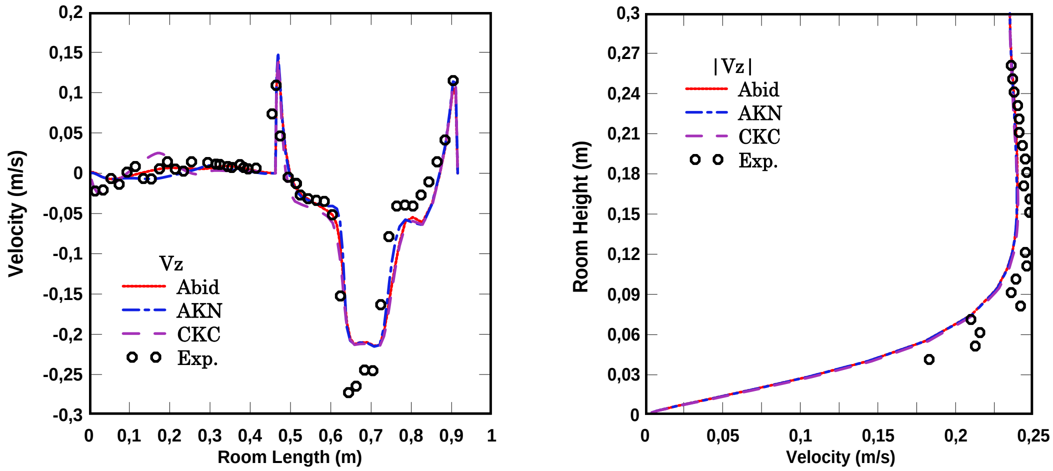

(a) Mid-height line

(b) Jet center-line

Fig. 4.13 Comparison of the predicted Z-velocity profiles with measurements using LRN k-ε models (Mesh size: 83x36x32)

It can been seen that the predictions show big improvement compared with those obtained using k-ε models with wall function approach, the recirculation flow near the partition wall is nicely predicted, but the recirculation flow near the right wall is still not well predicted, also the maximum Z-velocity near the partition wall is over-predicted. Further attempt to increase the mesh resolution do improve the prediction in this region, but the prediction near the partition wall becomes less well. Fig. 4.14 shows the predictions with four LRN k-ε models and with increased mesh resolutions, it can been seen that the prediction in the two recirculation regions and also along the jet center-line from the mesh 114x54x48 is slightly better than that from the mesh 101x46x32, but the improvement is marginal, and the maximum Z-velocity near the right wall is slightly over-predicted. It can be anticipated that a full resolution of the two recirculation regions will need very fine mesh which will then need much more computational resources to carry out the simulations. In general, it can be concluded that the LRN k-ε models can capture the main flow features in the flow, and the predicted Z-velocity profiles agree reasonably with measurements. In Fig. 4.15 an example is given to show the trends of the predicted results with increased mesh resolutions using AKN LRN models. For the other three models tested (Abid, CKC and LS), the general trends are the same as that shown in Fig. 4.15.

4.2.1.3 Prediction with two-equation k-ω models

The vorticity-based k-ω models show much better performance for the prediction of the strong recirculation flows and the flow separation near the partition wall. Fig. 4.16 is a comparison of the predicted velocity profiles with measurements using the standard and SST k-ω models and a mesh size of 74x36x32, it's the same mesh as that used in Figs. 4.10 and 4.12. It can be seen that the recirculation flow near the partition wall is well predicted, and the peak Z-velocities near the partition wall and the right wall are also very well predicted, but as with the LRN k-ε models, the recirculation flow near the right wall is not well predicted. The standard k-ω model predicts slightly better the recirculation flow near the partition wall than the SST k-ω model, but the Z-velocities in the impinging region and along the inlet jet center-line are less well predicted.

In Fig. 4.16, it is also shown the predicted Z-velocity profiles using the two k-ω models with transitional flow correction (the LRN version of the two models). It can be seen that with the transitional flow correction, the prediction in the recirculation flow regions and in the impinging region can be improved, but the peak Z-velocity near the partition wall is over-predicted, it seems that the LRN version of both the k-ε models and the k-ω model tends to over-predict the peak Z-velocity near the partition wall (cf. Figs. 4.13~4.15). Fig. 4.17 shows a close view of the five marked positions in Fig. 4.16a, where the difference of the predicted velocity profiles using different models can be more clearly appreciated.

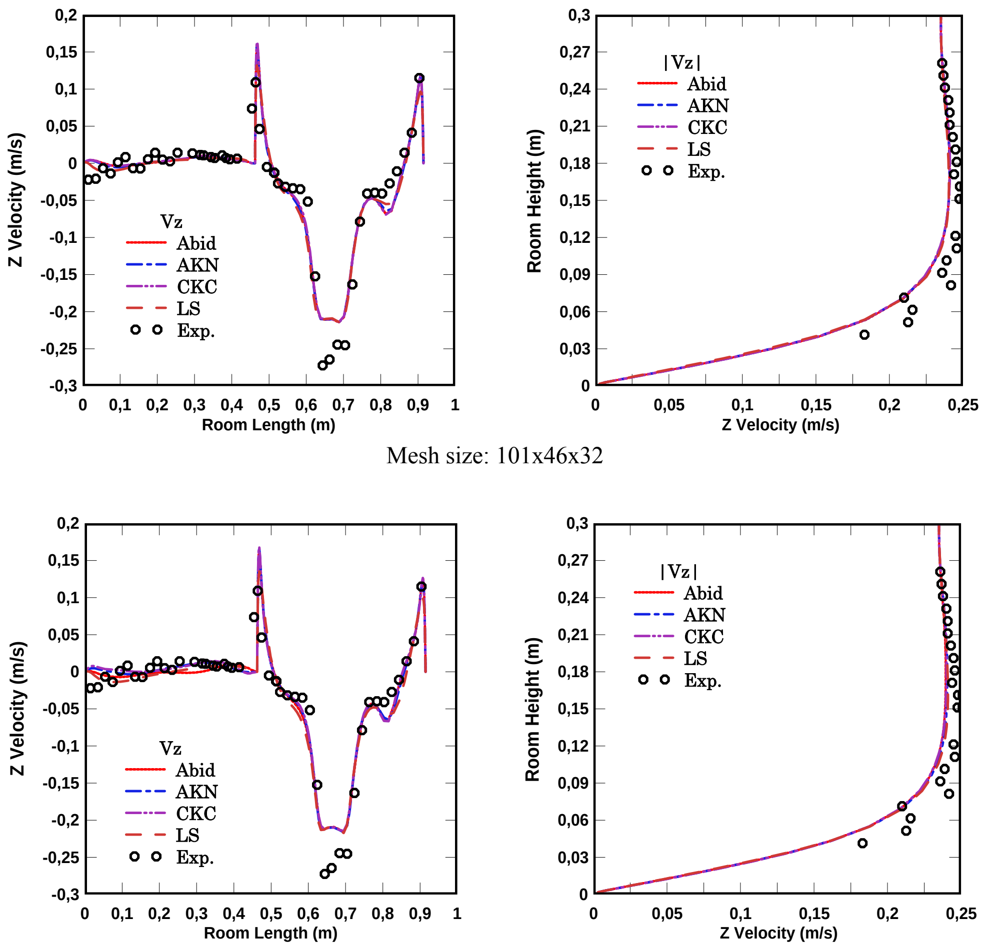

Mesh size: 101x46x32

Mesh size: 114x54x48

(a) Mid-height line

(b) Jet center-line

Fig. 4.14 Comparison of predicted Z-velocity profiles with measurements using LRN k-ε models

As with the LRN k-ε models, further attempt to refine the mesh do improve the prediction of recirculation flow region near the right wall, but the prediction near the partition wall becomes less well. Fig. 4.18 shows how the predicted Z-velocity profiles change with different mesh sizes. By comparing Figs.4.15 and 4.18, it can be seen that the predicted Z-velocity profiles are very similar, both of the LRN models over-predict the peak Z-velocity near the partition wall. The LRN k-ω models perform a little better than the LRN k-ε models, because by successively refining the mesh, the degradation of the prediction of the recirculation flow near the partition wall is less profound that as with LRN k-ε models. This can be easily seen by a comparison of the predicted velocity profiles using AKN LRN k-ε model and LRN SST k-ω model and the same mesh 114x54x48 as shown in Fig. 4.19.

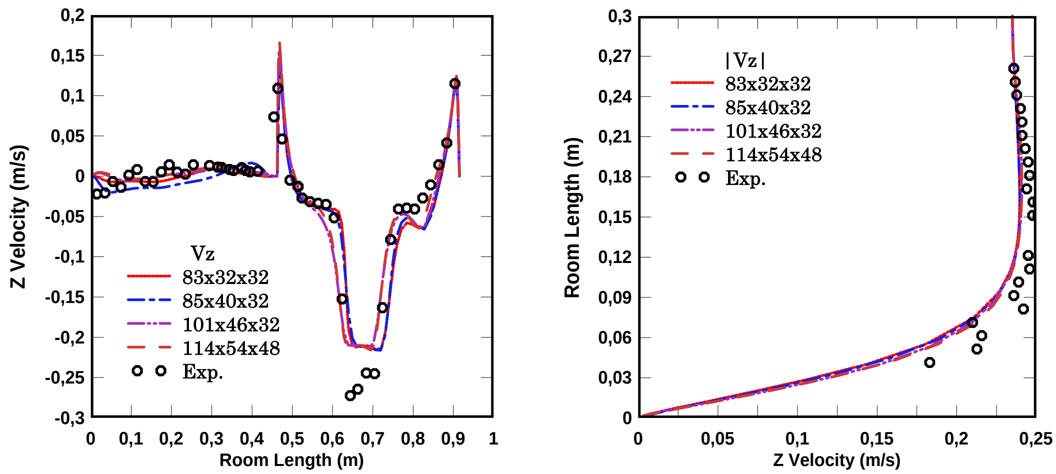

(a) Mid-height line (b) Jet center-line

Fig. 4.15 Comparison of predicted Z-velocity profiles using AKN LRN k-ε model and different mesh sizes

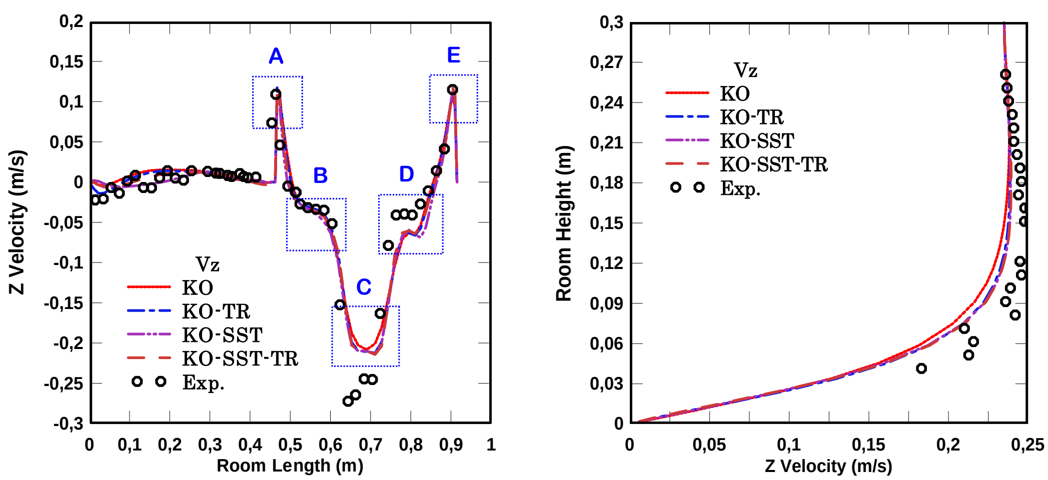

(a) Mid-height line (b) Jet center-line

Fig. 4.16 Comparison of predicted Z-velocity profiles with measurements using k-ω models
(Mesh size: 74x34x32)

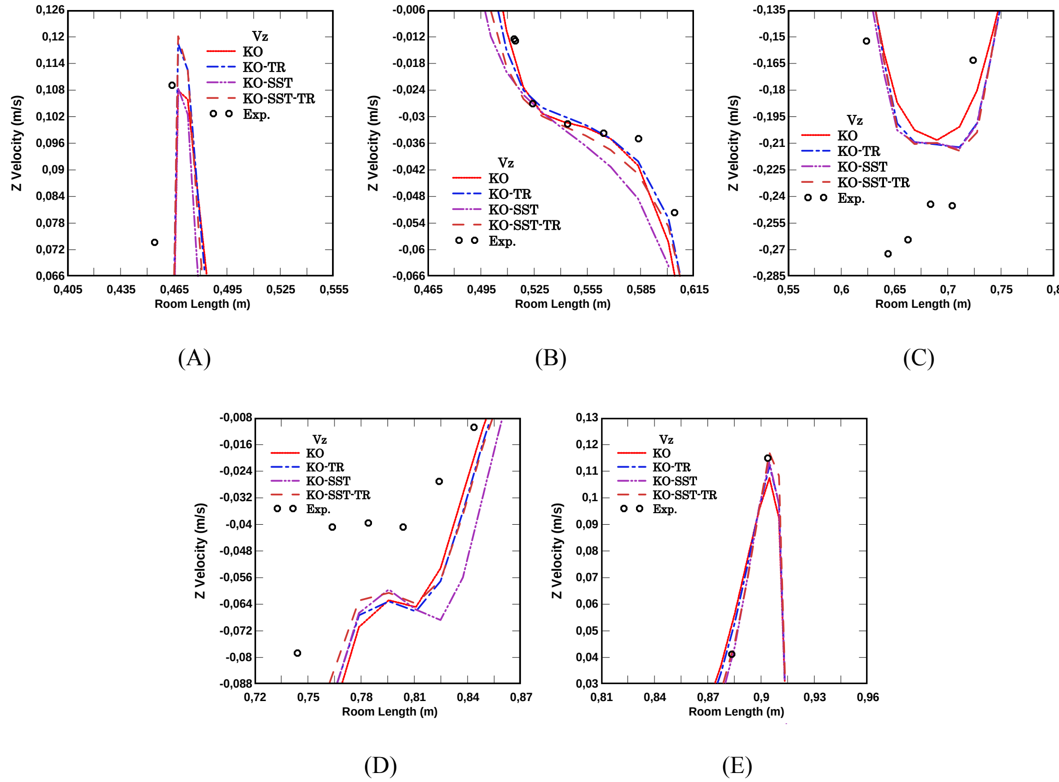

Fig. 4.17 Close views of the five marked positions in Fig. 4.16a

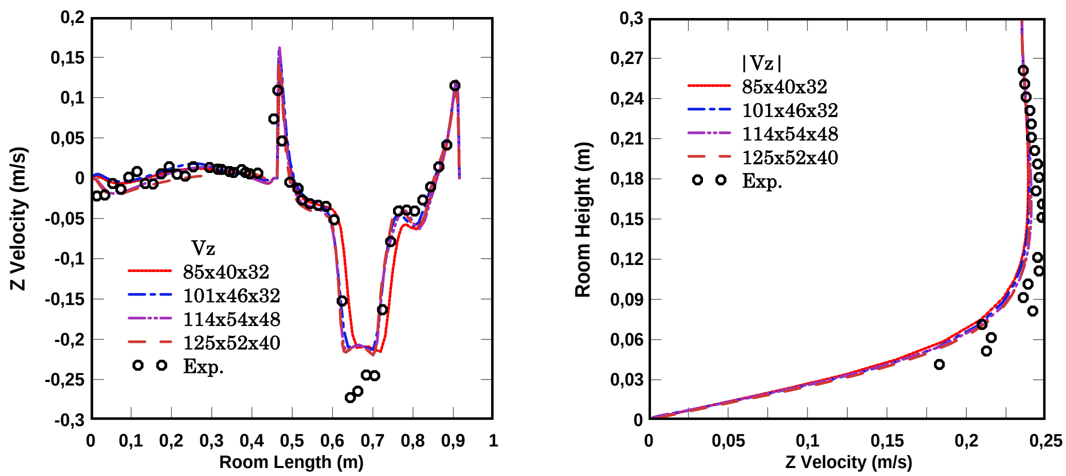

(a) Mid-height line

(b) Jet center-line

Fig. 4.18 Comparison of predicted results using SST k-ω model (with transitional flow correction) and different mesh sizes

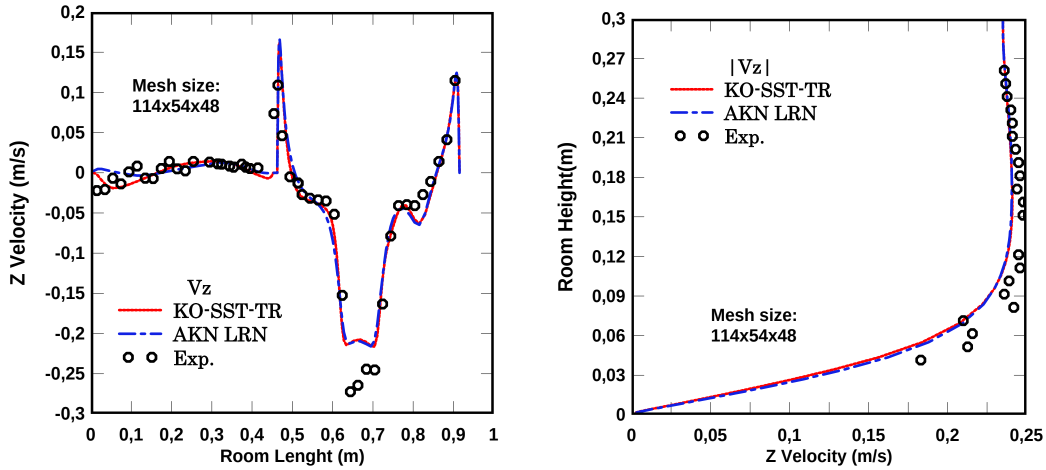

(a) Mid-height line

(b) Jet center-line

Fig. 4.19 Comparison of the predicted results using AKN LRN k-ε model and LRN SST k-ω model

4.2.2 Prediction with the RSM model

As shown above, none of the two-equation k-ε models and k-ω models can well predict the strong recirculation flow near the right wall, this may be a consequence of the isotropic eddy-viscosity hypothesis used in these models. The RSM model which solves directly the individual Reynolds-stresses may better represent the strong anisotropic flow feature in this region. Fig. 4.20 is a comparison of the predicted Z-velocity profiles with measurements using RSM model and a mesh size of 114x54x48. It can be seen that compared with the above two-equation eddy-viscosity models, the recirculation flow near the right wall is better predicted; the recirculation flow near the partition wall is well predicted too, but the peak Z-velocity near the partition wall is again over-predicted, this seems to be the consequence of finer mesh near the partition wall. In Fig. 4.20, three near-wall approaches, i.e., standard wall function (SWF), non-equilibrium wall function (NEWF) and enhanced wall treatment (EWF) are compared, also the predictions using RSM model with/without the wall-reflection (WR) term are compared. It can be seen that using SWF together with WR term gives the best overall prediction of the measured Z-velocity profiles; the prediction using NEWF and with WR term is good enough too, except that the peak Z-velocity near the right wall is a little under-predicted. With SWF, the peak Z-velocity near the right wall is well predicted but near the partition wall it is over-predicted. As with the two-equation k-ε models, the enhanced wall treatment gives the worst prediction for both of the Z-velocity profiles along the mid-height line and the Jet center-line.

It should be noticed that the near-wall mesh grids used in the above predictions are too fine to work with the SWF and NEWF approaches, because the maximum Y^+ value is only about 1.7, which is far less than the recommended Y^+ value (about 30) for working with SWF and NEWF. But from Fig. 4.20 it can be seen that the prediction reproduces enough well the measured velocity profiles. It is thus anticipated that with a LRN version of the RSM model or with a better near-wall treatment, the RSM model should be able to predict well the recirculation flows in the model room. It is also noticed that enough mesh resolution is essential to capture the anisotropic flow feature in the recirculation flow regions. Fig. 4.22 shows how the predicted Z-velocity profiles change with different mesh sizes, the SWF and the WR term were used in the predictions. It can be seen that compared with two-equation eddy-viscosity models, the RSM model gives the best prediction of the recirculation flows.

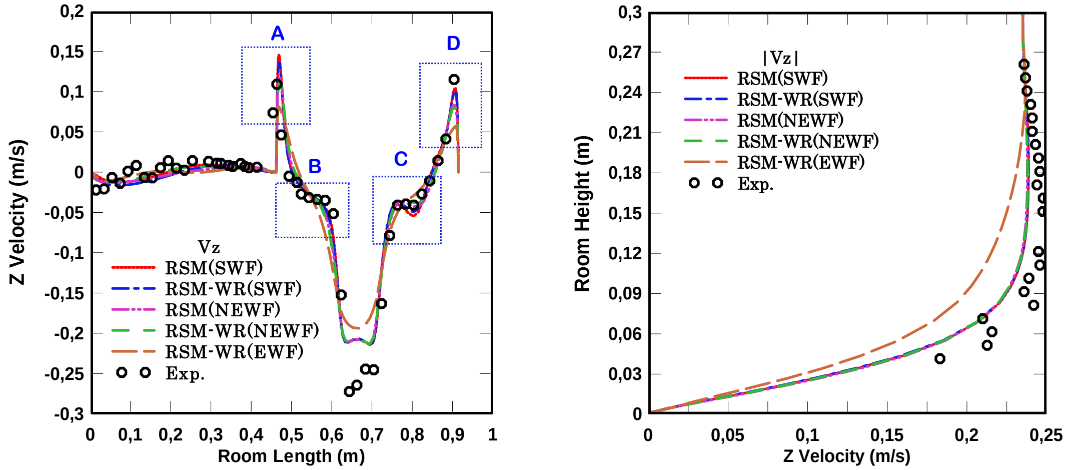

(a) Mid-height line (b) Jet center-line

Fig. 4.20 Comparison of the predicted Z-velocity profiles using RSM model with measurements

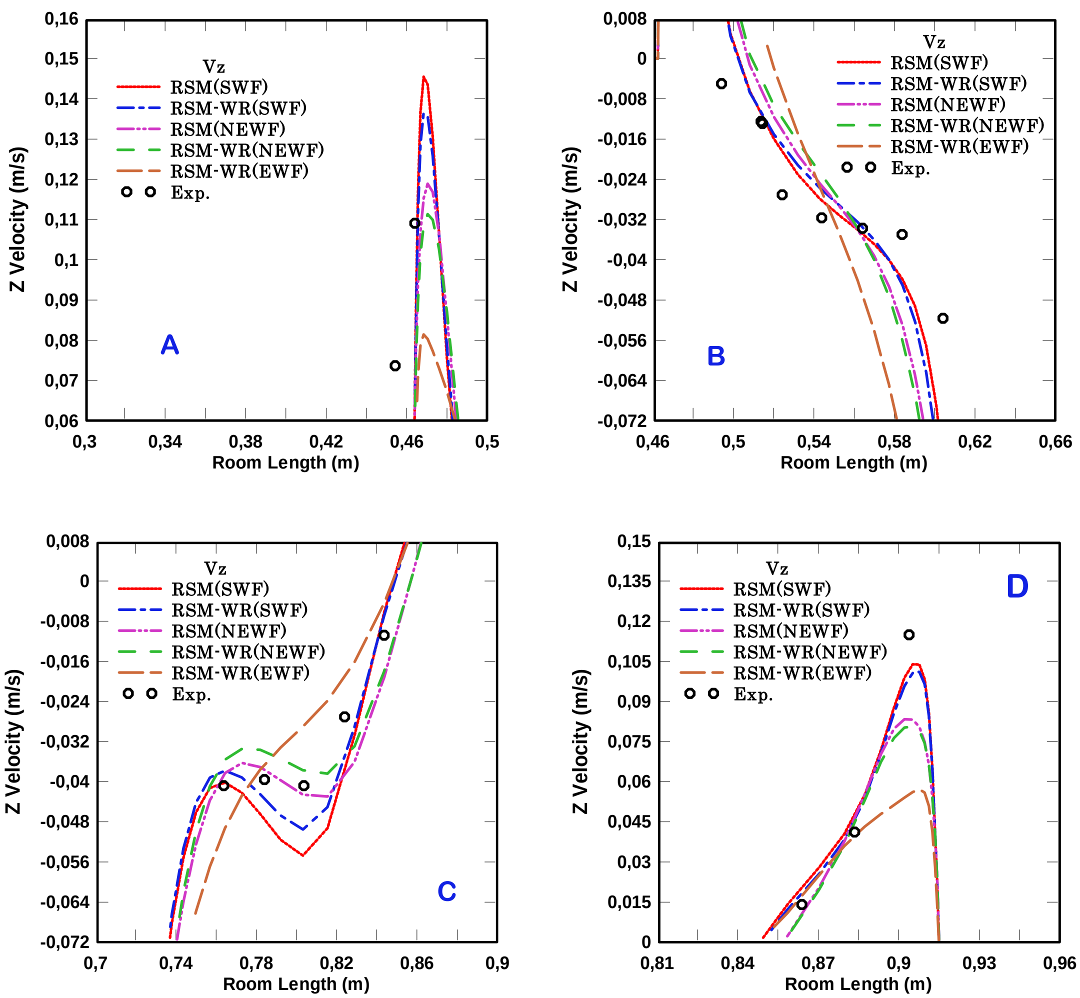

Fig. 4.21 Close views of the four marked places in Fig. 4.20a

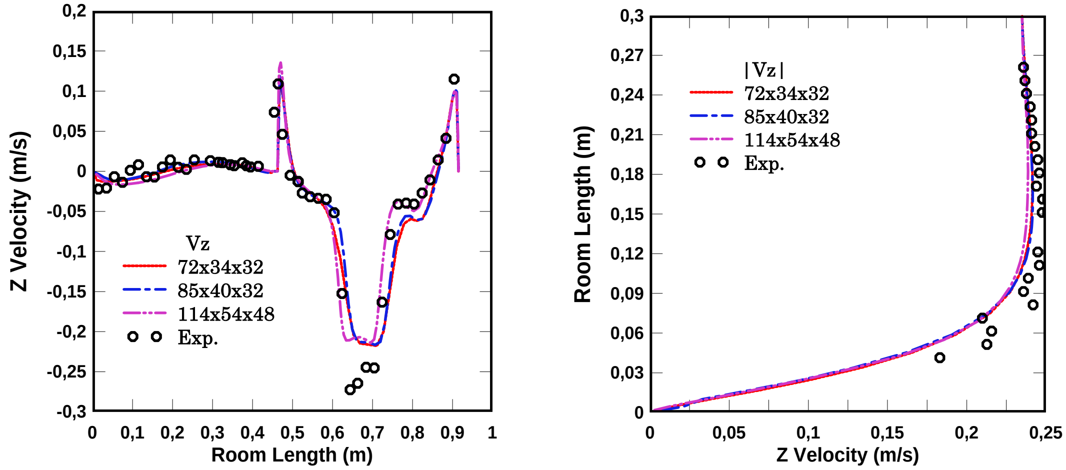

(a) Mid-height line

(b) Jet center-line

Fig. 4.22 Comparison of the predicted velocity profiles with measurements using RSM model and different mesh sizes

4.2.3 Large-eddy simulation

Large-eddy simulation is a promising approach to simulate ventilation flows and to study ventilation flow characteristics. By dividing the turbulent fluid motion into “large eddies” and “small eddies” and explicitly solving the large eddies in a three-dimensional, time-dependent manner and modeling only the unresolved small scale eddies, large-eddy simulation significantly reduces the dependence of the simulation results on the turbulence models used. It is generally believed from experiment evidences that the large eddies are more important in turbulence transport and more problem-dependent, whereas the small eddies are mainly responsible for the dissipation of turbulent kinetic energy and are more universal in nature, therefore their effects can be better represented by a general turbulence model, it is thus assumed that LES is physically superior to turbulent transport models. Much hope has been placed on large eddy simulation for more faithfully simulating complex turbulent flows—especially for the cases in which laminar, transitional and turbulent flows coexist—which is often the case in a ventilated space and is very difficult to handle with conventional turbulent transport models. There are very few reports on large-eddy simulation of indoor air flows in the literature, mainly due to the high computational cost needed to carry out large-eddy simulations because very fine mesh grids are needed to resolve the “larger energy carrying eddies”. Some recent exploratory work using LES to simulate indoor ventilation flows have been reported by Davidson (1996a, 1996b), Emmerich (1998), Bennetsen (1999) etc., all these LES simulations were for a simple 3D ventilated enclosure without any obstacle, good results were obtained compared with experimental data. These work also revealed that when the simple Smagorinsky subgrid scale (SGS) model is used, the predicted results show some dependence on the Smagorinsky constant Cs. It is the intention of the present study to further explore the performance of LES for simulating indoor ventilation flows with complicated flow features like impingement, recirculation and separation as found in this test case. The Smagorinsky-Lilly (SL) SGS model and a RNG-based SGS model are used to represent the influence of the subgrid scale turbulence on the resolved flow.

In the literature, the Smagorinsky constant Cs for the SL SGS model varies in the range from Cs=0.065 to Cs=0.25 (Davidson, 1996b). For simulating indoor air flows, Davidson tried Cs=0.14 and Cs=0.18, and found that the prediction result changes considerably as the Cs changes, he thought that this value may be both flow-dependent and grid-dependent. Emmerich (1998) used Cs=0.1, 0.14, 0.18 and 0.23, he found that the Cs value is somewhat grid dependent, Cs=0.18 seems to give better results when using a coarser mesh while Cs=0.14 appears to give better results for finer meshes. The model constant for RNG SGS model is given by theory and has a fixed value Crng=0.157, which is an advantage over the SL SGS model. In highly turbulent regions of the flow, the RNG-based subgrid-scale model reduces to the Smagorinsky-Lilly model with a different model constant. In low-Reynolds-number regions of the flow, the effective viscosity recovers molecular viscosity, this enables the RNG-based subgrid-scale eddy viscosity to model the low-Reynolds-number effects encountered in transitional flows and near-wall regions (Fluent Inc. 2001). It is thus anticipated that the RNG-based SGS model may be better suited for the prediction of indoor ventilation flows than the Smagorinsky-Lilly SGS.

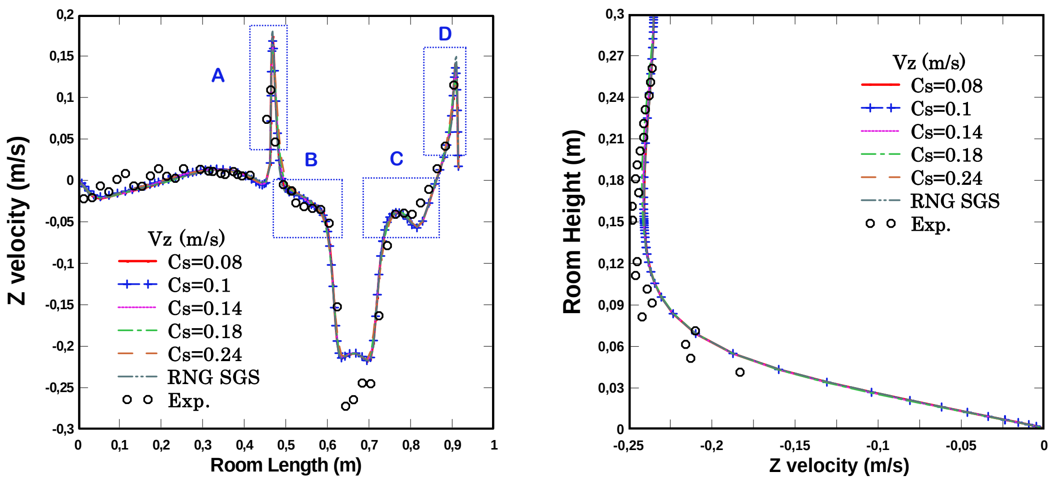

(a) Mid-height line (b) Jet center-line

Fig. 4.23 Comparison of the predicted Z-velocity profiles with measurements using SL and RNG SGS models

Fig. 4.23 shows a comparison of the predicted velocity profiles with measurements using SL and RNG SGS models, the mesh size used is 114x54x48. In the simulations, the convection terms as well as the diffusion terms are discretized using the second-order central-differencing scheme, the PISO scheme is used for the velocity-pressure coupling, the time-matching scheme is second-order implicit. It can been seen that the two SGS models have similar performance for this test case: the recirculation flows between the jet and the partition wall and the right wall are reasonably predicted, but the prediction is not as good as that obtained with the RSM model as shown in Figs. 4.20 and 4.21. This may be a consequence of using the isotropic eddy-viscosity SGS model and/or the insufficient mesh resolution in these regions. The RNG SGS model doesn't show any better performance than the SL SGS model. A close view of the four marked places in Fig. 4.23a revealed that as the value of the Smagorinsky constant Cs increases, the over-prediction of the peak Z-velocity near the partition wall and the right wall decreases, the RNG SGS model over-predicts most seriously the peak Z-velocities in these two regions. In the two recirculation-flow regions (B and C in Fig. 4.23a), the prediction using different Cs values and the RNG SGS model doesn't show significant difference. But when working with coarser meshes, there can be considerable difference between the predictions from different Cs values and RNG SGS model. Fig. 4.25 shows the predicted Z-velocity profiles using a coarser mesh with two different Cs values and with RNG SGS model. It can be seen that when working with coarser mesh, the RNG SGS model predicts better the recirculation flow between the jet and the right wall, but again the RNG SGS model over-predicts the peak Z-velocity near the partition wall more than the SL SGS model does, and it under-predicts the peak Z-velocity near the right wall more than the latter does too.

In Fig. 4.26, an example is given to show how the predicted results change with different mesh sizes. It can be seen that the predictions from the latter two meshes (102x48x48 and 114x54x48) have practically no difference, except the peak Z-velocities near the partition wall and the right wall, for which the finer mesh results in an increased over-prediction, it's the same result with all the other Cs values and also with all the other turbulence models.

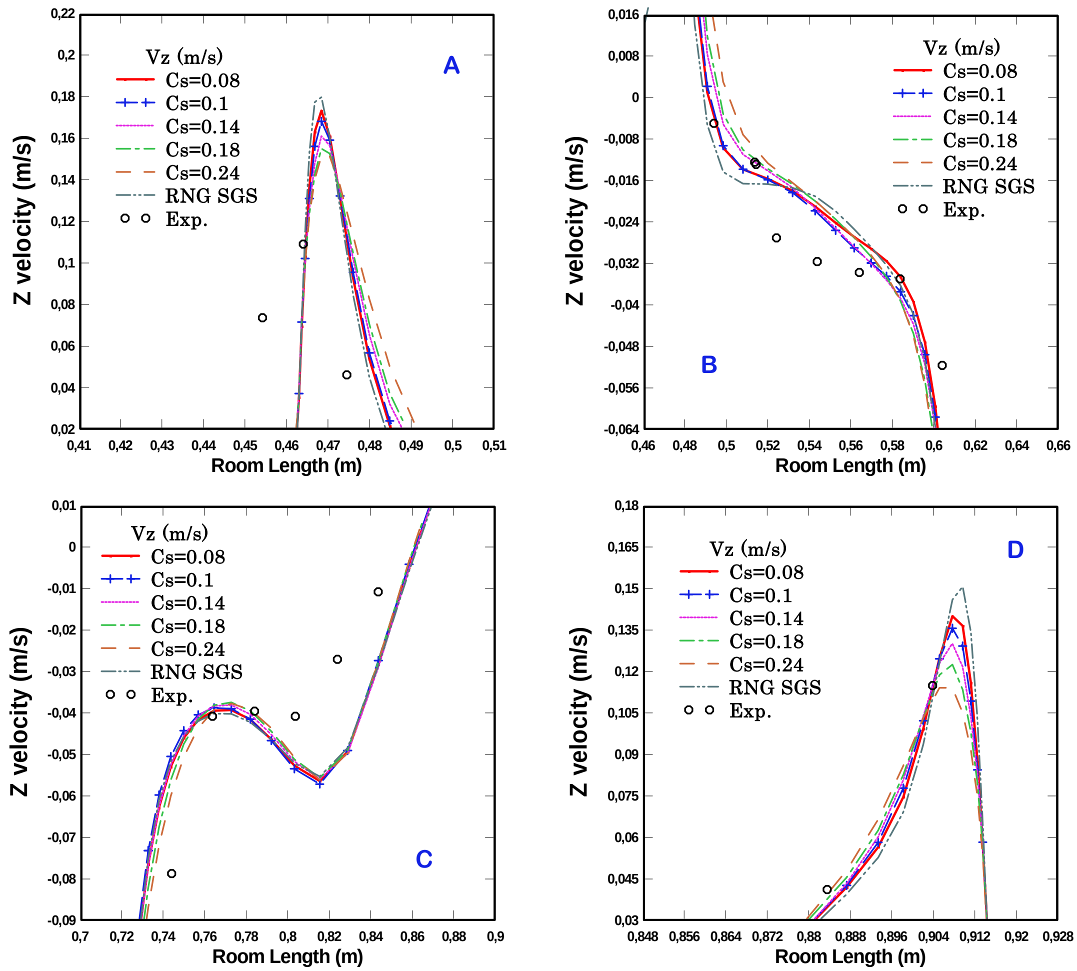

Fig. 4.24 Close views of the four marked places in Fig. 4.23a

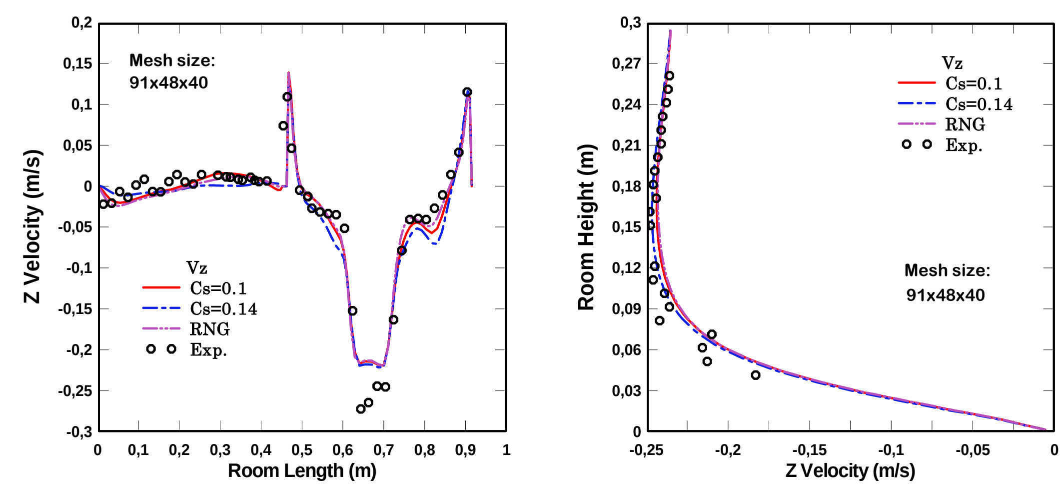

(a) Mid-height line

(b) Jet center-line

Fig. 4.25 Comparison of predicted Z-velocity profiles with measurements using coarser mesh

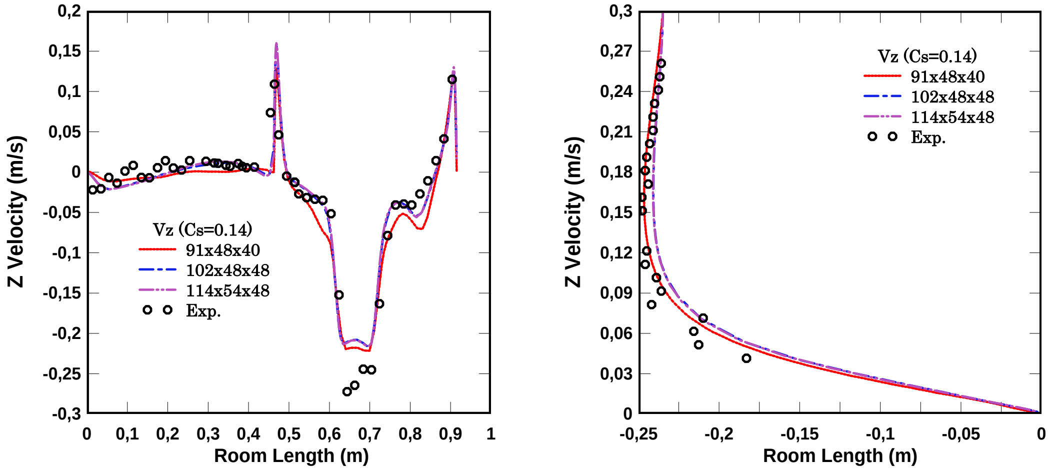

Fig. 4.26 Comparison of the predicted Z-velocity profiles with SL SGS and different mesh sizes (Cs=0.24)

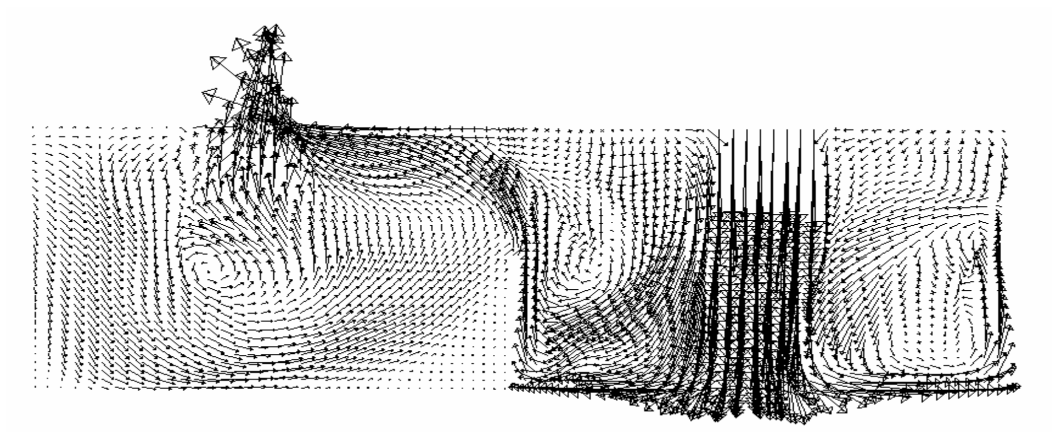

(a) Instantaneous flow field at T=570s

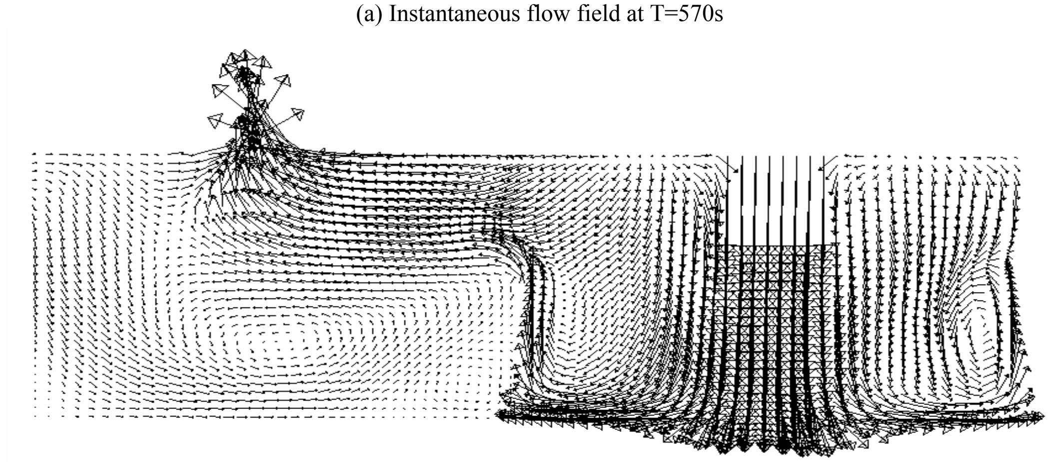

(b) Averaged flow field at T=570s

Fig. 4.27 Comparison of the instantaneous flow field and the averaged flow field at the symmetry plane of the model room obtained with LES at T=570s

Remarks

It can be seen from the above results that LES doesn't give a much "better" prediction of the Z-velocity profiles along the mid-height line and the jet center-line than do the conventional turbulence transport models, it suffers also from the defects of the eddy-viscosity model for the subgrid-scale Reynolds stresses, thus the strong recirculation flows in the room are not very well predicted. But a LES prediction can give much more information about the flow field, the turbulence etc., although it needs substantially more computational resources. By time-averaging, the conventional turbulence transport modeling approach results in a steady-state solution, the effect of the turbulent motions on the mean flow is not resolved but modeled by an empirical turbulence model, much information is lost in the averaging process. On the contrary, large eddy simulation explicitly solves the large, energy-carrying turbulent motions in a three-dimensional, time-dependent way, only the effect of the small eddies on the mean flow is modeled by a subgrid scale turbulence model, thus it retains much more information about the turbulent motions in the solution. Fig. 4.27 shows the differences between an instantaneous flow field and an "averaged" flow field obtained from a large eddy simulation result. It can be clearly seen that, by averaging, much information about the turbulent motion in the flow was lost.

4.3 Validation study: IEA Annex 20 Test Case B (Forced convection, isothermal)

The previous test case represents a ventilation flow with simple boundary conditions but with complicated flow features often encountered in a ventilated space such as impingement, recirculation, separation etc. It can be seen that it's not easy for a turbulence model to capture all these flow features, although the predictions from the LRN k-ε models, the k-ω models and the RSM model are in general satisfactory. The IEA Annex 20 test case B represents another case where the configuration is simple but the boundary conditions are complicated, notably the boundary conditions for the inlet diffuser. Because the room air motion is mainly driven by the momentum supplied from the inlet diffuser, it is thus of vital importance to correctly represent the inlet diffuser in the numerical simulation for an accurate prediction of the room air motion. This has been proved to be particularly difficult in the IEA Annex 20 project. Also this test case is from a full scale experiment measurement with 560 measuring points in a typically practical configuration, thus it is a real test for the turbulence models and modeling methods for the prediction of practical ventilation flows.

4.3.1 Experiment setup

Experimental measurements were carried out by Heikkinen (1991b) in a standard IEA Annex 20 test room with the dimensions of 4.2m x 3.6m x 2.5m (length x width x height). The air supply diffuser is a HESCO type nozzle diffuser and is located in the horizontal center of a rear wall and 0.2 m below the ceiling, the exhaust device is a simple rectangular opening of the dimensions of 0.2m x 0.3 m (height x width) which is located at the same wall and 0.23m below the diffuser (Fig. 4.28). The HESCO nozzle consists of 84 small round nozzles arranged in 4 rows and 21 columns on a rectangular plate of 0.71m x 0.17m size (Fig. 4.29a). All the round nozzles have an equal diameter of 11.8mm, each nozzle can be adjusted independently to a different direction and in the IEA Annex 20 project all the nozzles were adjusted to a 40° angle upward (Fig. 4.29b).

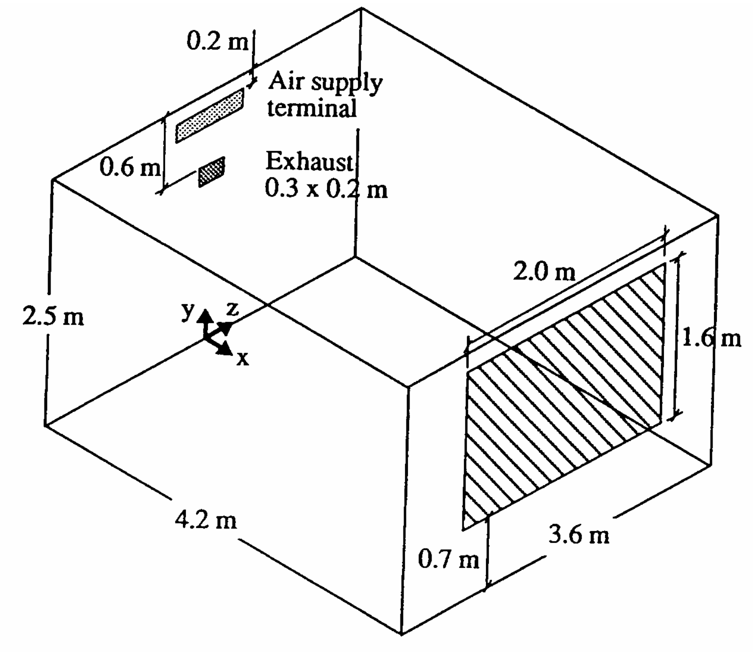

Fig. 4.28 Configuration of the experiment test room for IEA Annex 20 Test Case B (Heikkinen 1991b)

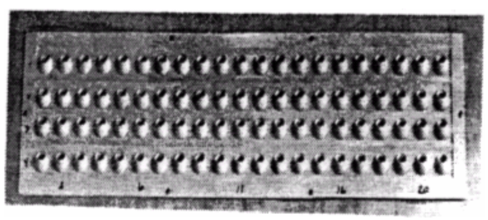

(a) HESCO nozzle diffuser

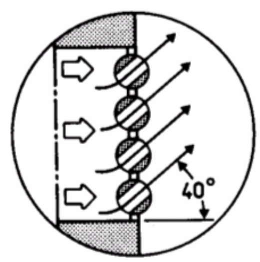

(b) Orientation of the nozzles

Fig. 4.29 The HESCO nozzle diffuser used in the IEA Annex 20 project (Chen et al. 2001)

Experiments were carried out for two ventilation rates under isothermal and steady-state conditions: 3ACH (Test Case B2) and 6ACH (Test Case B3). The key parameters for the two test cases are summarized in Table 1.

Table 4.1 Key parameters for the IEA Annex 20 Test Cases B2 and B3 (Heikkinen 1991b)

Case	Ventilation Rate (ACH)	Airflow Rate (m^3/s)	Supply Air Temperature (°C)	Reynolds number*
B2	3	0.0315	20	2620
B3	6	0.0630	20	5240

* The Reynolds numbers in the table are based on the diameter of the small nozzles.

Measurements were carried out using an omni-directional thermistor anemometer consisting of 40 individually calibrated sensors. A sampling interval of 0.2 seconds and an integration time of 180 seconds were used. The air speed and air temperature were recorded at 560 points inside the test room. The measuring points were arranged on 7 vertical planes (Z=constant), i.e., the symmetry plane (Z=0m) and 3 side planes at each side of the symmetry plane (Z=±0.6m, Z=±1.2m and Z=±1.7m, Fig. 4.30).

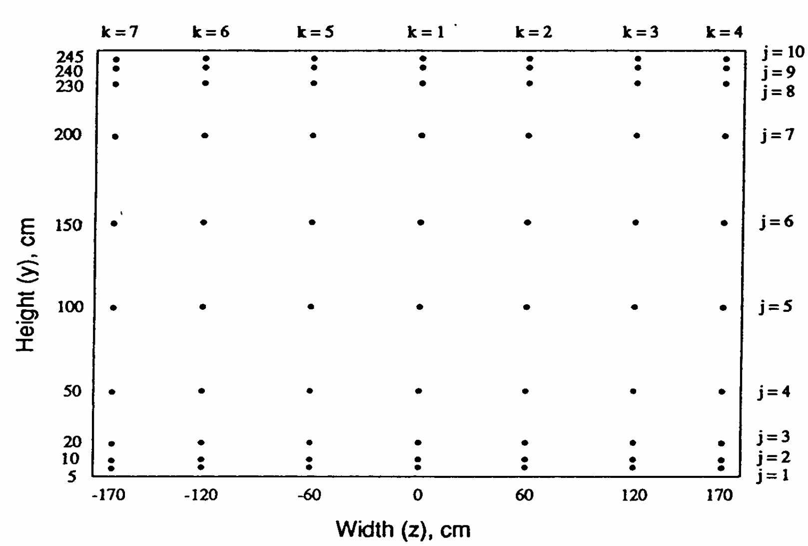

Fig. 4.30 Arrangement and distribution of the measuring points at a plane X=constant (Heikkinen 1991b)

4.3.2 Modeling of the diffuser

4.3.2.1 Introduction

In the IEA Annex 20 project, for evaluating the capability of CFD as a design tool for practical ventilation flows and for providing realistic benchmark data for evaluating CFD codes, a complicated HESCO-type nozzle diffuser as shown in Fig. 4.29 was purposely chosen as the air supply device with the intention to test how such a complicated air supply diffuser which is representative of modern air supply devices can be modeled in numerical simulations and what are the consequences of the different modeling approaches (Nielsen 1992). It was found that the modeling of such a diffuser is particularly difficult (Chen et al. 2001, Lemaire 1993). In the vicinity of the diffuser, the supplied air first forms 84 small round jets and then after a rapid mixing, the small jets soon merge into a single jet which then impinges at an oblique angle on the ceiling and develops into an attached 3D wall jet. Experiment showed that the decay of the maximum jet velocity is very fast due to the intensive mixing of the small jets. At a ventilation rate of 3ACH, the maximum jet velocity drops to 1.5 m/s at approximately 0.1m in front of the diffuser, where the small jets already merge into a large one (Fig. 4.31).

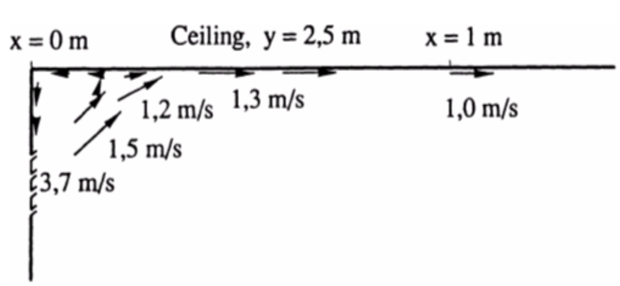

Fig. 4.31 Smoke visualization of the wall jet flow at the symmetry plane of the test room at 3ACH (Heikkinen 1991a)

The conventional turbulence models have difficulty to correctly handle the multi-jet mixing and the oblique 3D jet impingement. Also the complicated internal structure and the large scale difference between the diffuser and the test room preclude a full resolution of the diffuser in the numerical simulation, because that would necessitate a prohibitively large number of mesh grids in the jet region which would then demand too large a computational resource to carry out the numerical simulation. One objective of the IEA Annex 20 project is to evaluate the capability of simplified air flow models in predicting indoor airflow patterns (Lemaire 1993; Nielsen 1992), thus in the IEA Annex 20 framework, several simplified models for the nozzle diffuser have been proposed and tested in the numerical simulations. For the purpose of evaluating different modeling approaches, the wall jet profiles issued from the diffuser were measured in a full-scale experiment test room by Ewert et al. (1991) and Heikkinen (1991a). Fontaine et al. (1994) carried out also a 1/6 water scale model experiment to study the flow characteristics issued from the HESCO nozzle diffuser. The simplified models tested in the IEA Annex 20 project can be divided into two groups (after Chen et al. 2001):

- Momentum modeling at the air supply devices: in this approach the initial jet momentum of the diffuser is imposed directly at the supply opening as the boundary condition for the supply diffusers.
- Momentum modeling in front of the air supply diffusers: in this approach the momentum at some distance downstream of the diffuser is used as the boundary condition for the supply diffuser.

In the IEA Annex 20 framework, the models tested in the first group include simple rectangular slot model and momentum model; in the second group box model and prescribed velocity model (Lemaire 1993).

In the simple rectangular slot model, three variants – namely the basic model, the wide-slot model and the multiple slots model were tested (Fig. 4.32a-c). The basic model represents the supply diffuser as a single rectangular opening with the same effective flow area and aspect ratio as the real diffuser which is located at the center of the diffuser. It was found that this model can reasonably predict the room airflow patterns, but the jet profiles and decay are not well predicted because it predicts the diffuser with a very small jet area thus limits the spreading of the jet. Another study showed that this model is not suitable for non-isothermal airflow simulations (Chen et al. 2001). For this reason, a wide-slot model which is also a single rectangular opening with the same effective flow area but much bigger aspect ratio (width/height) than the real diffuser was tested. Heikkinen (1991a) showed that with the wide-slot model, the mixing in the core region and the jet penetration were over-predicted. A multiple slot model in which the diffuser was represented as 12 or 84 rectangular slots was also tested (Fig. 4.32b-c), it can give somewhat better prediction than the single slot models but the predicted result is still not satisfactory compared with experimental data. The momentum model was originally developed by Chen et al. (1991) in which the diffuser is represented as an opening with the same size of the real diffuser which can be regarded as evenly distributed infinite jets (Fig. 4.32d). To ensure the correct mass and momentum flows from the diffuser, the mass flow and momentum flow are de-coupled and specified separately at the supply opening.

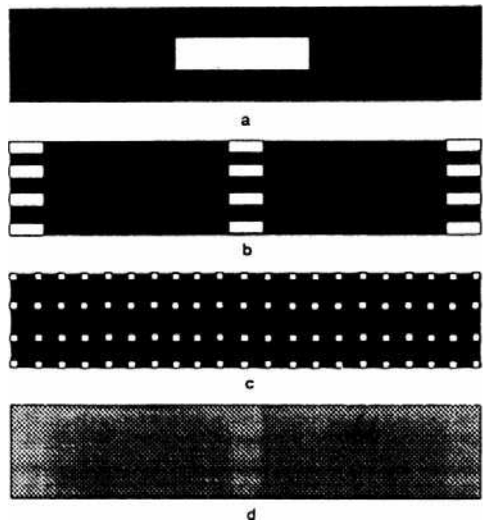

Fig. 4.32 Momentum modeling at the air supply devices (Nielsen 1992)
(a) Basic model, (b) 12 slots model, (c) 84 slots model, (d) Momentum model

The box model was first developed by Nielsen (1974) and has been successfully used by Nielsen et al. (1978) in a numerical simulation of a 2D ventilation flow. In this model the diffuser boundary condition is specified on an imaginary box surface around the diffuser (Fig. 4.33a), the flow field inside the box is ignored. Appropriate jet formulae can be used to specify the velocity profiles at the surface in front of the diffuser, or measured data can be used. On the other surfaces, a free boundary with zero gradients in the normal direction of the surfaces for flow parameters (velocity, temperature, concentration, etc.) is specified. Good agreement with experiment data was reported by Nielsen (1997) when using the box model, but in the study of Heikkinen (1991a), it was found that the box model over-predicts the maximum jet velocity more than other simplified models. A problem associated with the box model is how to determine the box size. If the jet formulae are to be used for providing the jet profiles on the box surfaces, the box should be large enough to ensure that the boundaries are in the fully developed jet region because only in that region the velocity and temperature profiles are self-similar. At the same time, the box should be small enough to avoid the impact of room air circulation and thermal plumes on the jet (Chen et al. 2001). A practical problem is that in most cases it is not known where the fully-developed jet region begins. Like the box model, the prescribed velocity model prescribes the velocity profiles of the jet on a plane at some distance downstream the diffuser which can be obtained from jet formulae or from measurements. Unlike the box model, the flow in the volume between the diffuser and the plane is included in the calculation domain and is continuously updated as the calculation progresses. At the supply opening, the boundary conditions can be specified using the basic model. A 2D illustration of the box model and the prescribed velocity (PV) model has been given by Nielsen (1992) as shown in Fig. 4.33.

In the hydraulic water scale model study of Fontaine et al. (1994), the box model was used to simulate the flow pattern in the scale model room. When using measured velocity profiles as the boundary condition for the box model, the result was not satisfactory. They supposed the problem may come from the measurement because in their hydraulic test bench it is very difficult to get reliable results very close to the ceiling using Laser Doppler Anemometer (LDA). They then used the jet formulae determined by Skovgaard et al. (1991) to specify the boundary condition on the box surfaces, and a good correlation between the predicted and measured velocity profiles at different places in the model room was obtained. The model they used is in reality the prescribed velocity model because the box volume was included in the calculation domain. At the supply opening, an averaged normal velocity was specified so that the flow rate at the inlet was equal to that of the experiment.

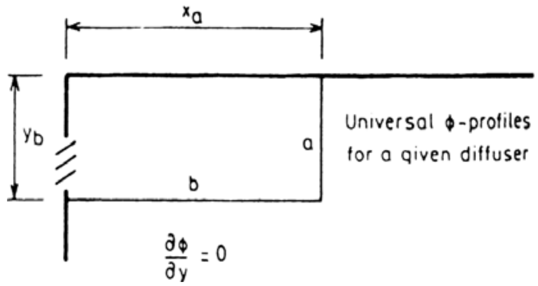

(a) Box model

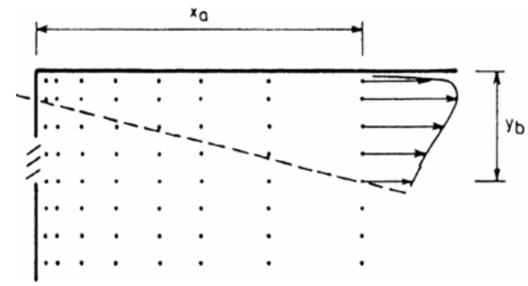

(b) Prescribed velocity model

Fig. 4.33 Momentum modeling in front of the air supply devices (Nielsen 1992)

Emvin et al. (1996) compared the basic model, the momentum model, the box model and a full resolution method of the nozzle diffuser in a numerical study. He concluded that the full resolution of the nozzle diffuser is precise but needs too many mesh grids near the diffuser and the best choice may be the box model if measured experimental data are available. Through a simple analysis, he concluded that the momentum model is not self-consistent and should not be used in numerical simulations. His analysis was based on the free jet assumption (momentum conservation) which is not valid for the HESCO nozzle diffuser: not only the jet momentum is not conserved because of the mixing of the small jets (Chen et al. 2001), but also the jet impinged on the ceiling and developed into an attached wall jet. On the other hand, the study of Heikkinen (1991a) showed that the momentum model performs better than the basic and wide-slot models and thus it was recommended that this model can be used more generally. Chen et al. (2001) showed that the prediction of Emvin et al. (1996) by a full resolution method did even not reproduce qualitatively the correct jet flow pattern observed with smoke visualization. He concluded that the full resolution method may not be a reliable design tool even though the associated computational effort is significantly increased.

In a recent ASHRAE report, Chen et al. (2001) reviewed different simplified models for some widely used air supply diffusers. They concluded that the momentum model in the first group and the box model in the second group are the most promising models for the modeling of air supply diffusers. In their own numerical simulation, the performances of the momentum model and the box model for the HESCO nozzle diffuser were compared. They found that the momentum model cannot predict the small recirculation flow between the diffuser and the ceiling on the upper left corner of the room – which was verified by smoke visualization of the jet flow as shown in Fig. 4.31 – while the box model can predict it. In their box model, measured velocity profiles were applied at two surfaces of a "tiny box": the surface before the diffuser and the top surface of the box. With the RNG k-ε turbulence model, they observed that the maximum jet velocity at the jet center plane (symmetry plane of the test room) was over-predicted approximately 25% for velocity profiles at two different sections of the test room, i.e., at 1m and 2.2m distance in front of the diffuser. They then artificially decreased the supply velocity by 25% on the two tiny box surfaces and the predicted maximum jet velocity agreed well with experiment measurement. They then concluded that the tiny box model is the best model for this kind of diffuser. In practice, their tiny box model requires the supply of measured velocity profiles at the box surfaces which is often not feasible. Even with the measured velocity profiles, the correct prediction still needs a calibration with measured jet profiles which are, in general, not readily available, and it is not known whether the calibration factor (-25%) is Reynolds-number dependent because the calibration was done against only one ventilation rate (3ACH). Also the size of the "tiny box" was determined by comparison with experiment data but was not determined *a priori*. Thus this model is more of an *ad hoc* model than a general one, and significant efforts are needed to specify the measured data on the box surfaces as the boundary conditions. A more general and easy-to-use model for this kind of diffuser is highly desirable for wider applications of numerical simulation of ventilation flows.

Because the jet flows issued from the small nozzles were oriented upward at a 40° angle, the flow in the vicinity of the diffuser is not aligned with any of the three coordinate directions which can increase the numerical diffusion in numerical simulations. A high-order numerical discretization scheme or a "local mesh refinement" is needed to achieve a better resolution of the jet flow especially in the vicinity of the diffuser. In the present study the possibility of better prediction of the jet flow by a simplified model for the diffuser — the momentum model together with local mesh refinement and/or higher-order numerical discretization scheme was re-evaluated using the experimental data of Ewert et al. (1991) and Heikkinen (1991a). The performances of different turbulence models for the prediction of the wall jet flow were also tested and compared. It was found that with the RNG k-ε turbulence model and the momentum model for the diffuser together with local mesh refinement, the wall jet flow issued from the nozzle diffuser can be nicely predicted.

4.3.2.2 Experiment set-up

In the IEA Annex 20 project, Ewert et al.(1991) measured the velocity profiles in the wall jet flow issued from the HESCO nozzle diffuser in an experiment test room with dimensions of 4.8m x 3m x 2.5m (length x width x height). The HESCO nozzle diffuser is located at the horizontal center of a rear wall and 0.2 m below the ceiling of the test room; the exhaust device is a simple opening located on the same wall and 1.4 m above the floor and it is of the size of 0.2m x 0.3 m (height x width). Measurements were carried out using LDA on an imaginary box surface in front of the supply diffuser, i.e., at X=1m in front of the diffuser and at three vertical sections: Z=0m (symmetry plane of the room), Z=0.25m and Z=0.5m and in the range of Y=2.1m~2.5m (Fig. 4.34), the velocity fluctuations (turbulent kinetic energy, TKE) in the three coordinate directions were also measured.

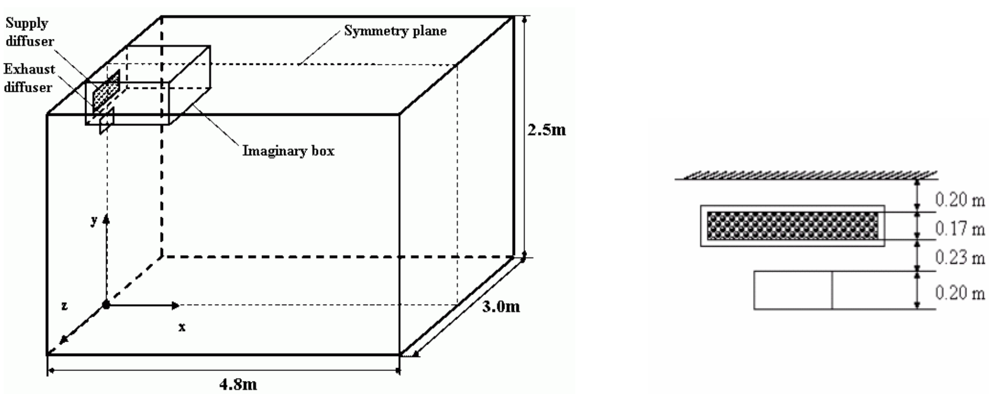

(a) Configuration of the test room (b) Location of the inlet diffuser and the exhaust opening

Fig. 4.34 Configuration of the diffuser test room (Chen et al. 2001)

Heikkinen (1991a) measured the jet velocity profiles at X=2.2m on the symmetry plane of the room using omni-directional anemometers under the same test condition. The ventilation rate for these tests was 3 ACH.

4.3.2.3 Modeling and numerical simulation

Turbulence models

Three k-ε type turbulence models, i.e. the standard k-ε model, the RNG k-ε model and the realizable k-ε model and two k-ω type turbulence models, i.e. the standard k-ω model and the shear-stress-transport (SST) k-ω model were tested. A second-moment RSM model mainly based on the proposals of Gibson et al. (1978) and Launder et al. (1975) with a wall-reflection term in the pressure-strain model was also tested. To bridge the main flow and the viscosity-affected near wall flow in the room, the enhanced wall treatment was used.

Boundary conditions and numerical schemes

Inlet diffuser

The momentum model is used to model the nozzle diffuser. The momentum flow provided by the diffuser is specified as a momentum source added to a volume (the first grid layer) adjacent to the diffuser (Fig. 4.38) and is calculated from the mass flow rate and the effective flow area of the diffuser. At the supply opening, the total mass flow rate and the flow direction are specified.

Exhaust opening

At the exhaust opening, a Dirichlet condition for the pressure is specified, i.e., the gauge pressure at the outlet is set as zero. The Neumann condition for the pressure is also tested and no difference is found between the predicted results with these two methods. Because there are often reversed flows at the exhaust opening at the initial iteration stage, the Dirichlet condition offers better stability and convergence in this case (Fluent Inc. 2001) and thus the Dirichlet condition is preferred.

Turbulence quantities

According to Skovgaard et al. (1991b) and Lemaire (1993), the inlet turbulence intensity is assumed to be 10% and the boundary conditions for k and ε when using k-ε models and the RSM model are calculated using the equations 4.4 and 4.5 (Skovgaard et al. 1991b). For the k-ω models, k and ω are calculated using equations 4.4 and 4.6 (Fluent Inc. 2001).

Alternate methods for specifying the turbulence quantities such as turbulence intensity and hydraulic diameter etc. are also tested and no essential difference was found between the results from these different methods. Further tests with higher turbulence intensities of 15% and 20% were also carried out; no significant influence was found for the predicted results. This is in accordance with those reported by Awbi (1989) and Jourbert et al. (1996).

Discretization schemes

The convection terms are discretized using the second-order upwind or the QUICK scheme and the diffusion terms the second-order central-differencing scheme. For the discretization of pressure, the PRESTO! (PREssure STaggering Option) scheme is used. The SIMPLEC (SIMPLE-Consistent) scheme is used for the pressure-velocity coupling for the steady-state simulation and the PISO (Pressure-Implicit with Splitting of Operators) scheme is used for the time-dependent simulation. The time-marching scheme in the time-dependent simulation is 1st-order implicit.

Comparison of predicted jet profiles with experimental data

Most of the simulations were carried out in a half room configuration. Some simulations were carried out in a full room configuration to investigate the flow asymmetry problem observed by Heikkinen (1991b) and Fontaine et al. (1994). The predicted jet flow profiles (velocity, TKE) at X=1.0m and X=2.2m were compared with the experimental data of Ewert et al. (1991) and Heikkinen (1991a).

After some initial tests, two meshes, 60x55x34 for half room configuration and 60x55x68 for full room configuration, are chosen as the main computation meshes. The mesh is more condense in the near wall regions and near the diffuser, where steeper velocity gradient is expected. A typical computation mesh (60x55x34, Mesh1) for half room configuration is shown in Fig. 4.35. In Fig. 4.36 and Fig. 4.37, the predicted velocity profiles and turbulent kinetic energy profiles in the wall jet flow from the mesh grid 60x55x34 using the RNG k-ε turbulence model and the momentum model for the diffuser are compared with those from finer meshes of 68x61x38 (Mesh2) and 80x61x38 (Mesh3) for the half room configuration. It can be seen from Fig. 4.36 and Fig. 4.37 that the predicted velocity and turbulent kinetic energy profiles obtained from these three meshes are nearly the same, except at the side section of Z=0.25m where the finer meshes yield a slightly better prediction for the velocity profile. Therefore in the following calculations the 60x55x34 mesh was used. The maximum jet velocity at the jet center line is under-predicted at X=1m but over-predicted at X=2.2m (Fig. 4.36). The turbulent kinetic energy profiles are seriously under-predicted especially at the side section of Z=0.5m – This has been investigated in IEA Annex 20 project when using standard k-ε turbulence model (Lemaire 1996) and has also been reported by Chen et al. (2001) when using RNG k-ε turbulence model and the box model for the diffuser.

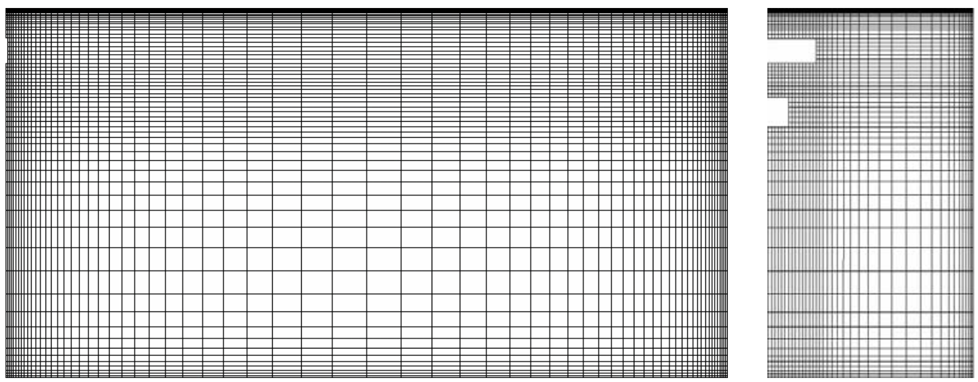

Fig. 4.35 The computation mesh for the jet flow of the IEA HESCO diffuser

In Figs. 4.36 and Fig. 4.37, the predicted velocity profiles and turbulent kinetic energy profiles using local mesh refinement from the 60x55x34 mesh (Mesh1) are also shown. It can be seen that with local mesh refinement, significant improvement for the prediction of both the velocity profiles and turbulent kinetic energy profiles can be achieved. Excellent agreement of the predicted velocity profiles with measurements is obtained at the jet center plane. At the two side sections of Z=0.25m and Z=0.5m, the prediction of the velocity profiles is reasonably well too. The agreement of the predicted turbulent kinetic energy profiles with measurements is less satisfactory, but the general trends are well predicted. Table 4.2 gives a quantitative comparison of the predicted maximum velocity and turbulent kinetic energy in the wall jet flow with the respective measured values.

Local mesh refinement

The local mesh refinement is applied in the region of X=0m to 0.3m, Y=2.13m to 2.5m and Z=0m to 0.355m. Each grid cell in the region is halved in each coordinate direction, thus each cell is divided into 8 cells, which increases the total mesh grid size from 112200 cells to 135720 cells [Mesh1 + LR1 (local refine1) in Figs. 4.36 and 4.37]. Mesh1+LR2 (local refine2) is done by repeating the process on the locally refined mesh (Mesh1 + LR1), except that the refinement range in the X direction is from X=0m to X=0.25m. The result obtained with this latter mesh is slightly better than with its parent mesh (Mesh1+LR1), but the total number of grid cells is more than doubled (from 135720 cells to 302978 cells). The total gain is very little compared with the computational cost increased. Thus in the following simulations, the computation mesh used is Mesh1+LR1.

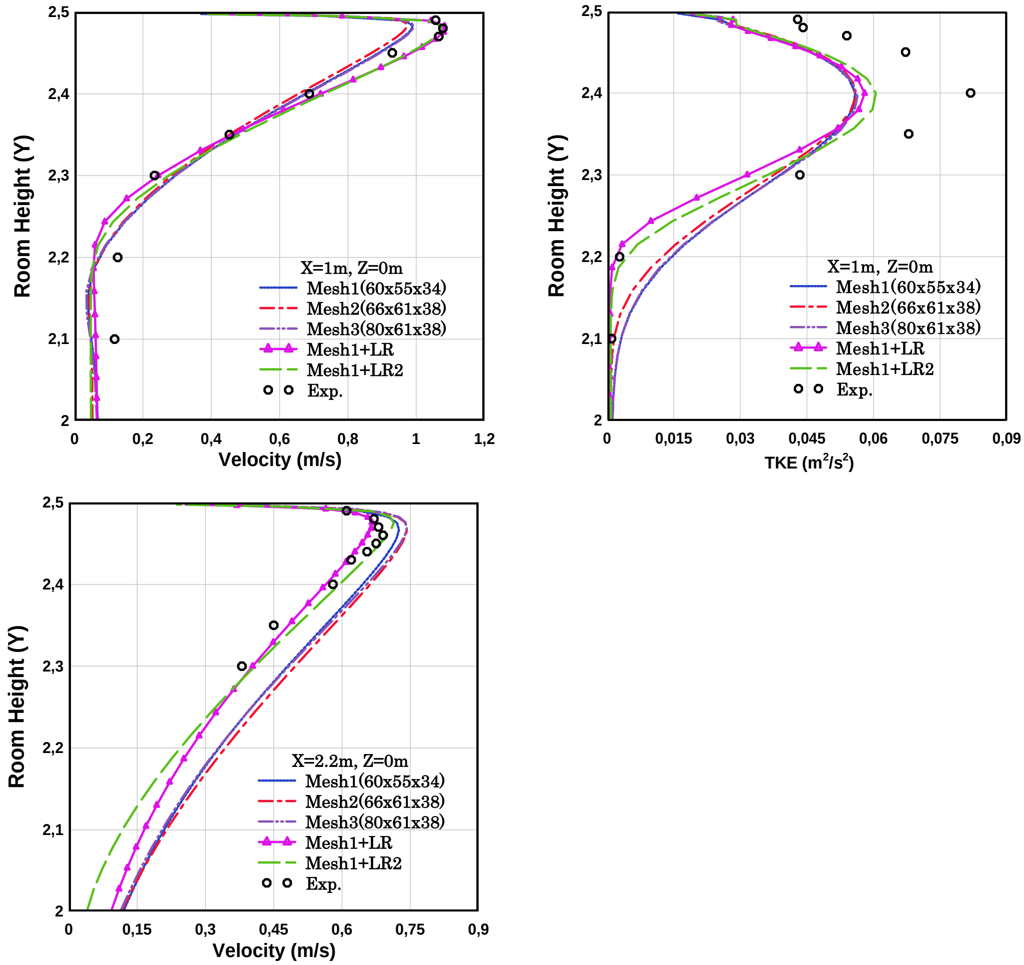

Fig. 4.36 Comparison of the calculated velocity and turbulent kinetic energy profiles with measurements at the jet center plane (Z=0m, X=1m and 2.2m)

Fig. 4.38 illustrates how the mesh is locally refined (Mesh1+LR1), it shows also the region where the momentum source is added (the first grid layer adjacent to the diffuser). It is found that it is essential that the local mesh refinement range in the streamwise direction, i.e. the X direction, should at least cover the impinging region (i.e., $x \geq 0.2 / \tan 40° \approx 0.24m$). When the refinement range in the X direction is less than 0.25m, the improvement for the prediction is greatly reduced.

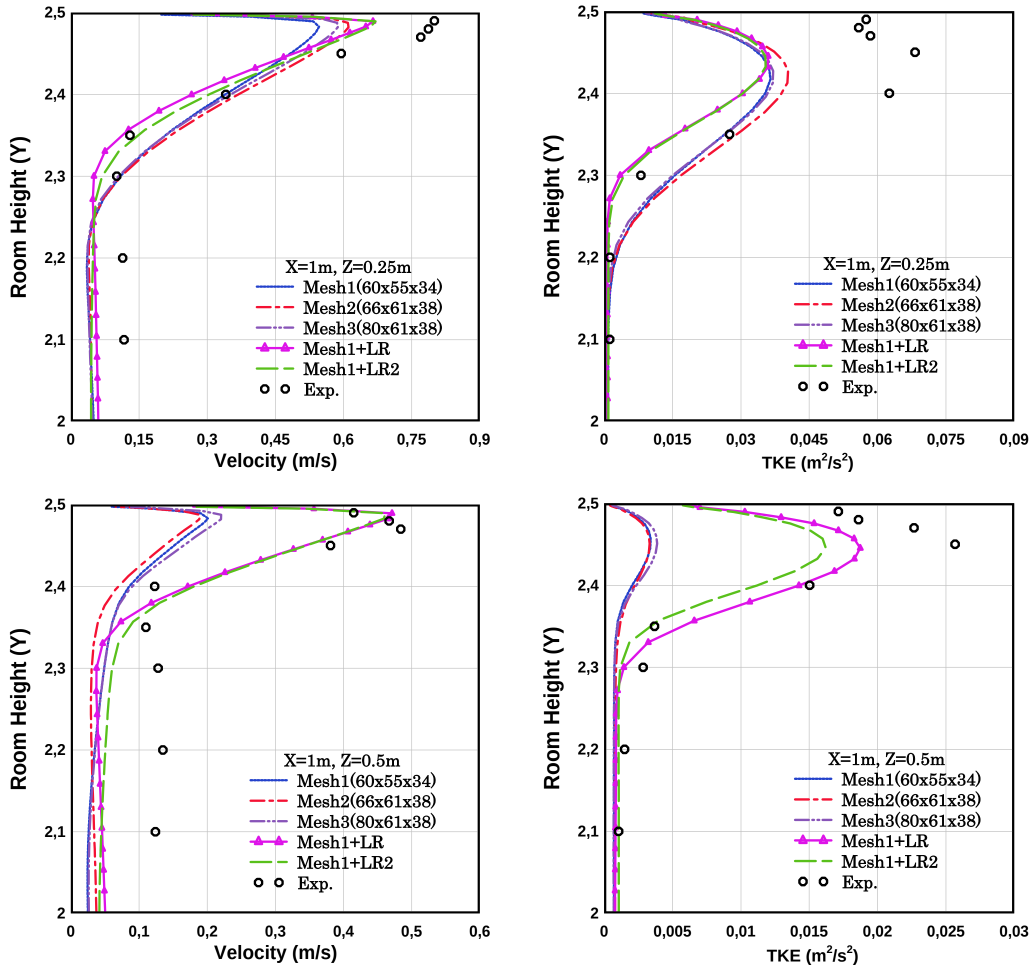

Fig. 4.37 Comparison of the calculated velocity and turbulent kinetic energy profiles with measurements at two planes parallel to the symmetry plane (X=1m and Z=0.25m, 0.5m)

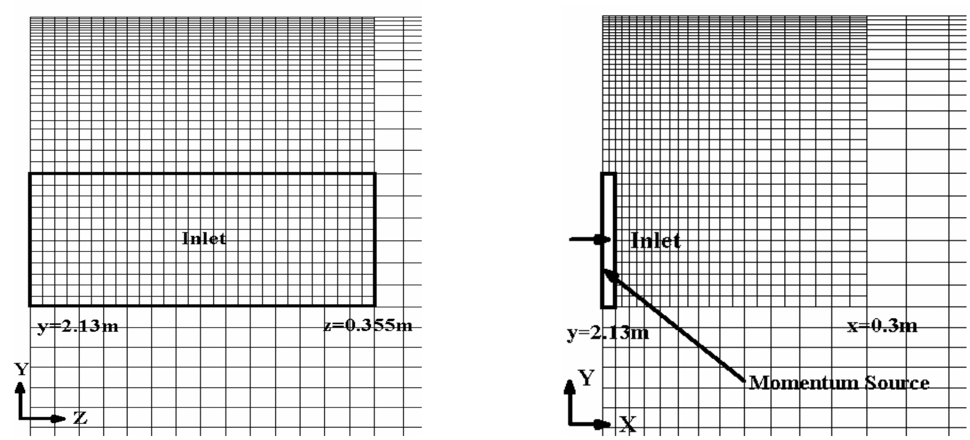

(a) X=0m Plane
(Inlet wall)

(b) Z=0 Plane
(Symmetry plane)

Fig. 4.38 Description of the local mesh refinement (Mesh1+LR1)

Table 4.2 Quantitative comparison of the predicted maximum velocity and turbulent kinetic energy at different sections of the wall jet flow with experiment data*

Position \ Mesh			Mesh 1 (60x55x34)	Mesh 2 (66x61x38)	Mesh3 (80x61x38)	Mesh 1+ LR1	Mesh 1+ LR2	Exp.
X=1m Z=0m	Vel.	Vmax (m/s)	0.99	0.974	0.99	1.083	1.073	1.078
		Error (%)	- 8.2	- 9.6	- 9.6	+ 0.46	- 0.46	
		Y Position (m)	2.48	2.483	2.482	2.483	2.483	2.48
	TKE	$k$max (m^2/s^2)	0.056	0.056	0.056	0.058	0.0605	0.08187
		Error(%)	- 31.6	- 31.6	- 31.6	- 29.2	- 26.1	
		Y Position (m)	2.4	2.4	2.4	2.4	2.4	2.4
X=1m Z=0.25m	Vel.	Vmax (m/s)	0.546	0.611	0.587	0.665	0.67	0.8
		Error (%)	- 31.8	- 23.6	- 26.6	- 16.9	- 16.3	
		Y Position (m)	2.483	2.483	2.482	2.49	2.49	2.49
	TKE	$k$max (m^2/s^2)	0.0365	0.0404	0.0371	0.036	0.0354	0.0682
		Error(%)	- 46.5	- 40.8	- 45.4	- 47.2	- 48.1	
		Y Position(m)	2.417	2.43	2.427	2.445	2.43	2.45
X=1m Z=0.5m	Vel.	Vmax (m/s)	0.201	0.189	0.221	0.471	0.462	0.467
		Error (%)	- 57	- 60	- 52.7	+ 0.86	- 1.07	
		Y Position (m)	2.483	2.488	2.488	2.489	2.489	2.48
	TKE	$k$max (m^2/s^2)	0.0034	0.0033	0.00387	0.0187	0.0162	0.02567
		Error(%)	- 86.8	- 87.1	- 84.9	- 27.2	- 36.9	
		Y Position (m)	2.457	2.45	2.451	2.445	2.445	2.45
X=2.2m Z=0m	Vel.	Vmax (m/s)	0.725	0.743	0.742	0.666	0.714	0.69
		Error (%)	+ 5.1	+ 7.7	+ 7.7	- 3.5	+ 3.4	
		Y Position (m)	2.467	2.469	2.469	2.476	2.475	2.46

* The " + " and the " - " signs in the above table indicate over- and under- prediction, respectively.

Prediction of the recirculation flow

Chen et al. (2001) reported that with the momentum model for the supply diffuser and a grid resolution of 50x32x35 (also in half room configuration), the recirculation flow at the upper left corner of the test room as shown in Fig. 4.31 cannot be predicted by the RNG k-ε model. They repeated their simulation with finer meshes, but still failed to predict the recirculation flow. In the present study, when using the RNG k-ε model and a grid resolution of 60x55x34, the recirculation flow cannot be predicted. However, when the mesh grids at the proximity of the diffuser are locally refined, the recirculation flow can be well predicted, although the size of the recirculation zone is slightly smaller than that found experimentally by smoke visualization (about 0.2m x 0.2m, Heikkinen 1991a). Fig. 4.39 is a comparison of the calculated flow fields at the upper left corner on the symmetry plane of the test room obtained with the RNG k-ε model and with/without local mesh refinement. It is also observed that as the grid resolution near the supply diffuser is increased, the size of the predicted recirculation zone at the upper left corner approaches more and more the measured size.

Influence of the pressure-gradient correction term in the enhanced wall treatment

In the enhanced wall treatment, an option accounting for the pressure-gradient effect is included. With this option, it is found that the prediction for the wall jet flow can be improved; it is especially beneficial for the prediction of the turbulent kinetic energy profiles (Fig. 4.40). The improvement may come from the fact that this term accounts for some effect of the sudden change of pressure at the jet impinging region.

Effect of different discretization schemes for the convection terms

The QUICK discretization scheme for convection terms is also tested, the predicted results degraded greatly as compared with those obtained with second-order upwind scheme as shown in Fig. 4.40, and it is found that the calculation with the QUICK scheme is more difficult to converge, a result also observed by Chen et al.(2001).

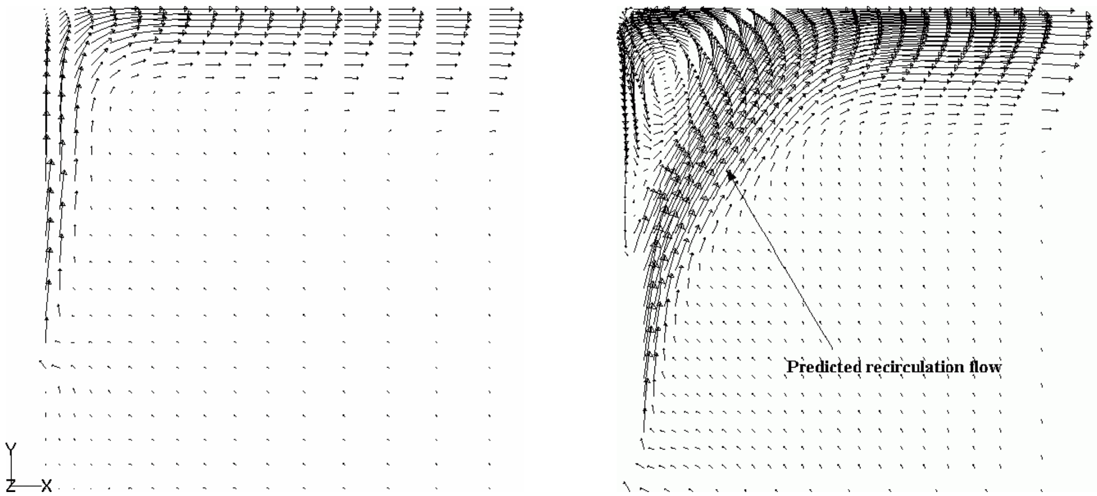

(a) Grid resolution 60x55x34 (Mesh1) (b) Mesh 1 + LR1

Fig. 4.39 Comparison of the predicted flow fields at the upper left corner on the symmetry plane using RNG k-ε model and with/ without local mesh refinement

Flow asymmetry in the test room

When the geometrical configuration is symmetric, a symmetric flow condition is often assumed in order to save computing time, but it is not always valid. There is experimental evidence to the contrary in some cases. In an experimental study Zhang et al. (2000) has reported asymmetric flow in a symmetric test room meant to produce 2D flow pattern when there is no any obvious disturbance. Fontaine et al. (1994) observed asymmetric flow behavior both in their water scale model experiment and in their numerical simulations for the IEA Annex 20 nozzle diffuser. This phenomenon was also observed in the full-scale experiments in IEA Annex 20 Test Room by different research groups (Heikkinen 1991b; Lemaire 1993).

In the present study, when the symmetry boundary condition is imposed at the symmetry plane (half room configuration), the computed flow pattern does not reach a steady solution even after many thousands of iterations. At a certain iteration step, the residuals no longer decrease but oscillate irregularly at an acceptable level. It is observed that whenever there is an oscillation peak in the residuals, it is accompanied by a change of flow pattern, and the solution is time-dependent with some irregular periodicity. Fig. 4.41 shows a comparison of the predicted velocity profiles with experimental data at different iteration stages. It can be seen that the predicted velocity profiles near the diffuser (at X=1m and Z=0m, 0.25m) are greatly influenced by the change of flow pattern, but at X=2.2m and Z=0.5m the influences are much smaller. The predicted turbulent kinetic energy profiles show similar trends. In Fig. 4.42, an example of the predicted velocity contours just under the room ceiling (Y=2.48m) at different iteration stages is shown. It can be seen that at the iteration steps 8440 and 15740, the predicted flow patterns at Y=2.48m plane are nearly the same, and nearly the same velocity profiles for the wall jet flow are obtained (Fig. 4.41). But at the iteration step 14604, the predicted jet flow pattern differs much from those at the above two steps, and much different velocity profiles at X=1m, Z=0m and X=1m, Z=0.25m are obtained.

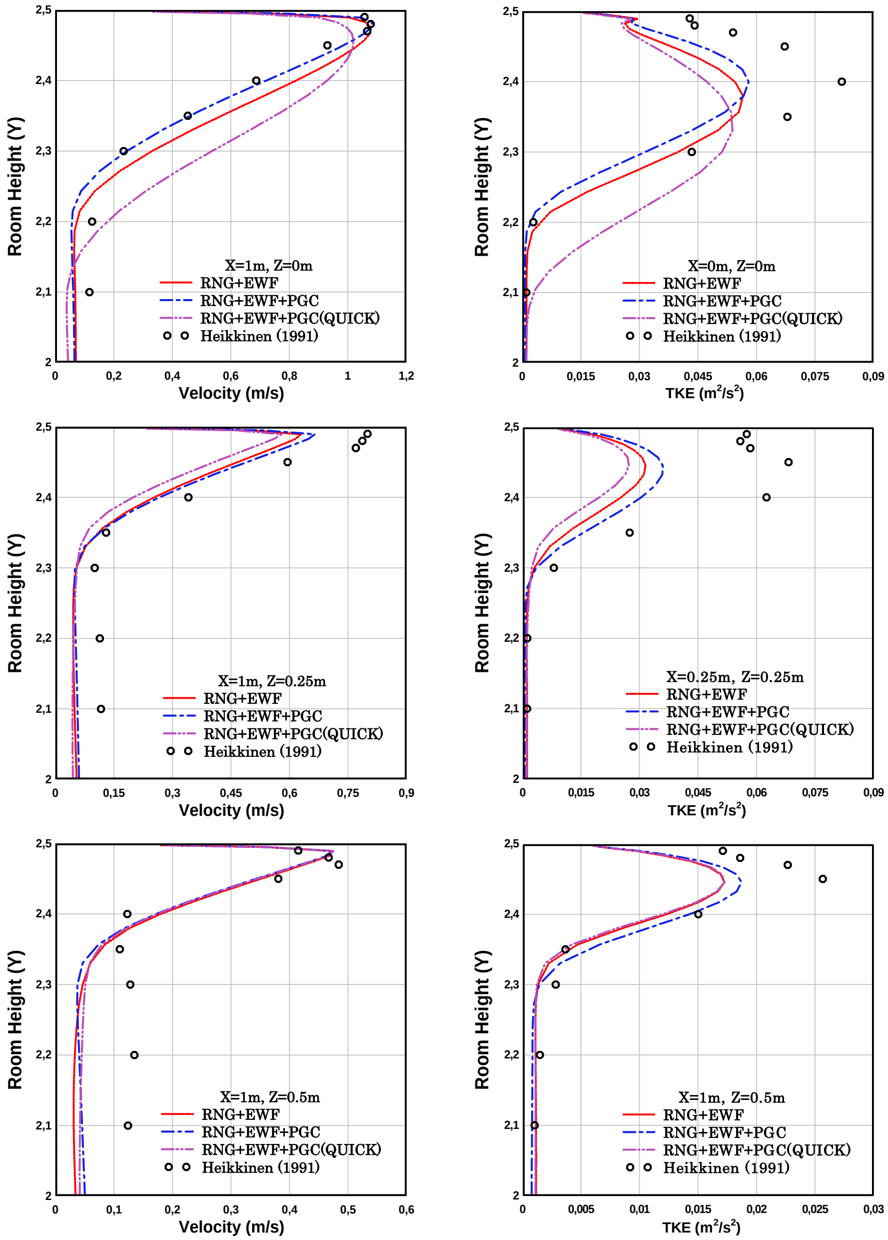

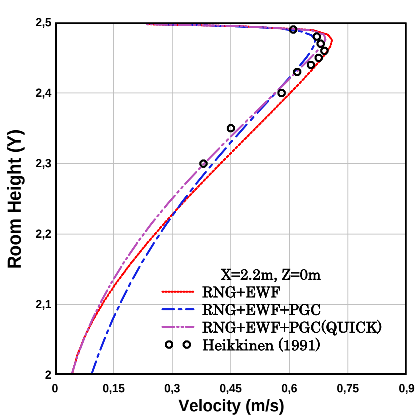

Notes:

Mesh size: 60x55x34
EWF—Enhanced wall-treatment
PGC—Pressure-gradient correction
QUICK—QUICK scheme for convection terms

Fig. 4.40 Comparison of calculated velocity and turbulence kinetic energy profiles with measurements

To further investigate such a flow phenomenon, a full room configuration with a mesh size of 60x55x68 (the other half of the room is mirrored from Mesh1) is used and both steady-state and time-dependent simulations are carried out. In the steady-state simulations, it is found that the wall jet flow sometimes turns to one side of the room in the course of iteration and then turns back to the symmetry plane. Fig. 4.43 is an example of the flow pattern under the ceiling (Y=2.48m) at different iteration steps from a steady-state simulation in a full room configuration, the mesh is locally refined from X=0~0.3m, Y=2.13~2.5m and Z=−0.355~0.355m. It clearly shows that the flow is not symmetric. The flow pattern changes also in a quasi-periodic manner as the iteration progresses. It can be seen for example that at the iteration steps 26464 and 48340, the flow patterns are nearly the same, and the jet flow always turns to one side of the room – but at different iteration steps the degree of asymmetry changes.

A time-dependent simulation using the same configuration and the same mesh resolution is also carried out. To minimize the numerical truncation errors, the simulation is done using the double precision solver in FLUENT. Similar change of flow patterns as in the steady-state simulation is observed in the time-dependent simulation. Fig. 4.44 compares the time history of the mass flow rate at the outlet and the Z-velocity at the point of (1, 2.45, 0), i.e. at 1m distance from the diffuser and 0.05m below the ceiling on the symmetry plane. It can be seen that the flow becomes "quasi-steady" after about 120s, and then the flow "sweeps" from one side of the symmetry plane to the other side irregularly at X=1m, the Z-velocity at the point (1, 2.45, 0) changes its sign accordingly, and there is a clear correlation between the fluctuations of the Z-velocity and the mass flow rate at the outlet: the phase of the Z-velocity fluctuation is opposite to the phase of the mass flow rate fluctuation.

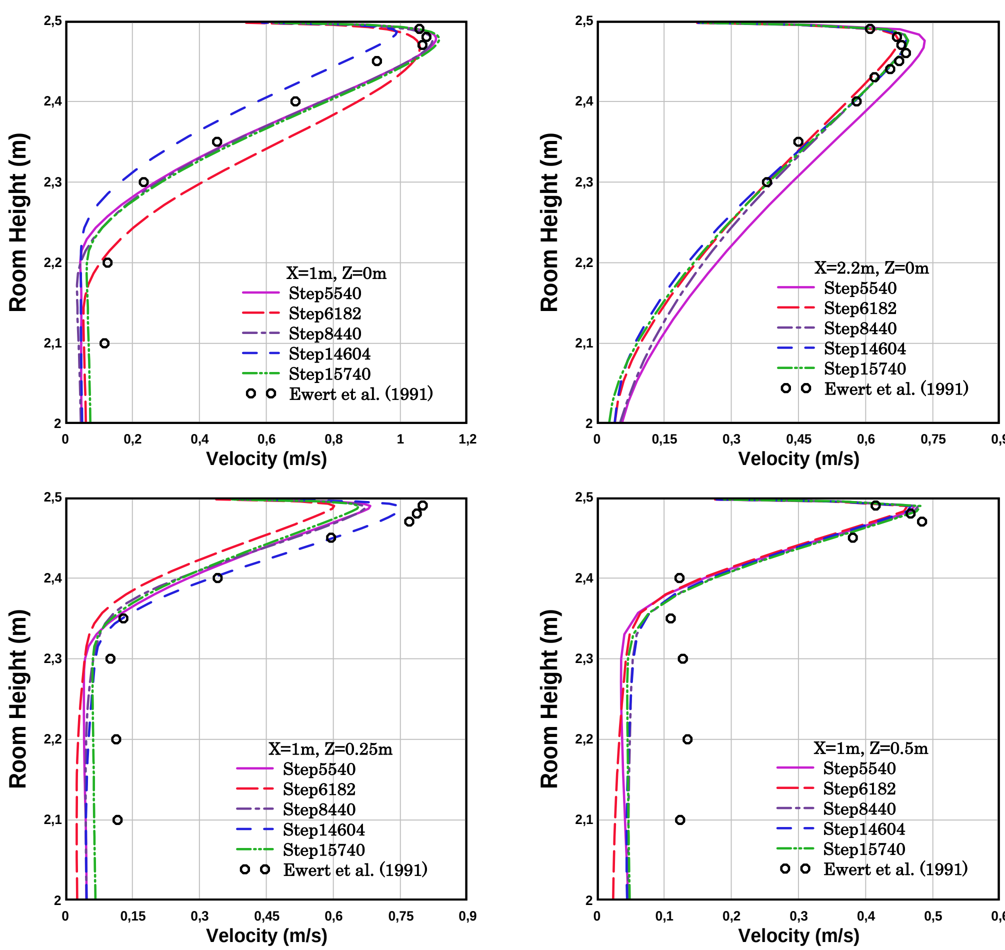

Fig. 4.41 Comparison of calculated velocity profiles with experiment data at different iteration stages (Mesh size: 60x55x34; with local mesh refinement: X=0~1.5m, Y=2.13~2.5m, Z=0~0.355m)

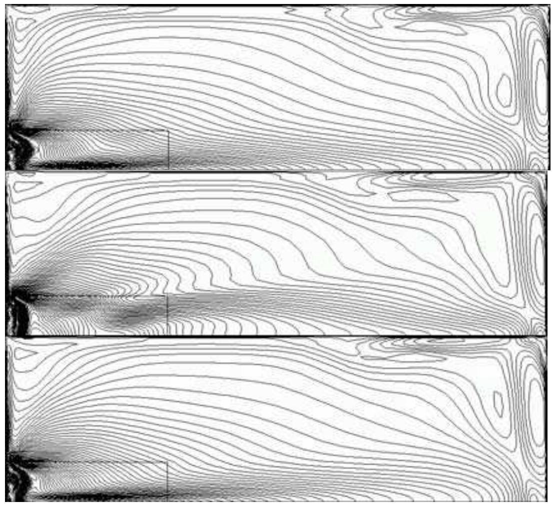

Step 8440

Step 14604

Step 15740

Fig. 4.42 Predicted velocity contours near the ceiling (Y=2.48m) at different iteration stages
(Mesh size: 60x55x34; with local mesh refinement: X=0~1.5m, Y=2.13~2.5m, Z=0~0.355m)

In Fig. 4.45, the time history of Z-velocities at the point (1, 2.45, 0) and the point (2.2, 2.48, 0) is compared. It can be seen that at the point (2.2, 2.48, 0), the Z-velocity doesn't change its sign, but has a very small positive value (its mean value is about 0.027m/s). The mean value of the Z-velocity at the point (1, 2.45, 0) is also positive and is approximately 0.0478m/s. It means that the jet flow is always asymmetric and turns to one side of the symmetry plane, but the degree of asymmetry changes with time – the same result is observed in the steady-state simulation as shown in Fig. 4.43. It can also be seen that the fluctuation of Z-velocity at these two points has an opposite phase too, but the phase of the fluctuation of Z-velocity at the point of (2.2, 2.48, 0) has a little lag. This is reasonable because the changes at the point (1, 2.45, 0) need some time to be transported to the point (2.2, 2.48, 0). Fig. 4.46 compares the time history of velocity magnitude at two symmetric points (2.2, 1.2, -0.5) and (2.2, 1.2, 0.5) in the occupied zone. It clearly shows that the degree of flow asymmetry changes with time and that in the time interval 520s~550s, the velocity magnitude at the two points is nearly the same. It means that although the jet flow is always asymmetric, the flow in the occupied zone can be symmetric sometimes. Fig. 4.47 shows the time history of the magnitude of the velocity at the point (2.2, 2.48, 0.5). It can be seen that after about 520s, the magnitude of the velocity at that point approaches to a fixed value, the maximum fluctuation is only about 0.002 m/s.

It seems that at a ventilation rate of 3ACH, there is an intrinsic instability in the flow, perhaps it is near a critical value of Reynolds number which represents the ratio of convective and diffusive rates of momentum transfer. A very small time step (0.005s) must be used in the time-dependent simulation. When the time step is increased to 0.008s, the calculation at each time step converges in only two or three iterations, but then suddenly in one time step even after more than 30 iterations the calculation does not converge, and the calculation diverges quickly. It seems that there are some high frequency disturbances occurring in the flow occasionally which trigger the change of the flow pattern, but the flow is not completely unstable but changes in a "quasi-periodic" manner. Chen et al. (1992) has discussed unsteady and unstable flow problems in ventilation flows in both numerical simulations and experiments. He suggested also that multiple solutions may exist for a special flow and the numerical simulation can pick one solution at one time and other solution at another time. In the present numerical study with the steady-state simulations, it is observed that after a certain number of iterations, the residuals for the flow variables no longer decrease but stay at some stable values with more or less regular oscillations, and the oscillations are not damped as also shown in Chen et al. (1992). But in the time-dependent simulations, after a long enough transient regime with damped oscillations, the flow tends to a steady-state regime (for t >700 s, Figs. 4.46 and 4.47).

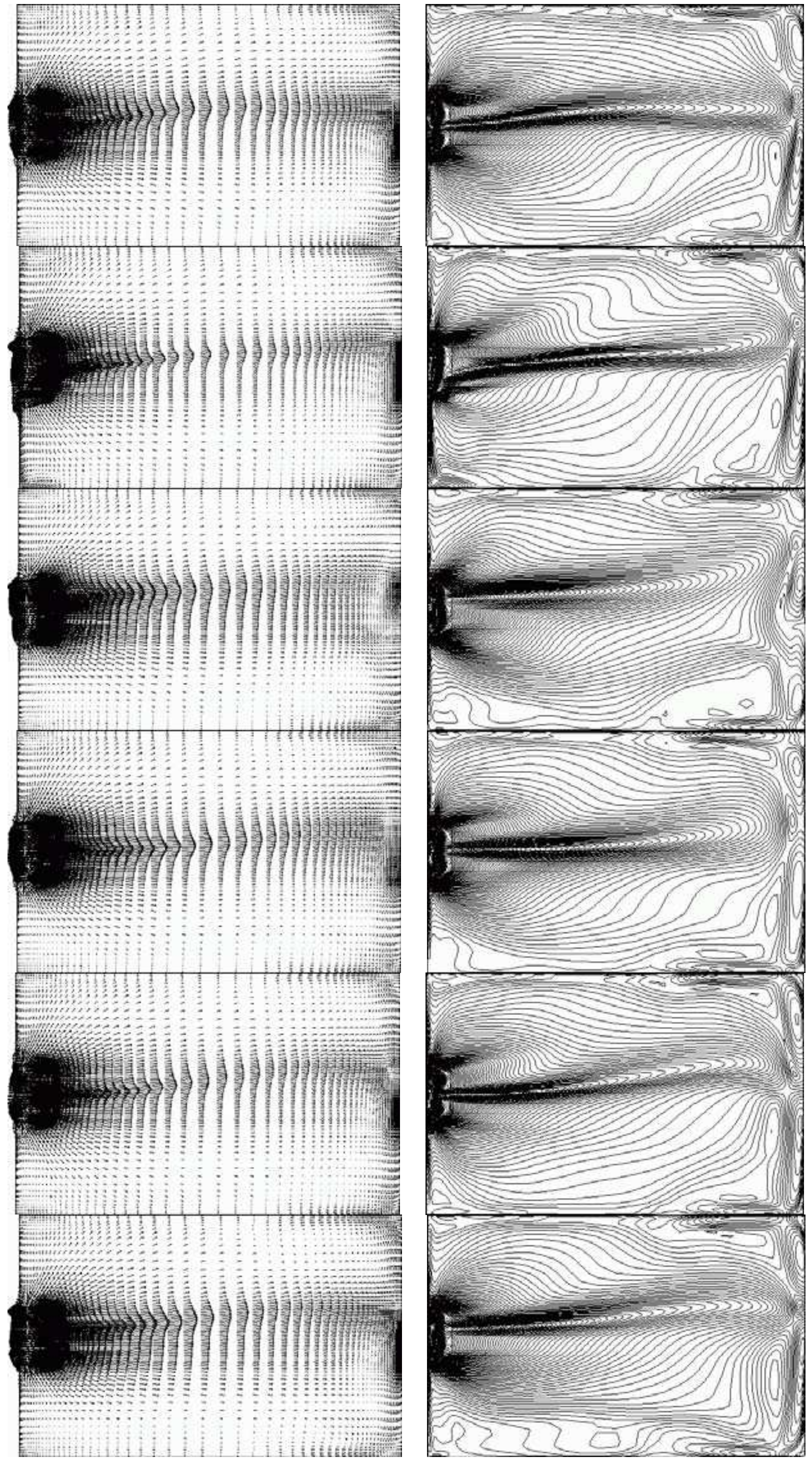

Step 26464

Step 27472

Step 29180

Step 35696

Step 48340

Step 55328

(a) Velocity vector (b) Velocity contours

Fig. 4.43 An example of the predicted flow asymmetry near the room ceiling (Y=2.48m) in a full room configuration at different iteration stages

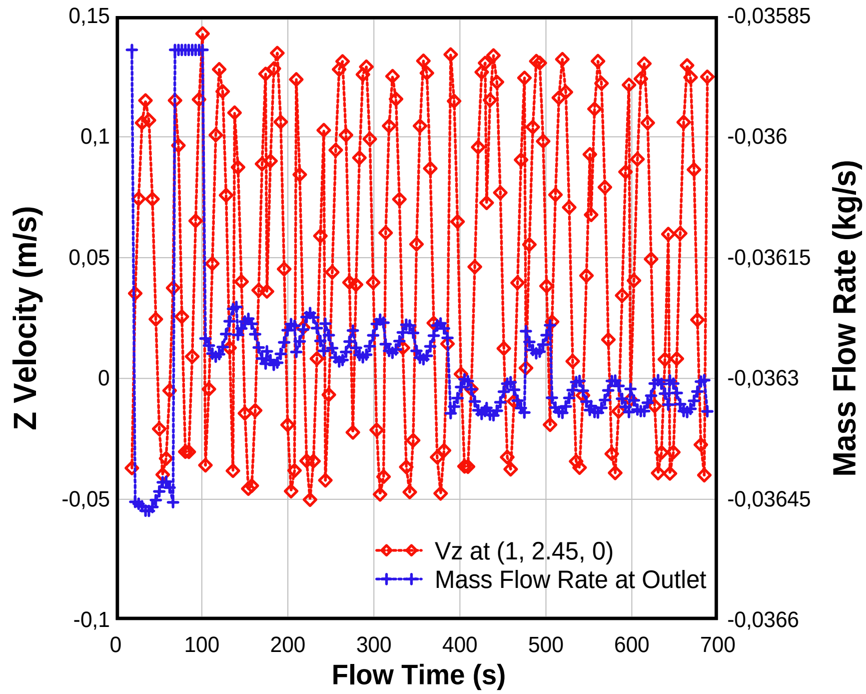

Fig. 4.44 Time history of mass flow rate at the outlet and Z-velocity at the point (1, 2.45, 0)

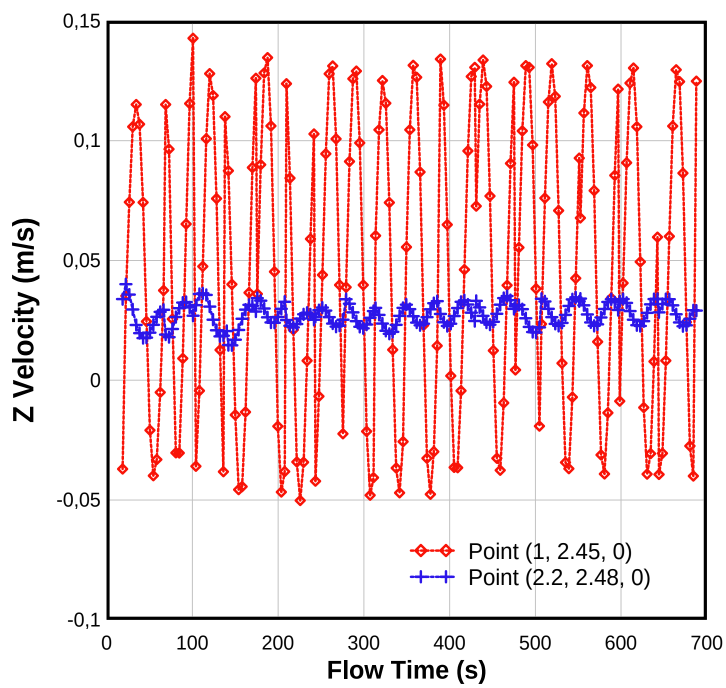

Fig. 4.45 Time history of Z-velocities at the points of (1, 2.45, 0) and (2.2, 2.48, 0)

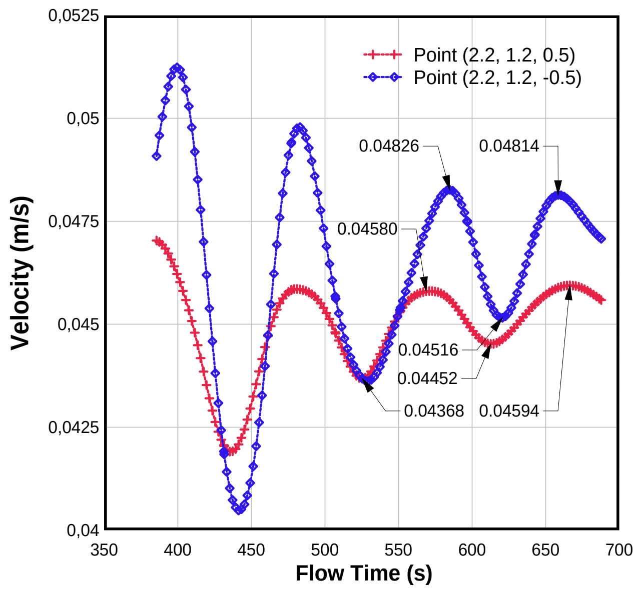

Fig. 4.46 Time history of the velocity magnitude at two symmetric points of (2.2, 1.2, 0.5) and (2.2, 1.2, -0.5) in the occupied zone

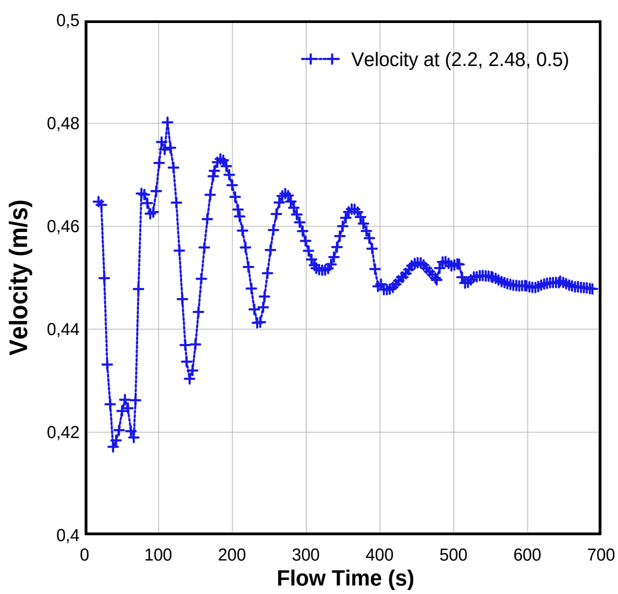

Fig. 4.47 Time history of the velocity magnitude at the point of (2.2, 2.48, 0.5)

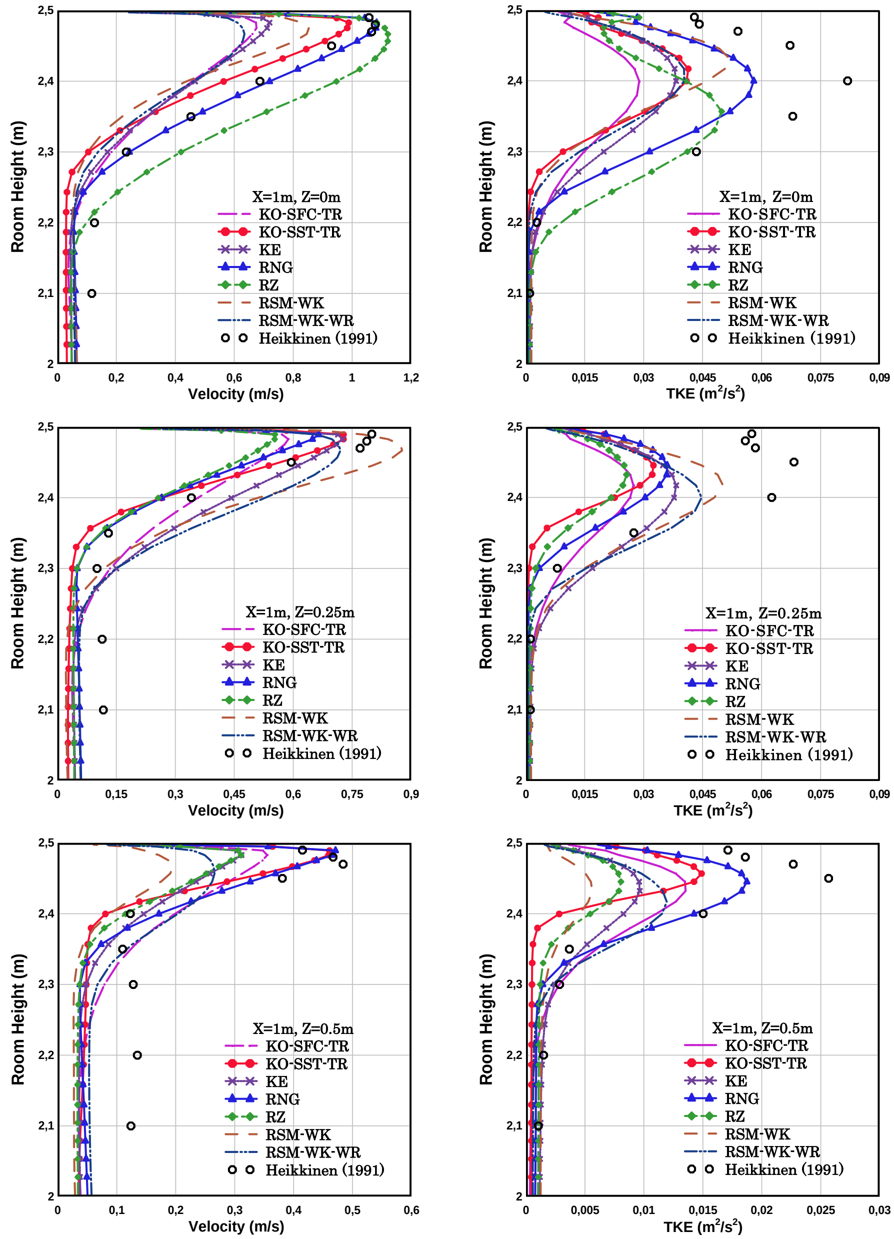

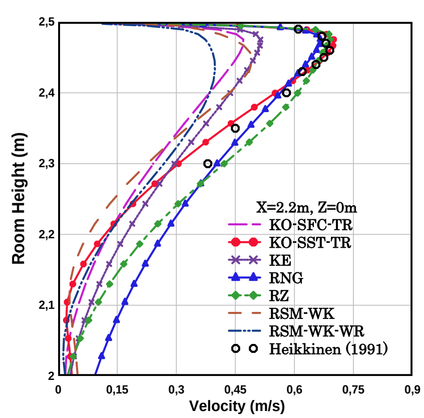

Notes:

Mesh size: 60x55x34 (Mesh1+LR1)
KE: Standard k-ε model
KO-SFC-TR: Standard k-ω model (LRN version)
KO-SST-TR: Mentor SST k-ω model (LRN version)
RNG: RNG k-ε model
RZ: Realizable k-ε model
RSM-WK: RSM model
RSM-WK-WR: RSM with wall reflection term

Fig. 4.48 Comparison of calculated velocity and turbulent kinetic energy profiles with different turbulence

Comparison of the predicted jet profiles with different turbulence models

The jet profiles predicted with different turbulence models and with local mesh refinement (Mesh1+LR1) are compared with experimental data in Fig. 4.48. It can be seen that the RNG k-ε model gives the best overall results, the SST k-ω model with transitional flow correction (low-Re version of the model) can yield a reasonable prediction for the jet velocity profiles, but the prediction for the turbulent kinetic energy profiles is less satisfactory. The standard k-ε model and the SST k-ω model can predict the recirculation flow at the upper left corner, while the realizable k-ε model can not.

The RSM model used is mainly based on the model proposed by Gibson et al. (1978), it contains a wall-reflection term in its pressure-strain model to account for the influence of the walls, which tends to damp the normal stress perpendicular to the walls while enhancing the stresses parallel to the walls (Fluent Inc. 2001). It can be seen from Fig. 4.48 that the inclusion of the wall-reflection term under-predicts the maximum velocity at the jet center plane but improves the prediction of the velocity profiles and the turbulent kinetic energy profiles at the two side planes parallel to the center plane. Further investigation reveals that without the wall-reflection term, the RSM model can predict the small recirculation flow at the upper left corner of the room, but when the wall-reflection term is included, the recirculation flow tends to diminish. Fig. 4.49 shows a comparison of the calculated flow fields at the upper left corner using RSM model with/without wall-reflection term. Since the momentum supplied by the diffuser is mainly contained at the jet center plane, the inclusion of the wall-reflection term in the RSM model will under-predict more of the total momentum than when this term is not included.

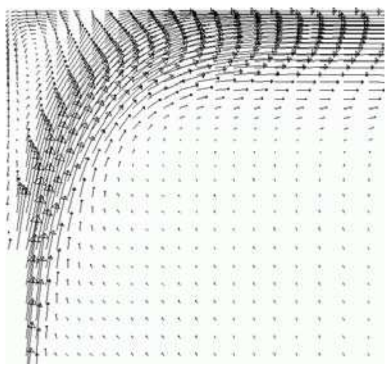

(a) Without wall-reflection term

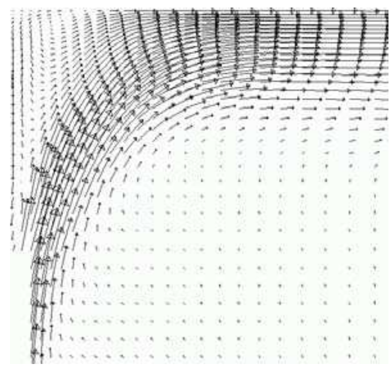

(b) With wall-reflection term

Fig. 4.49 Comparison of the flow field calculated with RSM model and with/without wall-reflection term at the symmetry plane of the room

4.3.2.4 Remarks

The above results showed that the RNG k-ε model together with local mesh refinement yields a good prediction of the jet profiles when momentum model is used for the nozzle diffuser. However, the successful use of the momentum model is not unconditional: it was found that there exists an optimum dimension of the momentum source cell in the streamwise direction (X direction in Fig. 4.38) for the correct prediction of the jet profiles. At 3ACH, the dimension of the momentum source cell in the X direction, ΔX_0, should be about 0.014 ~ 0.018 m. When using a value less than 0.014m, the maximum velocity in the jet profiles will be under-predicted; on the other hand, when using a value higher than 0.018m, the maximum jet velocity in the jet profiles will be over-predicted. For example, when ΔX_0=0.0108m, the predicted maximum jet velocities are 0.977m/s at X=1m and 0.663m/s at X=2m, while the measured maximum jet velocities are 1.078 m/s at X=1m and 0.69 m/s at X=2.2m; thus they are under-predicted about 9.37% and 3.91%, respectively; when ΔX_0=0.021m, the predicted maximum jet velocity at X=1m is nearly the same as that of measurement, but at X=2.2m, the predicted maximum jet velocity is

0.7463m/s, i.e., over-predicted about 8.16%. Because the above validation was carried out against only one ventilation rate (3ACH), it is not clear whether this value is Reynolds number dependent or whether we can find a scaling law for determining the optimum dimension of the momentum source cell. In the present study, it is found that when the dimension of the momentum source cell in the streamwise direction is maintained between 0.014 ~ 0.018m, little difference can be found among the predictions from different meshes. Tests have been done with Mesh1 (60x55x34), Mesh2 (66x61x38), Mesh3 (80x61x38) as shown in Figs. 4.36 and 4.37 and with the same local mesh refinement as shown in Fig. 4.38, the predicted jet profiles from these meshes are nearly the same. Another important point is that the mesh resolution in the proximity of the diffuser must be high enough to minimize numerical diffusion, especially in the impinging region, where very steep velocity gradients exist. Fig. 4.39 clearly shows the importance of proper grid resolution in this region; when the grid is not fine enough, the recirculation flow at the upper left corner of the room cannot be reproduced.

It can be seen from Figs. 4.36~4.37 and Fig. 4.48 that the velocities at the lower part of the jet flow ($Y\leq 2.3$m) are under-predicted especially at the side section of Z=0.5m, which is the region of jet entrainment. Thus, the main disadvantage of the momentum model is that it can not account well for jet entrainment, especially in the vicinity of the diffuser. On the other hand, the tiny-box model used by Chen et al. (2001) also under-predicts the jet velocities in this region, and they didn't give the comparison of their prediction at the two side sections (Z=0.25m and Z=0.5m) with the experiment measurements of Ewert et al. (1991), thus the performance of the box model in this region is unknown. Further investigation revealed that the discrepancy is mainly caused by the incorrect prediction of the spanwise and crosswise velocity components, i.e., the 3D development of the jet. Fig. 4.49 is a comparison of the predicted velocity magnitude profiles versus X velocity profiles with experiment measurements at X=1m before the diffuser, it can be seen that the agreement of the predicted X (streamwise) velocity profiles with those of experimental measurements is excellent.

The flow asymmetry is repeatedly observed both in steady-state simulation and in time-dependent simulation in the full room configuration. It may be caused by some intrinsic instability mechanism in the flow. When a simulation is carried out in the half room configuration, the imposed symmetry boundary condition at the symmetry plane limits the development of the flow asymmetry but a change of flow pattern can still be observed (Fig. 4.42). The results shown in Fig. 4.41 indicate that even though the flow pattern changes from time to time, the predicted jet velocity profiles still correlate reasonably well with measurements.

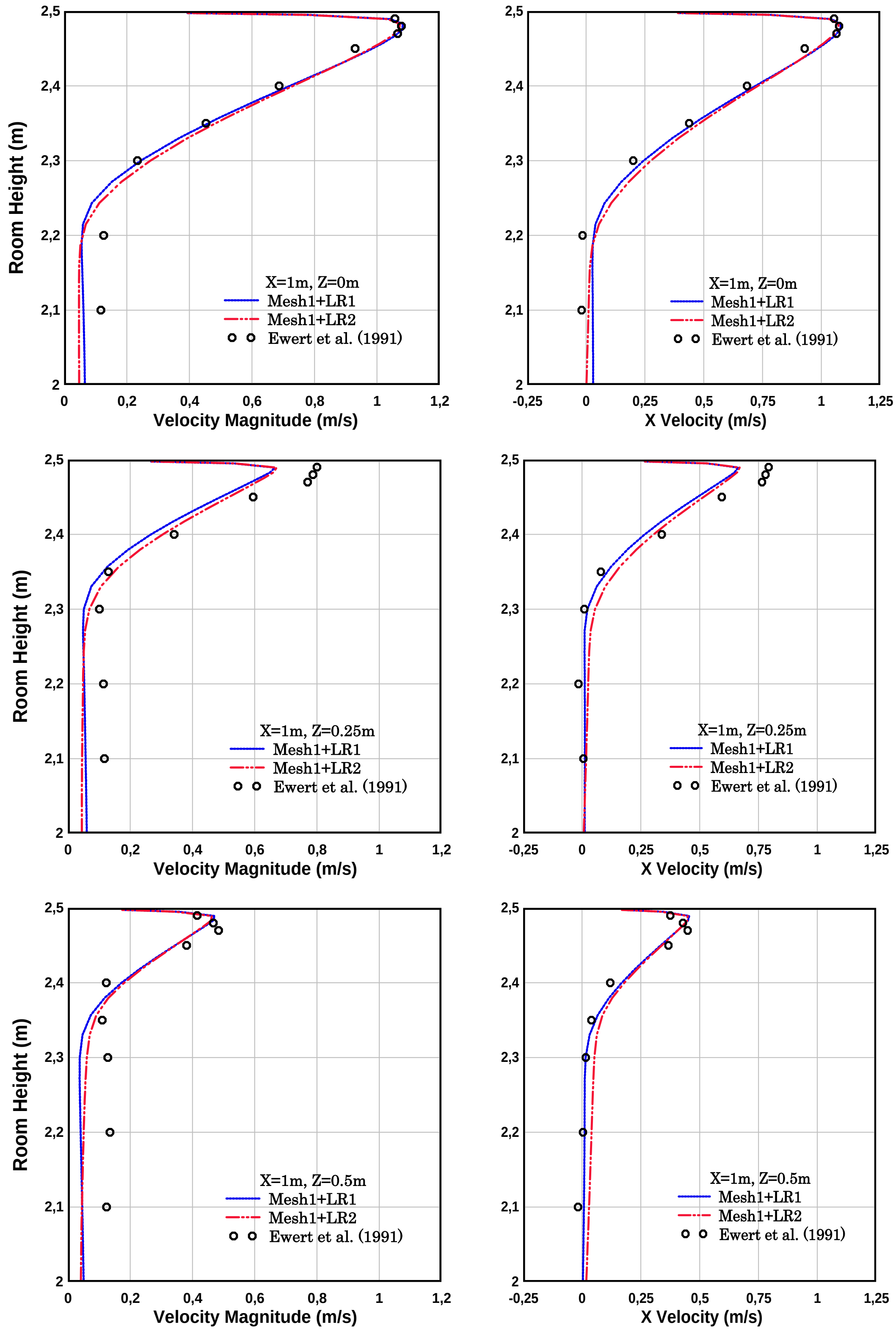

Fig. 4.50 Comparison of the predicted velocity magnitude and X velocity profiles with measurements for the HESCO nozzle diffuser (mesh size: 60x55x34 with local mesh refinement)

4.3.3 Simulation of the IEA Annex 20 Test Cases B2 and B3

4.3.3.1 Turbulence modeling

As has been shown in §4.3.2, the RNG k-ε model shows the best overall performance for the prediction of the wall jet flow issued from the diffuser (cf. Fig. 4.48), it is thus adopted for the prediction of the IEA Annex 20 Test Cases B2 and B3. From Fig. 4.48, it can be seen that the Realizable k-ε model and the SST k-ω model predict enough well the maximum jet velocities in the jet center plane, these two models are also tested for the prediction of the two Test Cases. Again the enhanced wall treatment is used to account for the viscosity-affected near wall regions which has been shown good performance for the prediction of the wall jet flow.

4.3.3.2 Boundary conditions and numerical methods

Boundary conditions
The boundary conditions for the inlet diffuser and the exhaust opening are the same as in §4.3.2.3. The HESCO nozzle diffuser is modeled using the momentum model with local mesh refinement as shown in Fig. 4.38. The momentum flow provided by the diffuser is calculated from the mass flow rate and the effective flow area of the diffuser. According to the measurement of Skovgaard et al. (1991b), the effective flow area of the nozzle diffuser is 0.00855m^2 for a ventilation rate of 3 ACH and 0.009m^2 for 6 ACH (the total gross flow area of the small nozzles is 0.00918m^2). At the supply opening, the total mass flow rate and the flow direction are specified. It was established from §4.3.2.3 that the volume of the momentum source cells is an important parameter for the correct prediction of the wall jet profiles. For a ventilation rate of 3ACH the dimension of the momentum source cells in the streamwise direction should be between 0.014m to 0.018m. Thus in this study, the dimension of the momentum source cells in the streamwise dimension is chosen as 0.015m for both the ventilation rates of 3ACH and 6ACH.

Discretization schemes
The second-order upwind scheme is used for the discretization of the convection terms and the second-order central-differencing scheme for the diffusion terms. For the discretization of the pressure, the PRESTO! (PREssure STaggering Option) scheme is used. The SIMPLEC scheme is used for the pressure-velocity coupling.

4.3.3.3 Computation meshes

As has shown in §4.3.2, flow asymmetry was observed in the predicted flow pattern for a ventilation rate of 3 ACH. In the full-scale experiment of Heikkinen (1991b), flow asymmetry was also observed for both the Test Cases B2 and B3. For this reason, simulations are carried out in both the half room and full room configurations. For the half room configuration, a symmetry boundary condition is applied at the symmetry plane (Z=0m) of the test room.

It was determined from §4.3.2 that for a ventilation rate of 3 ACH, a mesh grid of 55x57x38 for the half room configuration and 55x57x76 for the full room configuration (the other half mesh of the full room is mirrored from the half room mesh) represent a good compromise between the mesh resolution requirements and the available computational resources, these meshes are adopted for the prediction of both the Test Cases B2 and B3. The computation mesh is very similar to that shown in Fig. 4.35, i.e., the mesh grids are more condense near the walls and in the jet flow region, where more steep velocity gradients are expected.

A local mesh refinement was applied in the region near the diffuser which is crucial for the correct prediction of the wall jet profiles and the small recirculation flow between the diffuser and the room ceiling observed by smoke visualization as has been shown in §4.3.2. For the half room configuration, the local mesh refinement is applied in the region from X=0m to 0.3m, Y=2.13m to 2.5m and Z=0m to 0.355m, which results in a total of 140690 cells; for the full room configuration the mesh in the region of X=0m to 0.3m, Y=2.13m to 2.5m, Z=−0.355m to 0.355m is locally refined which results in a total of 281380 cells. The local mesh refinement method is the same as described in Fig. 4.38.

4.3.3.4 Velocity correction

Because the measurement of Heikkinen was carried out using an omni-directional thermistor anemometer (1991b), the reported mean velocity is in fact the mean air speed, i.e., the arithmetic average of the measured air speeds in the measuring period; while in CFD simulations the reported mean velocity is the magnitude of the mean velocity vector which is in general smaller than the mean air speed. The difference may become considerable when the local turbulence intensity is high and the air speed is slow (Koskela et al. 2001, 2002). For this reason, Koskela et al. (2001, 2002) developed a correction formula to correlate the magnitude of the mean velocity vector with the mean air speed based on a model for isotropic turbulence and on extensive measurements. Their correction formula is adopted in the present study to better compare the simulation results with experimental data. The correction formula has the following form (Koskela et al. 2002):

$$\frac{V_o}{V_v} = 1 + I_v^{\,2} \qquad (I_v \le 0.45) \qquad (4.7)$$

$$\frac{V_o}{V_v} = \frac{1.596 \times I_v^{\,2} + 0.266 \times I_v + 0.308}{0.173 + I_v} \qquad (I_v > 0.45) \qquad (4.8)$$

where V_o is the omni-directional mean air speed and V_v is the magnitude of the mean velocity vector. I_v is the turbulence intensity which by definition can be obtained from the turbulent kinetic energy k and V_v:

$$I_v = \frac{\sqrt{\frac{2}{3}k}}{V_v} \qquad (4.9)$$

4.3.3.5 Comparison of the predicted velocity profiles with measurements

The predicted velocity (mean air speed, modified according to equations 4.7 and 4.8) profiles at the symmetry plane of the test room from half and full room configurations are compared with experimental measurements of Heikkinen (1991b) for the IEA Annex 20 Test Cases B2 and B3 in Figs. 4.51 and 4.52, respectively. Because of the large number of figures, a complete comparison at the six side planes of the symmetry plane, i.e. Z=±0.6m, Z=±1.2m and Z=±1.7m planes (Fig. 4.30) is given as appendix: Appendix 1-1 (Test Case B2) and Appendix 1-2 (Test Case B3).

It can be seen from Figs. 4.51, 4.52 and Appendix 1-1~1-2 that good predictions can be obtained from both the half room and full room configurations for the Test Cases B2 and B3. Both the magnitude and the location of the maximum air speed in the occupied zone are reasonably predicted. It was noticed also that at the lower part of the test room (Y≤ 0.5m) the prediction for the Test Case B3 is a little less good than that for the Test Case B2, this may be the consequence of strong asymmetry in the flow at 6 ACH especially at the lower part of the test room, which can be easily seen by comparing the measured air speed profiles as shown in Appendix 1-2. On the other hand, the predicted velocity profiles correspond very well at the upper part (Y≥ 1m) of the test room where the flow asymmetry is less strong.

Influence of symmetry boundary condition

One noticeable difference between the full room and half room results is that at the lower part of the symmetry plane (Y≤ 0.5m, Figs. 4.51 and 4.52), the predicted velocity profiles from the half room configuration have some unphysical peaks near the inlet wall compared with experimental data; this phenomenon is repeatedly observed for both the Test Cases B2 and B3. Because this happens only at the symmetry plane, it may be a consequence of the symmetry boundary condition used in the half room configuration. It can be seen by comparing the measured velocity profiles in Appendix 1-1 and 1-2 that the flow asymmetry is most significant in this region, which is true for both the Test Cases B2 and B3. The imposed symmetry boundary condition in the half room configuration limits the development of the flow asymmetry, which causes the unphysical peaks in the predicted velocity profiles in this region.

It seems that using a symmetry boundary condition is not always justifiable even though the geometrical configuration is perfectly symmetric, because the physical flow may be strongly asymmetric in certain cases such as in the Test Case B3. It is not known what the cause of the flow asymmetry is — it was repeatedly observed in both the experimental measurements and numerical simulations (Heikkinen 1991b, Luo et al. 2003). In the experiment of Heikkinen (1991b), efforts have been taken by re-adjusting the nozzle direction and the flow equalizing devices to prevent the flow asymmetry, but without success. In the numerical simulations, the computational mesh of the full room configuration was constructed by mirroring the mesh of the half room configuration, and a double precision solver in FLUENT was used to minimize the truncation errors, but the flow asymmetry was still repeatedly observed. As was mentioned in §4.3.2, it seems that at a ventilation rate of 3~6 ACH, there is an intrinsic instability in the flow, perhaps it is beyond a critical value of the Reynolds number which represents the ratio of convective and diffusive rates of momentum transfer (the inertial force and the viscous force are of the same order).

On the other hand, it can been seen from Appendix 1-1 and 1-2 that the prediction from the half room configuration reproduces enough well the measured velocity profiles at the side planes (i.e. Z=0.6m, 1.2m and 1.7m), thus there is always a trade-off or compromise between the accuracy of prediction and the available computation resources and the turn-around time for the case under study. In total, the prediction from the full room configuration corresponds better with experimental measurements. At some places, even the observed flow asymmetry (for example at Y=0.5m and Z=±1.2m for the Test Case B2, Appendix Fig. A 1-1-4) is well reproduced.

Effect of velocity correction

The effect of velocity correction proposed by Koskela et al. (2001, 2002) can be significant when the velocity magnitude is small and the turbulence intensity is high, this can be illustrated by a comparison of the predicted velocity magnitude contours and the air speed contours at the symmetry plane with the measurements of Heikkinen (1991b) as shown in Fig. 4.53. It can be seen from Fig. 4.53a, Fig. 4.53b that the correction significantly improve the prediction of the jet flow at the upper right corner of the symmetry plane where the turbulence intensity is high, the maximum difference of the predicted velocity magnitude and the mean air speed is 0.04m/s, i.e., about 16.7% of the predicted velocity magnitude. The significance of the correction can be further appreciated from 2 examples taken at the room center (Y=0.5m, 1m and Z=0m) of the Test Case B2 where the air flow is very slow, the correction significantly improves the prediction compared with experimental measurements as shown in Fig. 4.54. It can be seen from Fig. 4.54 that in the region of X=2.4m to X=3m, the predicted velocity magnitude is only about one half of the predicted mean air speed, and the latter correlates much better with the measurements.

4.3.3.6 Remarks

In the summary report of the IEA Annex 20 subtask-1 “Room Air and Contaminant Flow” by Lemaire (1993), it has been concluded that for the evaluation of numerical models and modeling methods for the room air flow prediction, a point-to-point comparison of the prediction with experimental data can not yield meaningful results because the room air movement is characterized by large amplitude and low frequency velocity fluctuations. Therefore, in the IEA Annex 20 project, the evaluation of the numerical models and modeling methods was done by comparing only the general flow pattern and the key flow parameters such as maximum air speed in the occupied zone etc. with experimental measurements. The present study showed that if the boundary conditions for the air supply devices are appropriately represented, a point-to-point comparison of the simulation results with experimental data do yield meaningful results: although there are still some discrepancies between numerical predictions and experimental measurements, the trends of the measured velocity profiles are well predicted in most part of the test room, except near the bottom corners (Y<1m, near the two lateral walls). This highlights the importance of the correct modeling of air supply devices for the accurate prediction of room air flows.

The volume of the momentum source cells for the momentum model is an important parameter for the correct prediction of the wall jet flow issued from the nozzle diffuser. It has been determined that for a ventilation rate of 3 ACH, the dimension of the momentum source cells in the streamwise direction should be in the range of 0.014m to 0.018m (Luo et al. 2003). The present study showed that this value range yields also reasonable predictions for the Test Case B3 (6 ACH). A comparison with the measurements of Blomqvist (1991a) in the same test room at 4.5 ACH showed that this value range is valid for a ventilation rate of 4.5 ACH too (Fig. 4.55). Thus the previously determined optimum dimension of the momentum source cells in the streamwise direction for 3 ACH (0.014~0.018m) is valid for a ventilation rate up to 6 ACH.

When conducting comparison between numerical simulations and experimental measurements, it should bear in mind that the measured air speed obtained with omni-directional velocity anemometer and the mean air velocity magnitude reported by CFD packages are not the identical physical quantities, appropriate corrections should be applied if available before doing the comparisons. The present study demonstrated that the correction formula developed by Koskela et al. (2001, 2002) is suitable for isothermal room air flows.

4.4 Conclusion

In this chapter, validation studies on the numerical simulation of 2D and 3D indoor isothermal ventilation flows are reported. The three test cases represent a baseline case, a case with simple boundary conditions but with complicated flow features and a case with complicated boundary conditions (air supply device), respectively. From this study, the following general conclusions can be drawn:

1. As has been identified in the IEA Annex 20 project, the turbulence modeling and appropriate near-wall treatment remains as one of the most important problems for the correct prediction of indoor airflows. It can be seen that the turbulence models perform differently for different test cases. While the k-ω models perform badly for the 2D ventilation case compared with the k-ε models, they perform much better for the 3D ventilation case with a partition wall, where the flow features strong recirculation and separation; the same is for the RSM model. The enhance wall treatment works badly for the 3D ventilation with a partitioned wall case, but it works enough well with the IEA Annex 20 Test Cases B2 and B3. The standard k-ε model works very well for the 2D ventilation case, but for the 3D cases, its performance is less satisfactory. This highlights the importance of validation process. The unique advantage of using CFD to study indoor air flow pattern and air distribution is that: once the models and modeling methods are validated for a certain class of flows, it can be used to carry out parameter study for a wide range of configurations and air flow parameters.

2. The correct modeling of the air supply device is very important for the correct prediction of ventilation flows, thus special attention should be paid to correctly represent the air supply device in the numerical models when simulating ventilation flows.

3. When comparing predicted velocity profiles with experimental data obtained using omni-directional anemometer, appropriate corrections should be made before doing the comparisons (if available). The present study showed that the correction formula developed by Koskela et al. (2001, 2002) is suitable for isothermal ventilation flows.

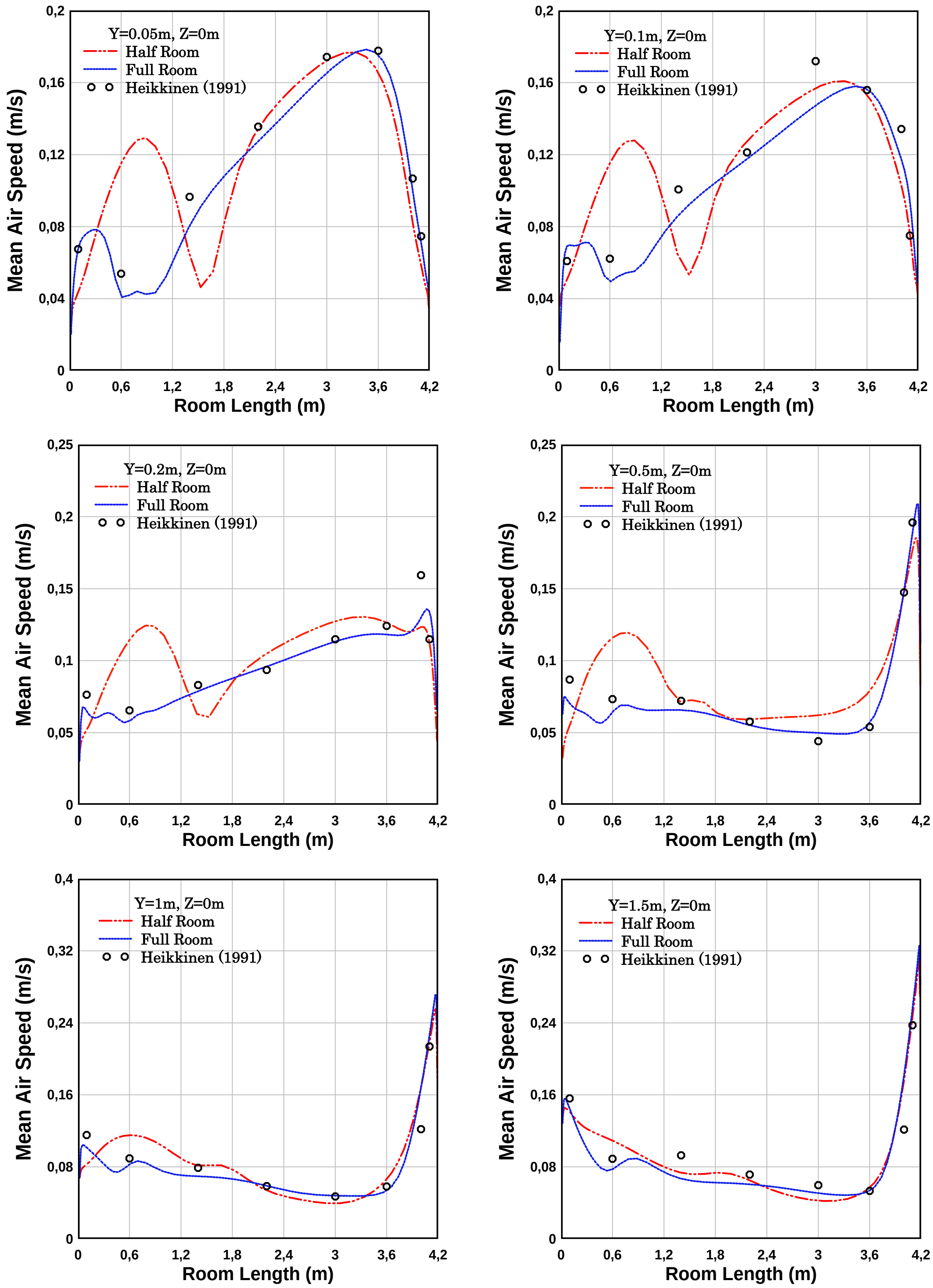

Fig. 4.51 Comparison of the predicted mean air speed profiles with experimental data at the symmetry plane of the test room with half and full room configurations (Test Case B2)

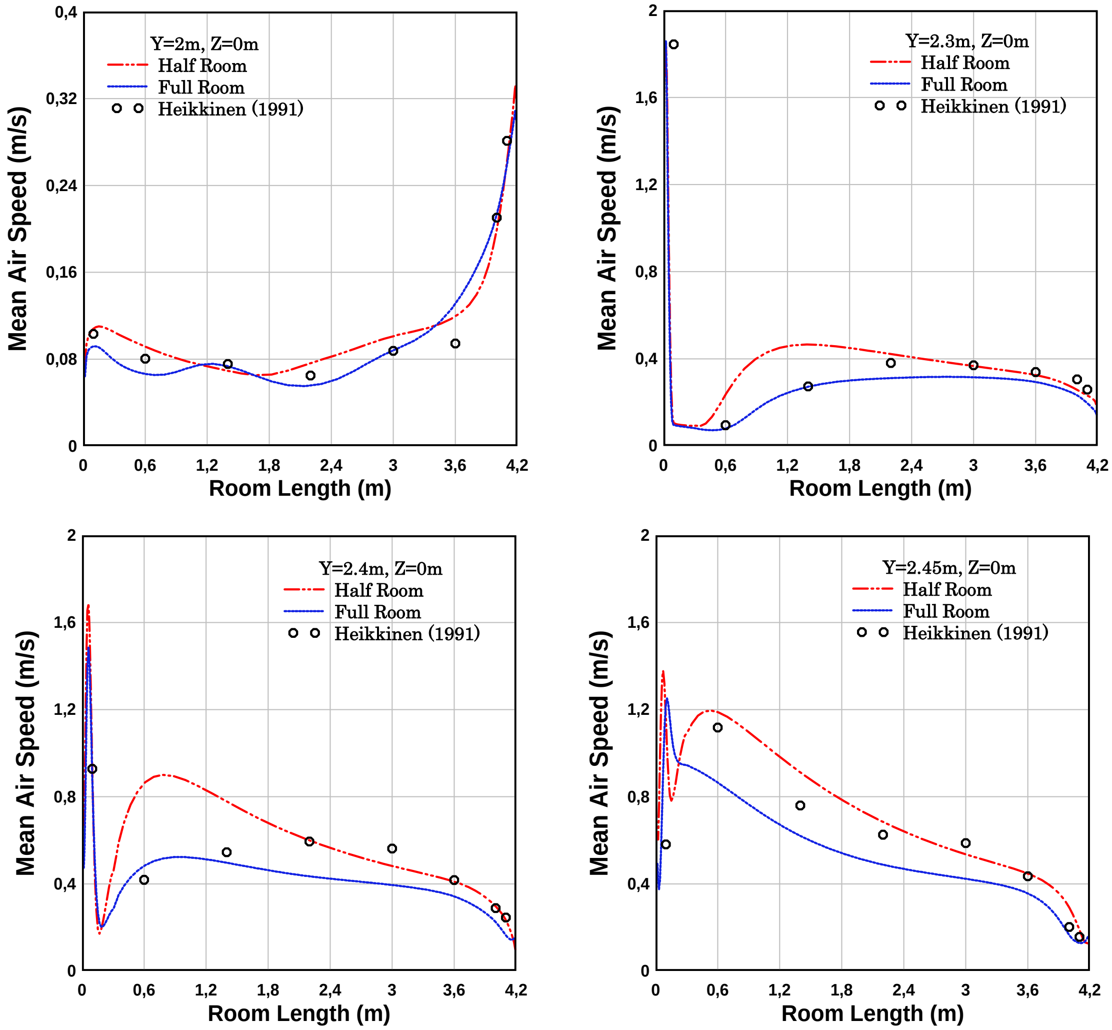

Fig. 4.51 Comparison of the predicted mean air speed profiles with experimental data at the symmetry plane of the test room with half and full room configurations (Test Case B2)
(Contd.)

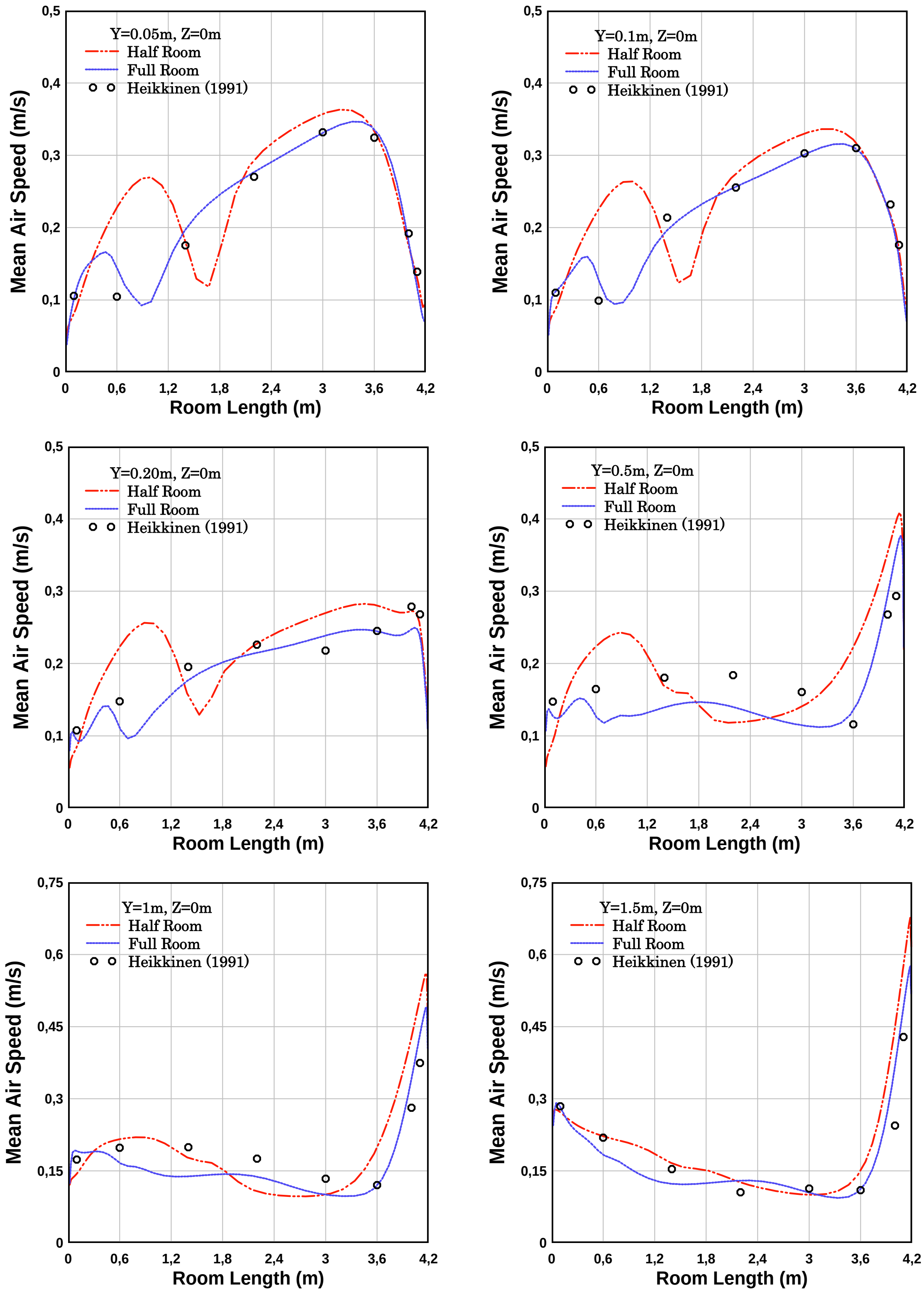

Fig. 4.52 Comparison of the predicted mean air speed profiles with experimental data at the symmetry plane of the test room with half and full room configurations (Test Case B3)

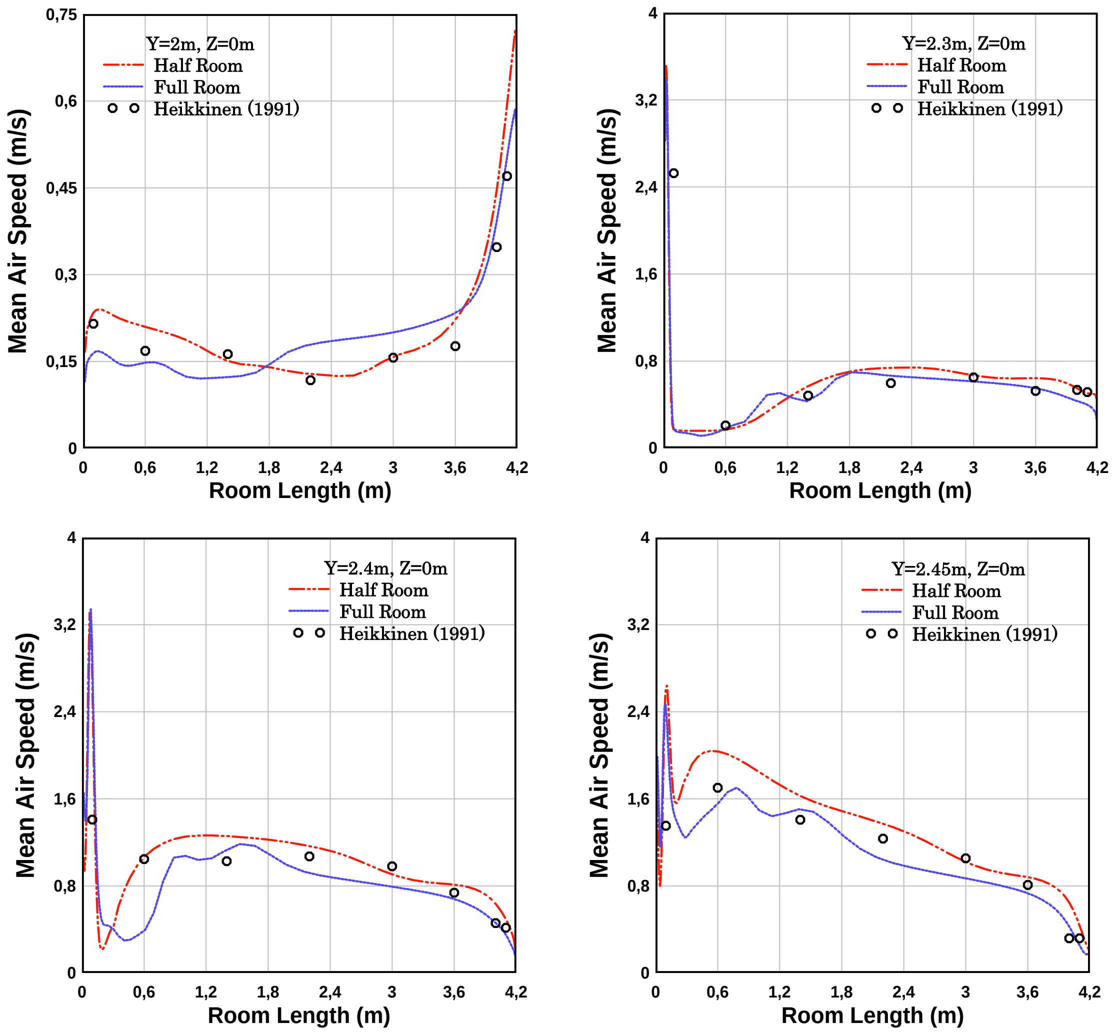

Fig. 4.52 Comparison of the predicted mean air speed profiles with experimental data at the symmetry plane of the test room with half and full room configurations (Test Case B3)
(Contd.)

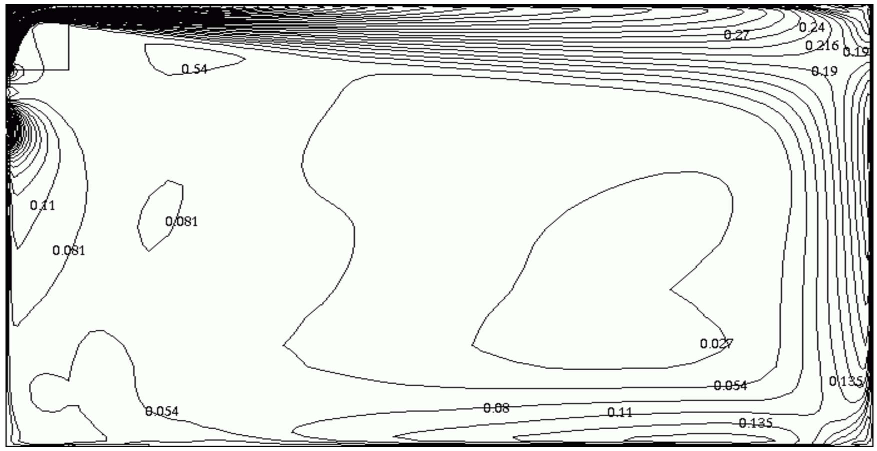

(a) Contours of the predicted velocity magnitude (symmetry plane)

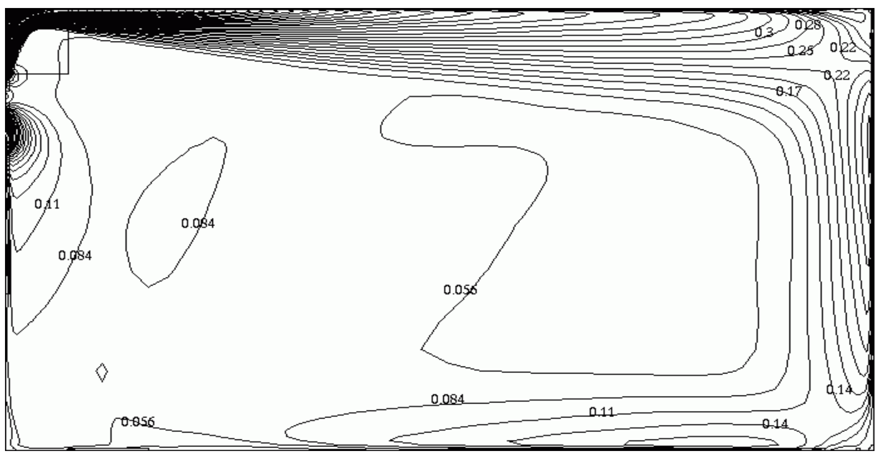

(b) Contours of the predicted mean air speed (symmetry plane)

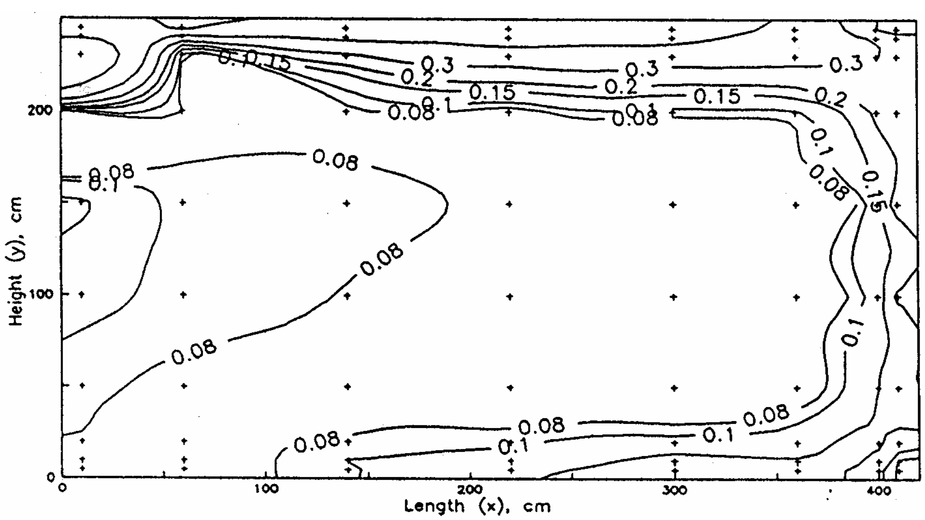

(c) Measured air speed contours (symmetry plane)

Fig. 4.53 Comparison of the predicted velocity magnitude and the mean air speed with measurements at the symmetry plane of the test room (Test Case B2)

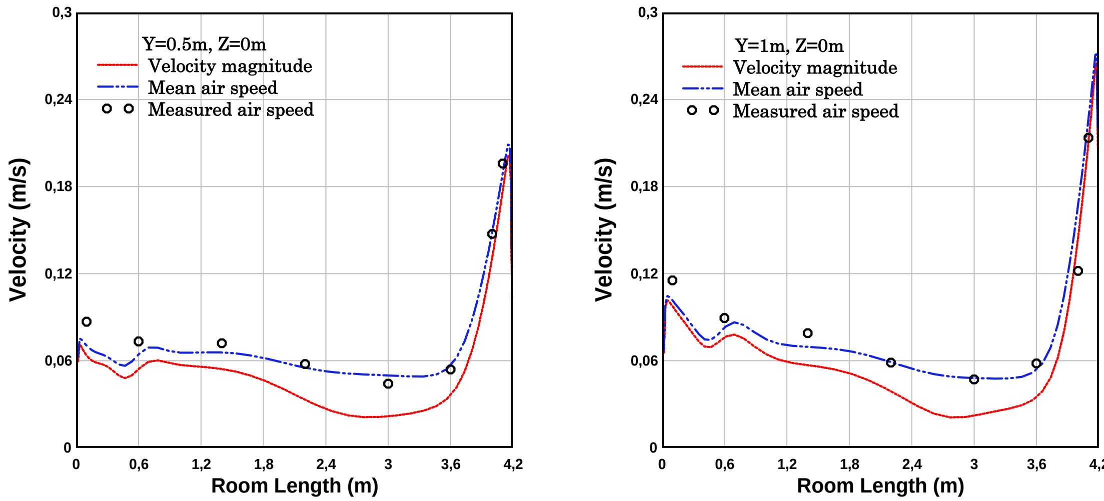

Fig. 4.54 Comparison of the predicted velocity magnitude and mean air speed at the room center (Y=0.5m, Y=1m and Z=0m) with measurements

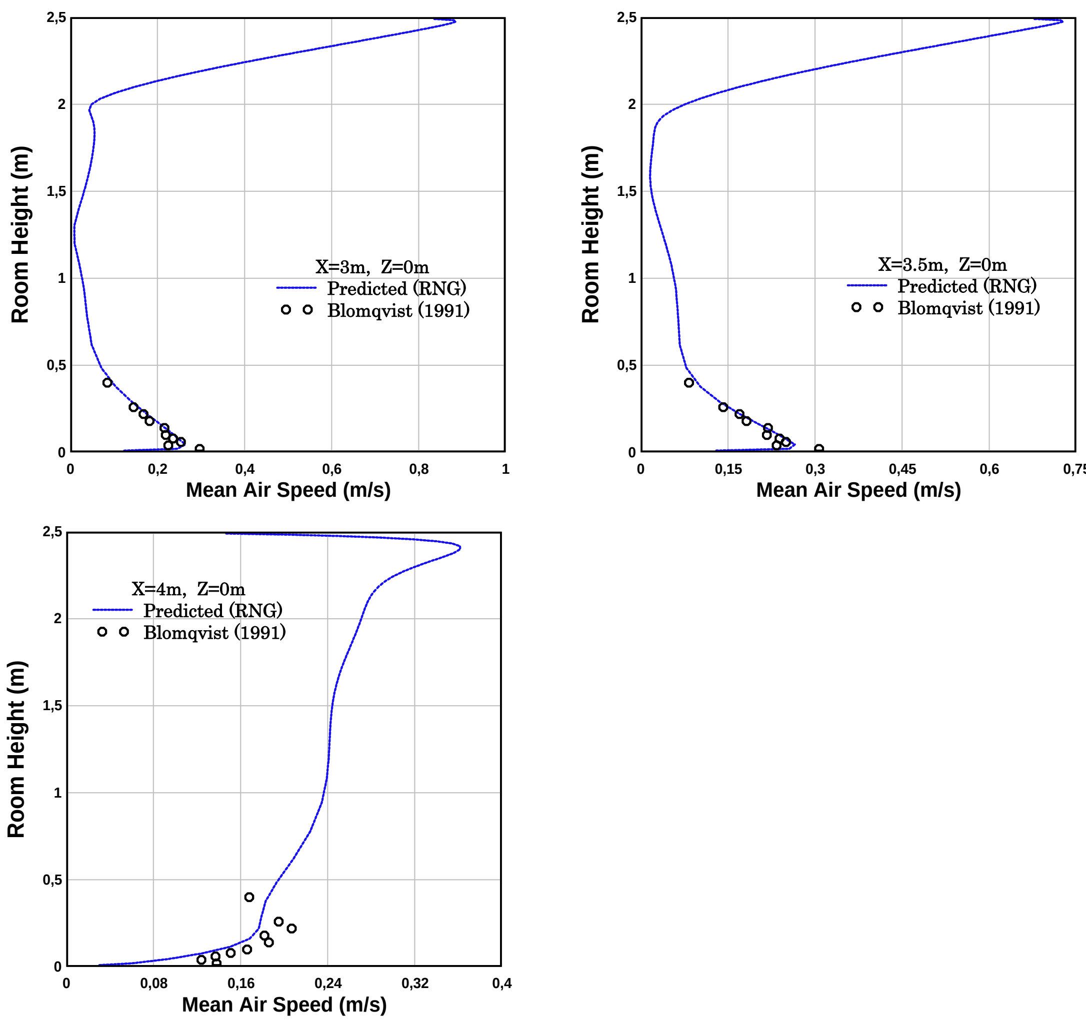

Fig. 4.55 Comparison of the predicted mean air speed profiles with measurements at 4.5 ACH

Chapter 5

3D Ventilation Flows with Coupled Heat or Mass Transfer

In this chapter, two 3D ventilation test cases with coupled heat or mass transfer are studied: the IEA Annex 20 Test Case E (Mixed convection, summer cooling) and the IEA Annex 20 Test Case F (Forced convection, isothermal with contaminants).

In Chapter 4, some typical isothermal ventilation problems including jet impingement, flow recirculation and separation have been studied. It can be seen that different turbulence models have different performance (advantages and drawbacks) for different ventilation problems, and a validation study is necessary to assure that the chosen turbulence model and near-wall treatment method can capture the basic flow features for the case considered. Indoor ventilation flows are often accompanied with significant heat and mass transfer such as ventilation in summer-cooling or in winter-heating condition. In an indoor environment, there are often many contaminant sources such as the CO_2 exhaled by the habitants, the smoke produced in the kitchen or by smokers, etc. While the contaminants often have very little impact on the global air flow pattern in rooms and are passively transported by the air flows, the heat transfer process may significantly influence the air flow pattern which will then influence the contaminant distribution and thermal comfort in the room. It is thus very important to investigate how well such heat and mass transfer processes can be predicted by numerical methods and what their influences are on the indoor air quality and thermal comfort. In the IEA Annex 20 project, for providing realistic benchmark data to validate numerical models and simulation results for such cases, two full-scale experiment measurements for summer-cooling (IEA Annex 20 Test Case E) and for contaminant transfer (IEA Annex 20 Test Case F) were carried out. In the present study, these two test cases are used to validate the numerical models and simulation results for heat and mass transfer in 3D ventilated spaces with practical relevance.

5.1 Validation study: IEA Annex 20 Test Case E (Mixed convection, summer cooling)

The IEA Annex 20 Test Case E was designed to provide full-scale experimental data for validating modeling methods and simulation results of ventilation with heat transfer. In the experiment, cooled air was introduced to the test room and a heated window was used to simulate the heating by solar radiation in summer. Experiments were carried out independently by several groups on different sites, the measurement results of Heikkinen (1991b) and Blomqvist (1991b) for Test Cases E2 (3ACH) and E3 (6ACH) are used in the present study to validate the numerical models for the prediction of heat transfer process in a 3D ventilated space.

5.1.1 Experiment setup

Experiment measurements were carried out in an IEA standard test room described in Fig. 4.28. The inlet diffuser and the exhaust opening and their locations are the same as in the Test Case B as shown in Figs. 4.29, 4.34b. A window of 2m x 1.6m size on the front wall as shown in Fig. 4.28 was heated to 30°C (Test Case E2) and 35°C (Test Case E3) to simulate the heating by solar radiation in summer. The inlet air was cooled to 15 °C to simulate summer-cooling condition, the room walls were assumed to be adiabatic during the experiments. Surface temperatures of 22°C for the front wall (the wall with the window) and 21°C for the remaining walls were proposed for use in the numerical simulations (Lemaire 1993). The ventilation rate for Test Case E2 is 3ACH and for Test Case E3, 6ACH. The key parameters for these two test cases are shown in Table 5.1.

Table 5.1 Key parameters for the IEA Annex 20 Test Cases E2 and E3 (Heikkinen 1991b)

Case	Ventilation Rate (ACH)	Airflow Rate (m^3/s)	Supply Air Temperature (°C)	Window Surface Temperature (°C)	Reynolds number*
E2	3	0.0315	15	30	2620
E3	6	0.0630	15	35	5240

* The Reynolds numbers in the table are based on the diameter of the small nozzles.

The measurements of Heikkinen (1991b) and Blomqvist (1991b) were carried out using an omni-directional thermistor anemometer. A sampling interval of 0.2 seconds and an integration time of 180 seconds were used by Heikkinen, and a sampling interval of 3 seconds and an integration time of 15 minutes were used by Blomqvist (1991b). For the Test Case E2, Heikkinen (1991b) and Blomqvist (1991b) measured the air speed and air temperature at 560 points inside the test room. For the Test Case E3, the measurement of Heikkinen was carried out at 560 points and that of Blomqvist was carried out at 240 points inside the room. The position and distribution of the measuring points of Heikkinen are the same as in the Test Cases B2 and B3 as shown in Fig. 4.30. The position and distribution of the measuring points of Blomqvist are slightly different from those of Heikkinen because of the difficulties to measure very low velocities with heated anemometers, but the measuring points from both of them were arranged on 7 vertical planes (Z=constant), i.e., the symmetry plane (Z=0m) and 3 side-planes at each side of the symmetry plane (Z=±0.6m, Z=±1.2m and Z=±1.7m; Fig. 4.30). For the Test Case E3, Blomqvist measured only the air speed and air temperature on the symmetry plane and on two side planes at Z=±0.6m.

5.1.2 Turbulence modeling

From §4.3, it has been shown that the RNG k-ε model and also the Realizable k-ε model and the SST k-ω model can give good prediction of the isothermal ventilation flows in the test room. These three models are tested in the present study for their capability of correct prediction of ventilation flows with heat transfer using the benchmark data of the IEA Annex 20 Test Case E. When working with the two k-ε models, the non-equilibrium wall function and the enhanced wall treatment were used to account for the viscosity-influenced near wall region. It was found that the non-equilibrium wall function yields better prediction for the convective heat transfer than the enhanced wall treatment does. For the buoyancy term, the Boussinesq approximation was used. Vieser et al. (2002) have computed nine test cases with heat transfer using k-ε model, k-ω model and SST k-ω model to compare their performances. They found that an appropriate near-wall treatment is of major importance for the accurate prediction of convective heat transfer at walls and many of the previously reported poor results are mainly a consequence of the applied near-wall treatments but not so much of the underlying turbulence models. Among the three models tested, they found that the SST k-ω model gives the best overall prediction for the nine test cases. In the present study, it was also found that the SST k-ω model gives the best overall prediction for the Test Cases E2 and E3.

5.1.3 Boundary conditions and numerical methods

Inlet diffuser

The inlet diffuser was modeled using the momentum model with local mesh refinement as introduced in §4.2.2. As for the Test Cases B2 and B3, the local mesh refinement was applied to the region of X=0~0.3m, Y=2.13~2.5m and Z=0~0.355m for half room configuration and X=0~0.3m, Y=2.13~2.5m and Z=−0.355~0.355m for full room configuration. The dimension of the momentum source cell in the streamwise direction (X direction) is about 0.015m for both the Test Cases E2 and E3. At the supply opening, the total mass flow rate and flow directions and also the inlet air temperature were specified. The boundary conditions for the inlet diffuser are summarized as follows:

Test Case E2:

- Inlet air temperature: 288 K (15°C);

- Mass flow rate: 0.0193 kg/s (half room) and 0.0386 kg/s (full room);
- Flow direction: 40° upward;
- Inlet air density: 1.22528 kg/m^3 at 15°C and 1 atm.;
- k, ε and ω: calculated using equations 4.4~4.6 respectively, with hydraulic diameter D=0.35m and turbulence intensity TI=10% (Nielsen 1992; Lemaire 1993) ;
- Effective flow area=0.00855m^2 (Skovgaard et al. 1991b).

Test Case E3:

- Inlet air temperature: 288 K (15°C);
- Mass flow rate: 0.0386 kg/s (half room) and 0.0772 kg/s (full room);
- Flow direction: 40° upward;
- Inlet air density: 1.22528 kg/m^3 at 15°C and 1 atm.;
- k, ε and ω: calculated using equations 4.4~4.6, respectively, with hydraulic diameter D=0.35m and turbulence intensity TI=10% (Nielsen 1992; Lemaire 1993);
- Effective flow area=0.009m^2 (Skovgaard et al. 1991b).

Exhaust opening

Pressure outlet, i.e., the gauge pressure at the outlet is set to zero for both the Test Cases E2 and E3.

Walls and the window

The surface temperature of the front wall (the wall with the window) is set to 295K (22°C) and that of the window is set to 303K (30°C) for the Test Case E2 and 308K (35°C) for the Test Case E3. The surface temperatures of the other walls are set to 294K (21°C) as suggested in Lemaire (1993).

Discretization schemes

The second-order upwind scheme is used for the discretization of the convection terms and the second-order central-differencing scheme for the diffusion terms. For the discretization of the pressure, the PRESTO! (PREssure STaggering Option, Fluent Inc. 2001) scheme is used. The SIMPLEC scheme is used for the pressure-velocity coupling.

5.1.4 Computation meshes

As with the Test Cases B2 and B3, flow asymmetry has been observed for both the Test Cases E2 and E3 by Heikkinen (1991b) and Blomqvist (1991b). For this reason, simulations were carried out in both the half room and full room configurations. After some initial tests, a mesh grid of 60x53x38 for the half room configuration and 60x53x76 for the full room configuration were chosen as the main computational meshes. They represent a good compromise between the mesh resolution requirements and the available computational resources. In §4.3.2 and §4.3.3, it has been also shown that a similar mesh can give reasonable prediction of the isothermal ventilation flows in the test room for both the Test Cases B2 and B3.

5.1.5 Comparison of numerical predictions with experimental data for the Test Case E2

In Fig. 5.1, a comparison of the predictions at the symmetry plane using the SST k-ω model under half and full room configurations with the experiment measurements of Heikkinen (1991b) and Blomqvist (1991b) is given for the Test Case E2. Because of the large number of the figures, a complete comparison of the predictions with experiment measurements is given in Appendix 2-1.

It can be seen from Fig. 5.1 and Appendix 2-1 that at the symmetry plane, the prediction from full room configuration shows a stronger jet flow than that from half room configuration; but the predicted temperature profiles show little difference at the symmetry plane and also at the side planes. Only near the front wall (window) and the side walls, i.e., between X=3.6m~4.1m and at Z=±1.7m, the predicted temperature profiles show some difference: the predicted temperatures from the full room configuration show better agreement with measurements near the floor and the predicted temperatures from half room configuration show better agreement with measurements near the ceiling. In the middle of the room, the predictions from the two configurations are nearly the same. It can be also seen from Appendix 2-1 that before X=2.2m, the predicted temperature profiles are nearer to the measured profiles of Blomqvist for the +Z side, but at the –Z side the predicted temperature profiles approach more to the measurements of Heikkinen. Beginning from X=2.2m, the predicted temperature profiles and velocity profiles are nearer to the measured ones of Heikkinen. By comparing the two experiment data sets shown in Appendix 2-1, it can be seen that both of the two data sets show strong asymmetry for both of the temperature profiles and velocity profiles, this can be more clearly illustrated by an example of the measured temperature (isotherm) contours and air speed (isovel) contours from the two data sets as shown in Figs. 5.3 and 5.4. The data of Heikkinen show strongest asymmetry at X=3.6m for both the temperature profiles and the velocity profiles; for example, at X=3.6m and Z=±1.2m, the maximum difference of the temperatures at the two sides of the room is more than 1°C (Fig. A-2-1-6); at X=3.6m and Z=±0.6m, the maximum difference of air speeds at the two sides of the room is more than 0.15m/s (at Y=1.5m), i.e., more than 50% of the maximum air speed (about 0.25m/s) in that section. In the predictions, the predicted temperature profiles are nearly symmetric, except in the jet region near the inlet wall (X=0.1m and Y>1.75m, Fig. A-2-1-1), where some degree of asymmetry exists in the predicted temperature profiles, but the asymmetry is much less than that of the measurements. The predicted velocity profiles do show some degree of asymmetry, but the asymmetry is much less profound than the measured profiles. From Fig. 5.4b it can be seen that beginning from about Y=1.5m there is a recirculation flow at the upper right corner of the test room, and the center of the recirculation flow is at about X=3.6m, that means that near the window the buoyancy force is stronger than the convection force, and an upward flow forms near the heated window. From Fig. 5.4a it can be seen that the buoyancy force is much stronger at one side than at the other side of the room, which can be also seen by comparing the measured air speed profiles at X=3.6m, Z=±0.6m and Z=±1.2m as shown in Fig. A-2-1-14, where the predicted air speeds show biggest discrepancies with those of measurements. The maximum discrepancy is at X=3.6m, Z=0.6m and Y=1.5m, where the predicted air speed is only about 0.05m/s but the measured one is about 0.25m/s. As indicated above, the measured air speeds on the two sides of the symmetry plane show biggest difference at this same position too, i.e., at X=3.6m and Y=1.5m, the measured air speed is about 0.25m/s at Z=0.6m but only about 0.1m/s at Z=−0.6m. In the prediction, this upwind buoyancy flow is not reproduced, that explains why the predicted temperatures between X=3.6m~4.1m show biggest discrepancies with measured data especially at the –Z side (cf. Figs. A-2-1-6 ~ A-2-1-8), the biggest difference is at X=3.6m and Z=−1.2m, where the difference between the predicted and measured temperatures is about 2°C. At the other places in the room, the predicted temperatures and air speeds are in general close to the measured values.

5.1.6 Comparison of numerical predictions with experimental data for the Test Case E3

The predictions at the symmetry plane using the RNG k-ε model, the Realizable k-ε model and the SST k-ω model for the Test Case E3 are compared with measured data of Heikkinen (1991b) and Blomqvist (1991b) in Fig. 5.2; the predictions were obtained from half room configuration and the non-equilibrium wall function was used with the two k-ε models. Because of the large number of the figures, a complete comparison of the predictions with experiment measurements is given in Appendix 2-2.

It can be seen from Fig. 5.2 and Appendix 2-2 that the predictions from these three turbulence models agree reasonably well with measurements for both the temperature profiles and the velocity profiles. For the temperature profiles, the prediction from the SST k-ω model correlates generally better with measurements than those from the two k-ε models; but for the air speed profiles, the predictions from the two k-ε models corresponds slightly better with measurements than that from the SST k-ω model. It can be seen also from Appendix 2-2 that beginning from X=2.2m, the predictions from these three models correlate slightly better with the measurements of Blomqvist, because in his measurements, the flow is less asymmetric than in the measurements of Heikkinen for this test case, which can be more clearly illustrated from an example taken from the two measured data sets as shown in Figs. 5.5 and 5.6. Comparing Figs. 5.4a and 5.6a, it seems that the flow is more asymmetric at 6ACH than at 3ACH in the case of Heikkinen, but in the case of Blomqvist, it is just the contrary, and in the case of 3ACH, the asymmetry is very strong.

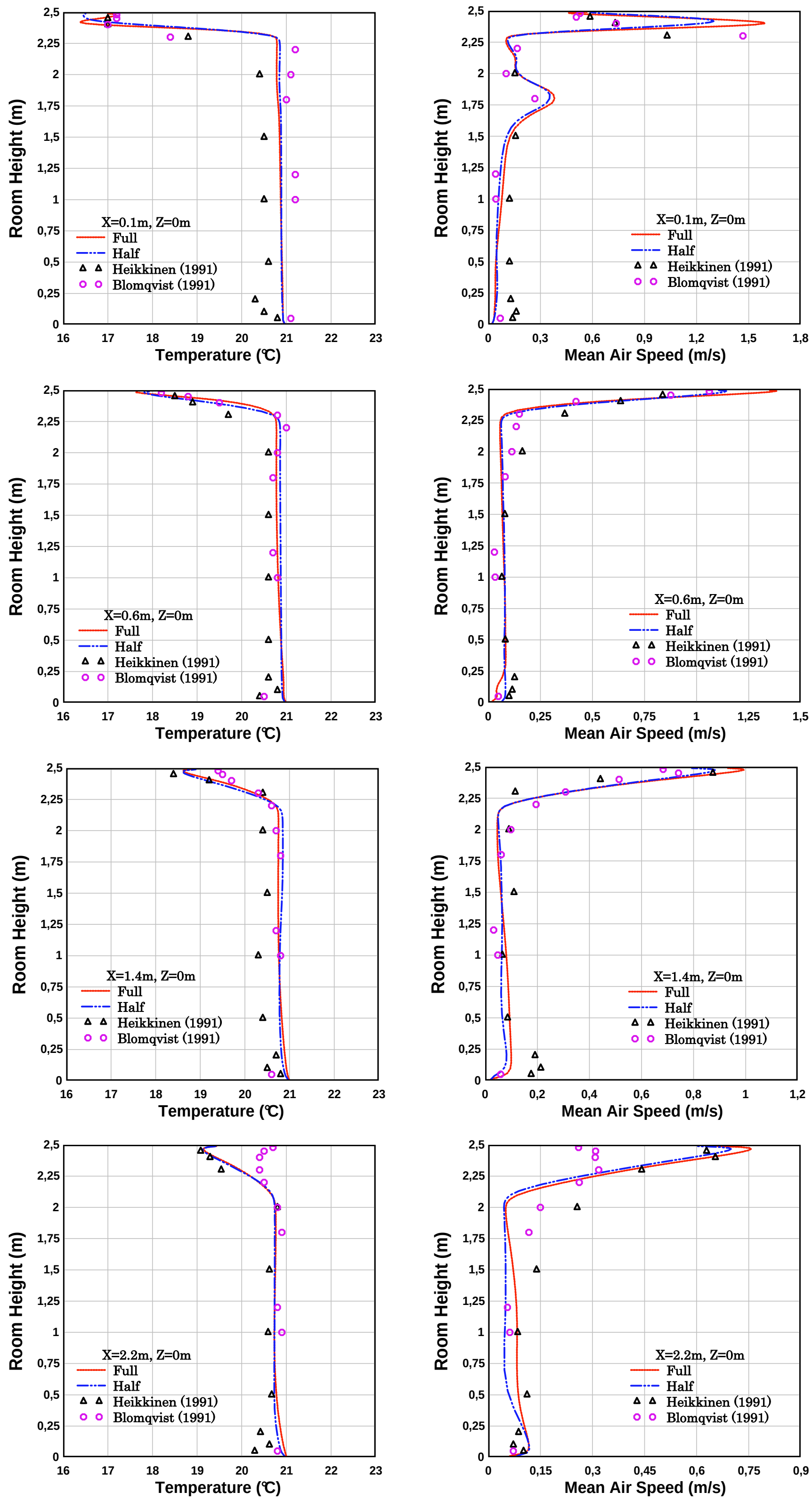

Fig. 5.1 Comparison of predicted temperature and mean air speed profiles (using SST k-ω model, under full and half room configurations) with measurements for the Test Case E2

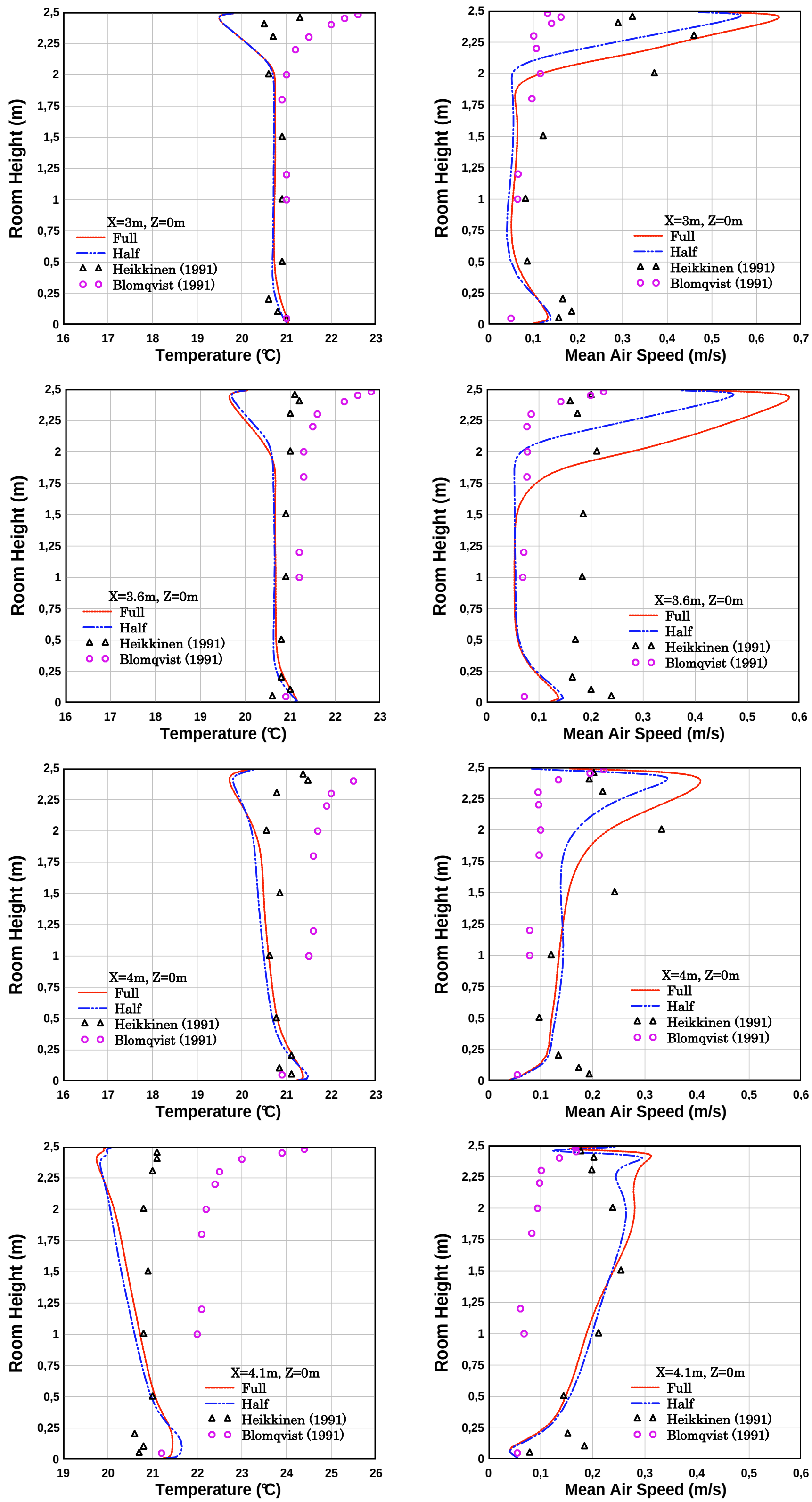

Fig. 5.1 Comparison of predicted temperature and mean air speed profiles (using SST k-ω model, under full and half room configurations) with measurements for the Test Case E2 (Contd.)

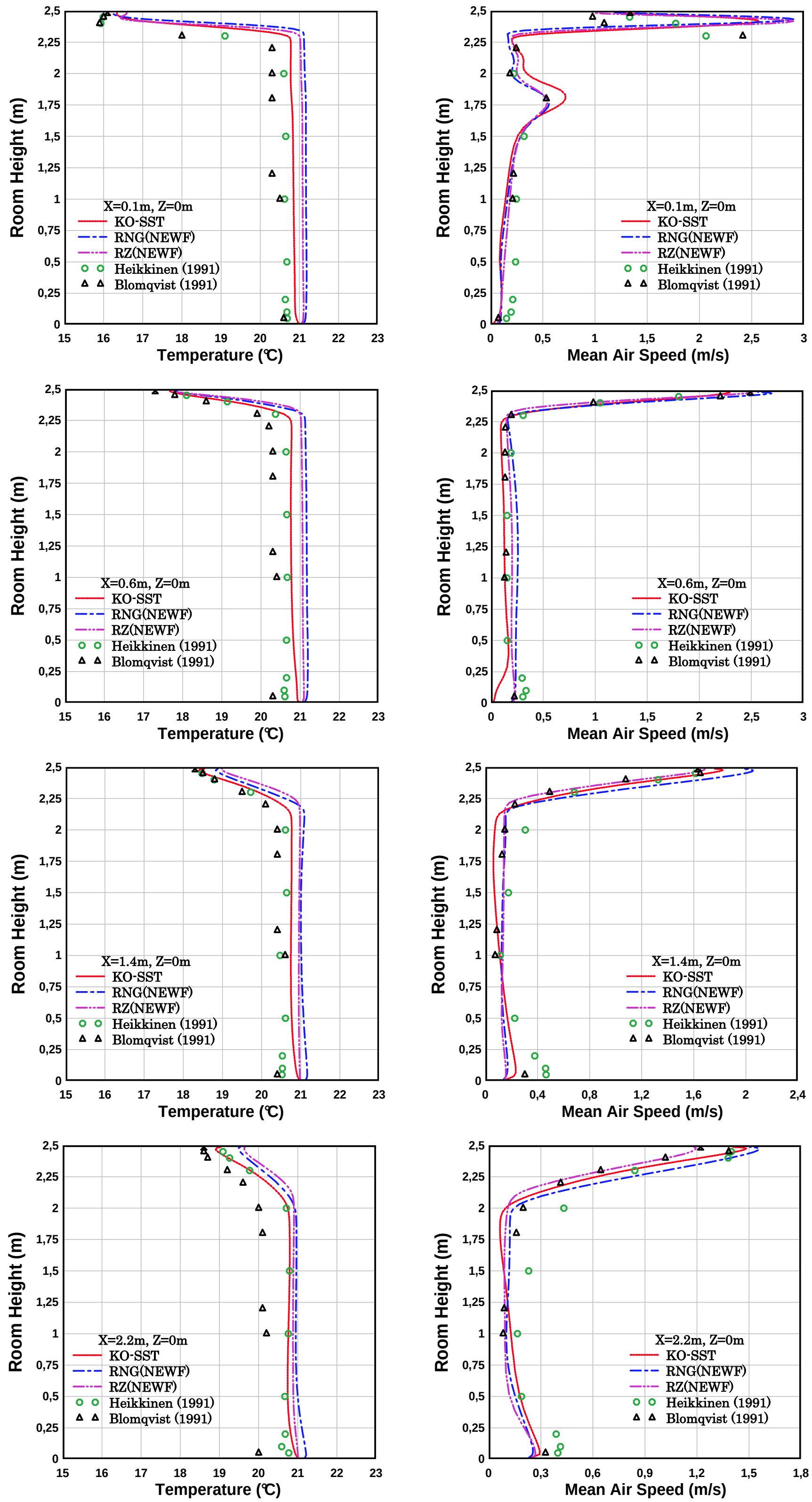

Fig. 5.2 Comparison of predicted temperature and mean air speed profiles (using RNG and Realizable k-ε models and SST k-ω model under half room configuration) with measurements for the Test Case E3

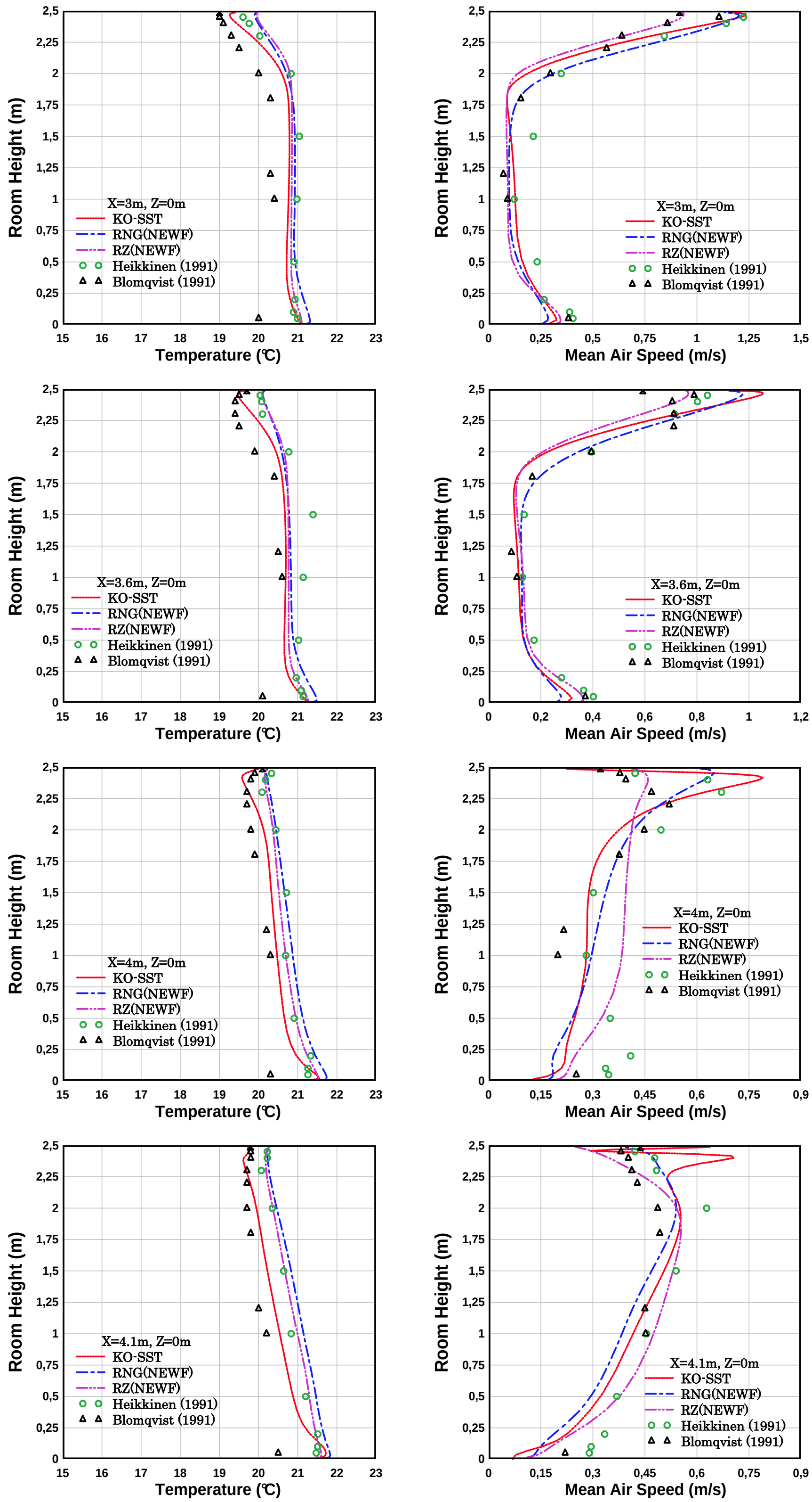

Fig. 5.2 Comparison of predicted temperature and mean air speed profiles (using RNG and Realizable k-ε models and SST k-ω model under half room configuration) with measurements for the Test Case E3 (Contd.)

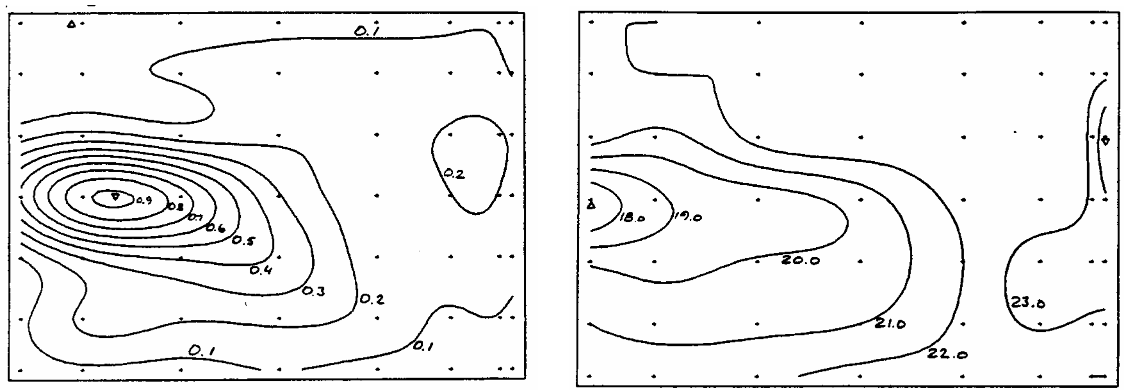

(a) Isovel at Y=2.45m

(b) Isotherm at Y=2.45m

Fig. 5.3 The measured temperature and air speed contours at Y=2.45m (Test Case E2) by Blomqvist (1991b)

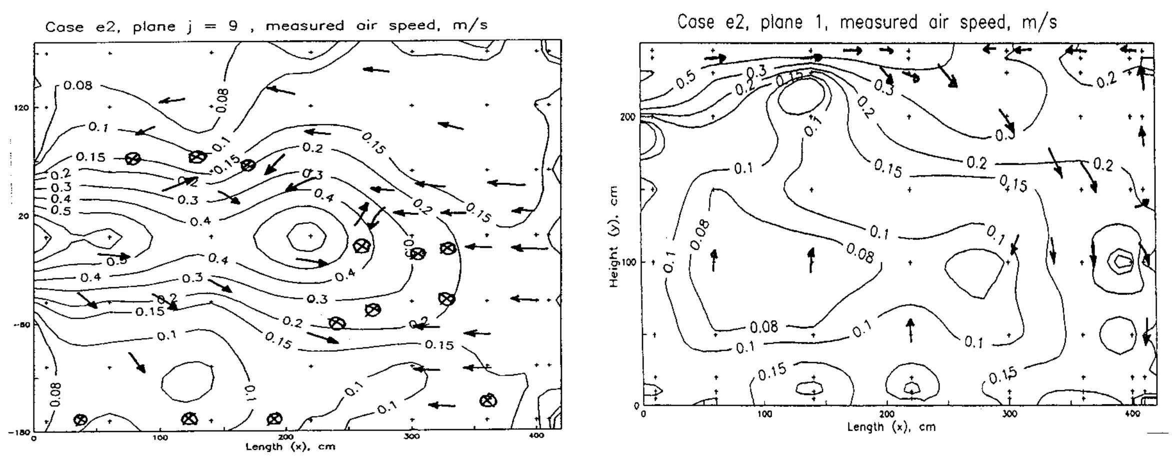

(a) Isovel at Y=2.4m

(b) Isovel at Z=0m

Fig. 5.4 The measured air speed contours at Y=2.4m and Z=0m (Test Case E2) by Heikkinen (1991b)

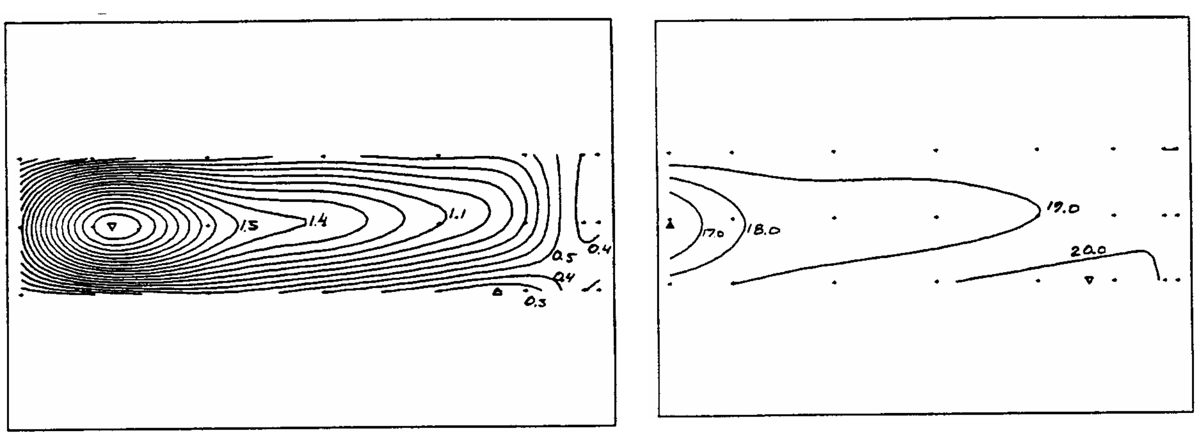

(a) Isovel at Y=2.45m

(b) Isotherm at Y=2.45m

Fig. 5.5 The measured temperature and air speed contours at Y=2.45m (Test Case E3) by Blomqvist (1991b)

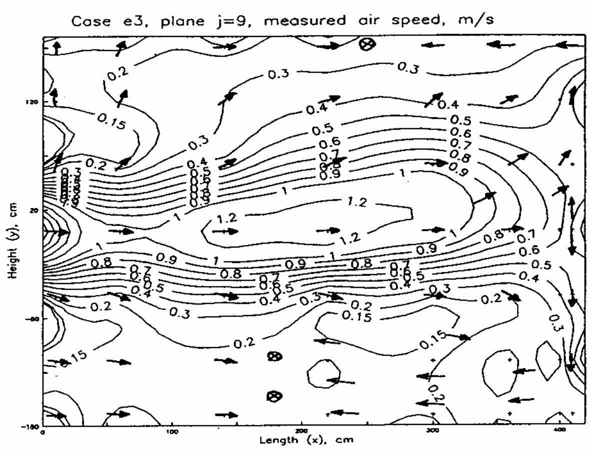

(a) Isovel at Y=2.4m

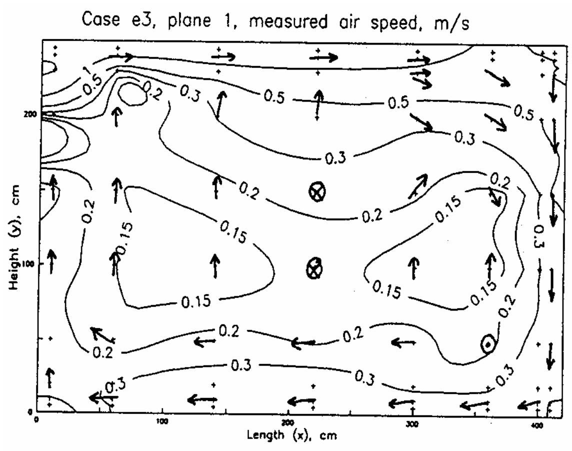

(b) Isovel at Z=0m

Fig. 5.6 The measured air speed contours at Y=2.4m and Z=0m (Test Case E3) by Heikkinen (1991b)

5.1.7 Remarks

As with the Test Case B3, when the flow is strongly asymmetric, it is more difficult for the numerical prediction to capture the asymmetric flow pattern because physically it is not clear what the cause of the flow asymmetry is and why and when it will take place.

From the comparisons in Figs. 5.1 and 5.2 and in Appendix 2-1 and 2-2, it can be concluded that the predictions for the Test Cases E2 and E3 are in general satisfactory. For the Test Case E2, the predicted results are close to either one set or another set of the measured data. Some big discrepancies exist for the predicted temperature and velocity profiles compared with the measurements, they are mainly found in the region near the window, where the buoyancy force is competing with the convection force. If we consider the strong asymmetric flow pattern observed in the experiments and the differences between the two experimental data sets, the predicted results can be accepted as reasonable. For example at X=4.1m and Z=0.6m in Fig. A-2-1-8, the difference of measured temperature between the two data sets near the ceiling is about 4°C, while the biggest difference of temperature between prediction and the measurement of Heikkinen is about 2°C, and in most part of the test room, the difference of temperature between prediction and measurement is less than 0.5°C; also at X= 4m and Z=1.7m in Fig. A-2-1-15, the measured air speed near the floor is about 0.02m/s from Blomqvist and 0.18m/s from Heikkinen, the difference being 9 times between the two data sets. For the Test Case E3, the prediction falls in between the two data sets in most part of the room.

The Test Case E2 is more difficult for the numerical methods to correctly predict because in this case the buoyancy force and the convection force are of the same order near the window; it is well known that in such cases the turbulence models don't work well. This has manifested in the present study too. For the two Test Cases, the maximum discrepancies between the predictions and the measurements are found in the regions near the window, and for the Test Case E2 the discrepancies are bigger than for the Test Case E3.

5.2 Validation study: IEA Annex 20 Test Case F (Forced convection, isothermal with contaminants)

Contaminant transport by ventilation is a very important process to be investigated because it is the transport mechanism that determines how the contaminants are distributed in a ventilated space, which influences directly the indoor air quality (IAQ). The distribution of contaminants is determined by the air flow pattern and by the characteristics of the contaminant sources. Experimental studies on this subject are very scarce in the literature. The IEA Annex Test Case F (forced convection with contaminants) is one of the very few test cases which deal with contaminant transport in a real 3D configuration with practical relevance. It is also one of the most difficult test cases to simulate in the IEA Annex 20 practice because in this case, the ventilation rate is only 1.5 ACH which is approximately the minimum value required to ventilate an office room (Heiselberg 1991), significant low-Reynolds number effects exist in both the flow regions in and near the diffuser and in the test room as suggested in the IEA subtask-1 summary report (Lemaire 1993) and in Shovgaard et al. (1990), which is a non-trivial test for both the turbulence models and near-wall models. It is thus chosen as the test case to validate the species transport models in FLUENT.

5.2.1 Problem description: The IEA Annex 20 Test Case F

The experiment for the IEA Annex 20 Test Case F (forced convection with contaminants) was conducted in an IEA Annex 20 standard test room under isothermal and steady-state conditions at the Department of Building Technology and Structural Engineering of the University of Aalborg (Denmark) and the measurement results were reported by Heiselberg (1991).

The test room is similar to that shown in Fig. 4.28 except the room height is 2.4m. The air supply device is the same as that used in the Test Case B and E as shown in Fig. 4.29. The locations of the inlet diffuser and the exhaust opening are the same as shown in Fig. 4.34, i.e., the inlet diffuser is located on the horizontal center of a rear wall and 0.2 m below the ceiling and the exhaust opening is 0.23m below the inlet diffuser. The contaminant is a mixture of CO_2 (Carbon Dioxide) and He (Helium) which was introduced through a ping-pong ball of 30 mm diameter on which 6 evenly distributed holes of 1mm diameter each were perforated. The ping-pong ball was placed approximately in the middle of the test room at the point of (x, y, z) = (2.2, 1.2, 0.0). The mixture can have different densities according to the ratio of CO_2 and He and was continuously introduced to the room at a constant flow rate of 0.025 l/s. The experiment configuration is shown in Fig. 5.7.

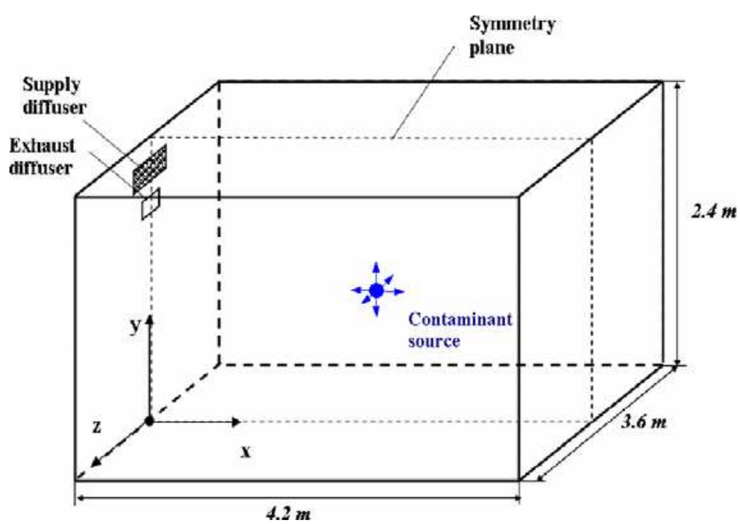

Fig. 5.7 Configuration of the Test Room for the IEA Annex 20 Test Case F (Heiselberg 1991)

The ventilation rate in the experiments is 1.5 ACH which is approximately the minimum value required to ventilate an office room (Heiselberg 1991). Three test cases with contaminant densities of ρ=0.8 kg/m^3, ρ=1.2 kg/m^3 and ρ=1.8 kg/m^3 were carried out which represent, respectively, a case with low density of the contamination source with a tendency of the contaminants to migrate to the ceiling region (with buoyancy effect), a basic case with neutral density and a case with high density of the contamination source with a tendency of the contaminants to migrate to the floor region.

Experiment measurements were carried out under isothermal and steady state conditions. In each test case the CO_2 concentrations were measured at 110 points in the symmetry plane of the test room. The position and distribution of the measuring points are shown in Fig. 5.8 (Heiselberg 1991). The measured results were reported as dimensionless mean values with standard deviation. The concentration values are normalized relative to the mean concentration at the exhaust opening.

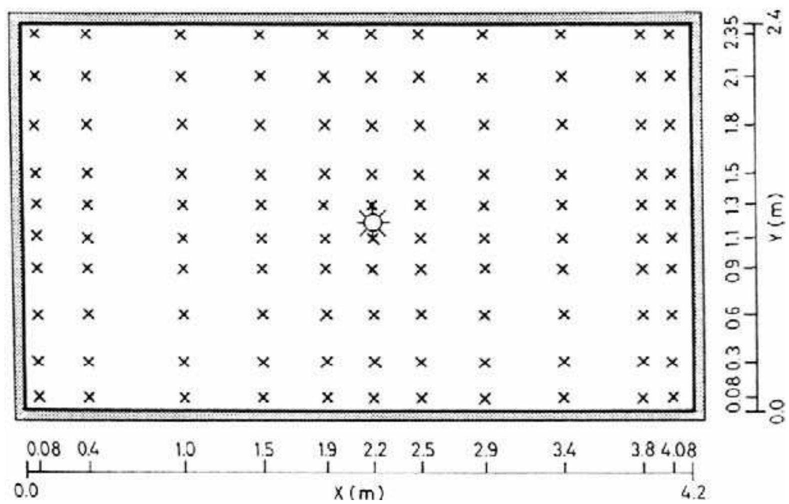

Fig. 5.8 Position and distribution of the measuring points at the symmetry plane of the test room (Heiselberg 1991)

The key parameters for the test cases are summarized in Table 5.2.

Table 5.2 Key parameters of the IEA Annex 20 Test Case F (Heiselberg 1991)

Test Case	Air Change Rate ACH (h^{-1})	Air Flow Rate m^3/s	Contaminant Density kg/m^3	Contaminant Total Flow Rate l/s
F1	1.5	0.0151	0.8	0.025
F2	1.5	0.0151	1.2	0.025
F2	1.5	0.0151	1.8	0.025

5.2.2 Modeling and simulation of the IEA Annex 20 Test Case F

Having validated that the RNG k-ε model together with the momentum method work well for the HESCO nozzle diffuser, simulation of the IEA Test Case F was first carried out with the RNG k-ε model as suggested by Chen (1995, 2001) and Gan (1998). For all the simulations, a converged flow field without contaminant transport was first calculated with the RNG k-ε model, it was then used as the initial guess of the flow field for the subsequent calculations.

5.2.2.1 Boundary conditions and numerical schemes

The following boundary conditions and numerical schemes are commonly used for all the three test cases.

Inlet diffuser

As with the Test Case B and E, the inlet diffuser was modeled using the momentum method and local mesh refinement at the vicinity of the diffuser. The refinement region was from X=0~0.3m, Y=2.03~2.4m and Z=0~0.35m for half room configuration and X=0~0.3m, Y=2.03~2.4m and Z=−0.35 ~ 0.35m for full room configuration. A mass flow rate was imposed at the supply opening and a momentum source term was added to a volume adjacent to the diffuser.

Contaminant source

The contaminant source was modeled as a momentumless volumetric mass source which was imposed on one or several grid cells centered at the point (x, y, z) = (2.2, 1.2, 0). The volumetric mass flow rates of CO_2 and He are specified separately on the source cell(s) which is the source term S_Φ in equation 3.8 or 3.12.

Exhaust opening

At the exhaust opening, the Dirichlet condition was specified, i.e., the gauge pressure at the outlet is set as zero.

Discretization scheme

The discretization schemes are the same as used in the Test Case E as shown in §5.1.3.

Physical properties

One of the most important problems in modeling mass transfer process in fluids is how to appropriately specify the transport properties for the fluids mixture. In this study, the transport properties of the individual gases were specified according to appropriate data sources. The specific heat, viscosity and thermal conductivity of the mixture as well as its density were calculated using ideal gas mixing law, and the mass diffusivity of the gases was specified using the dilute approximation, i.e., CO_2 and He were taken as dilutes and only the diffusion coefficients of CO_2 and He in air were specified, air was considered as the carrier gas and its diffusion coefficient (in air) was set to zero.

5.2.2.2 Computation meshes

Simulation was carried out in both the full room and the half room configurations. Although in some of the IEA Annex 20 experiments, evidence of asymmetric flow in the test room has been observed as in the Test Cases B and E, in this test case, no significant difference was found between the results from full-room simulation and half room simulation with similar mesh grid resolutions. Thus the simulations were mainly carried out in half room configuration, i.e., a symmetric flow in the test room was assumed and a symmetry boundary condition was applied at the symmetry plane of the room.

For mesh dependence test, simulations with different mesh grids were carried out in both the half room configuration and full room configuration. The tested cases are summarized in Table 5.3.

It was found that in the half room configuration, beginning from the mesh grid of 57x64x34 (Case 8 in Table 5.3), the difference between the results from different mesh grids tends to diminish, some differences exist mainly in the region near the contaminant source. When mesh size was increased to 73x74x40, no essential difference exists between the results from this mesh and from denser meshes. For the consideration of a balance of prediction precision and computational cost, the calculations were mainly carried out with the mesh grid of 73x74x40 (216080 cells). When the local mesh refinement was applied in the region near the supply diffuser (from X=0 ~ 0.3m, Y=2.03 ~ 2.4 m, Z=0 ~ 0.35m), the mesh size increased further to 237640 cells.

Table 5.3 Summary of Tested Simulation Cases

Case	Mesh	Cell Number		Source Cells		Configuration
		Original	+Local Refine	Count	Volume (m^3)	
1	36x36x39	50544		2	0.0004285	Full Room
2	43x41x39	68757		1	0.0000816328	Full Room
				6	0.0004897969	
				7	0.0005714297	
3	55x54x49	145530		1	0.0001268214	Full Room
4	52x52x56	151412		16	0.0002412209	Full Room
5	56x56x50	156800	171472	8	0.0001268214	Full Room
6	60x59x55	194700		4	0.0000707215	Full Room
7	57x68x30	116280		1	0.000017009	Half Room
8	57x64x34	124032	142932	1 or 5	0.0000188987	Half Room
			138228	1 or 5	or	
			156610	1 or 5	0.000100682	
9	57x67x33	126027		1	0.0000226784	Half Room
10	61x72x34	149328	165204	1	0.0000188987	Half Room
11	73x74x40	216080	237640	1	0.0000188987	Half Room
				594	0.01652897	
12	78x74x40	230880	252440	2	0.0000184062	Half Room
13	87x74x40	257520	279080	50	0.0007027292	Half Room

5.2.2.3 Test Case F1: contaminant transport with strong buoyancy

In the test case F1, the density of the contaminant mixture is 0.8 kg/m^3, which is much lighter than the ambient air (≈1.2kg/m^3), a strong buoyancy force formed which tends to force the contaminant mixture to migrate to the upper region of the room. Simulation for this test case was first carried out with the RNG k-ε model and with the RSM model because of the presence of strong buoyancy as suggested by Chen (1995, 1996) and Gan (1998).

It was found that although the RNG model can predict reasonably well the jet flow from the inlet diffuser, when coupled with mass transfer and with the presence of buoyancy force, it predicts a very strong upward contaminant jet flow above the contaminant source as shown in Fig. 5.9 which is non-physical compared with experiment measurement. The strong upward jet flow predicted by the RNG k-ε model is repeated with different mesh grids in both the half and full room configurations. Thus further test with this model for the Test Case F1 (TF1) was not pursued.

In Fig. 5.9, the predicted relative CO_2 concentration contours using the RSM model and the same mesh grids are also shown, it can be seen that the predicted result using the RSM model is much better than that obtained with the RNG k-ε model, but both models under-predict the CO_2 concentration downstream the contaminant source, i.e., at the sections of X > 2.2m. Fig. 5.10 is a point-to-point comparison of the simulation result using the RSM model with experimental data. It can be seen that the CO_2 concentration downstream the contaminant source is largely under-predicted in the lower part of the room.

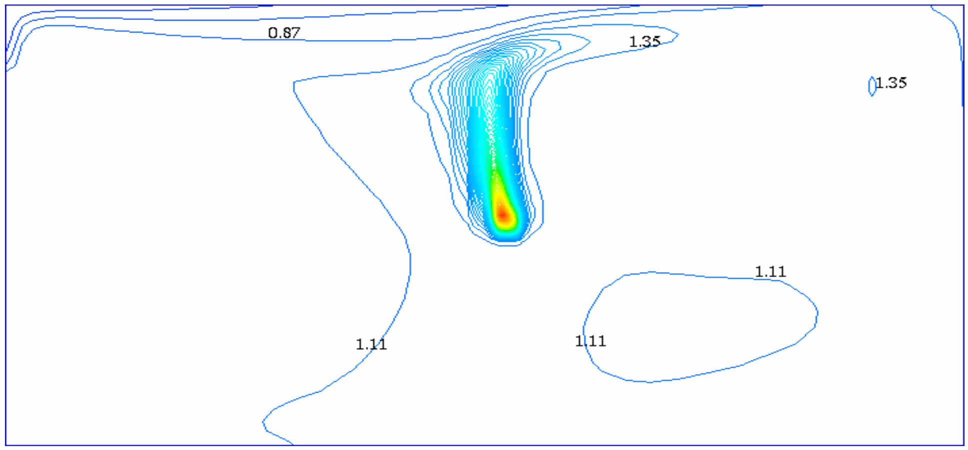

(a) Relative CO_2 concentration contours at the symmetry plane predicted using RNG k-ε model

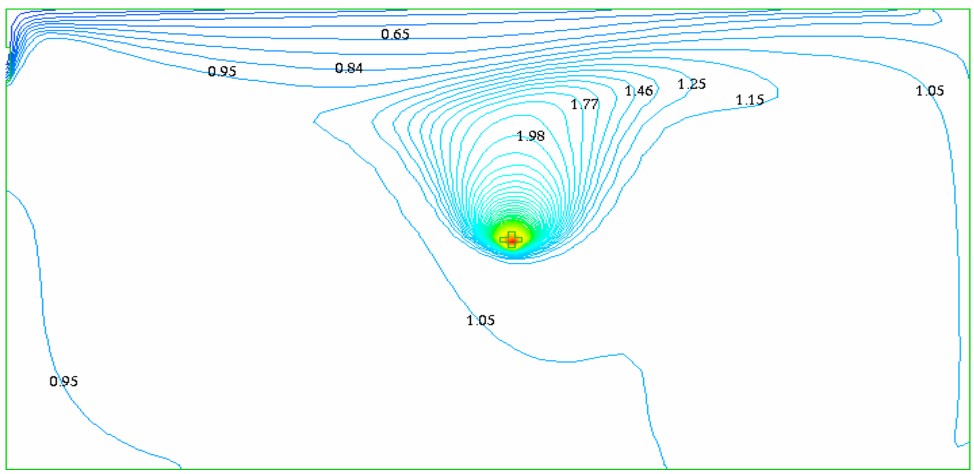

(b) Relative CO_2 concentration contours at the symmetry plane predicted using RSM model

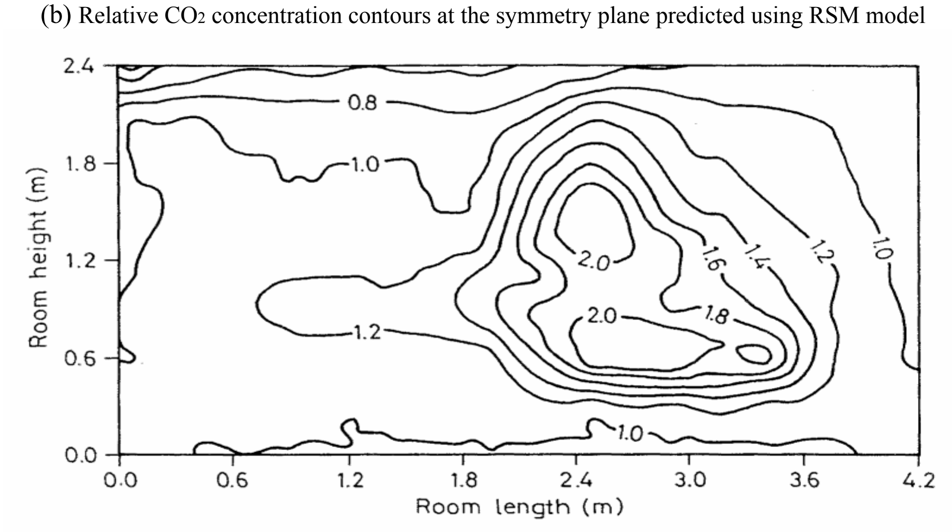

(c) Measured relative CO_2 concentration contours at the symmetry plane

Fig. 5.9 Comparison of the measured and computed relative CO_2 concentration contours on the symmetry plane using the RNG k-ε model and the RSM model (Mesh grid: 57x63x34 – Case 8 in Table 5.3)

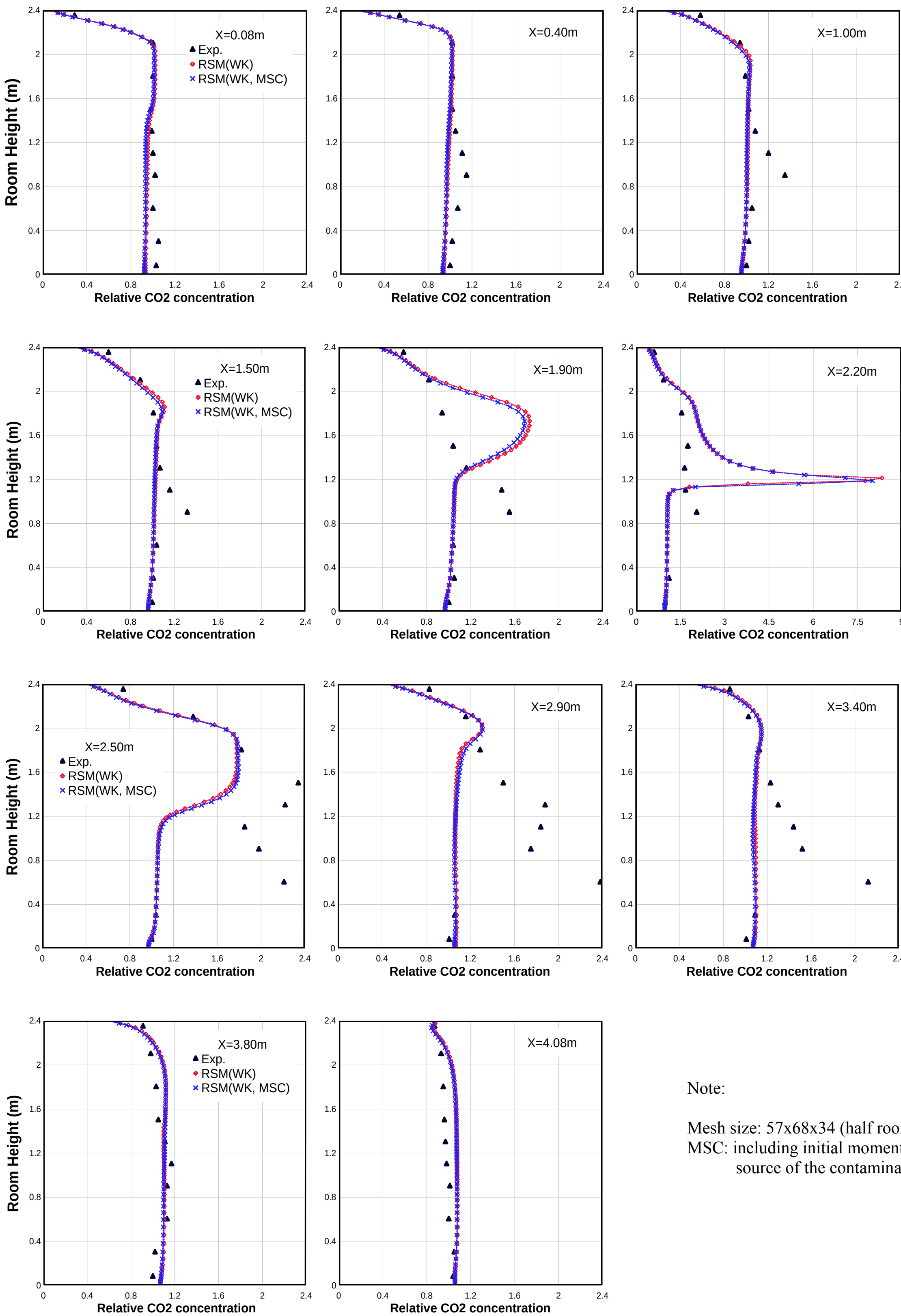

Note:

Mesh size: 57x68x34 (half room)
MSC: including initial momentum source of the contaminants

Fig. 5.10 Comparison of the predicted CO_2 concentration distribution with experimental data using the RSM turbulence model

Modeling of the contaminant source

In the above calculations, the contaminant source was modeled as a momentumless volumetric mass source, thus the distribution of CO_2 and He in the room is determined by the interaction of the convection, the diffusion and the buoyancy forces. Because the initial velocity of the contaminant mixture leaving the ping-pong ball is more than 5m/s which is rather large compared with the mean velocities in the test room, to verify if the initial momentum of the contaminant source influences the distribution of CO_2 and He, calculation was repeated using the same mesh but the contaminant source was modeled as a volumetric mass source plus a momentum source as shown in Fig. 5.11a. The momentum source is determined by calculating the total initial momentum flow rate and it was then evenly distributed in the six coordinate directions (X, -X; Y, -Y; Z, -Z) as shown in Fig. 5.7. In the half room configuration, because of the symmetry boundary condition, the momentum flow rate at each source cell (except the source cell in Z direction) in Fig. 5.11a is only half of the value in the respective coordinate direction.

Initial velocity of the contaminant mixture Uc:

$$U_c = \frac{\dot{q}_c}{\frac{\pi d^2}{4} \times 6} = \frac{0.025 \times 10^{-3}}{3.14 \times (0.001)^2 \times 1.5} = 5.31\, m/s$$

where $\dot{q}_c$ is the total volume flow rate of the contaminant mixture, $\dot{q}_c = 0.025\ l/s$;
d is the diameter of the small openings on the ping-pong ball, d=1.0 mm.

Total initial momentum flow rate of the contaminant mixture $\dot{M}_c$:

$$\dot{M}_c = \rho_c \dot{q}_c U_c = 0.8 \times 0.025 \times 10^{-3} \times 5.31 = 1.062 \times 10^{-4}\, N$$

where ρ_c is the density of the contaminant mixture, $\rho_c = 0.8 kg / m^3$ for the Test Case F1.

Thus the momentum flow at each source cell (except the source cell in Z direction) in Fig. 5.11a can be calculated as:

$$\frac{1.062 \times 10^{-4}}{6} \times \frac{1}{2} = 8.85 \times 10^{-6}\ N$$

For the source cell in Z direction, the momentum flow is $8.85x10^{-6}x2 = 1.77x10^{-6}$ N.

The mass flow source in each cell is determined by a similar process.

A comparison of the calculated relative CO_2 concentration at the symmetry plane with/without the consideration of the initial momentum of the contaminant mixture is also given in Fig. 5.10. It can be seen that the inclusion of the initial momentum of the contaminant mixture in the calculation doesn't change the prediction results, in other words, the under-prediction of the CO_2 concentration downstream the contaminant source was not caused by not considering its initial momentum. This result was also verified in the simulation with full room configuration (Case 2 in Table 5.3), where 6 or 7 grid cells were used as the contaminant source cell (see Figs. 5.11b and 5.11c).

When 6 cells were used as the contaminant source cells, a volumetric mass source and a momentum source were added to each cell in one of the six coordinate directions as shown in Fig. 5.11b. When 7 cells were used as the contaminant source cell, the entrained air by the small jets from the six round holes on the ping-pong ball was calculated using round jet formulae and was added as part of the volumetric mass source to each cell in the six coordinate directions (Launder 2002). In addition to the six source cells as shown in Fig. 5.11b, a negative volumetric mass source (sink) equal to the total entrained air mass was added to the center cell to compensate the added air in the 6 contaminant source cells to maintain mass balance (Fig. 5.11c). The predicted CO_2 concentration profiles using momentumless contaminant mass source, mass source plus momentum source, mass source plus entrained air source and the momentum source show essentially no difference.

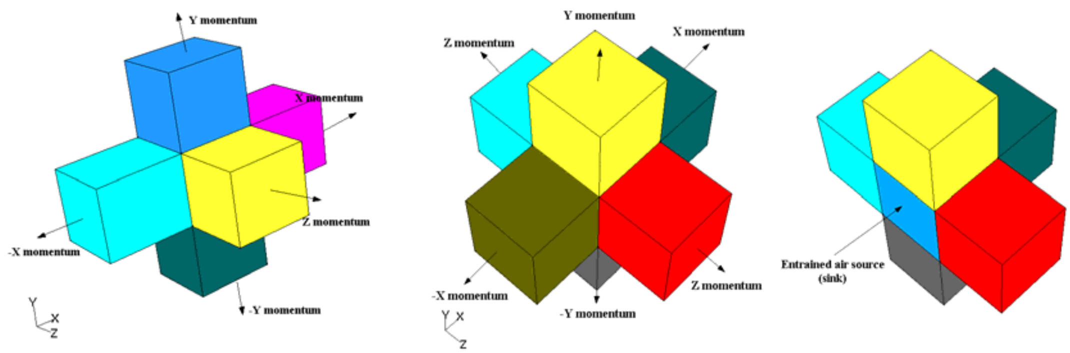

(a) 5 source cells (half room) (b) 6 source cells (c) 7 source cells

Fig. 5.11 Contaminant source cells (including initial momentum source of the contaminants) in half and full room configurations

Influence of the source cells volume on the prediction results

In the experiment, the contaminant source can be considered as a point source because its dimension is very small (diameter Φ=30mm) compared with the dimensions of the test room (4.2mx2.4mx3.6m). In the numerical simulation it is impractical to fully resolve the geometrical details of the ping-pong ball with the small openings on it because that would necessitate too many mesh grids in the region around the source, thus the contaminant source was modeled as a volumetric mass source contained in one or more grid cells. Having verified that the initial momentum of the contaminant mixture doesn't have significant impact on the prediction results, the next logical step is to see how the volume size of the source cells influences the prediction results. For this purpose, simulations with a small source (a single cell) and a very large source (594 cells) and the same mesh grid (73x74x40) were carried out, the ratio of the large source volume to that of the small source is about 875. The predicted results are compared in Fig. 5.12. It can be seen that the predicted results are nearly the same everywhere except at the section of X=2.2m, where the peak CO_2 concentration is lower with the big source. This is a logical consequence because the section X=2.2m cuts through the source cells. When a big source is used, the initial CO_2 concentration in the cells is much lower, that means also that the initial CO_2 concentration gradient at the interface of the CO_2 source cells and the rest of the room is much smaller, but it doesn't influence the global distribution of CO_2 in the room, just has a very limited local effect.

Influence of mesh resolution on the prediction results

To examine how the mesh grids influence the prediction results, local refinement of the mesh grids was applied to the regions near the supply diffuser and around the contaminant source. Fig. 5.13 shows three locally refined meshes: (a) local refinement around the contaminant source; (b) local refinement at the region near the supply diffuser; (c) local refinement near the supply diffuser and around the contaminant source. Fig. 5.14 is a comparison of the predicted relative CO_2 concentration contours with these three meshes using the RSM turbulence model. Fig. 5.15 is a point-to-point comparison of the predicted results using the three mesh grids with experimental data. Comparing Fig. 5.9b and Fig. 5.14a, it can be easily seen that the local mesh refinement around the contaminant source has very little influence on the predicted results. On the contrary, the local mesh refinement near the supply diffuser significantly changes the predicted CO_2 concentration contours on the symmetry plane of the test room, and a combination of the above two local mesh refinements gives nearly the same result with that of only locally refined near the supply diffuser. This result is consistent with the result from §5.3.2: when the mesh near the diffuser is locally refined, the predicted maximum velocity in the wall jet increases, that means that the convection force becomes stronger, and then the peak

CO_2 concentration at X=1.9m section is blown off, as a consequence, the CO_2 concentration downstream the contaminant source (X >2.2m) is also reduced, resulting in a more even distribution of CO_2 in the test room (cf. Figs. 4.36 and 4.37). This result can be further illustrated by a comparison of the simulation results with different mesh grids as show in Fig. 5.16. It can be seen from Fig. 5.16 that as the mesh size increases, the peak CO_2 concentration at X=1.9m section decreases, and then the peak CO_2 concentration downstream the contaminant source (X=2.5m, 2.9m and 3.4 m) also decreases. The predicted CO_2 concentrations near the two rear walls (front wall and end wall) don't change much as the mesh size changes, they are all about 1, i.e., nearly the same concentration as that at the exhaust opening. By a comparison of Fig. 5.15 and Fig. 5.16, it can be seen that when the mesh is locally refined near the supply diffuser, the coarser mesh (57x64x34) can give nearly the same result as with the much finer mesh 73x74x40, that means the predicted CO_2 concentration distribution is mainly controlled by the mesh resolution near the supply diffuser, it is a direct indication that the room air distribution is mainly controlled by the supply diffuser, thus the correct modeling of the supply diffuser is very important.

It was observed also that as the mesh size increases, the difference between the predicted results from the initial mesh and its locally refined mesh (near the supply diffuser) decreases. This means that when the mesh grids at the jet flow region are fine enough, the influence of local mesh refinement near the diffuser on the prediction results decreases. Fig. 5.17 is a comparison of the predicted results with two different mesh grids and their locally refined meshes. It can be seen that with the mesh 73x74x40 (Case 11 in Table 5.3), there is practically no difference between the results from the initial mesh and from the locally refined mesh. This is contrary to that shown in Fig. 5.14 and Fig. 5.15 where the initial mesh size is 57x64x34. With this mesh, the influence of local mesh refinement in the vicinity of the supply diffuser on the prediction results is very significant.

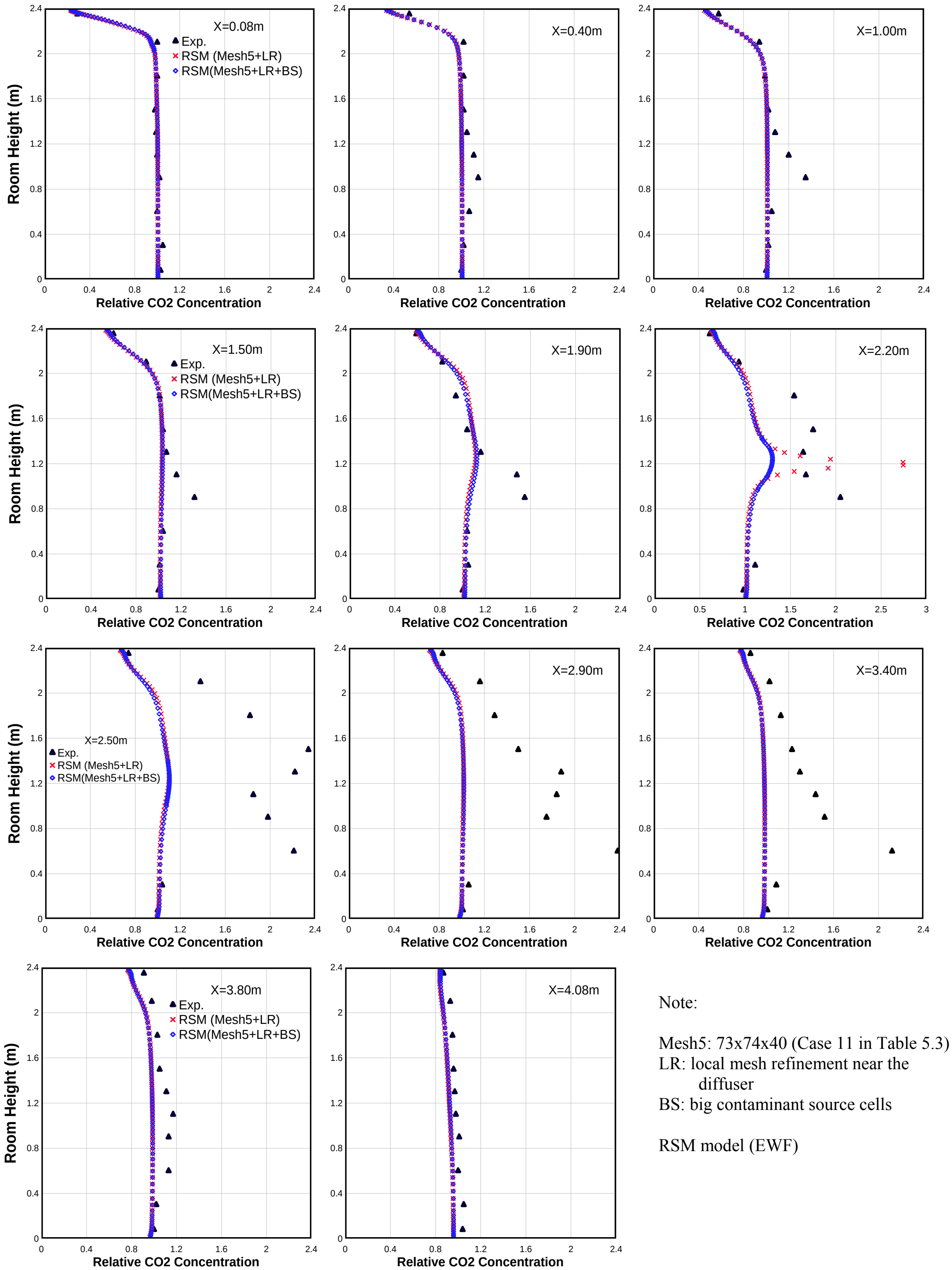

Note:

Mesh5: 73x74x40 (Case 11 in Table 5.3)
LR: local mesh refinement near the diffuser
BS: big contaminant source cells

RSM model (EWF)

Fig. 5.12 Comparison of the predicted CO_2 concentration distribution using small and big source cells for the contaminant mixture

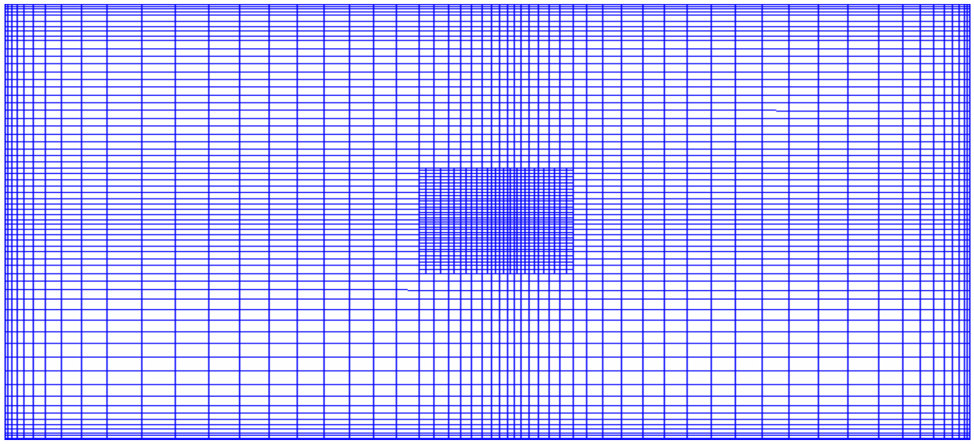

(a) Local mesh refinement around the contaminant source (from X=1.8 ~2.5m, Y=0.9 ~1.5m, Z=0 ~ 0.3m)

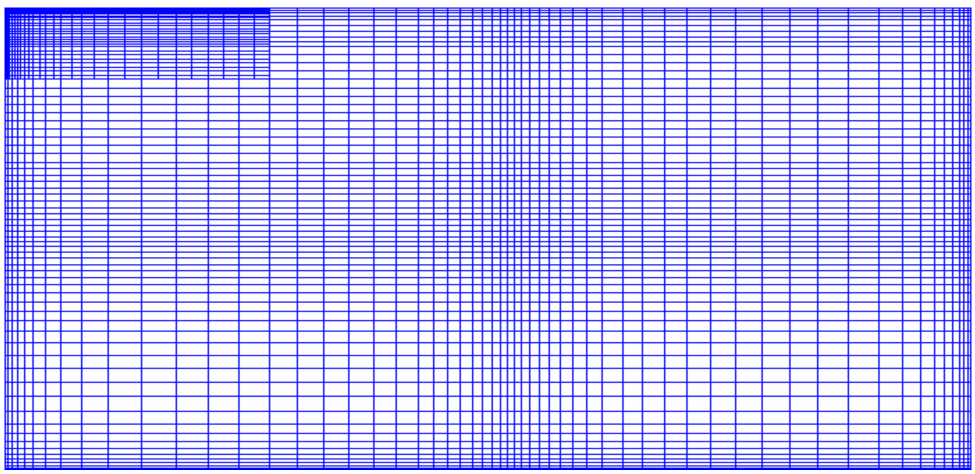

(b) Local mesh refinement near the supply diffuser (from X=0 ~1m, Y=2.03 ~ 2.4m, Z=0 ~ 0.35m)

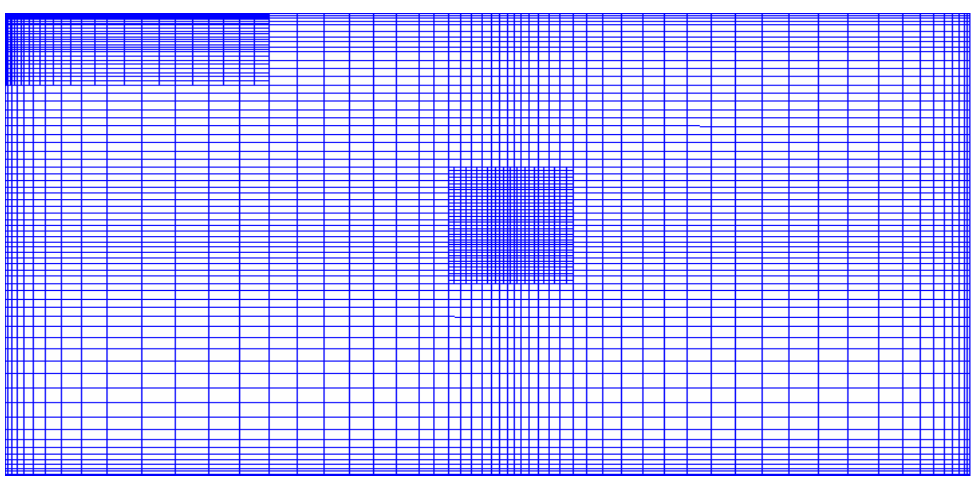

(c) Local mesh refinement near the supply diffuser and around the contaminant source
(from X=0 ~1m, Y=2.03 ~2.4m, Z=0 ~ 0.35m and X=1.9 ~ 2.5m, Y=1 ~ 1.6m, Z=0 ~ 0.3m)

Fig. 5.13 Local mesh refinement near the supply diffuser and around the contaminant source
(Initial mesh: 57x64x34 – Case 8 in Table 5.3)

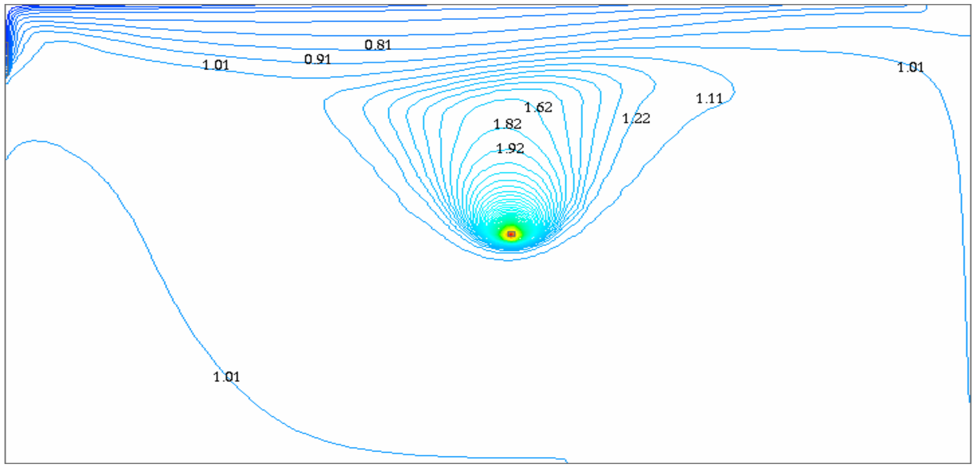

(a) Relative CO_2 concentration contours predicted with mesh grid (a) in Fig. 5.13

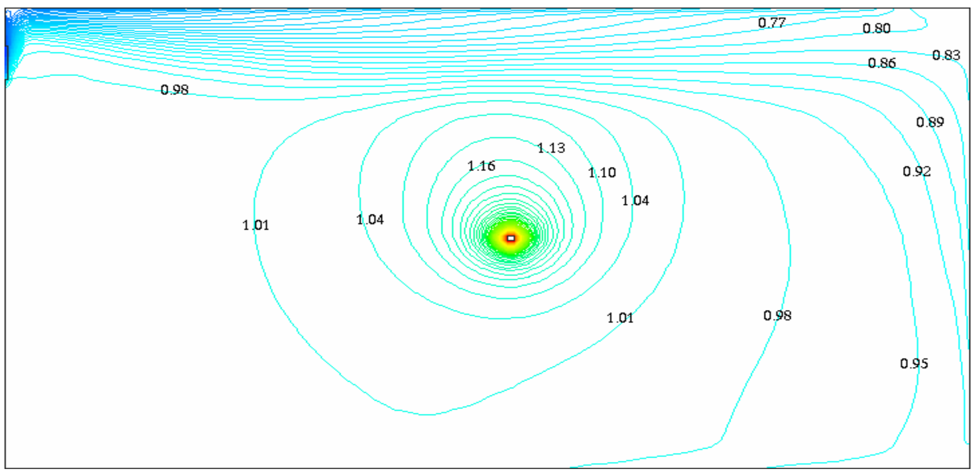

(b) Relative CO_2 concentration contours predicted with mesh grid (b) in Fig. 5.13

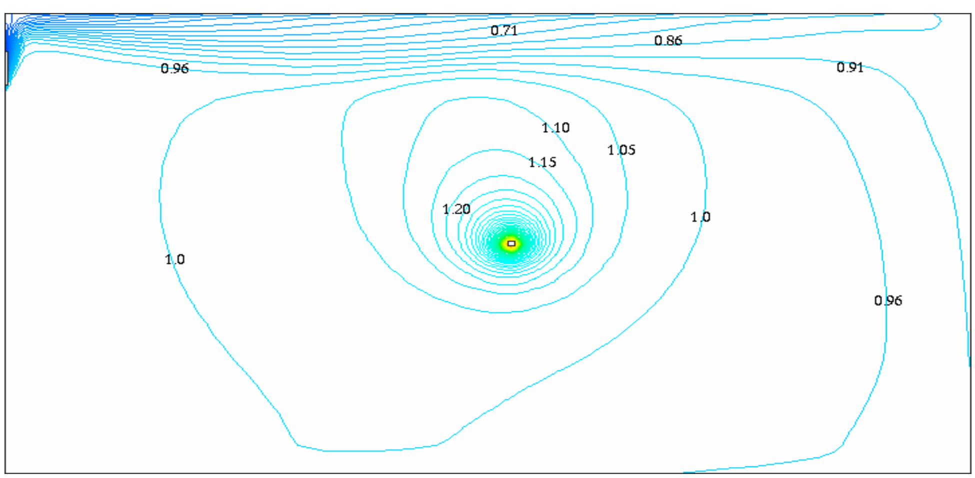

(c) Relative CO_2 concentration contours predicted with mesh grid (c) in Fig. 5.13

Fig. 5.14 Comparison of the predicted relative CO_2 concentration contours with different local mesh refinements (RSM turbulence model with enhanced wall treatment. Initial mesh: 57x64x34)

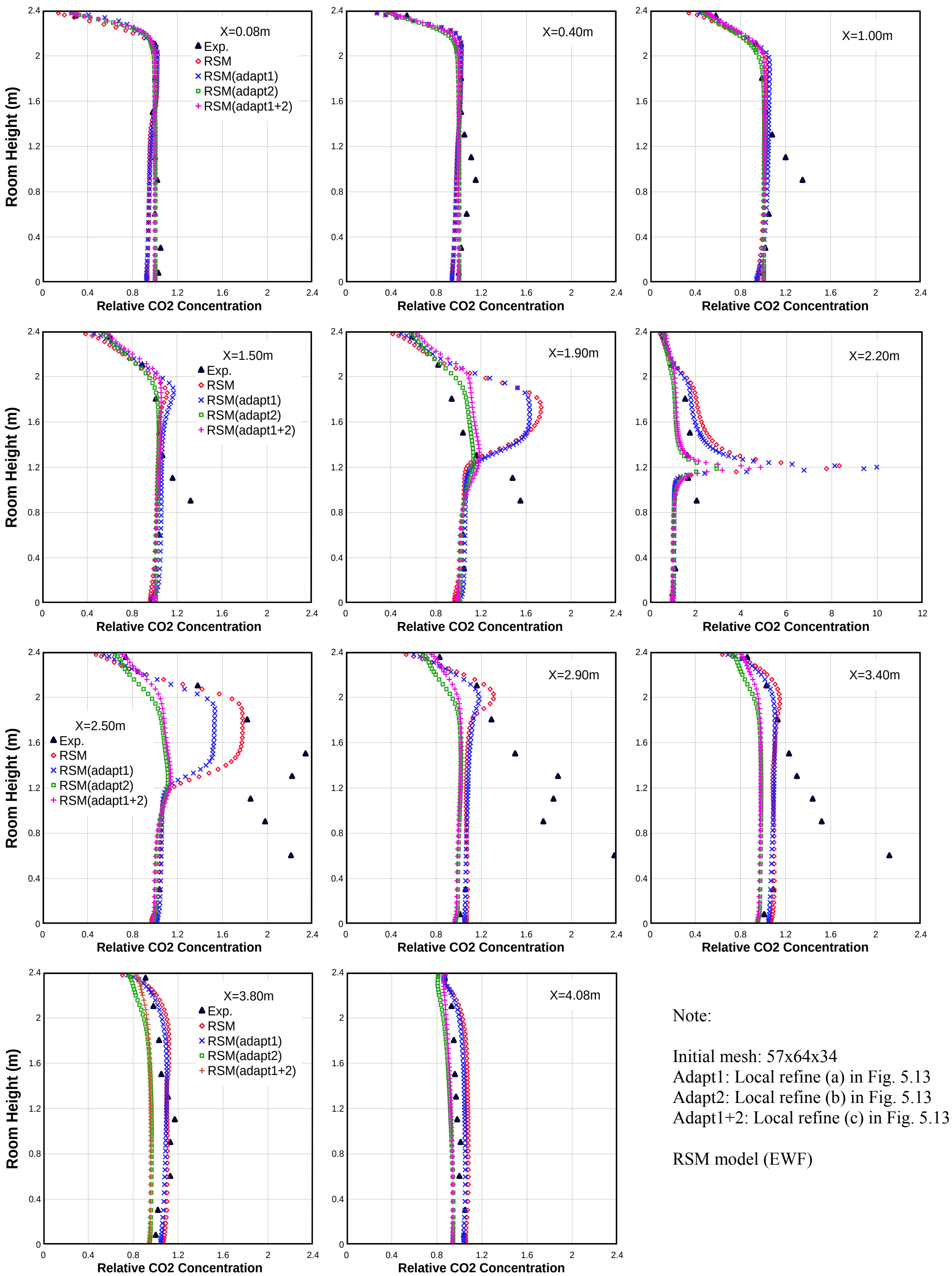

Fig. 5.15 Comparison of the predicted CO_2 concentration distribution using different local mesh refinements and the RSM model with experimental data

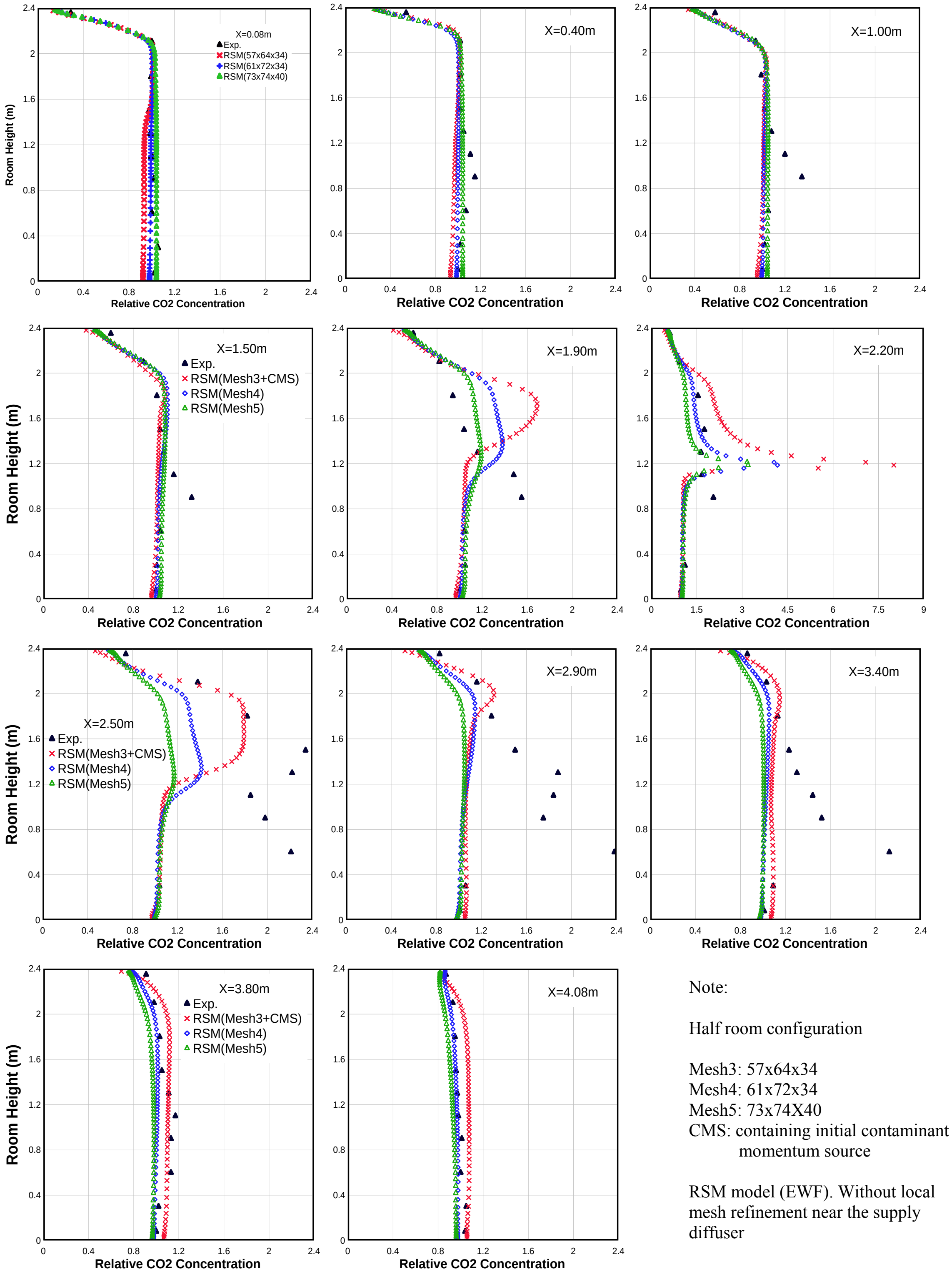

Fig. 5.16 Comparison of the predicted CO_2 concentration distribution with the RSM model and different mesh sizes

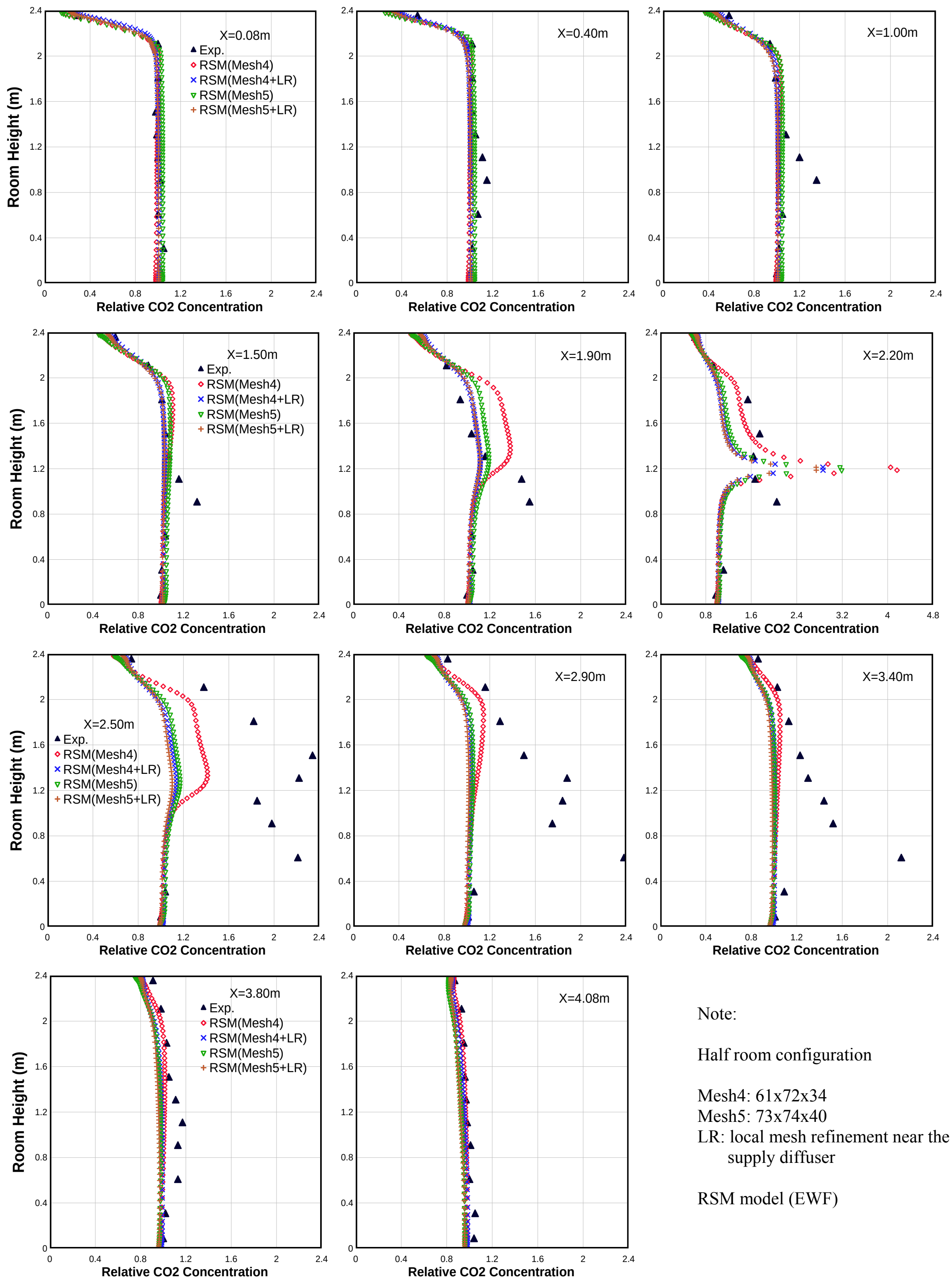

Fig. 5.17 Comparison of the predicted CO_2 concentration distribution with different mesh girds and local mesh refinement near the supply diffuser (RSM model)

Prediction of the Test Case F1 using other turbulence models

SST k-ω model

The SST k-ω model was also tried out for this test case because it can give a better prediction of the wall jet velocity profiles as shown in Fig. 4.48. Unfortunately, like the RNG k-ε model, it predicts a very strong upward contaminant jet flow just above the contaminant source which is non-physical. Fig. 5.18 shows the predicted relative CO_2 concentration contours at the symmetry plane from both the full room configuration (Fig. 5.18a, 56x56x50) and half room configuration (Fig. 5.18b, 73x74x40), both with local mesh refinement near the supply diffuser. Compared with Fig. 5.9a, it can be seen that the relative CO_2 concentration contours predicted by the SST k-ω model are very similar to those predicted by the RNG k-ε model, although the upward jet predicted by the latter is a little stronger.

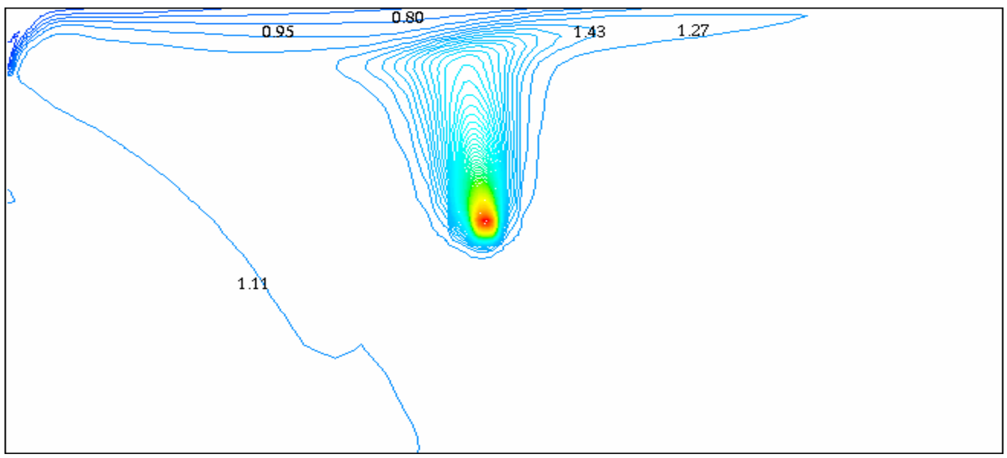

(a) Full room configuration (mesh size 56x56x52), with local mesh refinement near the supply diffuser

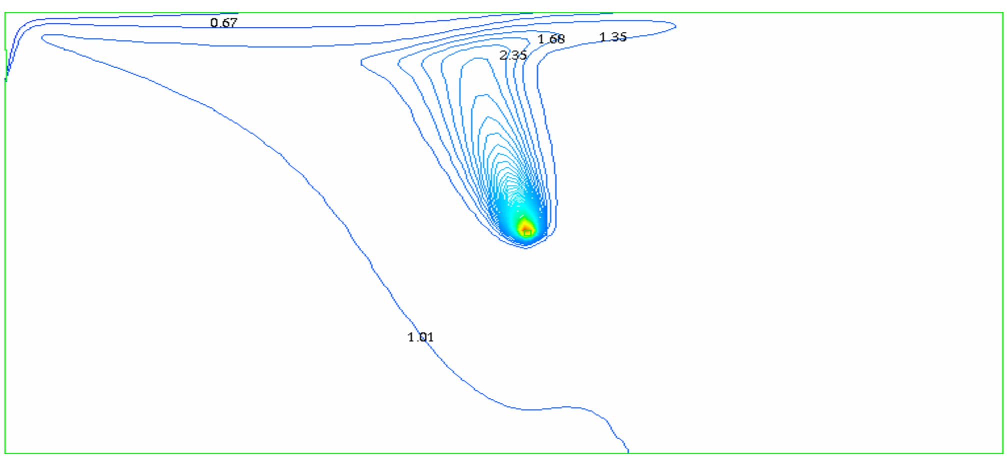

(b) Half room configuration (mesh size 73x74x40), with local mesh refinement near the supply diffuser

Fig. 5.18 Predicted relative CO_2 concentration contours at the symmetry plane using the SST k-ω model

Standard k-ε model

The standard k-ε model has some better performance for the prediction of the Test Case 1 (TF1) than do the RNG k-ε model and the SST k-ω model. Fig. 5.19 shows the predicted relative CO_2 concentration contours with a mesh grid of 61x72x34 (Case 10 in Table 5.3) and with local mesh refinement near the supply diffuser.

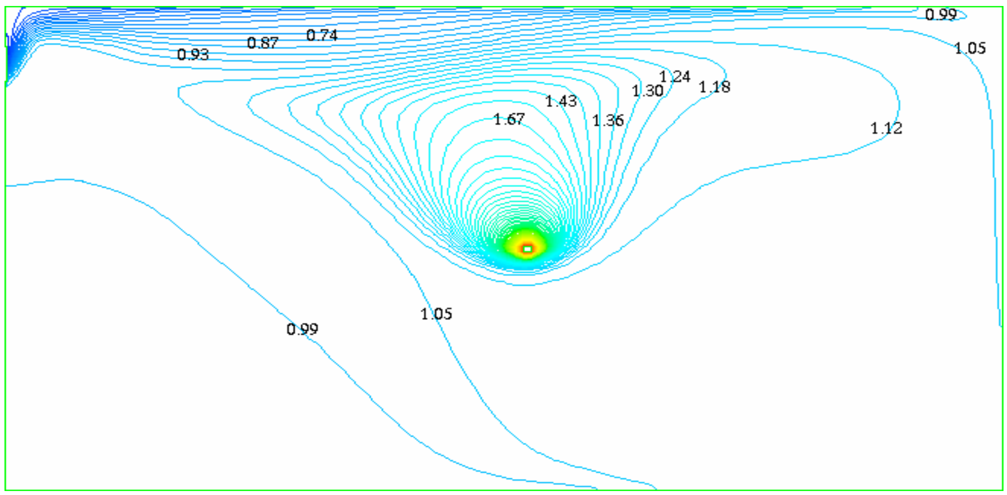

Fig. 5.19 Predicted Relative CO_2 concentration profiles at the symmetry plane with the standard k-ε model and with local mesh refinement near the supply diffuser (half room configuration)

Fig. 5.20 shows a point-to-point comparison of the predicted CO_2 concentration distribution using the standard k-ε model and the RSM model with the above mesh grid. It can be seen that the CO_2 concentration near the front wall ($X < 1.5m$) is slightly under-predicted by the standard k-ε model; at the other places in the test room, this model can give comparable results with that predicted by the RSM model, although in total the result predicted by the latter is a little better.

Realizable k-ε model

It was found that the realizable k-ε model doesn't offer any advantages over the other turbulence models for all the three test cases (F1, F2 and F3) and it is not stable for the cases tested. Further test with this model was not continued.

Influences of the Prandtl number and Schmidt number on the prediction results

At present, it is not known how the Prandtl number and Schmidt number change in the low-Reynolds number flow region near walls (Versteeg 1995). In FLUENT, the wall Prandtl number is set to 0.85, and the Schmidt number is assumed to be a constant as 0.7. In literature, a Prandtl number between 0.5 ~ 0.9 (Awbi 1989) and a Schmidt number between 0.7 ~ 1.0 (Chen et al. 2000, Versteeg et al. 1995) have been used by different authors. Nielsen et al. (1979) and Ideriah (1980) have used an expression for the Prandtl number based on boundary layer measurement but Awbi (1989) found that using such expressions doesn't improve the numerical simulation for air flow in rooms. In the present study, several combinations of different Prandtl numbers and Schmidt numbers have been tested and no essential difference was found between the predicted results for the CO_2 concentration distribution on the symmetry plane. Fig. 5.21 is a sample comparison of the predicted CO_2 concentration distribution using 3 different combinations of Prandtl number and Schmidt number: (a) $\sigma_t = 0.85$, $Sc_t = 0.7$ (default in FLUENT); (b) $\sigma_t = 0.9$, $Sc_t = 0.6$; (c) $\sigma_t = 0.9$, $Sc_t = 0.8$. It can be seen that nearly no difference exists between the predicted results. The same result was also found for the other two test cases: F2 and F3.

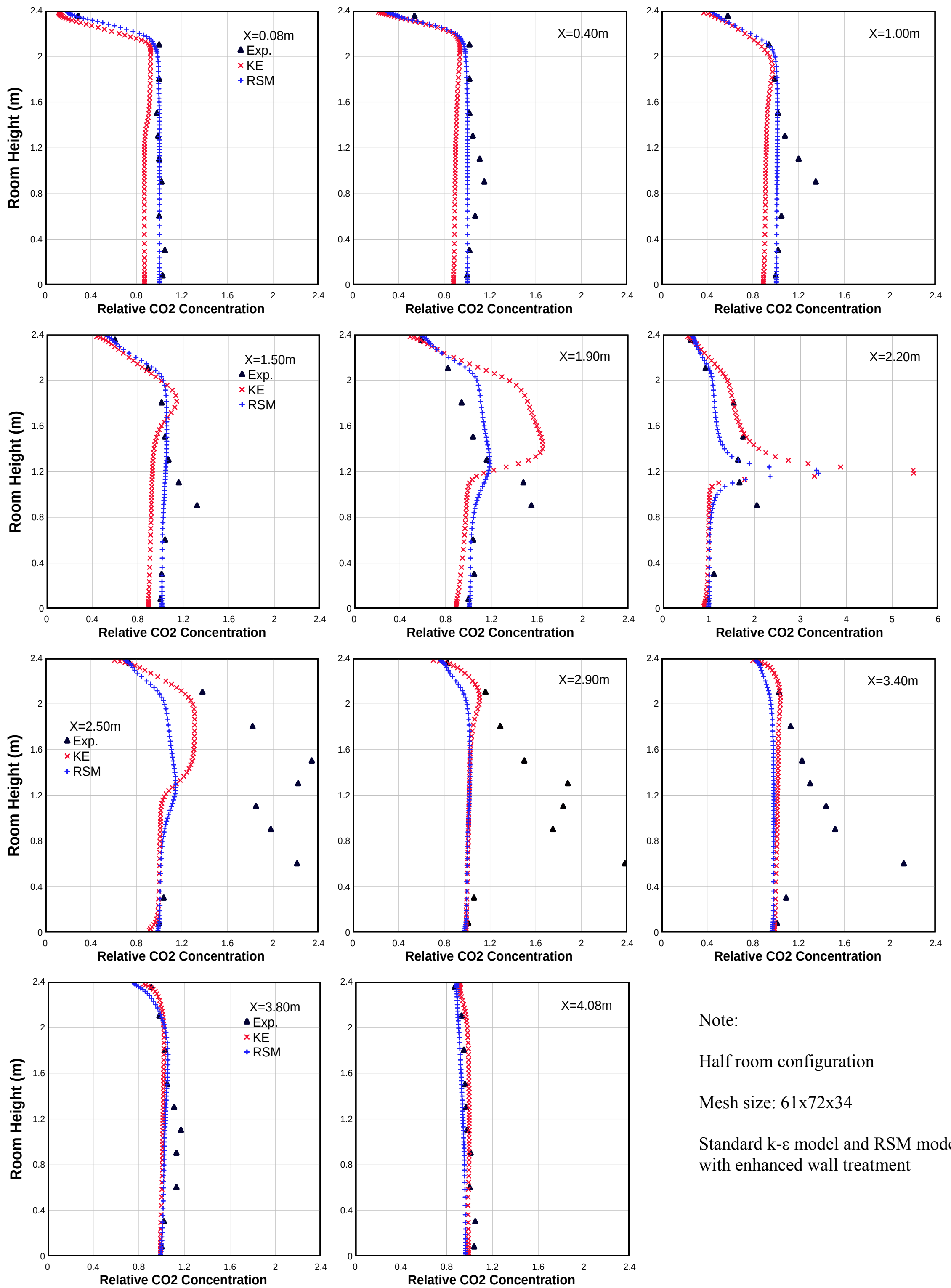

Note:

Half room configuration

Mesh size: 61x72x34

Standard k-ε model and RSM model with enhanced wall treatment

Fig. 5.20 Comparison of the predicted CO_2 concentration distribution on the symmetry plane using the standard k-ε model and the RSM model with experimental data

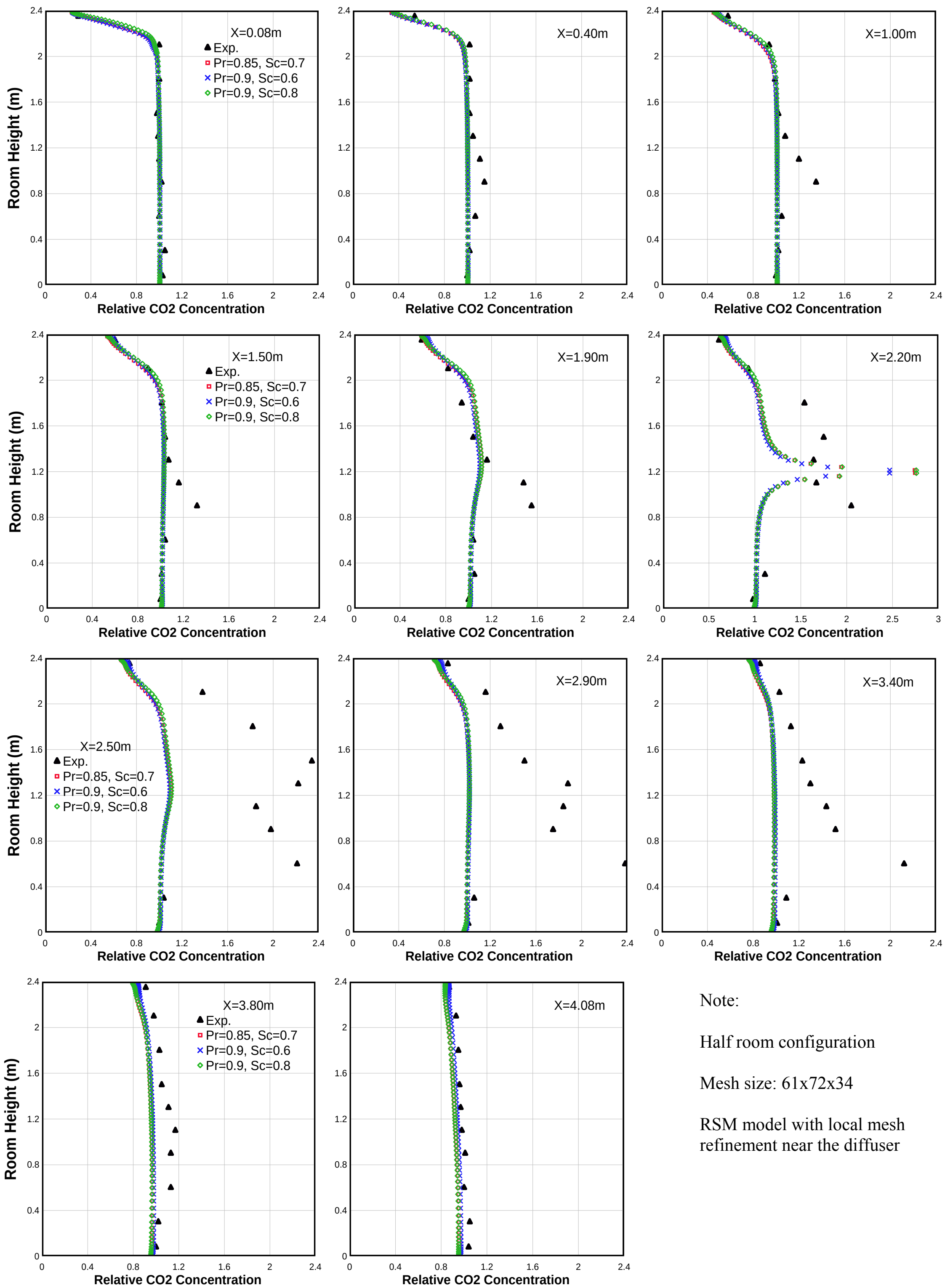

Fig. 5.21 Comparison of predicted CO_2 concentration distribution on the symmetry plane using the RSM model and different Prandtl – Schmidt numbers

Prescribed velocity method

The RNG k-ε model predicts very well the jet flow issued from the diffuser, but when coupled with mass transfer and with mass buoyancy, it predicts a very strong upward jet flow above the contaminant source which is non-physical. An interesting question is: if we take the jet velocity profiles predicted by the RNG k-ε model and use it as the initial condition for the jet flow using prescribed velocity method, what can we get?

As has been shown in Fig. 4.50 the RNG k-ε model predicts very well the X velocity (streamwise) profiles, but less satisfactory for the Y (crosswise) and Z (spanwise) velocity profiles of the jet flow. Thus the X velocity profiles calculated using the RNG k-ε model and local mesh refinement without contaminant transfer were taken at the three vertical sections of X=0.5m, X=1m and X=2.2m for Y=2 ~ 2.4m and Z=0 ~ 0.5 m, which were then used as the prescribed X velocity profiles and were imposed at the corresponding position at the subsequent calculations. In FLUENT, it is possible to fix the values of variables in a cell or in a fluid or solid zone. When a value is fixed in a given cell, the transport equation for that variable is not solved in the cell, the fixed value is used to calculate the face fluxes between the cell and its neighbors, resulting in a smooth transition between the fixed value of the variable and the values at the neighboring cells (Fluent Inc. 2001). In Fig. 5.22 a comparison of the predicted CO_2 concentration distribution using the RSM model and prescribed X velocity profiles at X=0.5m, X=1m and X=2.2m is given. It can be seen that there is essentially no difference between the predicted results when the prescribed X velocity profiles were added to all the three sections at X=0.5m, X=1m and X=2.2m or to two of them. When the prescribed X velocity profile is added only to X=2.2m section, the predicted CO_2 distribution is similar to the result from the same mesh but without local mesh refinement near the supply diffuser. From Fig. 5.23, it can be clearly seen how the position of the prescribed X velocity profiles influence the prediction results: as the profiles are added to a position nearer to the end wall, the peak CO_2 concentrations at X=1.9m and X=2.5m sections become lower, and the results approach more the results predicted by local mesh refinement near the diffuser.

Fig. 5.24 is a comparison of the predicted CO_2 concentration distribution using the standard k-ε model and the prescribed velocity profile method. It can be seen that when the prescribed velocity profiles are added to one or more places, the prediction of CO_2 concentration near the front wall of the room (X=0 ~ 1m) is improved. When the prescribed X velocity profiles are added to all three sections of X=0.5m, X=1m and X=2.2m or to only two sections of X=1m and X=2.2m, the predicted CO_2 concentration distribution is significantly improved.

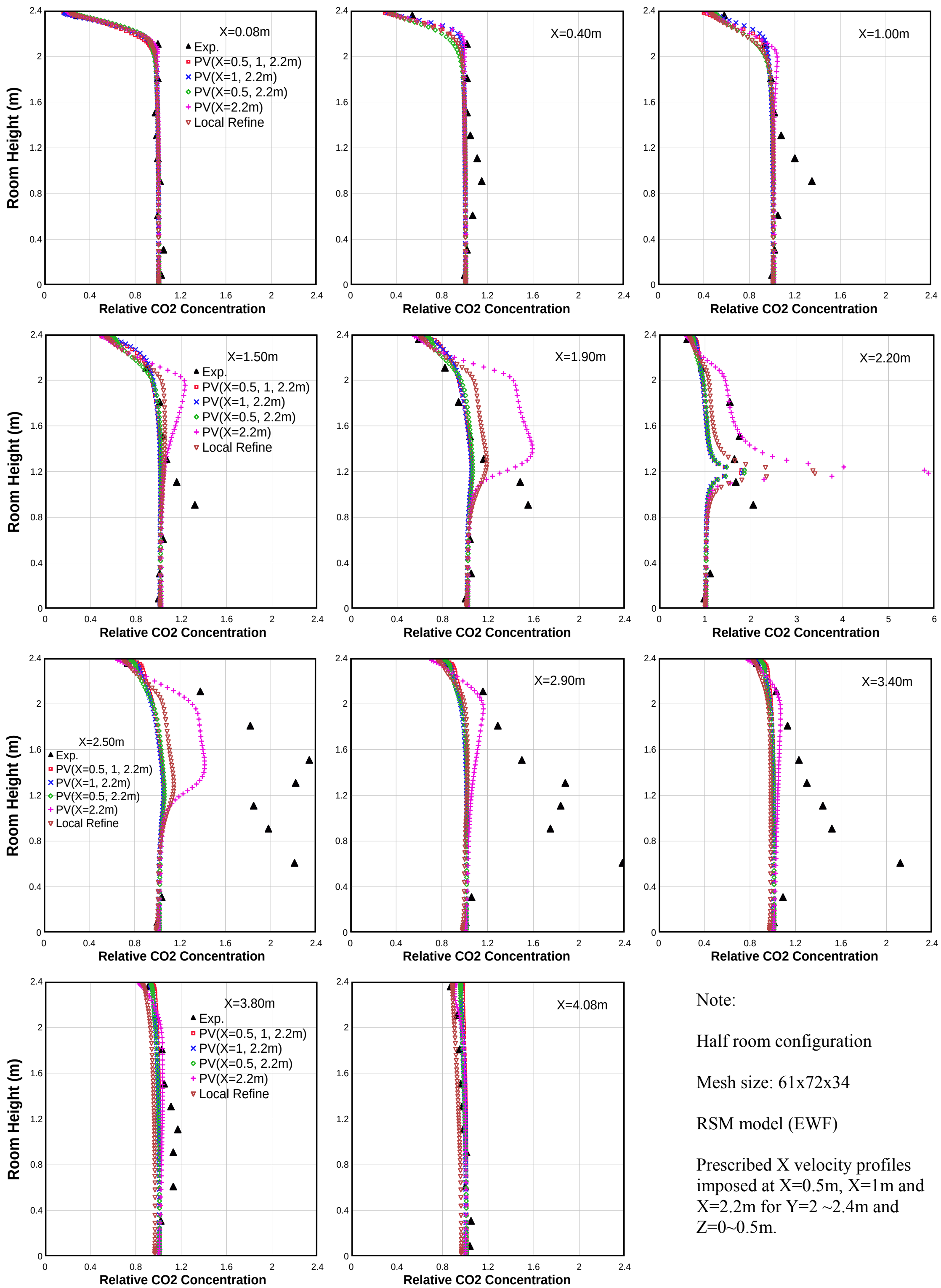

Fig. 5.22 Comparison of the predicted the CO_2 concentration distribution using RSM model and prescribed velocity profiles at different positions

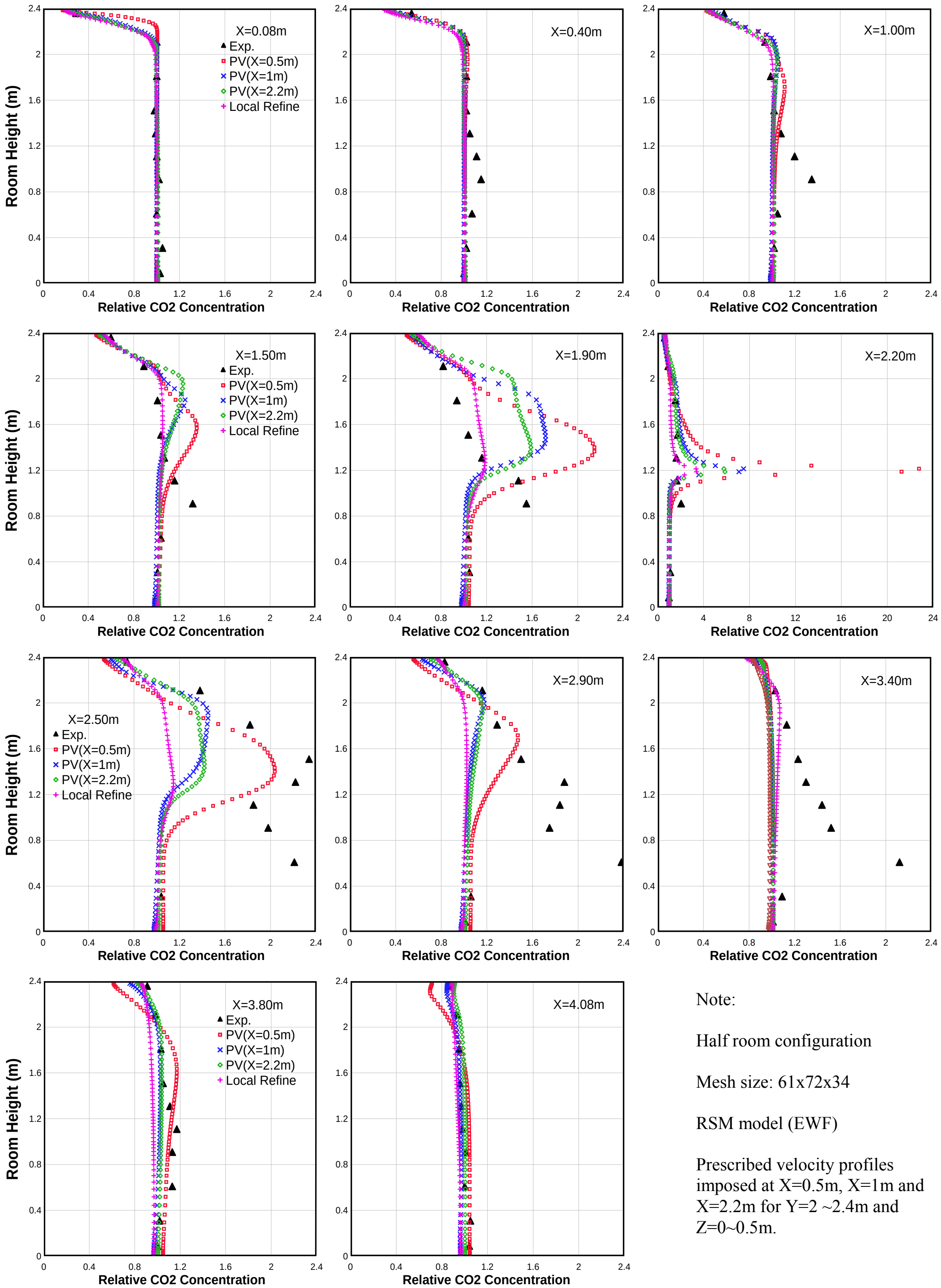

Fig. 5.23 Comparison of the predicted CO_2 concentration distribution using RSM model and a single prescribed velocity profile at different positions

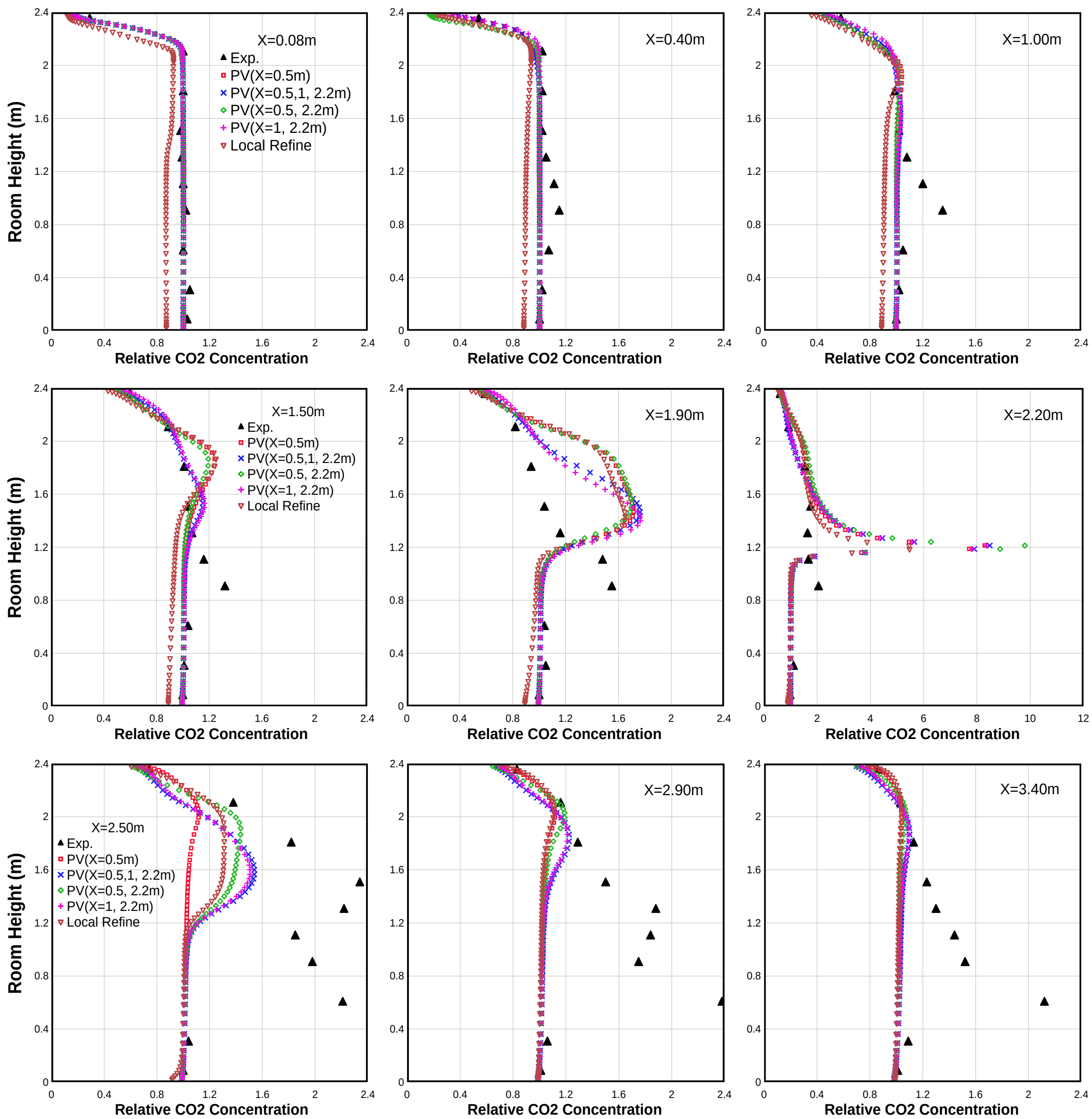

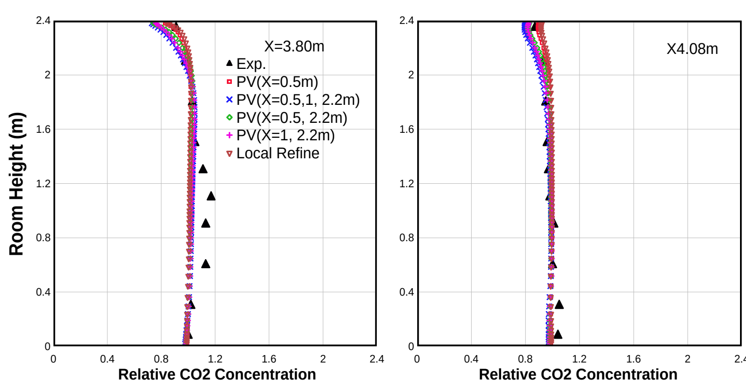

Note:

Half room configuration

Mesh size: 61x72x34

Standard k-ε model (EWF)

Prescribed X velocity profiles imposed at X=0.5m, X=1m and X=2.2m for Y=2 ~2.4m and Z=0~0.5m.

Fig. 5.24 Comparison of the predicted CO_2 concentration distribution at the symmetry plane using the standard k-ε model and prescribed velocity profiles at different positions

5.2.2.4 Test Case F2: contaminant transport by ventilation

In Test Case F2, the contaminant mixture has the same density as that of the room air, thus its distribution is purely determined by the interaction of convection force and diffusion force. The RNG k-ε model was tried first. It was found that this model can give reasonable predictions for the CO_2 concentration in the room compared with experiment data, but there exists significant difference between the predictions with and without the momentum source for the supply diffuser, better prediction results were obtained when the momentum source was not included. Fig. 5.25 shows a comparison of the predicted relative CO_2 concentration contours using the RNG k-ε model and with/without the momentum source for the supply diffuser. It can be seen that the predicted relative CO_2 concentration contours without the momentum source for the supply diffuser correspond much better to the measurements, but as with the Test Case F1, the CO_2 concentration at the lower part of the room is still under-predicted. Fig. 5.26 is a point-to-point comparison of the predicted results with experiment data.

The same locally refined meshes using the same initial mesh (57x64x34 — Case 8 in Table 5.3) as shown in Fig. 5.13 were used together with the RNG k-ε model to explore the influence of grid resolution on the prediction results. Fig. 5.27 is a comparison of the predicted relative CO_2 concentration contours with the three locally refined meshes: (a) locally refined around the contaminant source (Fig. 5.13a); (b) locally refined near the supply diffuser (Fig. 5.13b); (c) locally refined around the contaminant source and near the supply diffuser (Fig. 5.13c). In Fig. 5.28 a point-to-point comparison of the results obtained from these three locally refined meshes and also from the initial mesh is given. It can be seen that the results from the first two locally refined meshes are nearly the same and also the same as that from the initial mesh, the result from the third refined mesh (combined local refine near the supply diffuser and around the contaminant source) is slightly different from the other three cases, but the difference is small.

The same modeling of the contaminant source including its initial momentum as shown in Fig. 5.11 was also tried for this case. It was found that when the initial momentum of the contaminant source is included in the modeling, all the turbulence models can not give a stable result if the momentum source for the supply diffuser is not included. And when the momentum source for the supply diffuser is included in the calculations, the predicted results from different turbulence models are very similar, they are all like that shown in Fig. 5.26. The influence of the contaminant source cell volume on the prediction results was also tested. As with the Test Case F1, simulations with a small contaminant source cell (a single cell) and a very large contaminant source cell (594 cells) and with the same mesh grid (73x74x40) were conducted. The results from these two meshes are nearly the same except at the section of X=2.2m, where the peak CO_2 concentration is much lower when a big source cell is used. Fig. 5.29 is a comparison of the predicted results with small and big source cells.

The low-Reynolds number (LRN) version of the RNG k-ε model (differential viscosity) was also tested for this test case, successive mesh adaptation was carried out to assure that the dimensionless wall distance Y^+ is about 1. When using an initial mesh of 57x64x34, the final mesh size increased from the original 124032 cells to 232882 cells. It was found that when the momentum source for the supply diffuser is not included, the low-Re RNG k-ε model gives nearly the same prediction results as its high-Re version with enhanced wall treatment, but the computational cost increased substantially because very fine mesh is needed when using the LRN version of the model. When the momentum source for the supply diffuser is included in the calculation, the LRN version gives a similar result as shown in Fig. 5.25b, and it's very difficult to assure that all the Y^+ values fall in the range of about 1, because the mesh size will become prohibitively high.

It was found that the RNG k-ε model is the only model which can consistently give reasonable prediction results for this test case: there is no much difference between the results from a mesh with local mesh refinement near the diffuser and with the initial mesh as show in Fig. 5.29, that means that the initial mesh (73x74x40) is enough fine for this test case. Also the sensitivity of the simulation results to the mesh grid size is less as compared with the Test Case F1. Fig. 5.30 is a comparison of simulation results with the RNG k-ε model and different mesh sizes. It can be seen that the prediction from a coarser mesh 57x64x34 (124032 cells) has only a very small difference with that from a much finer mesh 87x74x40 (257520 cells).

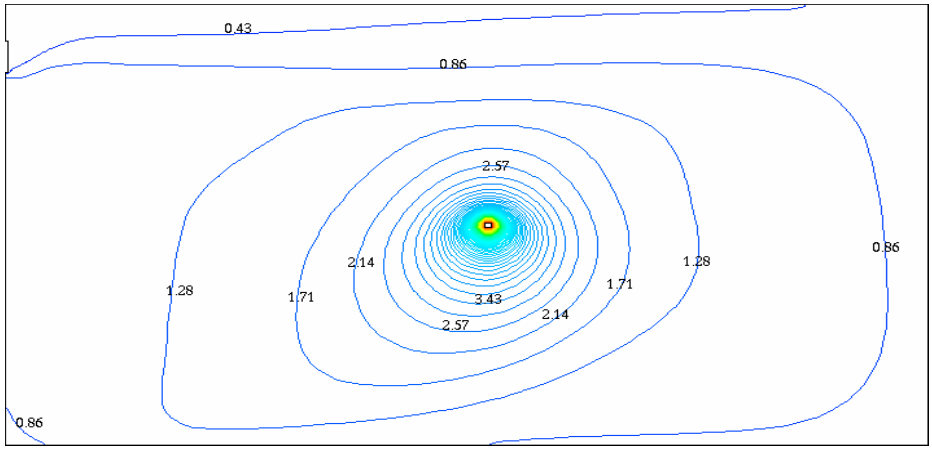

(a) Without momentum source for the supply diffuser

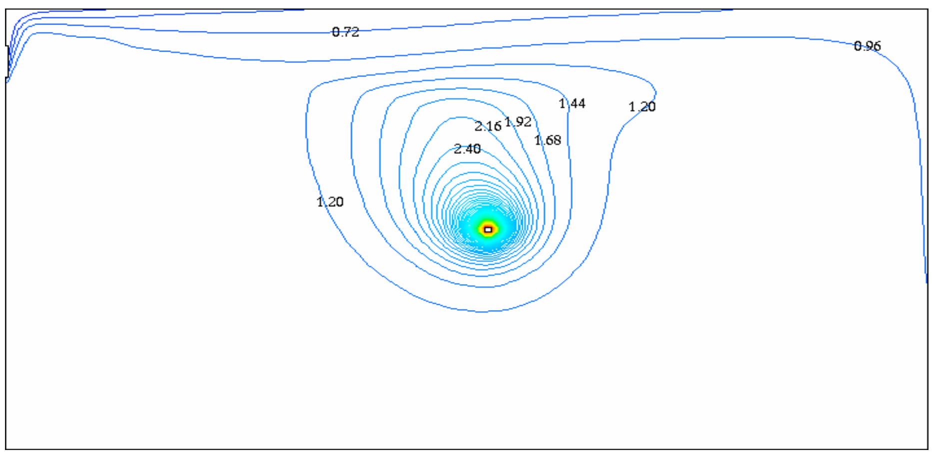

(b) With momentum source for the supply diffuser

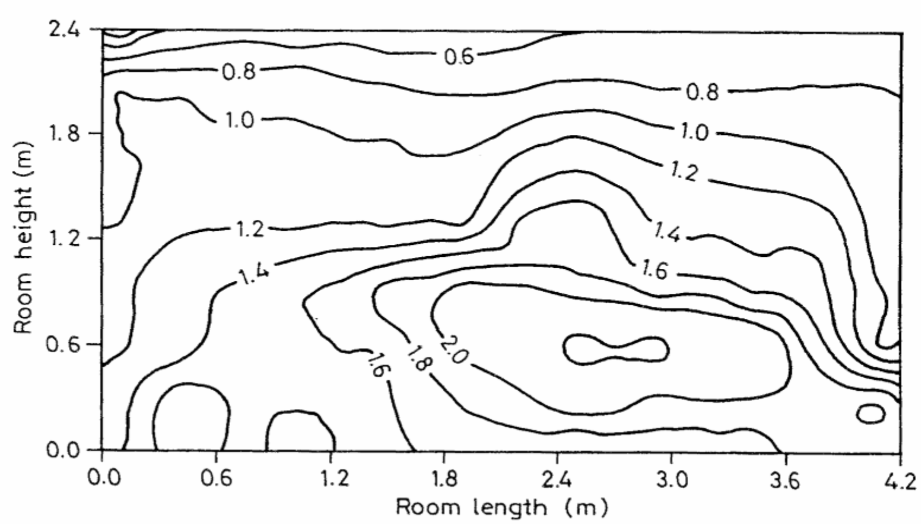

(c) Measurements

Fig. 5.25 Comparison of the measured and predicted relative CO_2 concentration contours using the RNG k-ε model with/without momentum source for the supply diffuser

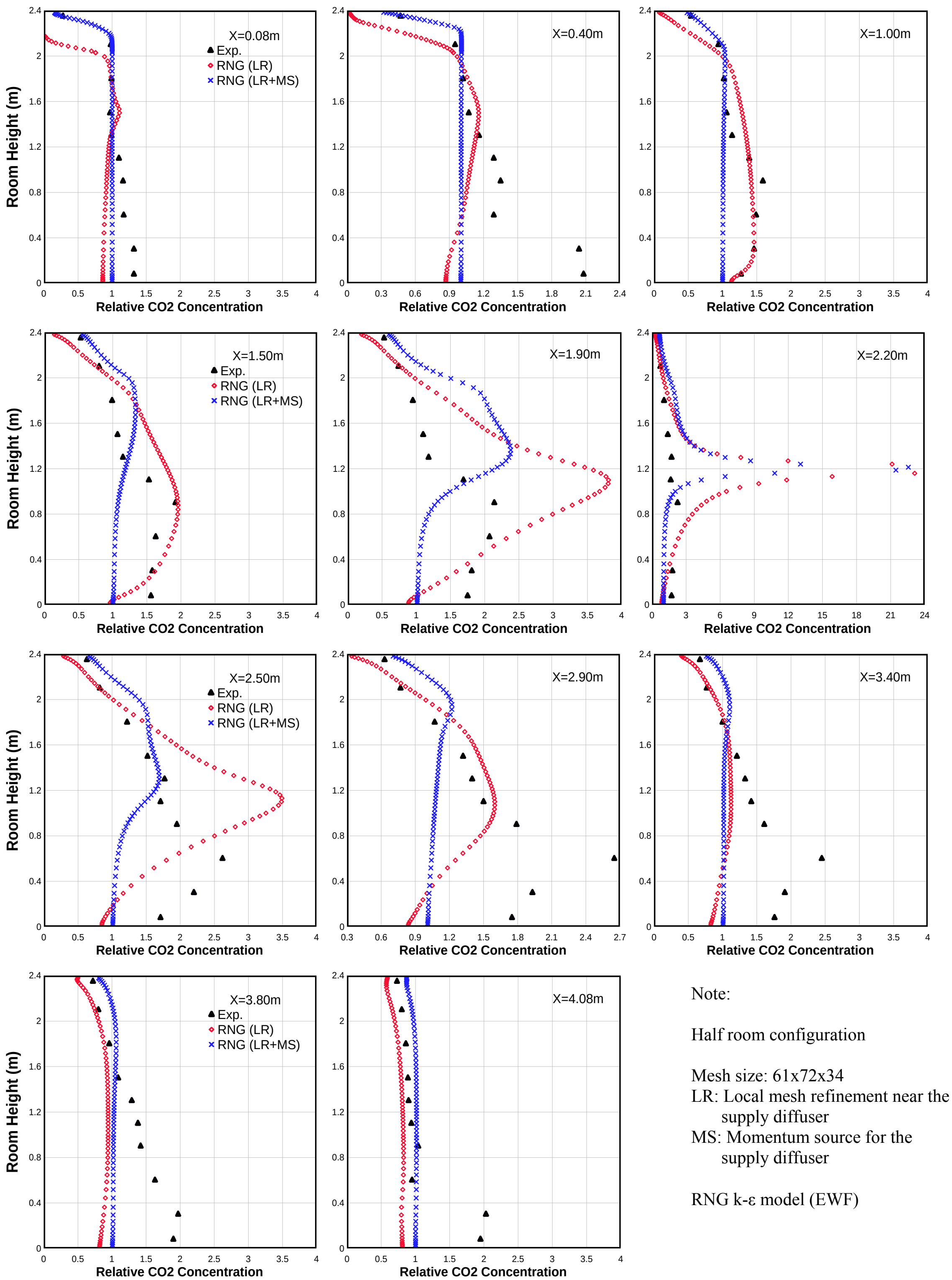

Note:

Half room configuration

Mesh size: 61x72x34
LR: Local mesh refinement near the supply diffuser
MS: Momentum source for the supply diffuser

RNG k-ε model (EWF)

Fig. 5.26 Comparison of the measured and predicted CO_2 concentration distribution using the RNG k-ε and with/without momentum source for the supply diffuser

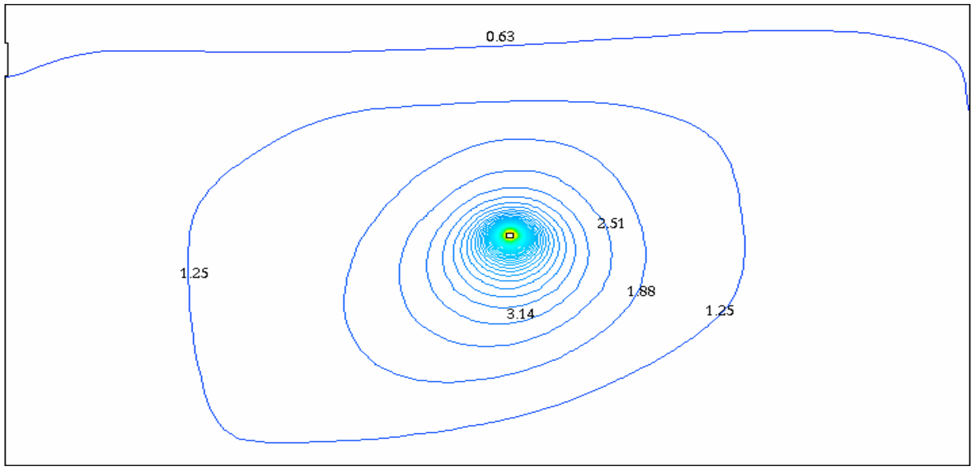

(a) Relative CO_2 concentration contours predicted with mesh grid (a) in Fig. 5.13

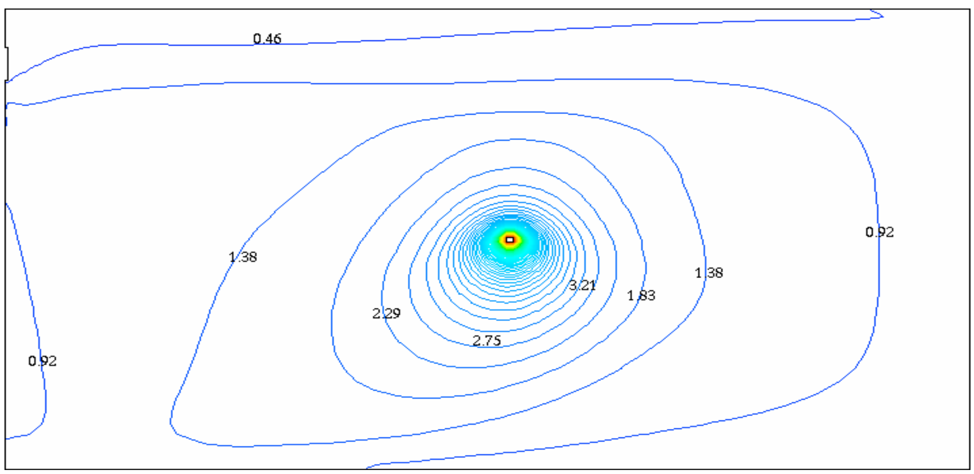

(b) Relative CO2 concentration contours predicted with mesh grid (b) in Fig. 5.13

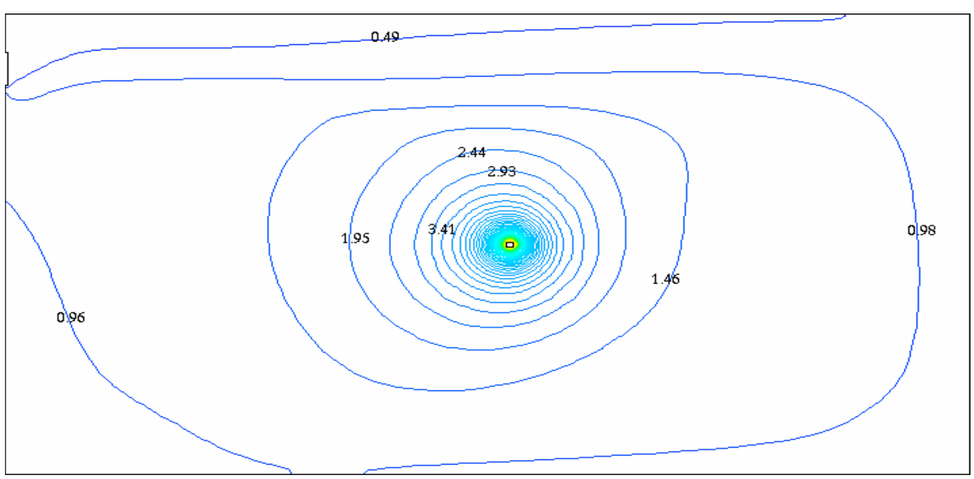

(c) Relative CO2 concentration contours predicted with mesh grid (c) in Fig. 5.13

Fig. 5.27 Comparison of the predicted relative CO_2 concentration contours using the RNG k-ε model and different local mesh refinements (with enhanced wall treatment. Initial mesh: 57x64x34)

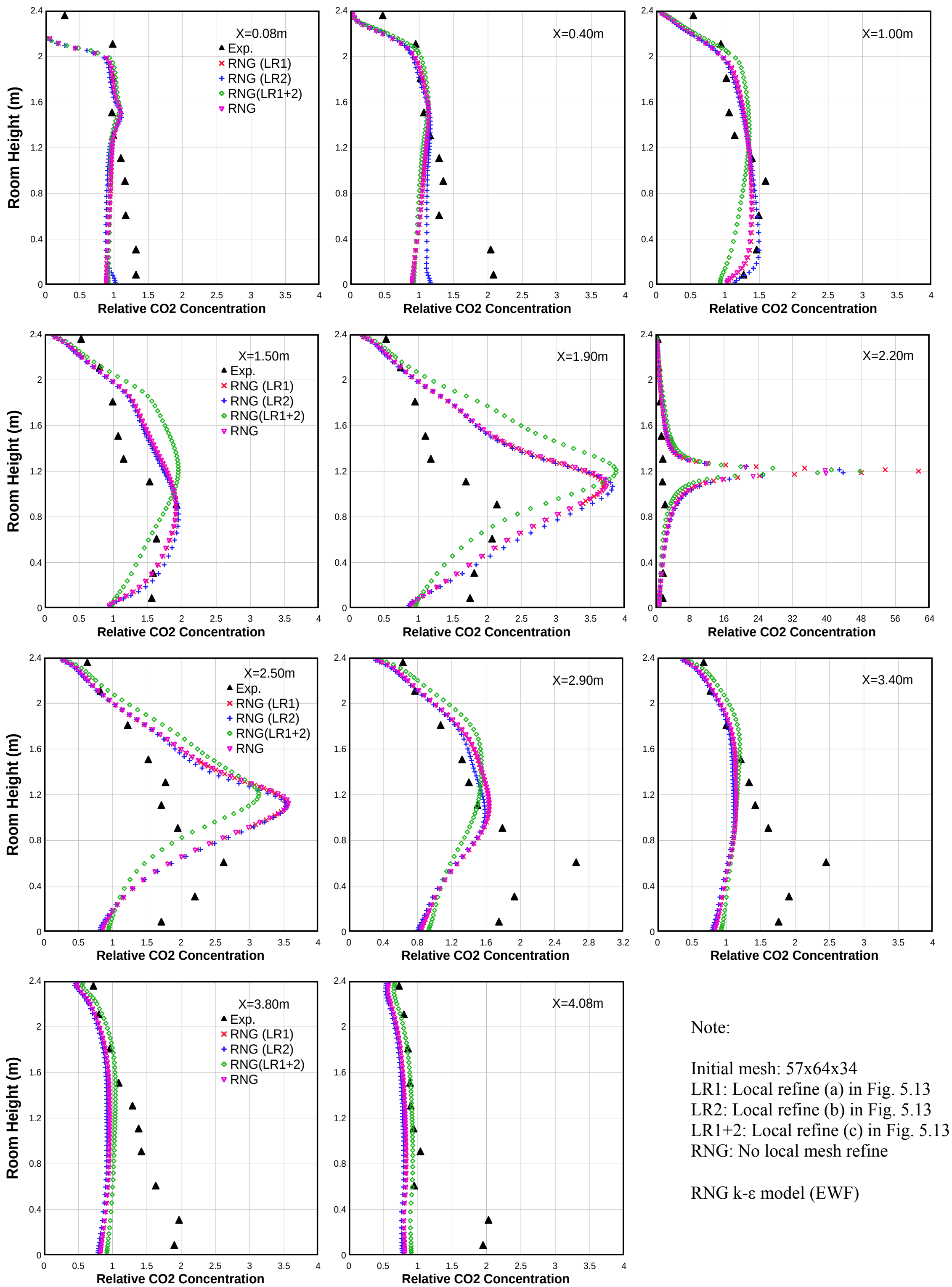

Note:

Initial mesh: 57x64x34
LR1: Local refine (a) in Fig. 5.13
LR2: Local refine (b) in Fig. 5.13
LR1+2: Local refine (c) in Fig. 5.13
RNG: No local mesh refine

RNG k-ε model (EWF)

Fig. 5.28 Comparison of the predicted CO_2 concentration distribution using different local mesh refinements and the RNG k-ε model with experiment data

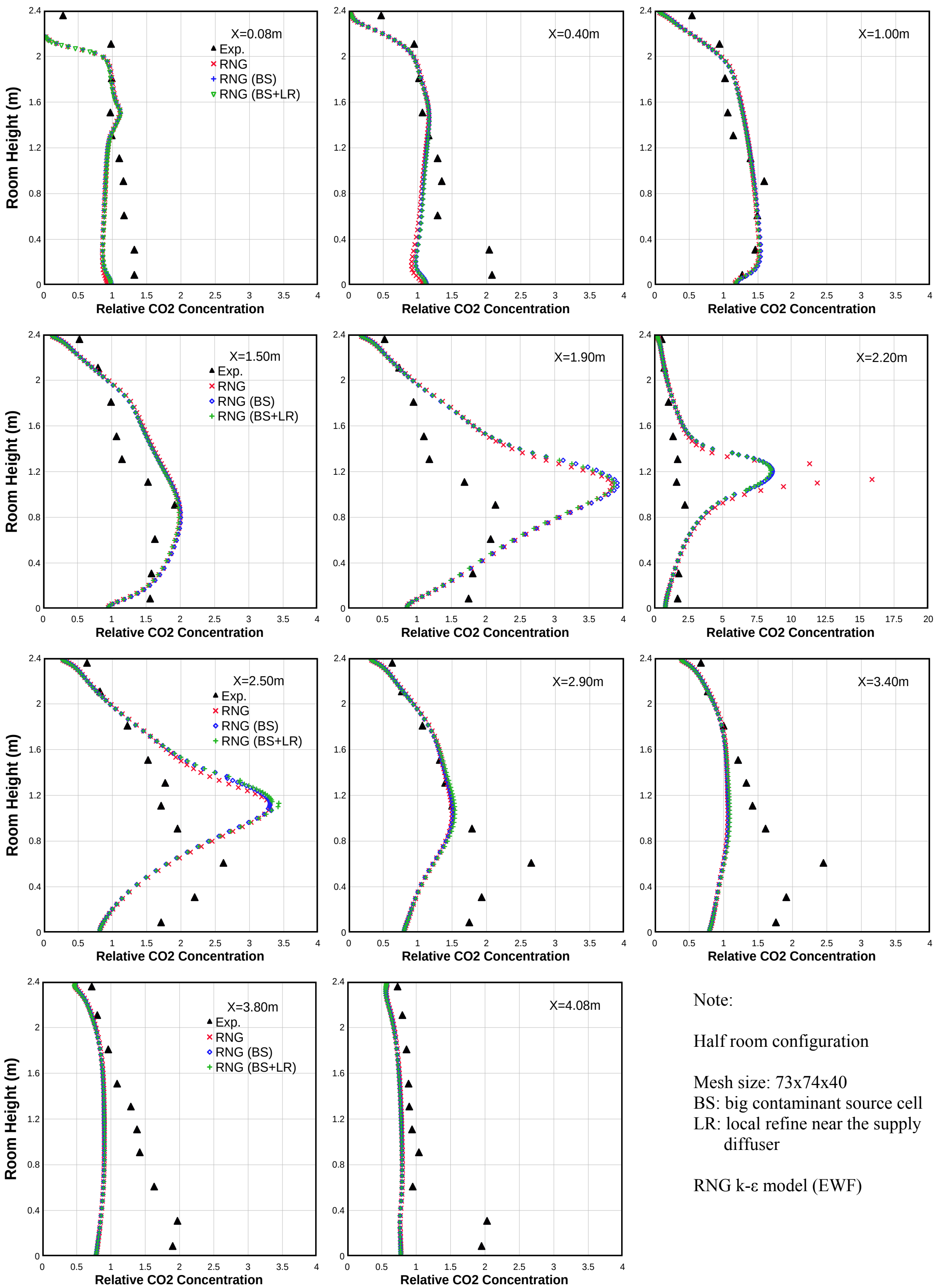

Fig. 5.29 Comparison of the predicted CO_2 concentration distribution at the symmetry plane with small and big contaminant sources cells and with the RNG k-ε model

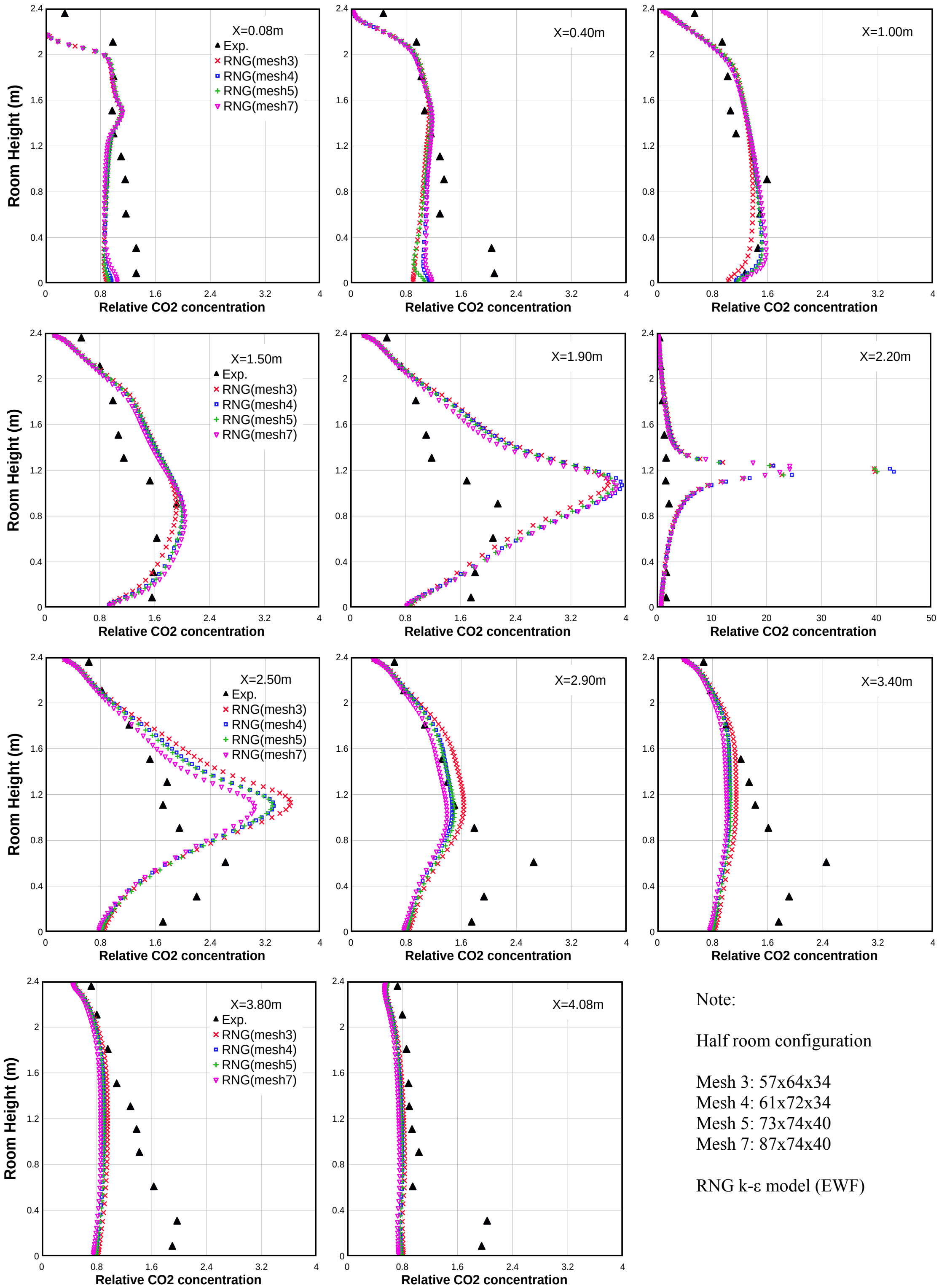

Fig. 5.30 Comparison of the predicted CO_2 concentration distribution at the symmetry plane using the RNG k-ε model and different mesh sizes

5.2.2.5 Test Case F3: contaminant transport with stable stratification

In Test Case F3, the contaminant mixture is much heavier than air, it tends to migrate to the lower part of the room and a stable stratification forms. The RNG k-ε model was tried first. As with the Test Case F1, this model predicts a very strong downward contaminant jet flow resulting in a high level of CO_2 concentration below the contaminant source. This phenomenon was observed with different mesh sizes and with half and full room configurations. The RSM model is very sensitive to the mesh size for this case: sometimes the CO_2 concentration in the lower part of the room is under-predicted; sometimes it is over-predicted, it is hard to obtain a grid independent and consistent result. The k-ω models always under-predict the CO_2 concentration in the lower part of the room, the standard version of this model under-predicts also the CO_2 concentration in the upper part of the room. The best simulation result was obtained with the standard k-ε model. Fig. 5.31 is a comparison of the measured and the predicted relative CO_2 concentration contours using the RNG and the standard k-ε models and a mesh grid of 57x64x34, Fig. 5.32 is a comparison of the predicted CO_2 concentration distribution using the RSM model and different mesh sizes, Fig. 5.33 is a comparison of the predicted CO_2 concentration distribution using the standard and the SST k-ω models with a mesh size of 73x74x40.

Local mesh refinements similar to those shown in Fig. 5.13 together with the standard k-ε model were tested: (a) local mesh refinement around the contaminant source (from X=1.9 ~ 2.5m, Y=0.7 ~ 1.4m, Z=0 ~ 0.3m); (b) local mesh refinement near the supply diffuser (X=0 ~ 1m, Y=2.03 ~ 2.4m, Z=0 ~ 0.3m); (c) local mesh refinement around the contaminant source and near the supply diffuser [(a)+(b)]. The predicted relative CO_2 concentration contours with these three mesh grids were compared in Fig. 5.34, a point-to-point comparison of the predicted results using these three locally refined meshes and also the original mesh (57x64x34) with experiment data is given in Fig. 5.35. It can be seen that the CO_2 concentrations at the upper part of the room are a little under-predicted, and the results from these four meshes are nearly the same. At the lower part of the room, the predicted CO_2 concentrations are a little higher than measured values when using locally refined mesh around the contaminant source, and they are a little lower than measurements when using locally refined mesh near the supply diffuser and locally refined mesh near the supply diffuser and around the contaminant source. The best result is from the original mesh (i.e. without local refinement).

The sensitivity of the predicted results to the mesh size was tested using three different meshes. Fig. 5.36 is a comparison of the predicted results from three different meshes using the standard k-ε model and local mesh refinement near the supply diffuser. It can be seen that the predicted results from the mesh grids 61x72x34 and 78x74x40 are nearly the same.

As has been done with the Test Cases F1 and F2, a big contaminant source (594 cells) with a mesh size of 73x74x40 was used to explore the influence of the contaminant source cell size on the predicted results. A comparison of the predicted CO_2 concentration distributions using this big contaminant source cell and a small contaminant source cell is given in Fig. 5.37. It can been seen that except at the section of X=2.20m, the predicted CO_2 concentration distributions from the small and big contaminant source cells have very little difference, again it demonstrated that the source cell size has only very limited local influence on the prediction results. Also the same modeling of the contaminant source including its initial momentum as shown in Fig. 5.11 was tested for this test case. In Fig. 5.38 the predicted results were compared with experimental data and also with the results from the same mesh but without considering the initial momentum of the contaminant source. For this test case, when the initial momentum of the contaminant source was included in the calculations, the CO_2 concentration in the lower part of the room is greatly over-predicted and the calculation becomes unstable.

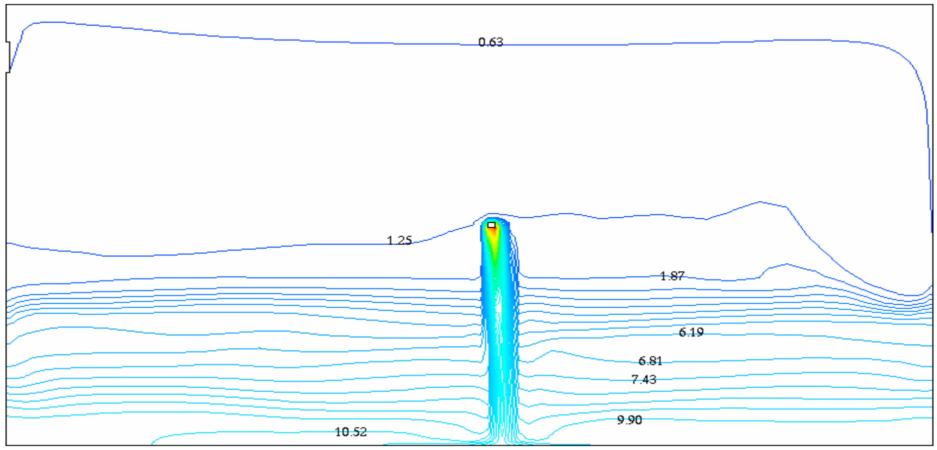

(a) Predicted relative CO_2 concentration using RNG k-ε model

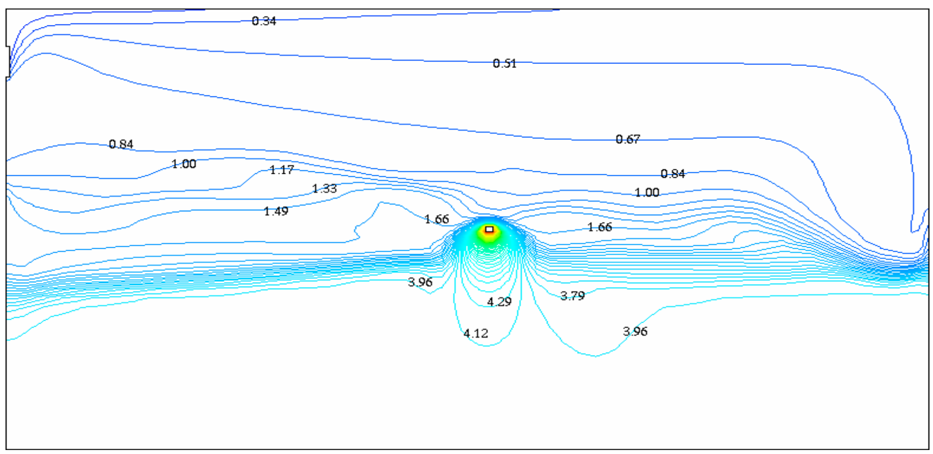

(b) Predicted relative CO_2 concentration using standard k-ε model

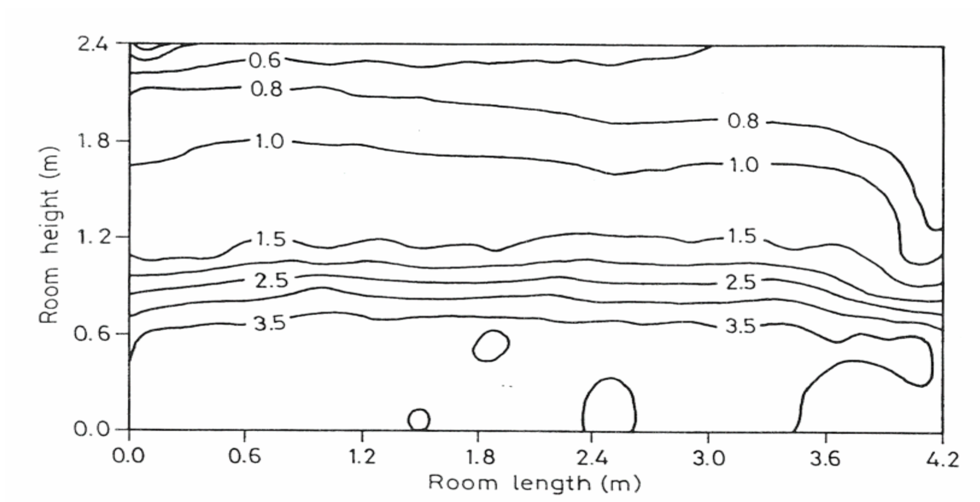

(c) Measured relative CO_2 concentration contours

Fig. 5.31 Comparison of the measured and the predicted relative CO_2 concentration contours on the symmetry plane using the standard and the RNG k-ε model (mesh size: 57x64x34)

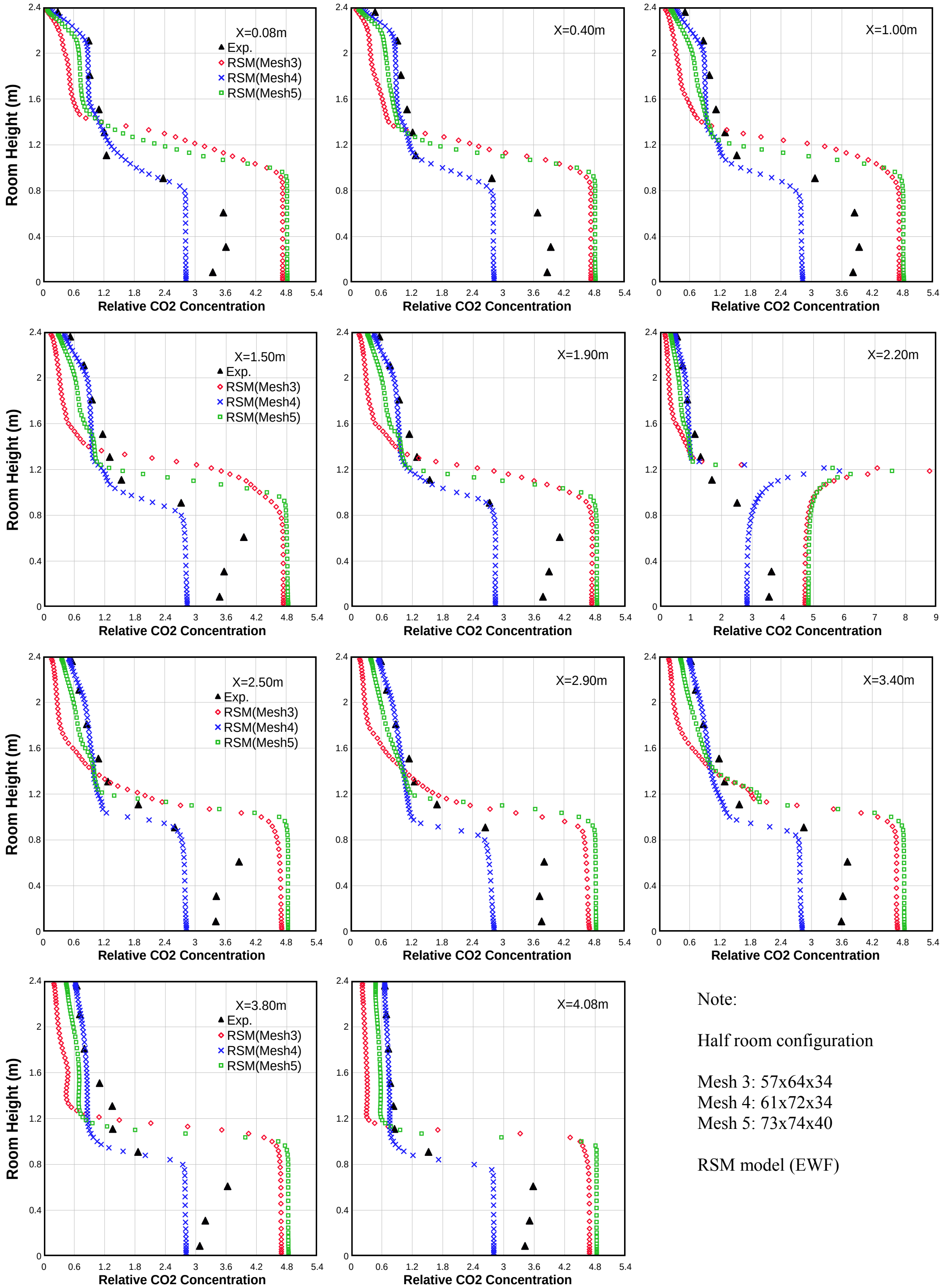

Fig. 5.32 Comparison of the predicted CO_2 concentration distribution using the RSM model and different mesh sizes

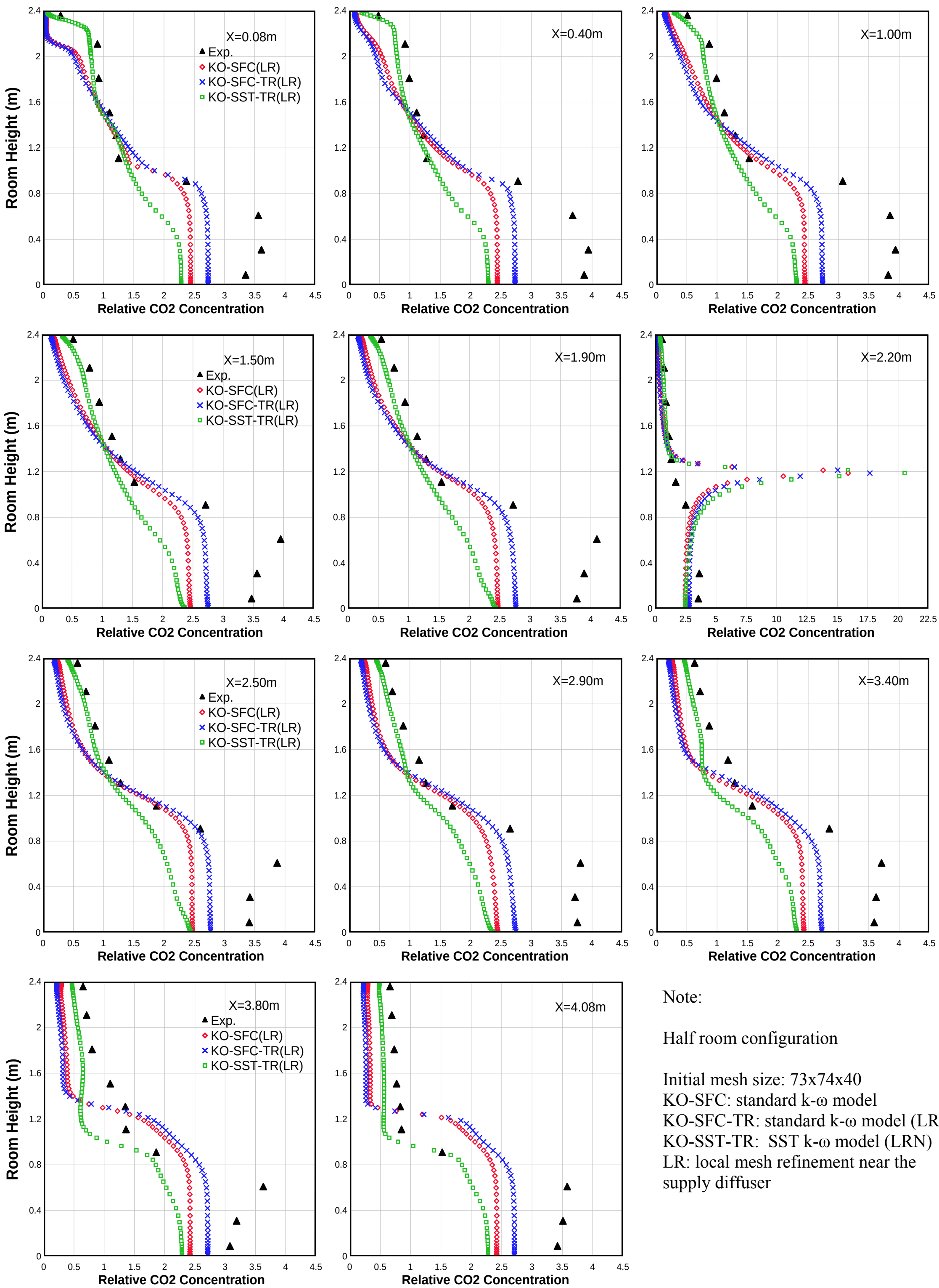

Note:

Half room configuration

Initial mesh size: 73x74x40
KO-SFC: standard k-ω model
KO-SFC-TR: standard k-ω model (LRN)
KO-SST-TR: SST k-ω model (LRN)
LR: local mesh refinement near the supply diffuser

Fig. 5.33 Comparison of the predicted CO_2 concentration distribution using the standard and the SST k-ω models

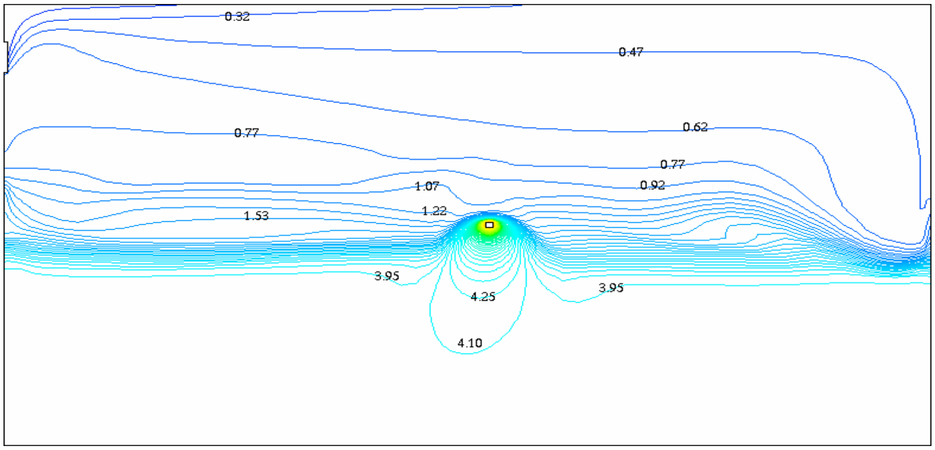

(a) Local refine around the contaminant source (X=1.9~2.5m, Y=0.7~1.4m, Z=0~0.3m)

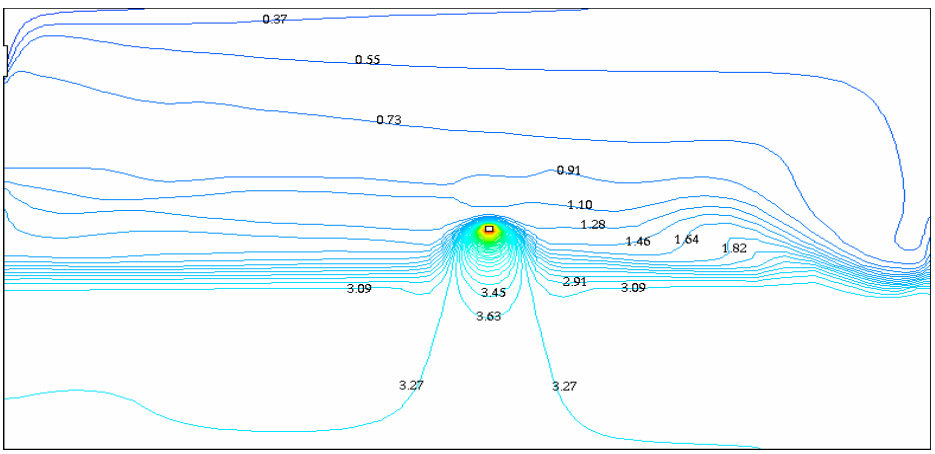

(b) Local refine near the supply diffuser (X=0~1m, Y=2.03~2.4m, Z=0~0.3m)

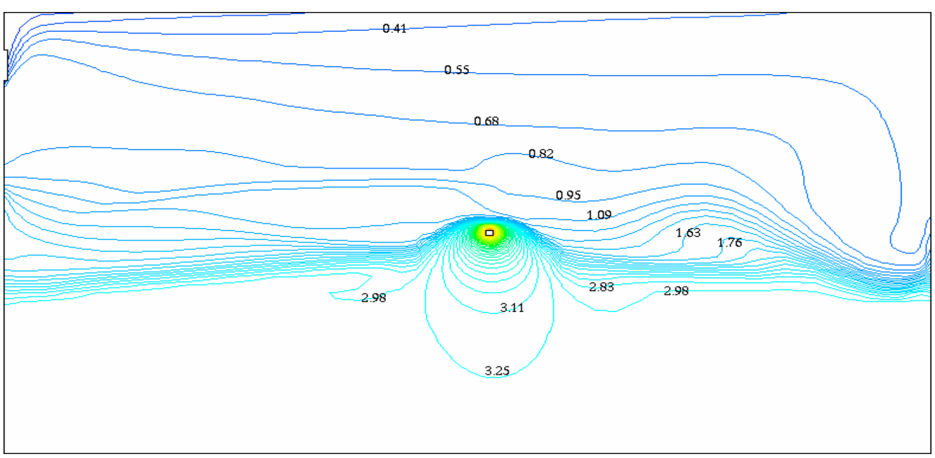

(c) Local refine near the supply diffuser and around the contaminant source [(a)+(b)]

Fig. 5.34 Comparison of the predicted relative CO_2 concentration contours using different local mesh refinements and the standard k-ε model

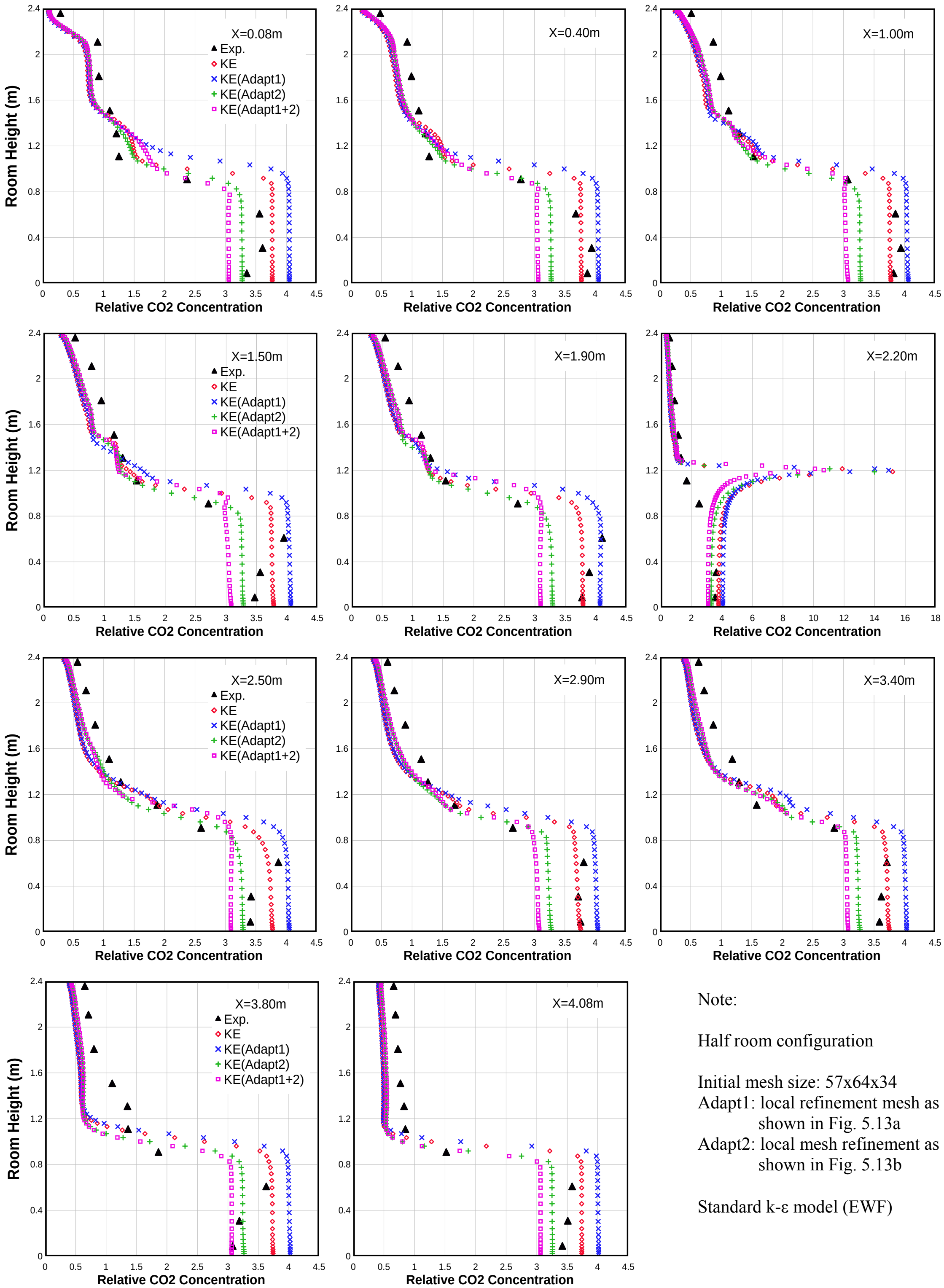

Fig. 5.35 Comparison of the predicted relative CO_2 concentration distribution using the standard k-ε model and different locally refined meshes

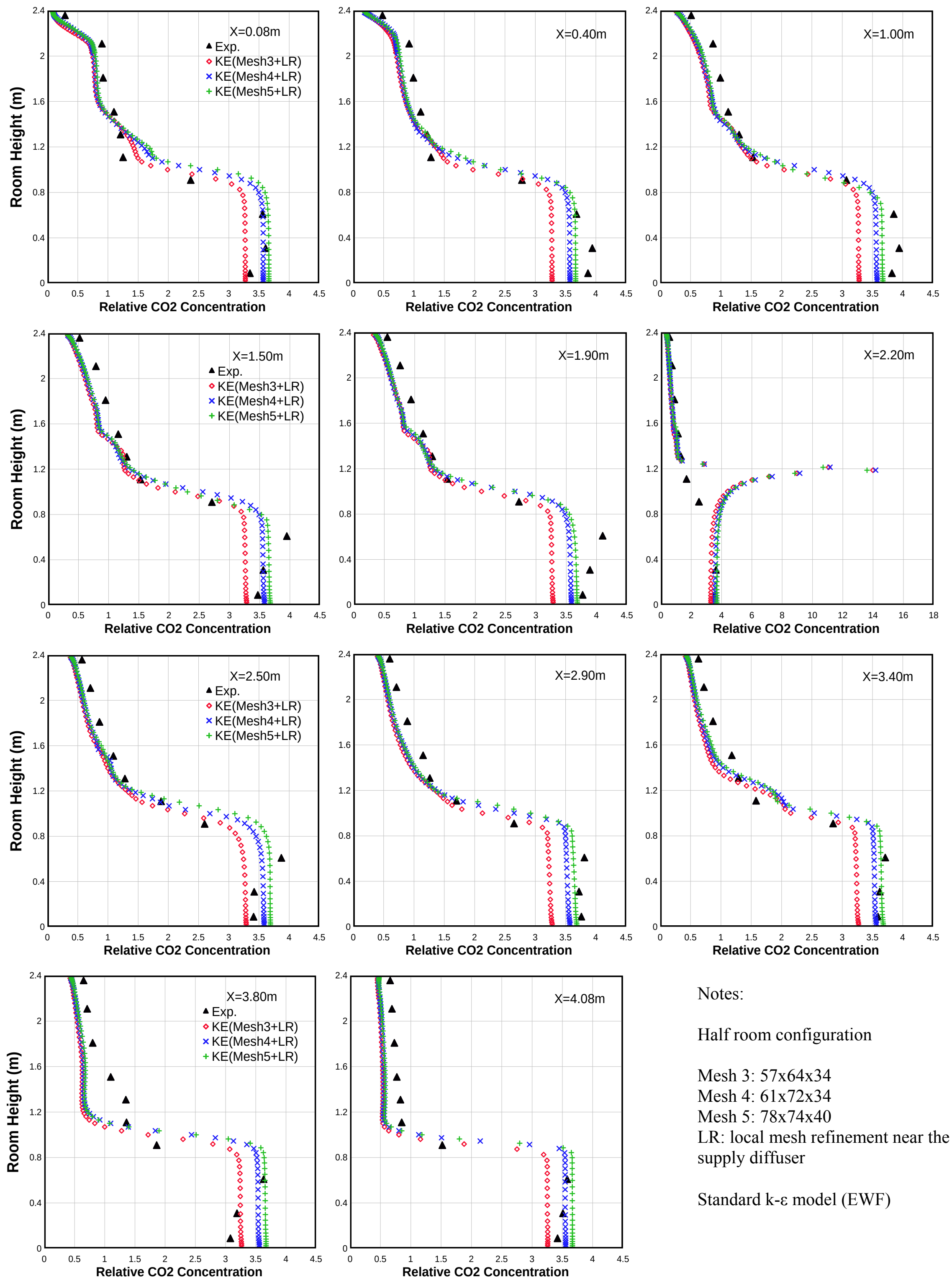

Fig. 5.36 Comparison of the predicted CO_2 concentration distribution using the standard k-ε model and local mesh refinement near the supply diffuser with different mesh sizes

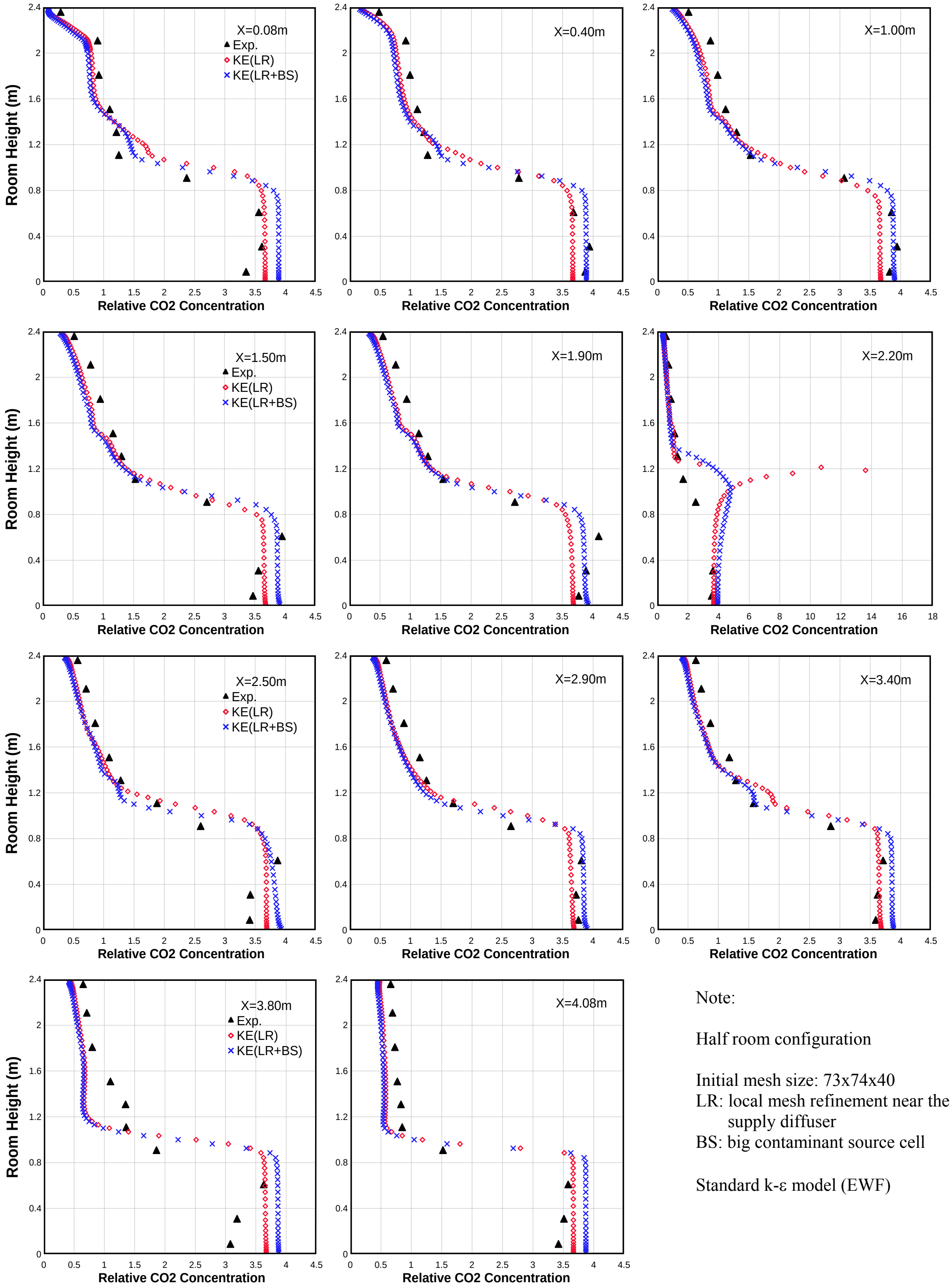

Fig. 5.37 Comparison of the predicted CO_2 concentration distribution using the standard k-ε model and small and big contaminant source cells

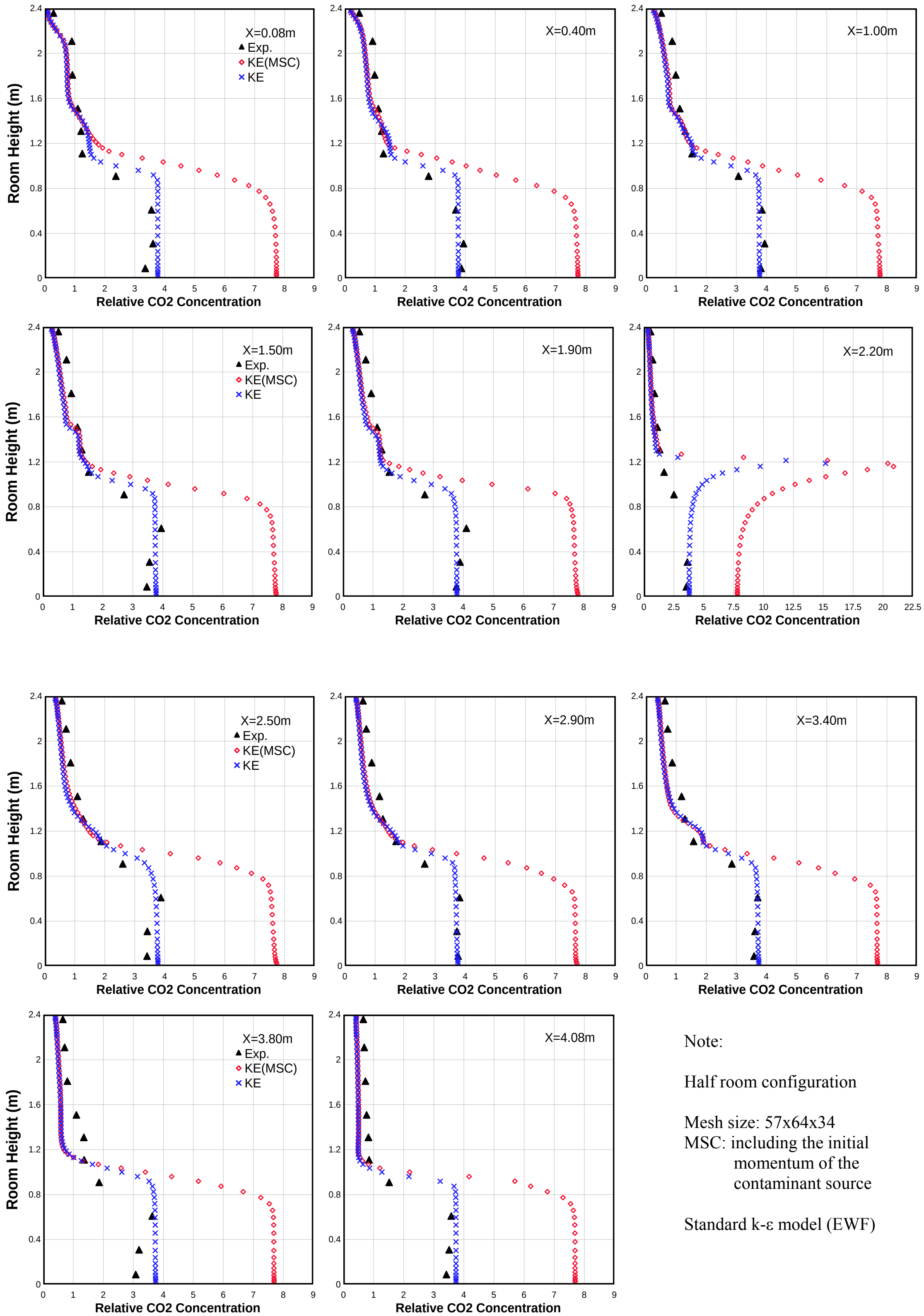

Fig. 5.38 Comparison of the predicted CO_2 concentration using the standard k-ε model and with/without the initial momentum of the contaminant source

5.2.3 Remarks

The above comparisons showed that for the Test Case F1, the RSM model and the standard k-ε model can give reasonable prediction for the CO_2 distribution on the symmetry plane of the test room compared with experimental data. But big discrepancies exist around the contaminant source. A possible reason is that the concentration variation is too high in this region. From equation 3.30, it can be seen that when $\partial\rho / \partial x_i > 0$, i.e., in the case of unstable stratification, the term $G_b > 0$, which acts as a turbulence production source in equation 3.25 and the turbulent kinetic energy tends to be augmented. In the experiment, the measured maximum standard deviation of relative CO_2 concentration at X=1.9m and X=2.9 section is about 24%, at X=2.2m and X=2.5m sections is about 29%, and at X=3.4m is about 21%, All of them are found at Y=0.9 ~ 1.5m region, which is at ±0.3 m range of the contaminant source (at Y=1.2m). Measurements were repeated at X=2.2 m and X=3.8m sections for this test case. A comparison of the measured mean relative CO_2 concentrations and their upper bound (UB) and lower bound (LB) values between the two experimental data sets is given in Fig. 5.39. It can be seen that at the section of X= 2.20m, big discrepancies exist between the two measured data sets, especially at the region of Y= 0.9 ~1.5m, where very large variations of CO_2 concentration exist too. At the section of X=3.8m, the difference between the two measured data sets is much smaller, and the fluctuations of CO_2 concentration are much smaller too. It is because of this reason that in the IEA Annex 20 practice, the validation approach by point-to-point comparison of simulation results with experiment data has been abandoned, the validation (or evaluation) was done mainly by the comparison of the characteristic key parameters such as the maximum air flow velocity and air temperature in the occupied zone and the global concentration contours etc. (Lemaire 1993). But from the above point-to-point comparisons for the Test Case F1, it can be seen that in regions where the turbulence level is not too high, the predictions using the RSM model and the standard k-ε model can yield reasonable results compared with experimental data. If the deviation of the measured results and experiment uncertainty are considered, even the peak CO_2 concentration at X=1.9m section which is outside of the measured value as shown in Fig. 5.10 is acceptable because it is still in the range of the upper bound value at that region, and we can then see that the RSM model can give good enough prediction results even without using local mesh refinement near the supply diffuser — comparing the predicted and the measured CO_2 concentration contours shown in Fig. 5.9b and Fig. 5.9c, it can be seen that except in the region near the contaminant source, the predicted CO_2 concentrations in the other part of the test room correspond enough well to the measured values.

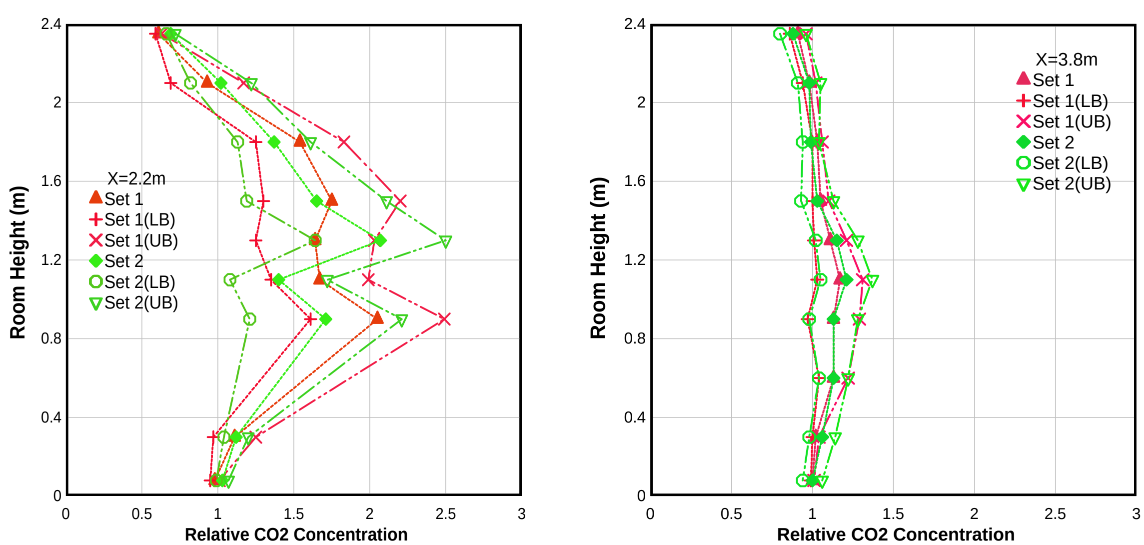

Fig. 5.39 Comparison of two sets of experimental data at X=2.2m and X=3.8m for the Test Case F1

In the IEA Annex 20 practice, it was found that the turbulence quantities are often under-predicted by the turbulence models, even for the simple 2D cases (Lemaire 1993) as has also been shown in §4.1. In the studies on turbulence models for predicting indoor air flows, Chen (1995, 1996) has also found that the prediction of the mean velocity is more accurate than that of the turbulent velocity. Markatos (1986) indicated that it is the fluctuating velocity field that drives the fluctuating scalar field, the effect of the latter on the former being usually negligible. Thus if the turbulent velocity can not be well predicted by the turbulence models, it is a direct consequence that the contaminant concentration will not be well predicted. Because the turbulence models often under-predict the turbulence velocity as has shown in Figs. 4.36, 4.37 and 4.48, it can explain why the CO_2 concentration near the contaminant source is under-predicted for the Test Case F1.

For the Test Case F2, the CO_2 distribution is purely determined by the interaction of the convection and the diffusion processes, thus the accurate prediction of the flow field is a prerequisite for the accurate prediction of the CO_2 distribution. Although the RNG k-ε model can predict very well the streamwise velocity profiles in the wall jet flow as shown in Fig. 4.50, the predicted spanwise and crosswise velocity profiles are much less satisfactory compared with experiment measurements, thus the spatial development of the 3D wall jet is not well predicted which influences further the accurate prediction of the CO_2 distribution in the room. The box method and the prescribed velocity method using predicted X velocity profiles by the RNG k-ε model have been tried together with other turbulence models (the standard k-ε model and the k-ω models), no improvement for the prediction has been found. The result obtained with the RNG k-ε model as shown in Fig. 5.28 and Fig. 5.29 is the only reasonable result compared with experimental data, all the other models cannot give a consistent prediction result. From Fig. 5.30 it can be seen that this case is less sensitive to the mesh grid used.

For the Test Case F3, the term G_b in equation 3.25 is negative, it acts as a sink for the turbulent kinetic energy which tends to damp the turbulence level in the region near the contaminant source. In the calculations, it was always observed that at some point of calculation, the residual for the continuity equation increases suddenly and rapidly, a very small under-relaxation factor (less than 0.1) for the momentum should be used, otherwise the contaminant will burst out towards the floor, resulting in a strong downward jet flow similar to that shown in Fig. 5.31a, leading to a very high level of CO_2 concentration in the lower part of the room. It may be an indication of a local transition or re-laminarization flow in that region. Only the standard k-ε model can give reasonable prediction results and the under-relaxation factors should be carefully adjusted to assure convergence in the course of calculations. The prescribed velocity method and the box method using the calculated X velocity profiles from the RNG k-ε model were also tested for this case, no improvement for prediction was observed.

Many authors have discussed the significance of the empirical coefficient $C_{3\varepsilon}$ in the ε equation 3.26. In the literature, values from 0 to 1 have been used by different authors. Rodi (1979) has suggested that the coefficient is close to 1 in vertical boundary layers and close to 0 in horizontal boundary layers. An approximation that satisfies both limits is that shown in equation 3.32 which has been used by Henkes et al. (1991) and is adopted in FLUENT. But some authors argued also that the effect of buoyancy on the dissipation rate is insignificant and can be safely omitted (Markatos et al. 1982, Holzbecher et al. 1995). In the present study, it was also observed that there is nearly no difference between the predicted results by using $C_{3\varepsilon}$ as that shown in equation 3.32 and by simply using $C_{3\varepsilon}$=0 for the three test cases. It was found also when the formulation $C_{3\varepsilon} = \tanh|v/u|$ is used, the calculation becomes less stable, but no improvement for prediction was observed. Thus all the above presented results were obtained by assuming $C_{3\varepsilon}$=0.

Chapter 6

3D Ventilation Flows with Coupled Heat and Mass Transfer

In this chapter, two 3D ventilation test cases with complicated internal configuration and simultaneous heat and mass (SF6) transfer are studied: displacement ventilation (buoyancy-driven) and ceiling slot ventilation (forced convection). The later case is studied under normal-g and zero-g conditions to compare the difference of temperature and contaminant (SF6) distributions under these two conditions.

In Chapter 5, two 3D ventilation test cases with coupled heat or mass transfer are studied. It can be seen that numerical simulation is capable of yielding reasonable prediction of ventilation flows with coupled heat or mass transfer, although with reduced reliability as compared with the isothermal cases which has also been noted in the IEA Annex 20 project. In this chapter, two ventilation test cases with simultaneous heat and mass transfer and with complicated internal configuration are studied to further evaluate the capability of numerical simulation for the prediction of practical ventilation flows, because ventilation flows in real life are almost always coupled with heat and mass transfer and with complicated configurations. Two typical ventilation flow cases are considered: displacement ventilation and ceiling slot ventilation in summer cooling condition. In the former case, the ventilation flow is mainly driven by buoyancy created by the temperature differences between the supplied air and the internal heat sources; in the latter case the air flow is driven by forced convection which has more relevance to the ventilation flow in a spacecraft cabin. The two test cases are taken from a recent report ASHRAE RP-1009 "Simplified Diffuser Boundary Conditions for Numerical Room Airflow Models" (Chen et al. 2001), both test cases have the same internal configuration including two human simulators, two computers, two cabinets, two tables (for PC) and four fluorescent lamps. The differences between the two test cases are the type and position of the inlet diffuser and the outlet, and the ventilation rate.

6.1 Experiment setup of the test chamber

Experiments were carried out in an environment test chamber of the dimensions of 5.16m x 3.65m x 2.43m (length x width x height). The layout of the test room and the coordinate axes are shown in Fig. 6.1.

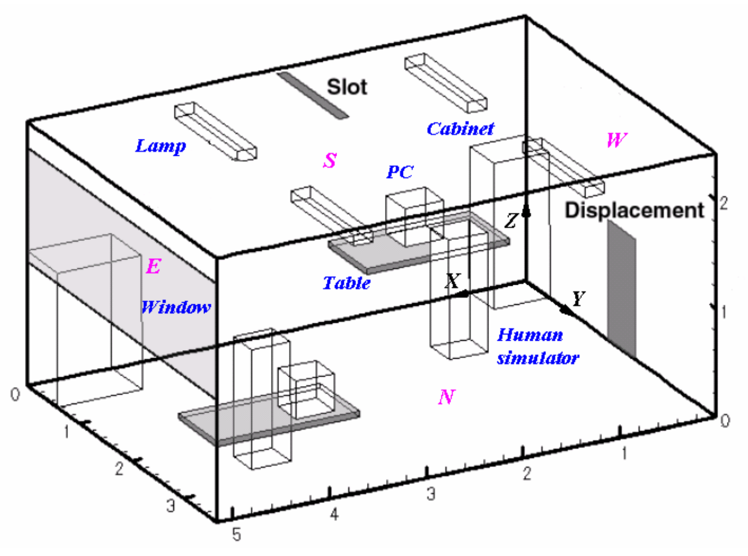

Fig. 6.1 The notation of the test room walls and the layout of the test room
(Chen et al. 2001)

The dimensions of the internal objects (human simulators, computers, tables, lamps and cabinets) and their positions as well as heat generating rates are presented in Table 6.1.

Table 6.1 Configuration of the test chamber (Chen et al. 2001)

	Size			Location			Heat
	ΔX [m]	ΔY [m]	ΔZ [m]	X [m]	Y [m]	Z [m]	Q [W]
Room	5.16	3.65	2.43	0.0	0.0	0.0	-
Window	0.00	3.65	1.16	5.16	0.0	0.94	-
Person 1	0.4	0.35	1.1	1.1	0.95	0.0	75
Person 2	0.4	0.35	1.1	3.90	2.40	0.0	75
Computer1	0.4	0.35	0.35	1.1	0.1	0.75	108
Computer2	0.4	0.35	0.35	3.90	3.2	0.75	173
Table 1	1.47	0.75	0.01	0.58	0.0	0.74	-
Table 2	1.47	0.75	0.01	3.69	2.90	0.74	-
Lamp 1	0.2	1.2	0.15	1.03	0.16	2.18	34
Lamp 2	0.2	1.2	0.15	3.61	0.16	2.18	34
Lamp 3	0.2	1.2	0.15	2.33	2.29	2.18	34
Lamp 4	0.2	1.2	0.15	3.61	2.29	2.18	34
Cabinet 1	0.58	0.33	1.32	0.0	0.0	0.0	-
Cabinet 2	0.95	0.58	1.24	4.21	0.0	0.0	-

Note:

(1) ΔX, ΔY, and ΔZ are dimensions of an object in X, Y and Z directions

(2) Heat generated includes radiation and convection

6.2 Displacement ventilation

6.2.1 Test conditions

The displacement ventilation test case was carried out under a ventilation rate of 5ACH. The inlet diffuser is located near the west wall and the exhaust opening is at the center of the ceiling as shown in Fig. 6.2. The size and position of the inlet and outlet diffusers are listed in Table 6.2.

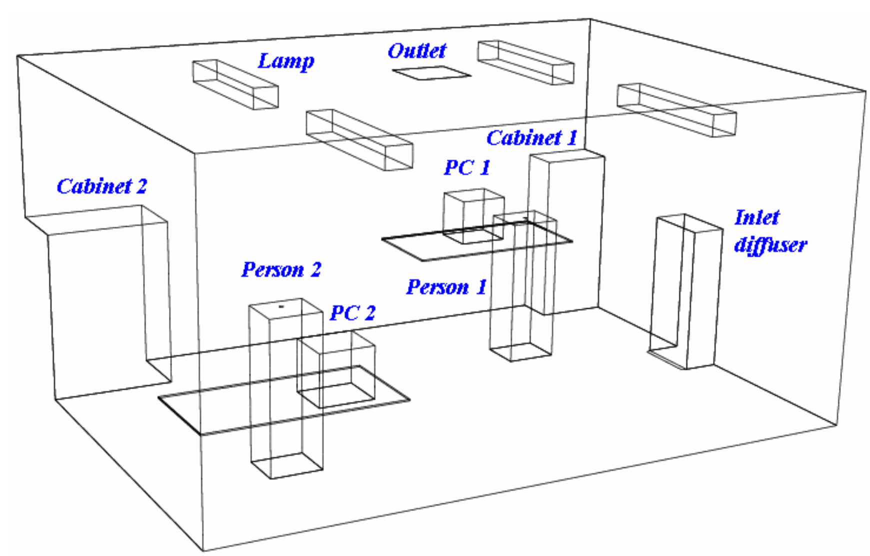

Fig. 6.2 Configuration of the displacement ventilation test case

Table 6.2 Size and position of the displacement and exhaust diffusers (Chen et al. 2001)

	Size			Location			Temp.
	ΔX [m]	ΔY [m]	ΔZ [m]	X [m]	Y [m]	Z [m]	T [^oC]
Supply	0.28	0.53	1.1	0.28	1.56	0.03	13.0
Exhaust	0.43	0.43	0.0	2.365	1.61	2.43	22.2

A tracer gas (SF6) source was added at the center of the top surface of each human simulator to simulate the breathing process; and it is continuously introduced at a flow rate of 0.1331 l/h. The position of the tracer gas sources and the tracer gas concentration at the inlet and outlet are as follows:

Tracer-gas source 1: 0.1331 l/h at (x, y, z) = (1.3, 1.12, 1.1)
Tracer-gas source 2: 0.1331 l/h at (x, y, z) = (4.1, 2.52, 1.1)
Supply concentration: 0.0449 ppm
Exhaust concentration: 1.0078 ppm

In the experiment, the inlet diffuser is 0.03m above the floor, because it is difficult to create computation mesh with such a small gap--it is thus ignored in the simulation, i.e., the inlet diffuser is considered to be directly on the floor. The wall temperatures are continuously monitored at five points on the south wall (S wall in Fig. 6.1) and east wall (E wall in Fig. 6.1), two points on the north wall (N wall in Fig. 6.1) and one point on the west wall (W wall in Fig. 6.1) using thermocouples. The positions of the measuring points and the measured temperatures on the walls are given below:

South wall temperature (X=2.58m, Y=0m)

Z [m]	0.1	0.6	1.1	1.8	2.38
T [^oC]	19.638	20.174	20.995	21.665	21.133

East wall & window temperature (X=5.16 m, Y=1.83 m)

Z [m]	0.1	0.6	1.1	1.8	2.38
T [^oC]	20.267	20.602	24.471	25.741	23.868

North wall temperature (X=2.58 m, Y= 3.65 m)

Z [m]	1.1	1.8
T [^oC]	21.076	21.727

West wall temperature (X= 0m, Y=1.83 m)

Z [m]	1.8
T [^oC]	20.990

Air velocity and temperature at chosen points were monitored using omni-directional hot-sphere anemometers. The repeatability of the velocity measurements is 0.01m/s (about ±2% of the readings). The SF6 concentration was measured using a gas analyzer based on a photoacoustic infrared detection method. The hot-sphere anemometers are attached to movable poles. Each of the five poles supports six anemometers that measure air velocities and temperatures in 30 points simultaneously. Additionally, two thermocouples are affixed to the poles to measure air temperatures near the floor and ceiling. The data were collected in one plane (Y=1.825m) through the entire chamber as well as close to the diffusers. The positions of the five poles carrying the anemometers and tracer gas sampling tubes for the measurements are shown in Fig. 6.3.

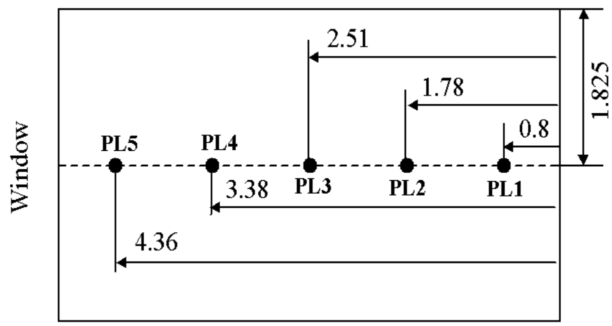

Fig. 6.3 The positions of the measuring poles for the displacement ventilation test case (Chen et al. 2001)

The measurements were conducted under steady-state conditions by stabilizing the room thermal and fluid conditions for more than 12 hours before recording the data.

6.2.2 Modeling and simulation

6.2.2.1 Boundary conditions

Inlet diffuser:

In the experiment, the supply air was discharged horizontally from the front surface of the diffuser, this corresponds to a discharge velocity of 0.11m/s. Because the front surface of the inlet diffuser is covered with a perforated metal sheet, the actual flow area is less than the gross area of the surface and the actual discharge velocity from the diffuser is 0.35m/s. To assure the correct supply of the momentum flow from the diffuser, the diffuser is modeled using the momentum method introduced in chapter 4, i.e., a momentum source is added to a volume adjacent to the diffuser. The momentum method works well for the displacement diffuser which has been validated by Chen et al. (2001). At the front surface of the diffuser, a mass flow rate of 0.0768kg/s and a turbulence intensity of 4% are specified. The turbulence quantities (k, ε or ω) at the inlet are calculated using equations 4.4~4.6. The inlet air temperature is 13°C and the SF6 concentration is 0.0449 ppm.

Outlet:

The outlet is specified as pressure outlet, i.e., the gauge pressure at the outlet is specified as zero.

Tracer gas sources:

The tracer gas sources are modeled as momentumless volumetric mass source and are added to one or two grid cells centered at (1.3, 1.12, 1.1) and (4.1, 2.52; 1.1), respectively. As has been shown in Chapter 5, the initial momentum of the trace gas source and the volume of the tracer gas source cells have little influence on the global distribution of tracer gas.

Thermal conditions:

Temperature or heat flux at the walls is used to specify the thermal conditions for different objects in the flow field:

The thermal conditions of the following objects are specified as heat flux:

- Computer 1: 171.43 W/m^2
- Computer 2: 274.6 W/m^2

- Human simulators: 41.9 W/m^2
- Lamps: 37.78 W/m^2

The average of the measured temperatures at the walls is used to specify the thermal condition for the walls:

- Ceiling: 295 K (22°C)
- Floor: 292 K (19°C)
- Inlet wall (West wall): 294 K (21°C)
- Front wall (East Wall): 296 K (23°C)
- Side walls (South and North walls): 294 K (21°C)
- Table 1: 293 K (20°C)
- Table 2: 294 K (21°C)
- Diffuser wall: 290K (17°C)

6.2.2.2 Turbulence modeling

In Chapter 5, it has been shown that the RNG and the Realizable k-ε models and the SST k-ω model can give reasonable prediction for ventilation flows coupled with heat transfer, these models are further evaluated in this test case.

6.2.2.3 Computation meshes

Because there are many flow obstacles in the flow field, using a structured mesh will result in lots of unnecessary mesh cells in the regions far from the walls, so an unstructured mesh is used instead. Several different mesh sizes are tested, it is found that different mesh resolutions influence mainly the predicted tracer gas profiles and have very little influence on the predicted velocity and temperature profiles. After some tests, a mesh size of 373240 cells is chosen as the main computation mesh which represents a good compromise between mesh resolution requirements and the available computational resources.

6.2.2.4 Numerical schemes

The convection terms are discretized using the second-order upwind scheme, and the second-order central differencing scheme is used for the discretization of the diffusion terms. For the discretization of pressure, the PRESTO! (PREssure STaggering Option) scheme is used. The SIMPLEC scheme is used for the pressure-velocity coupling. When working with unstructured meshes, a high-order scheme is preferred for the discretization of convection terms to minimize the discretization errors. The QUICK scheme is tested but the calculation is not stable, so the second-order upwind scheme is used instead.

6.2.2.5 Simulation results

In Figs. 6.4, 6.5 and 6.6, a comparison of the predicted velocity (mean air speed, corrected using equations 4.7 and 4.8), temperature and SF6 concentration profiles using SST k-ω model with experiment measurements is given, respectively. It can be seen that the predicted mean air speed, temperature and SF6 concentration profiles correspond reasonably well with those of measurements. The predicted temperatures have some discrepancies with measured data near ceiling and floor, this may be a consequence of the imposed thermal boundary conditions at the ceiling and the floor: in the experiment, the measured temperature near the diffuser (17.42°C at X=0.8m) has 3°C difference with the temperature near the front wall (20.43°C at X=4.36m) at the floor, by imposing an averaged temperature (19.14°C) at the floor will create a stronger thermal plume near the diffuser which will draw more cooled air into the region thus the predicted temperature is lower than the measured value. In the middle of the floor (at X=2.51m to X=3.38m), the imposed temperature is near to the measured values (19.55°C at X=2.51m and 19.85 at X=3.38m), thus the predicted temperatures at this region are very close to the measured ones. Another influence may come from the fact that in the experiment, the inlet diffuser is 0.03m above the floor but in the simulation, the diffuser is considered directly on the floor, thus cooled air is supplied directly to the floor region, which results in an under-prediction of temperature near the floor area. From Fig. 6.5, it can be seen that the predicted temperatures near the floor are generally lower than the measured ones. At the ceiling region, the imposed averaged temperature is higher than measured temperature near the inlet wall (west wall) which enhances the heat exchange between the ceiling and the air in that region, thus the predicted air temperature is higher than measured value in this region. Despite the discrepancies, the vertical temperature gradient in the middle of the room is well predicted, which is an important parameter influencing thermal comfort for displacement ventilation.

In Figs. 6.4~6.6, a comparison of the predicted velocity, temperature and SF6 concentration profiles with experimental data using successive mesh adaptation according to Y^+ value near walls is also given, it can be seen that the mesh adaptation influences mainly the predicted SF6 concentration profiles, its influences on the predicted velocity profiles and temperature profiles are very small, this is also the case with different mesh resolutions. Tests have been done with mesh sizes of 293874, 353620 and 373240 cells, the predicted velocity and temperature profiles change very little with these different mesh sizes, only the predicted SF6 concentration profiles change as the mesh resolution changes. It seems that the mass transport is more linked to the microscopic fluid motion than the other scalars such as temperature, etc. It can be shown that by successive mesh adaptation, the predicted maximum velocity and temperature in the flow field don't have much changes, but the predicted average velocity in the flow field increases as the mesh resolution increases, for example, in Fig. 6.4 the predicted average mean air speed is 0.0821m/s with the original mesh (375144 cells), 0.1055 m/s with the mesh of Adapt1 (454573 cells) and 0.1058 m/s with the mesh of Adapt2 (455868 cells), while the predicted maximum mean air speed is 0.5244 m/s, 0.5270 m/s and 0.5265 m/s, respectively.

The RNG k-ε model and the Realizable k-ε can give reasonable prediction of the velocity and temperature profiles, but for the SF6 concentrations profiles, the predicted results are less satisfactory. Figs. 6.7~6.9 give a comparison of the predicted velocity (mean air speed, corrected using equations 4.7 and 4.8), temperature and SF6 concentration profiles using the two k-ε models and the SST k-ω model with experiment measurements. The enhanced wall treatment is used when working with the two k-ε models. It can be seen that the three turbulence models predict reasonably well the mean air speed and temperature profiles at the five measuring poles, the SST model predicts best the velocity profiles in the floor region. Both of the k-ε models tend to over-predict the SF6 concentration near the front wall (X=3.38m and 4.36m) -- this has been repeatedly observed with different mesh resolutions. In total, the SST k-ω gives the best overall prediction for this test case.

Figs. 6.10~6.13 give some examples of the predicted flow field, temperature and SF6 concentration distribution in the test room. Fig. 6.10 clearly shows that the supplied air forms a gravity current on the floor; when it reaches near the front wall (east wall), an upward plume forms because of thermal buoyancy which creates a recirculation flow in the floor region. From Fig. 6.11, it can be seen that a stable vertical temperature stratification forms in the room, and the entrainment of SF6 from the sources to the ceiling region by the upward thermal plumes can be seen from Fig. 6.12. In Fig. 6.13, the strong upward thermal plumes arising from the computer simulators are clearly seen, it can be seen also that some recirculation flows form around the top of the human simulators.

To better appreciate the effect of velocity correction using the formula developed by Koskela et al. (2001, 2002), a comparison of the predicted mean velocity magnitude and mean air speed with measured data is given in Fig. 6.14. It can be seen that the corrected velocity profiles (mean air speed) correspond better with experiment measurements, and the effect of correction is more significant in the regions where the air flow is slow (X=3.38m and 4.36m), because the hot-sphere anemometers have difficulty to accurately measure the slow air flow speed in these regions due to self-heating.

6.2.2.6 Remarks

It can be concluded that the numerical simulation with the SST k-ω model can predict the displacement ventilation flows with reasonable accuracy both qualitatively and quantitatively. The correction formula developed by Koskela et al. (2001, 2002) works also for the non-isothermal ventilation flows.

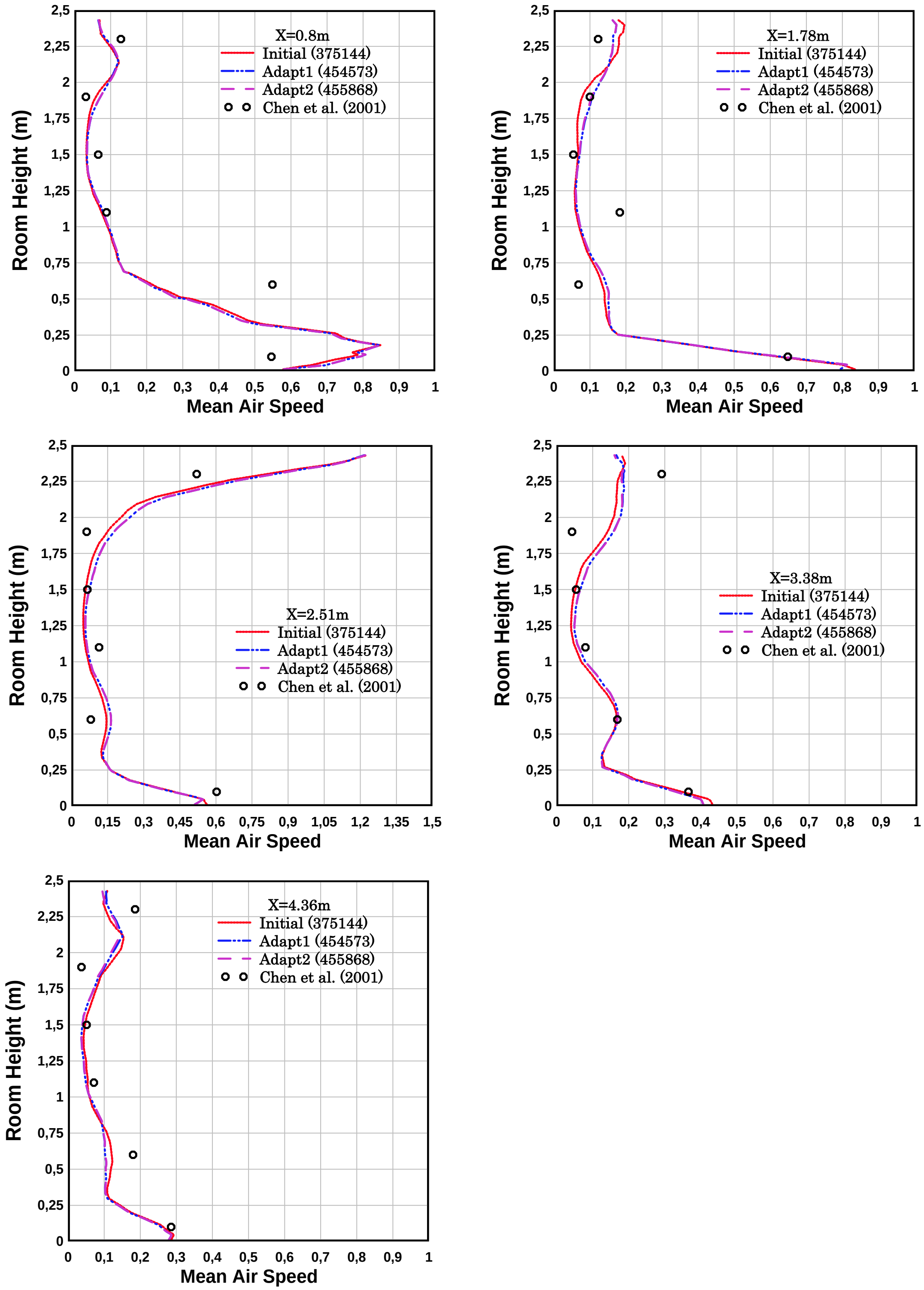

Fig. 6.4 Comparison of predicted mean air speed profiles with measurements (SST k-ω model)
(Normalized as $V^*=V/V_{in}$, V_{in}=0.35m/s)

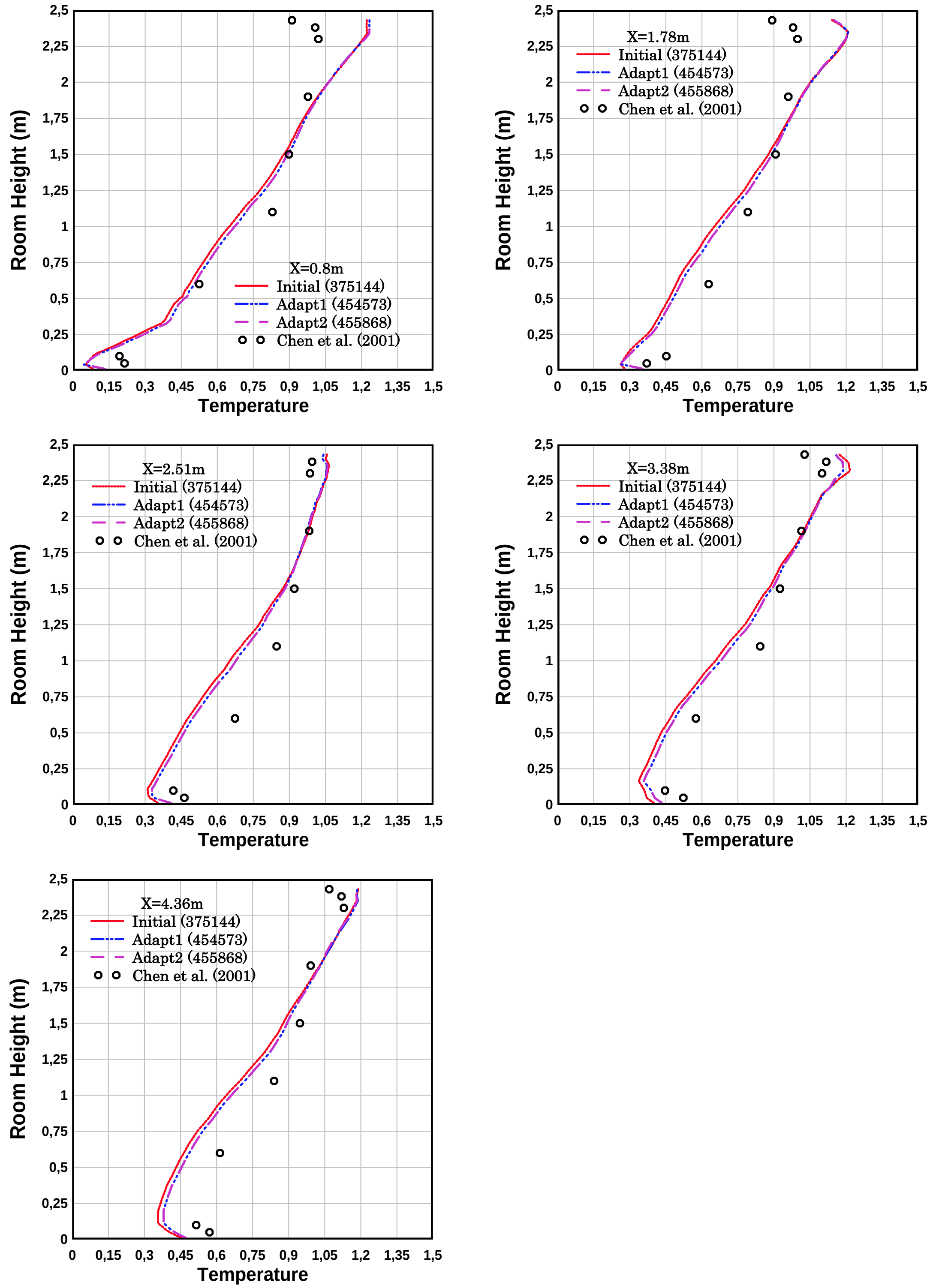

Fig. 6.5 Comparison of predicted temperature profiles with measurements (SST k-ω model)
(Normalized as $T^{*}=(T-T_{in})/(T_{out}-T_{in})$, T_{in}=13°C, C_{out}=22.2°C)

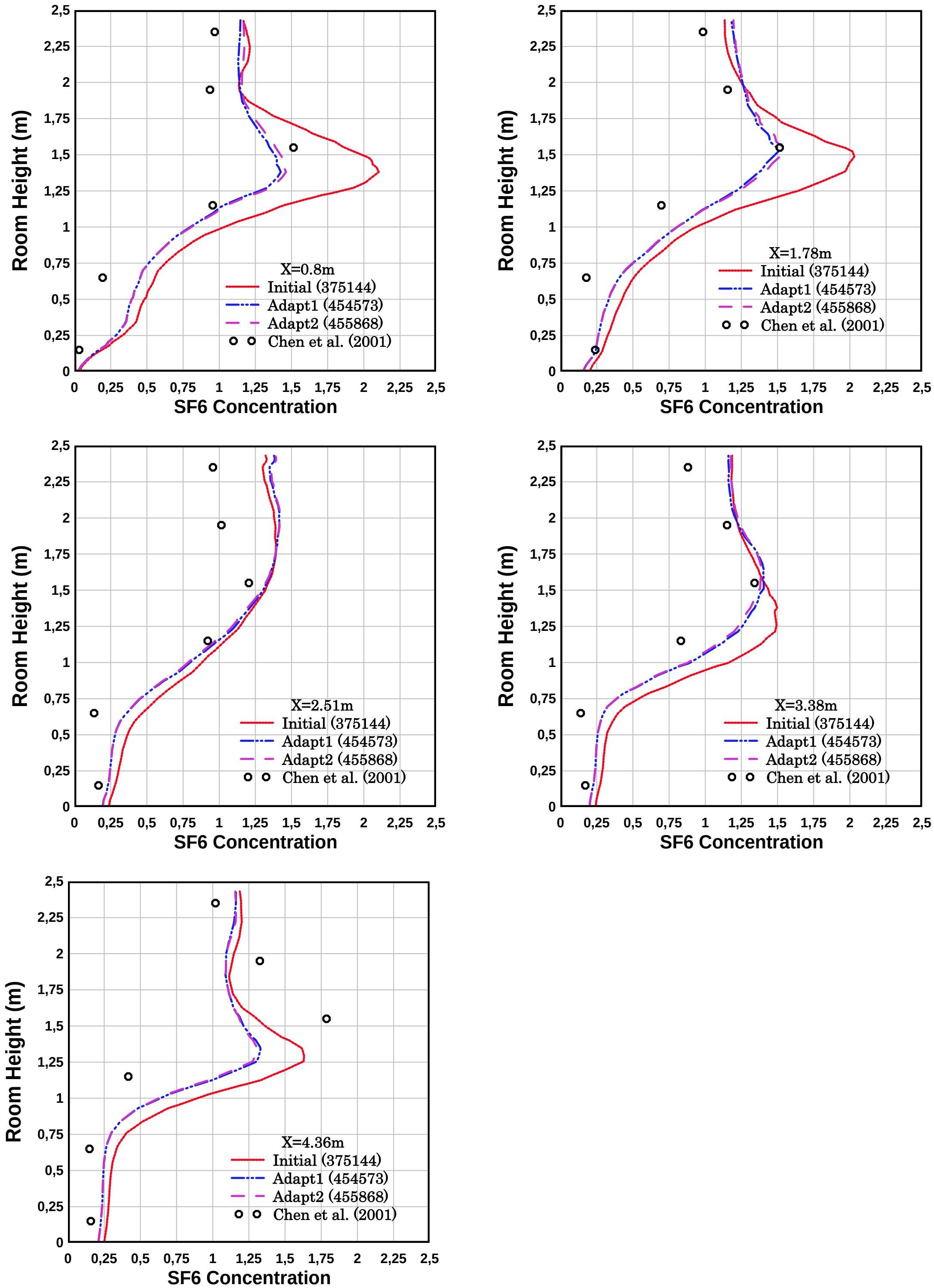

Fig. 6.6 Comparison of predicted SF6 concentration profiles with measurements (SST k-ω model)
(Normalized as $C^*=(C-C_{in})/(C_{out}-C_{in})$, C_{in}=0.04489ppm, C_{out}=1.0078ppm)

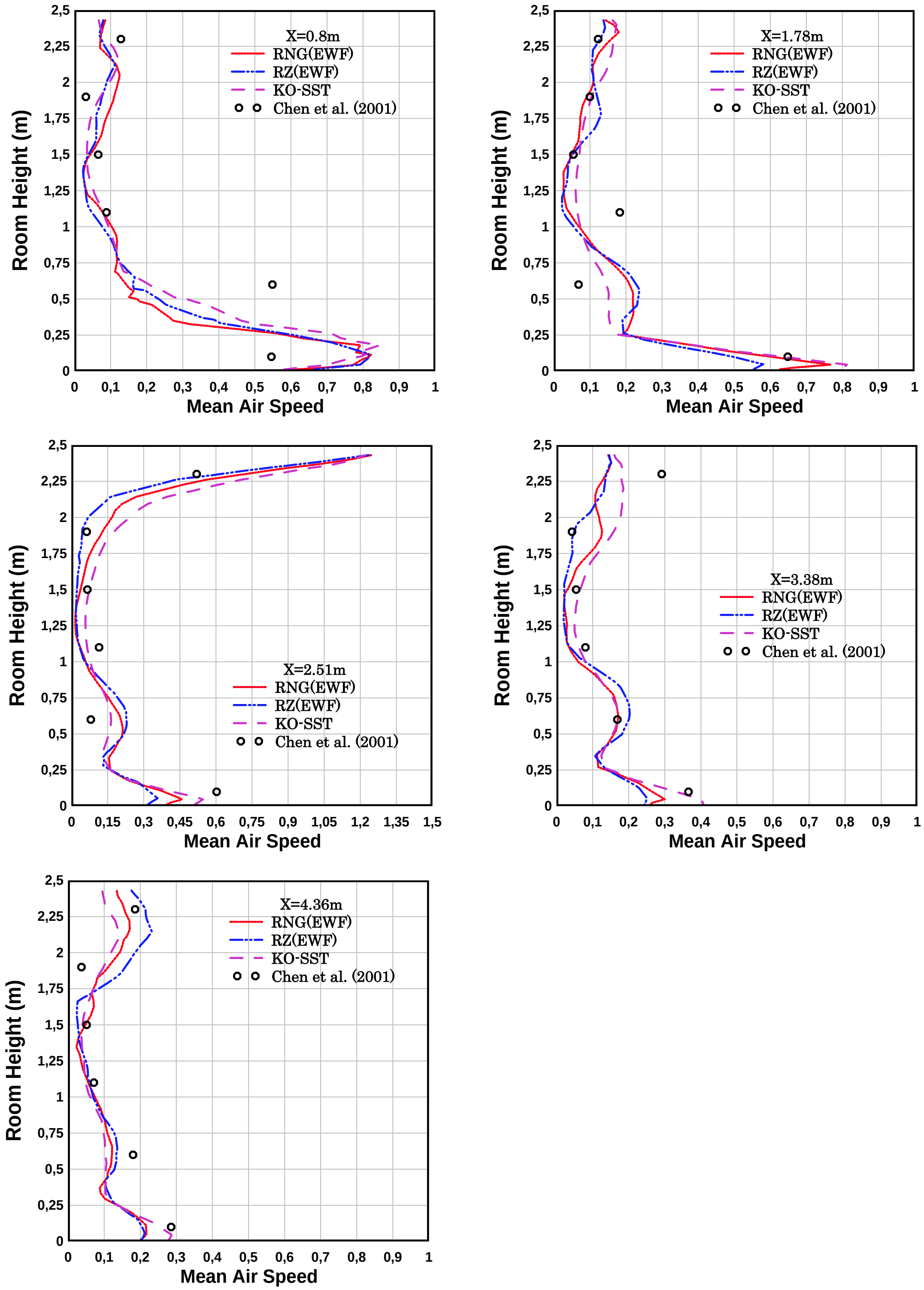

Fig. 6.7 Comparison of predicted mean air speed profiles with measurements using different turbulence models (Normalized as $V^*=V/V_{in}$, V_{in}=0.35m/s)

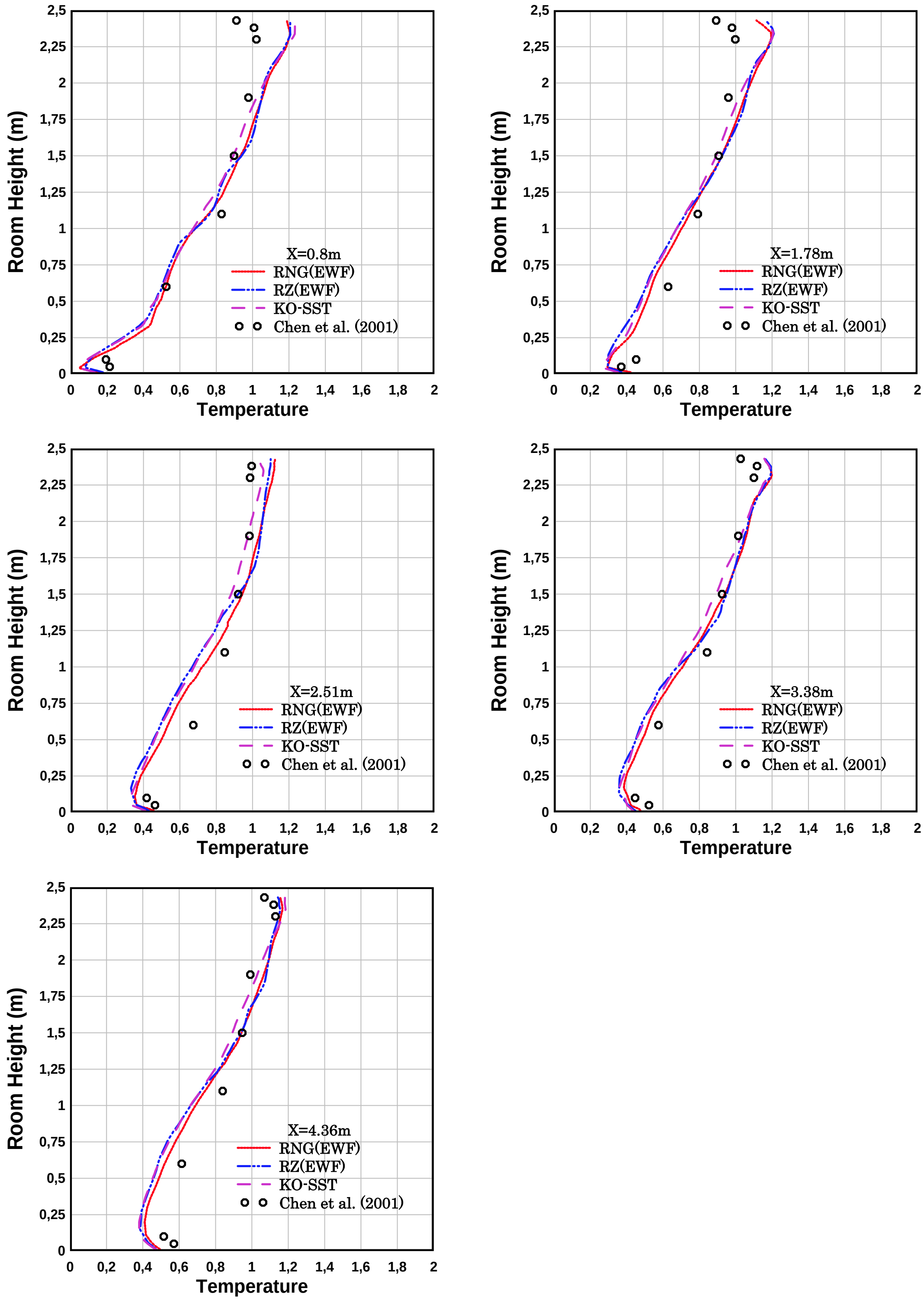

Fig. 6.8 Comparison of predicted temperature profiles with measurements using different turbulence models (Normalized as $T^{*}=(T-T_{in})/(T_{out}-T_{in})$, T_{in}=13°C, T_{out}=22.2°C)

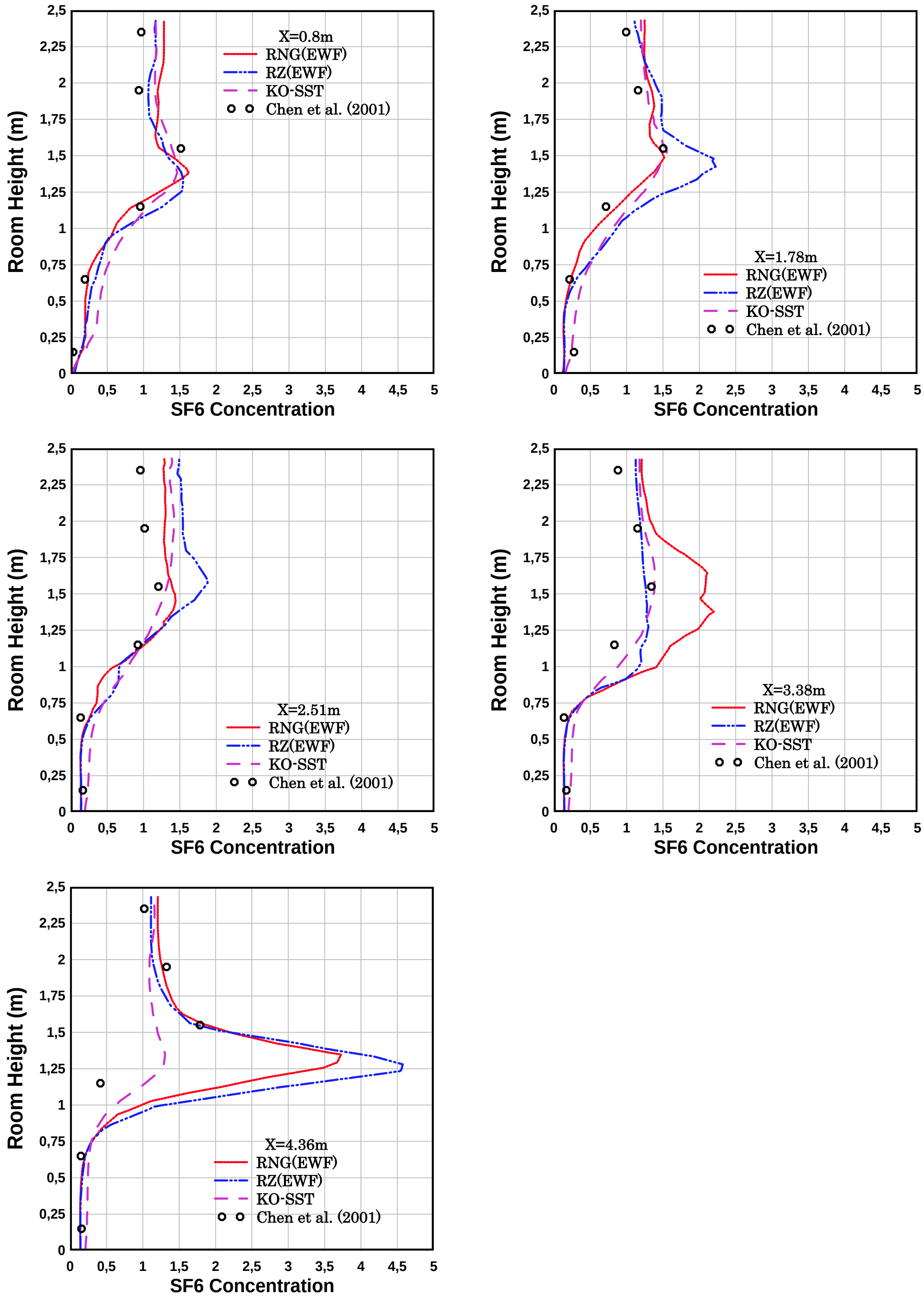

Fig. 6.9 Comparison of predicted SF6 concentration profiles with measurements using different turbulence models (Normalized as $C^*=(C-C_{in})/(C_{out}-C_{in})$, C_{in}=0.04489ppm, C_{out}=1.0078ppm)

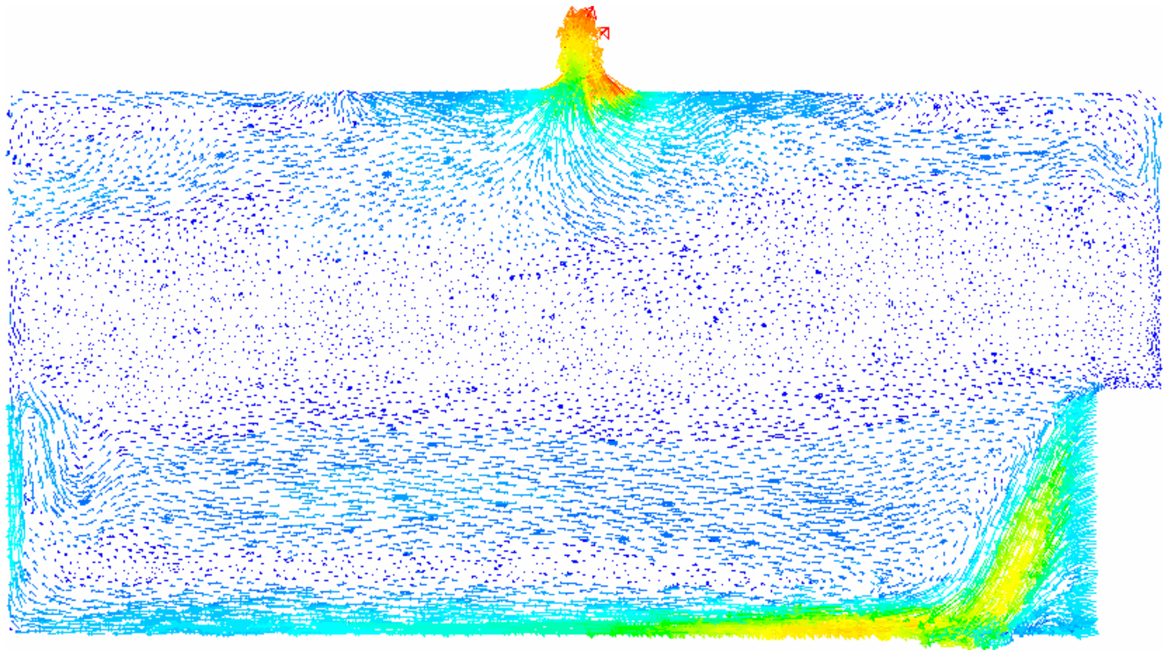

Fig. 6.10 Predicted flow field at the plane Y=1.825m

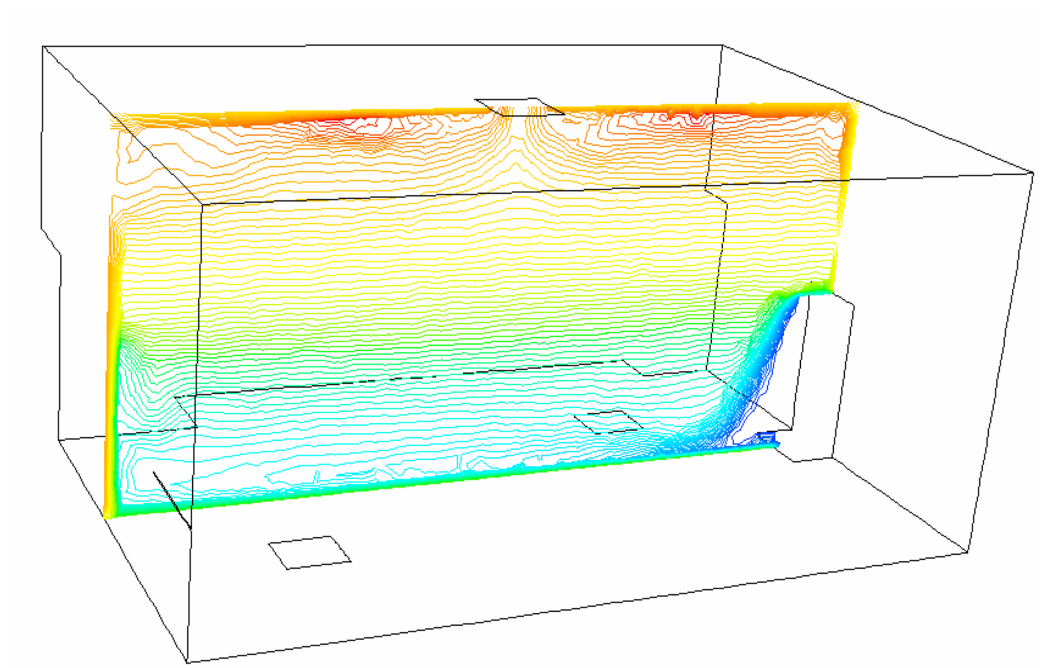

Fig. 6.11 Predicted temperature contours at the plane X=1.825m

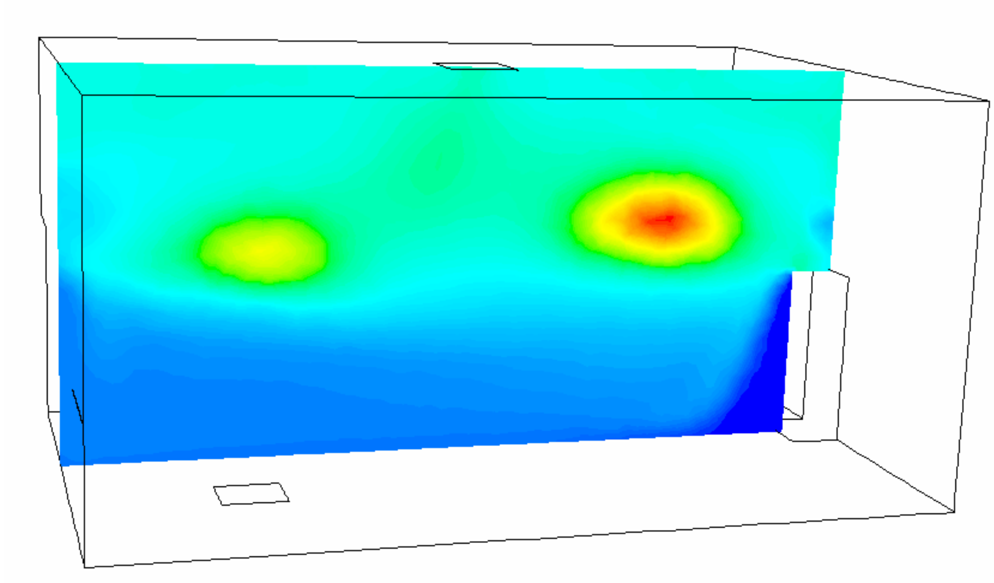

Fig. 6.12 Predicted SF6 concentration distribution at the plane Y=1.825m

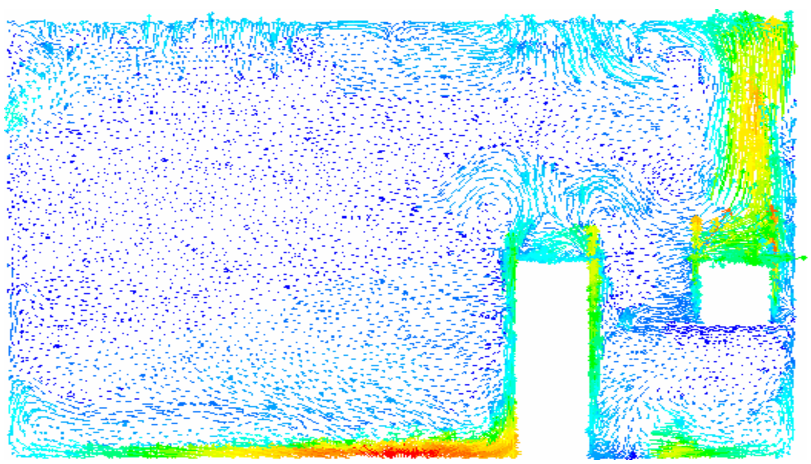

(a) X=1.3m

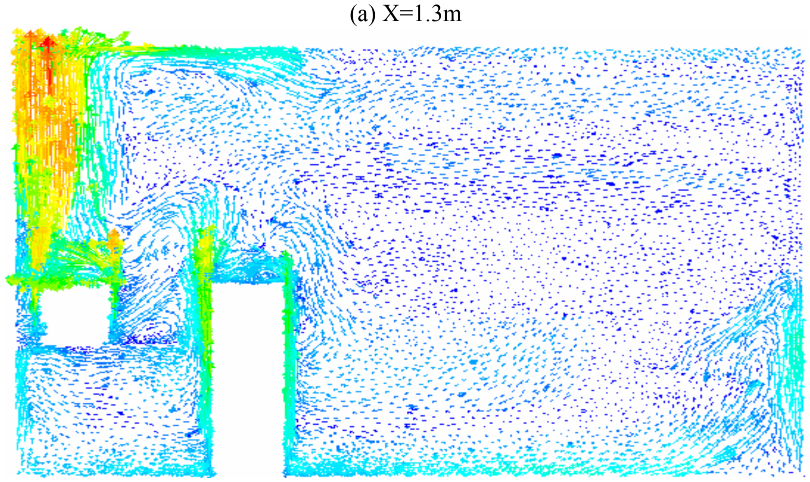

(b) X=4.1m

Fig. 6.13 Thermal plums arising above the computers and the human simulators

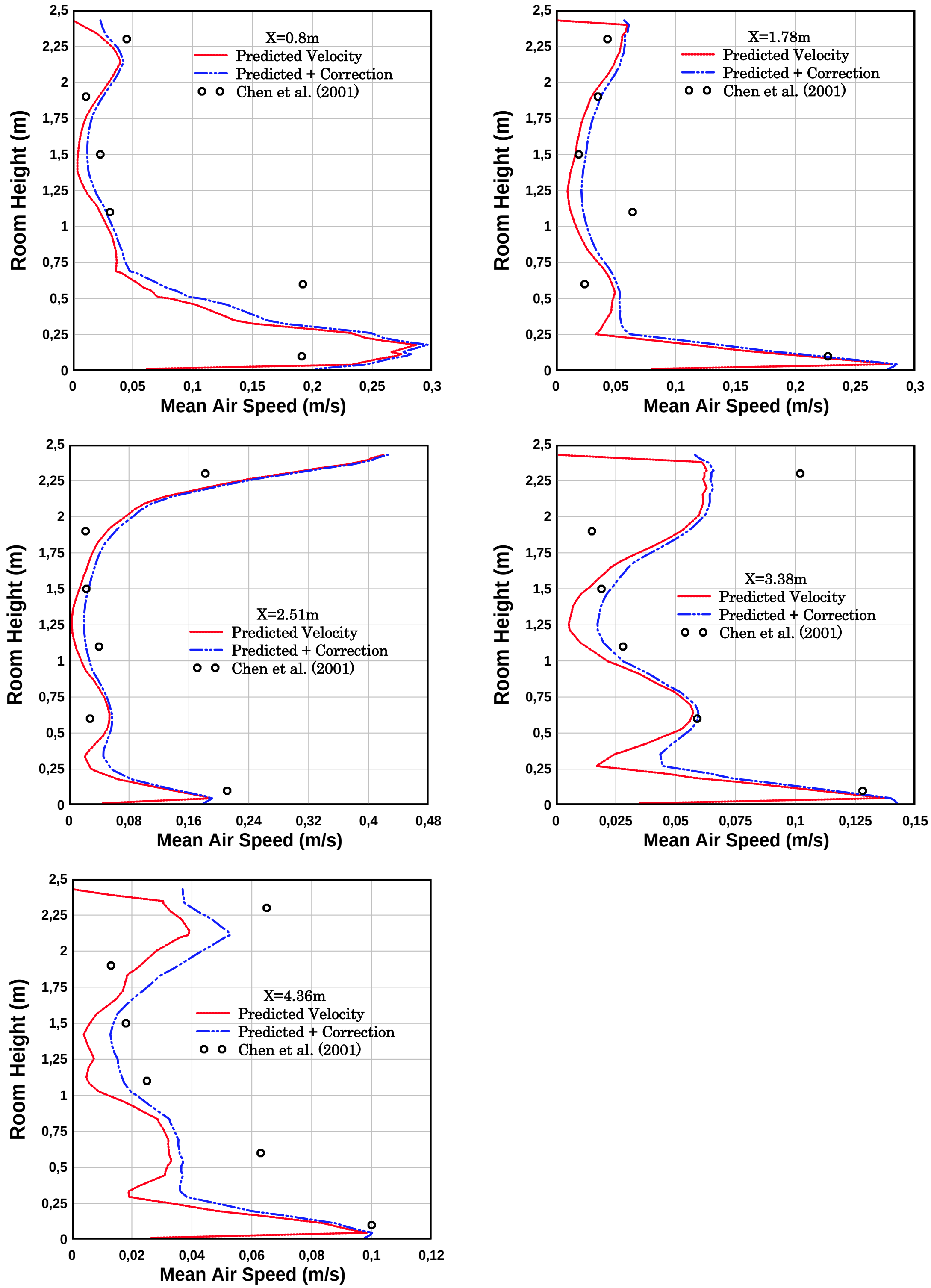

Fig. 6.14 Comparison of predicted velocity magnitude and mean air speed profiles with experiment measurements (SST k-ω model)

6.3 Ceiling slot ventilation

6.3.1 Test conditions

The ceiling slot ventilation test case was carried out under a ventilation rate of 9.2 ACH. The inlet diffuser is installed on the ceiling and 0.15m from one of the side walls (south wall), the exhaust opening is on the west wall and 0.02m above the floor as shown in Fig. 6.15. The size and position of the inlet and outlet diffusers are listed in Table 6.3. All the other objects (human simulators, computers, tables, lamps and cabinets) in the flow field are the same as in the displacement ventilation test case, their dimension and position as well as heat generating rate are presented in Table 6.1.

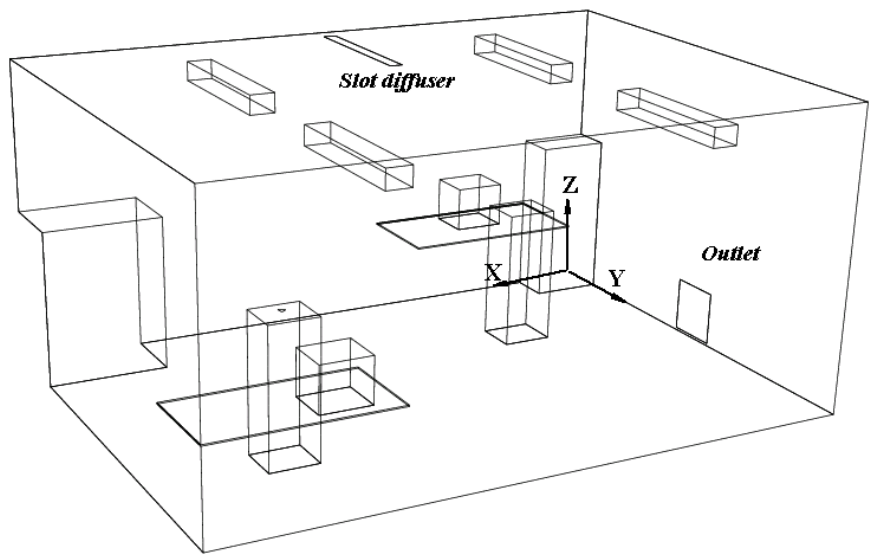

Fig. 6.15 Configuration of ceiling slot ventilation test case

Table 6.3 Position and size of the slot and exhaust diffusers (Chen et al. 2001)

	Size			Location			Temp.
	ΔX [m]	ΔY [m]	ΔZ [m]	X [m]	Y [m]	Z [m]	T [^oC]
Supply	0.1	1.15	0.0	2.53	0.15	2.43	16.3
Exhaust	0.0	0.43	0.43	0.0	1.61	0.02	21.4

As in the displacement ventilation test case, a tracer gas (SF6) source was added at the center of the top surface of each human simulator to simulate the breathing process; and it is introduced at a constant flow rate of 0.1104 l/h. The position of the tracer gas sources and the tracer gas concentration at the inlet and outlet are as follows:

Tracer-gas source 1: 0.1104 l/h at (x, y, z) = (1.3, 1.12, 1.1)
Tracer-gas source 2: 0.1104 l/h at (x, y, z) = (4.1, 2.52, 1.1)
Supply concentration: 0.0327 ppm
Exhaust concentration: 0.5546 ppm

The wall temperatures were continuously monitored at the same places as in the displacement ventilation test case using thermocouples. The positions of the measuring points and the measured temperatures on the walls are given below:

South wall temperature (X = 2.58 m, Y = 0 m)

Z [m]	0.1	0.6	1.1	1.8	2.38
T [^{o}C]	22.562	22.138	22.732	22.711	21.037

East wall & window temperature (X = 5.16 m, Y = 1.83 m)

Z [m]	0.1	0.6	1.1	1.8	2.38
T [^{o}C]	23.212	23.047	25.277	26.151	24.203

North wall temperature (X = 2.58 m, Y = 3.65 m)

Z [m]	1.1	1.8
T [^{o}C]	22.422	22.452

West wall temperature (X = 0 m, Y = 1.83 m)

Z [m]	1.8
T [^{o}C]	22.217

The notation of the walls (South, West, etc.) is the same as in the displacement ventilation test case and is shown in Fig. 6.1. The same method and equipment for measuring air velocity and temperature as in the displacement ventilation test case are used in this test case, the only difference between the two test cases is that the measuring plane is closer to one of the side planes, i.e., the measuring plane is at Y=0.85m in this test case instead of Y=1.825m in the displacement ventilation case, the positions of the five poles carrying the anemometers and tracer gas sampling tubes for the measurements are shown in Fig. 6.16.

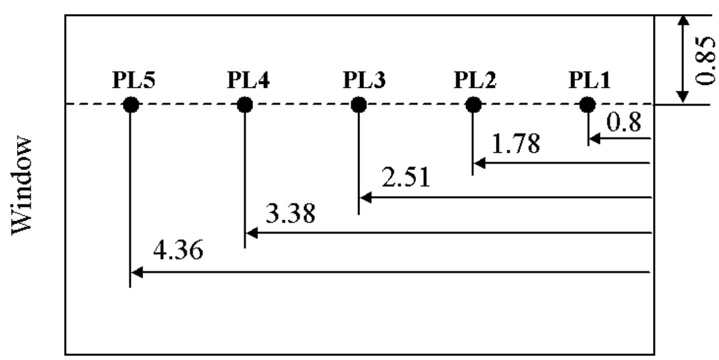

Fig. 6.16 The positions of the measuring poles for the ceiling slot ventilation test case (Chen et al. 2001)

As in the previous test case, the measurements were conducted under steady-state conditions by stabilizing the room thermal and fluid conditions for more than 12 hours before recording the data.

6.3.2 Modeling and simulation

6.3.2.1 Boundary conditions

Inlet diffuser:

The slot diffuser has three 1.143m x 0.019m openings and the inflow passes through the three openings to enter the test room (Fig. 6.16a). In the experiment, it was observed by smoke visualization that the inlet flow from the slot diffuser turned 45° downwards toward the west wall (Fig. 6.16b). To assure the correct momentum flow from the diffuser, the momentum method is used to model the slot diffuser, i.e., a momentum source is added to a volume over an area of 0.1m x 1.15m adjacent to the diffuser and the momentum flow direction is 45° downwards as shown in Fig. 6.16b.

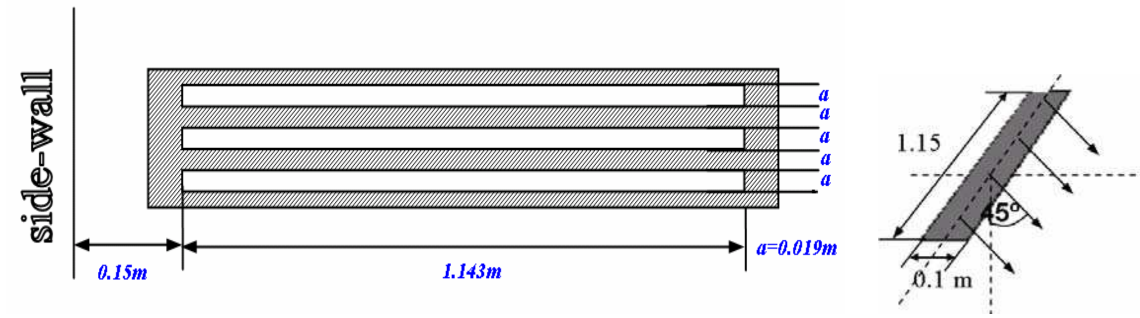

(a) Detail of the slot diffuser (b) Inflow direction

Fig. 6.16 Installation and details of the slot diffuser (Chen et al. 2001)

At the supply opening, a mass flow rate of 0.138 kg/s and a turbulence intensity of 5% are specified. The boundary condition for the turbulence quantities (k, ε or ω) are calculated using equations 4.4~4.6, the hydraulic diameter of the inlet opening is about 0.34m. The temperature of the inlet air is 289.3 K (16.3°C) and the SF6 concentration in the inlet flow is 0.0327 ppm.

Outlet:

The outlet is specified as pressure outlet, i.e., the gauge pressure at the outlet is specified as zero.

Tracer gas sources:

As in §6.2, the tracer gas sources are modeled as momentumless volumetric mass source and are added to one or more grid cells centered at (1.3, 1.12, 1.1) and (4.1, 2.52; 1.1), respectively. The mass flow rate of both the tracer gas sources is 1.89×10^{-7} kg/s.

Thermal conditions:

As in the displacement ventilation case, temperature or heat flux at the walls is used to specify the thermal conditions for different objects in the flow field:

The thermal conditions of the following objects are specified as heat flux:

- Computer 1: 171.43 W/m^2
- Computer 2: 274.6 W/m^2
- Human simulators: 41.9 W/m^2
- Lamps: 37.78 W/m^2

The average of the measured temperatures at the walls is used to specify the thermal condition for the walls:

- Ceiling: 295.82 K (22.82°C)
- Floor: 295.35 K (22.35°C)
- West wall: 295.217 K (22.217°C)

- East Wall: 297.38 K (24.38°C)
- South wall: 295.23 K (22.23°C)
- North wall: 295.43 K (22.43°C)
- Tables 1 and 2: 294 K (21°C)

6.3.2.2 Turbulence modeling

As in §6.2, the influence of turbulence on the mean flow is modeled using the RNG and the Realizable k-ε models and the SST k-ω model. The non-equilibrium wall function or the enhanced wall treatment is used when working with the two k-ε models.

6.3.2.3 Computation meshes

As in §6.2, an unstructured mesh is used to discretize the flow domain. Several different mesh sizes are tested, it is found also that the predicted tracer gas profiles are more sensitive to the mesh size used and the predicted velocity and temperature profiles change much less as the mesh resolution changes. After some tests, a mesh size of 302102 cells is chosen as the main computation mesh which represents a good compromise between mesh resolution requirements and the available computational resources.

6.3.2.4 Numerical schemes

The discretization schemes are the same as in §6.2.2.4.

6.3.2.5 Simulation results

Simulations are carried out with the RNG and Realizable k-ε models and the SST k-ω model. Figs. 6.17, 6.18 and 6.19 give a comparison of the predicted mean air speed (with velocity correction), temperature and SF6 concentration profiles using SST k-ω model with experimental data, respectively. It can be seen that the predicted profiles correspond reasonably well with measured ones. In Fig. 6.19, the predicted temperature profiles at X=0.8m, 1.78m and 3.38m have some big discrepancies compared with measured data in the ceiling region, this is likely due to the momentum model used for the inlet diffuser, because in Chen et al. (2001) when using the momentum model for the diffuser and the RNG k-ε model, they obtained the same results for the predicted temperature profiles; they then tested the box model using measured velocity and temperature profiles in the vicinity of the diffuser as the boundary conditions, the discrepancies at X=0.8m and 1.78m decrease, but the discrepancy at X=3.38m still exists. In the experiment, the flow direction of the supplied air was detected by smoke visualization, the observed flow direction (45° downwards) is only an approximation. When it is used with the momentum model, it may also contribute to some degree to the discrepancies between the predicted temperature profiles and the measured ones. In the occupied zone, the predicted temperature profiles correspond enough well to the measured data, thus the prediction using the momentum model for the diffuser is acceptable for practical purposes. In Figs. 6.17~6.19, it is also shown the predicted profiles using successive mesh adaptation according to Y^+ value near walls. As with the displacement ventilation case, it can be seen that the mesh adaptation changes mainly the predicted SF6 concentration profiles, its influence on the predicted velocity and temperature profiles is marginal.

In Figs. 6.20~6.22, the predictions using the RNG and Realizable k-ε models and the SST k-ω model and the same mesh (302102) are compared. It can be seen that the three models can yield comparable prediction results, the predictions of the SF6 concentration profiles from the two k-ε models are a little less well than that from the SST k-ω model, thus the latter model is preferred.

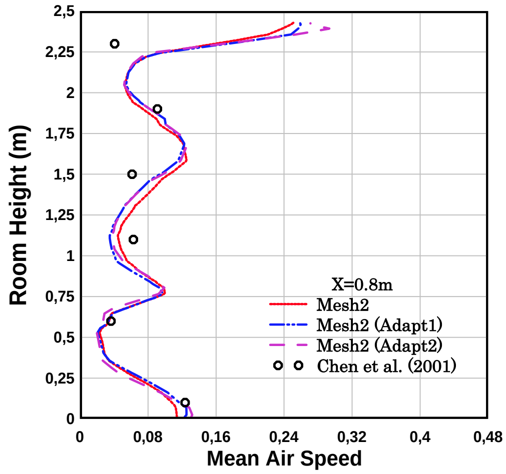

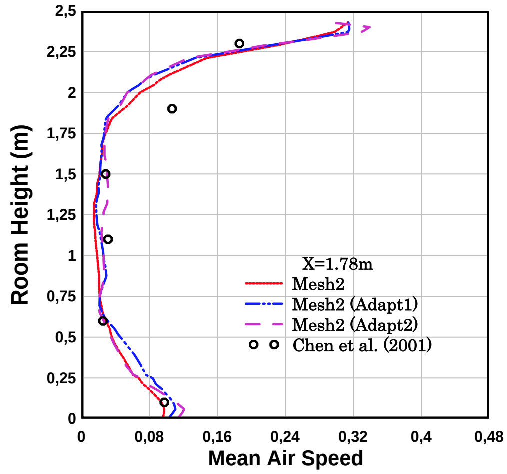

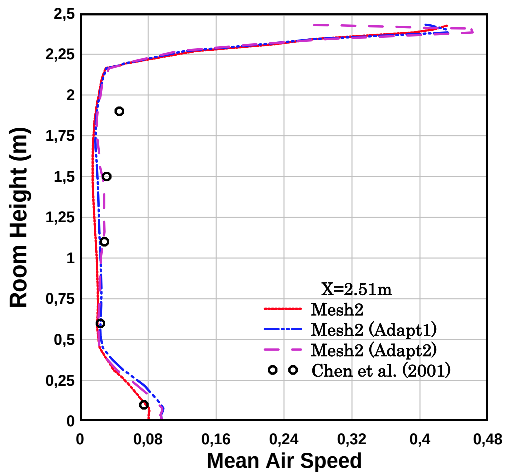

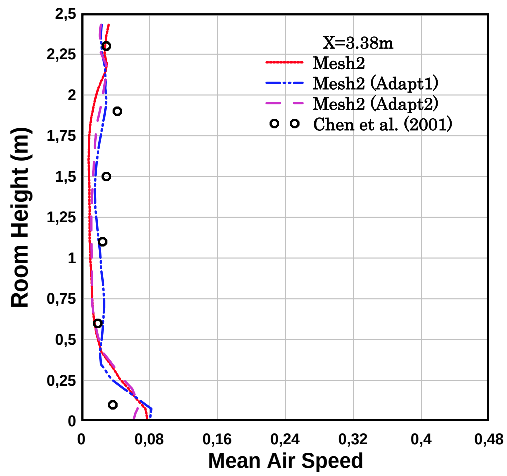

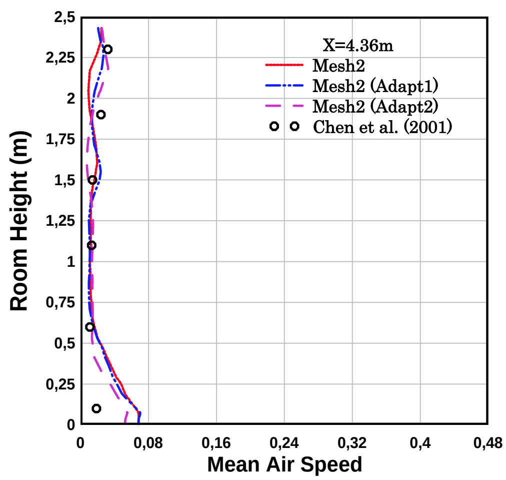

Note:

Initial mesh size : 302102 cells
Adapt1 : 336955 cells
Adapt2 : 485733 cells

SST k-ω model

Fig. 6.17 Comparison of predicted mean air speed profiles with experiment measurements (Normalized as $V^*=V/V_{in}$, V_{in}=3.9m/s)

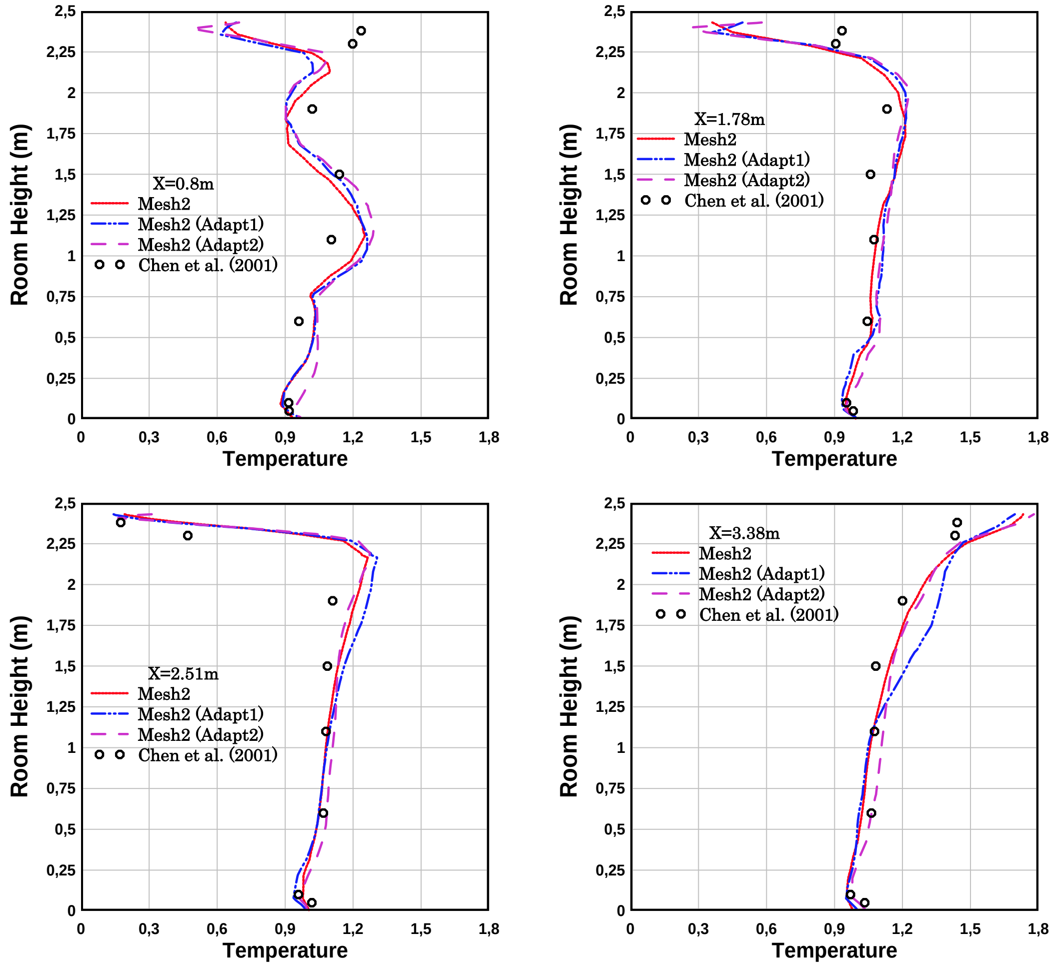

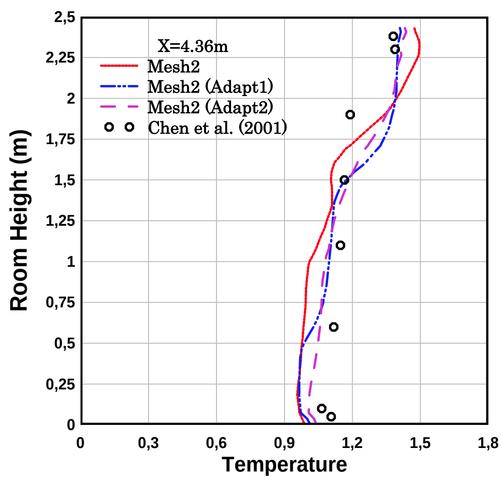

Note:

Initial mesh size : 302102
Adapt1 : 336955
Adapt2 : 485733

SST k-ω model

Fig. 6.18 Comparison of predicted air temperature profiles with experiment measurements (Normalized as $T^*= (T-T_{in})/(T_{out}-T_{in})$, T_{in}=16.3°C, T_{out}=21.4°C)

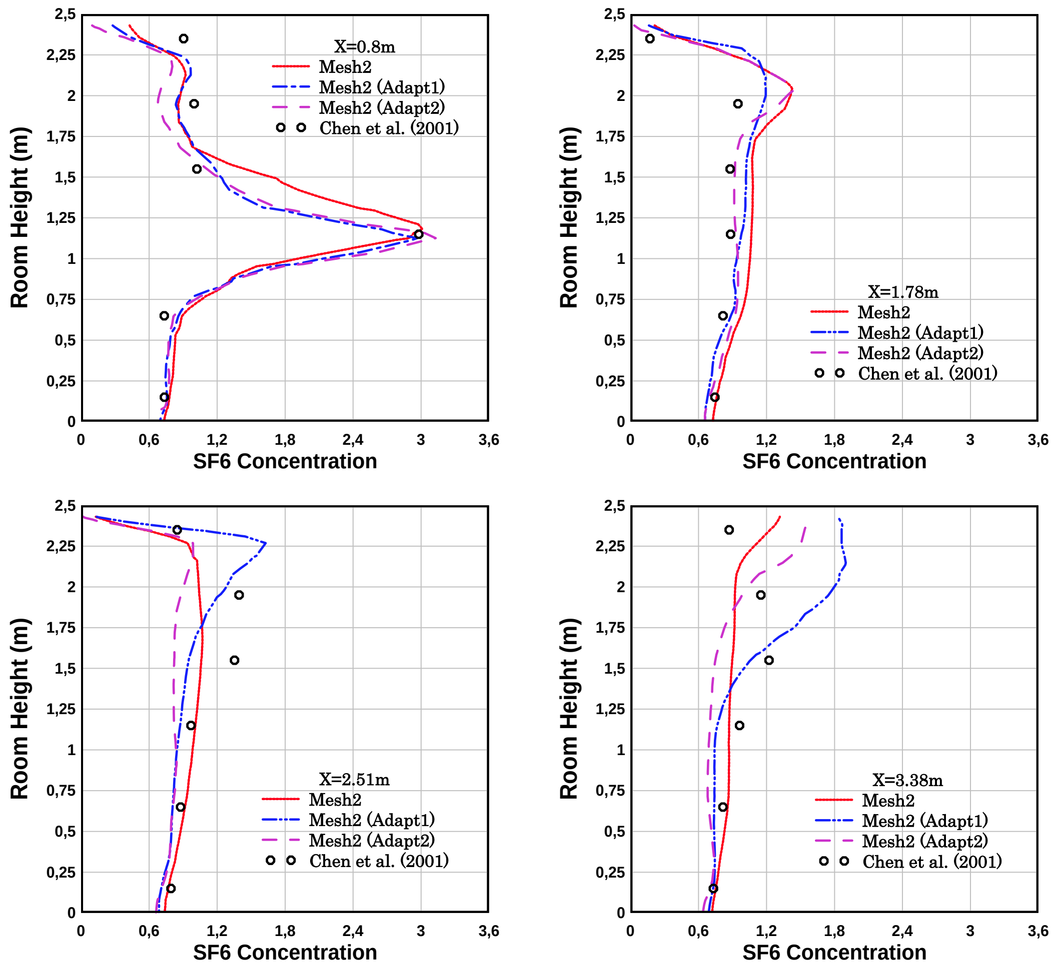

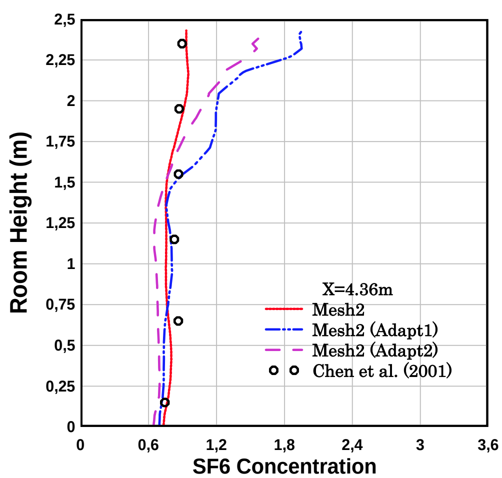

Note:

Initial mesh size : 302102
Adapt1 : 336955
Adapt2 : 485733

SST k-ω model

Fig. 6.19 Comparison of predicted SF6 concentration profiles with experiment measurements (Normalized as $C^*=(C-C_{in})/(C_{out}-C_{in})$, C_{in}=0.0327 ppm, C_{out}=0.5546 ppm)

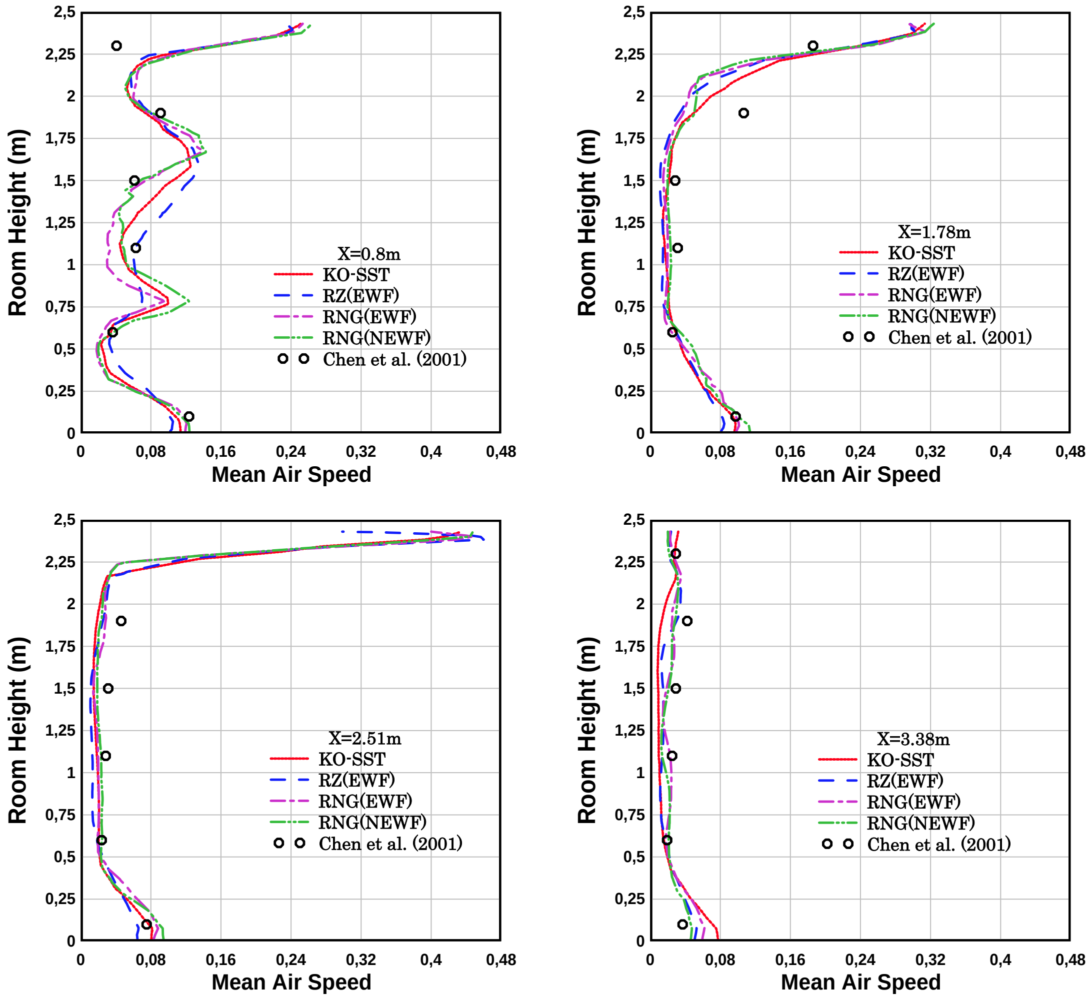

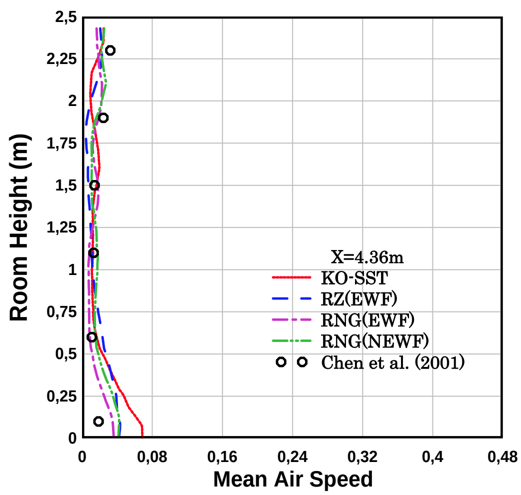

Note:

Mesh size : 302102 cells

Fig. 6.20 Comparison of predicted mean air speed profiles using different turbulence models with experiment measurements (Normalized as $V^*=V/V_{in}$, V_{in}=3.9m/s)

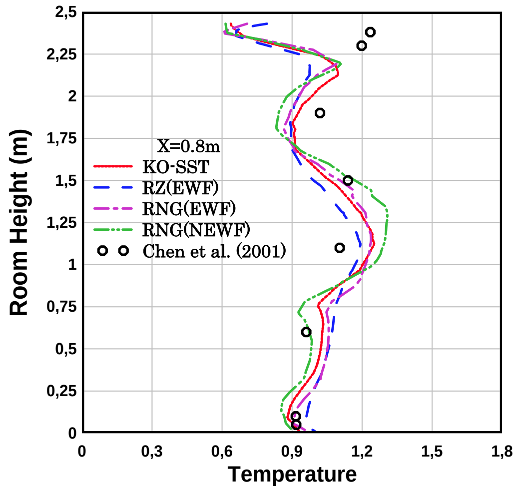

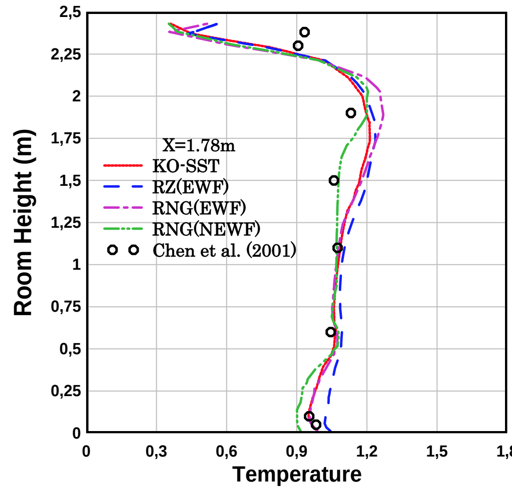

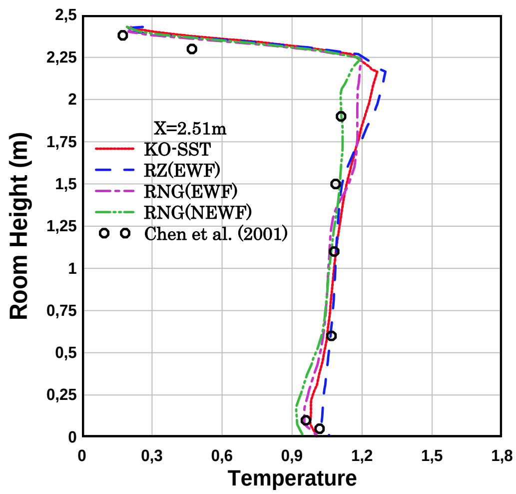

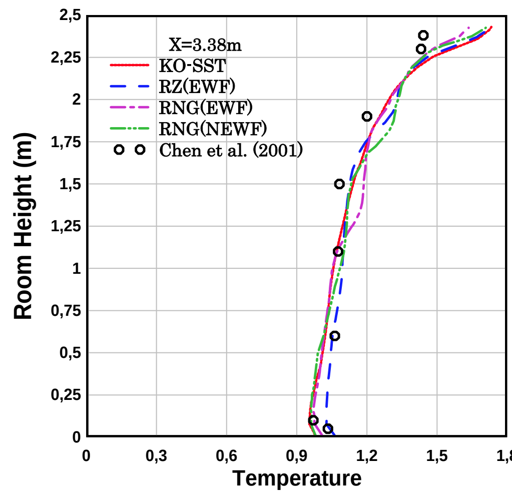

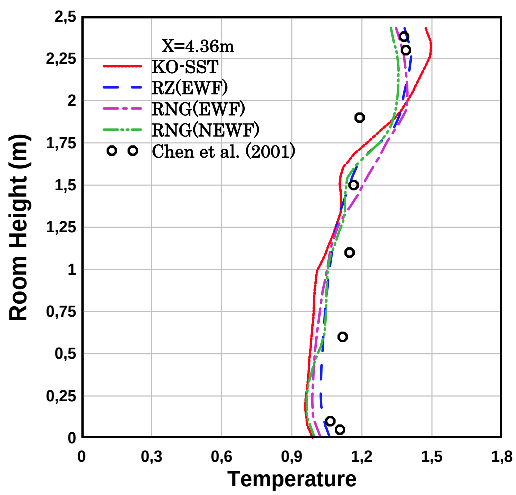

Note:

Mesh size : 302102

Fig. 6.21 Comparison of predicted air temperature profiles using different turbulence models with experiment measurements (Normalized as $T^* = (T-T_{in})/(T_{out}-T_{in})$, T_{in}=16.3°C, T_{out}=21.4°C)

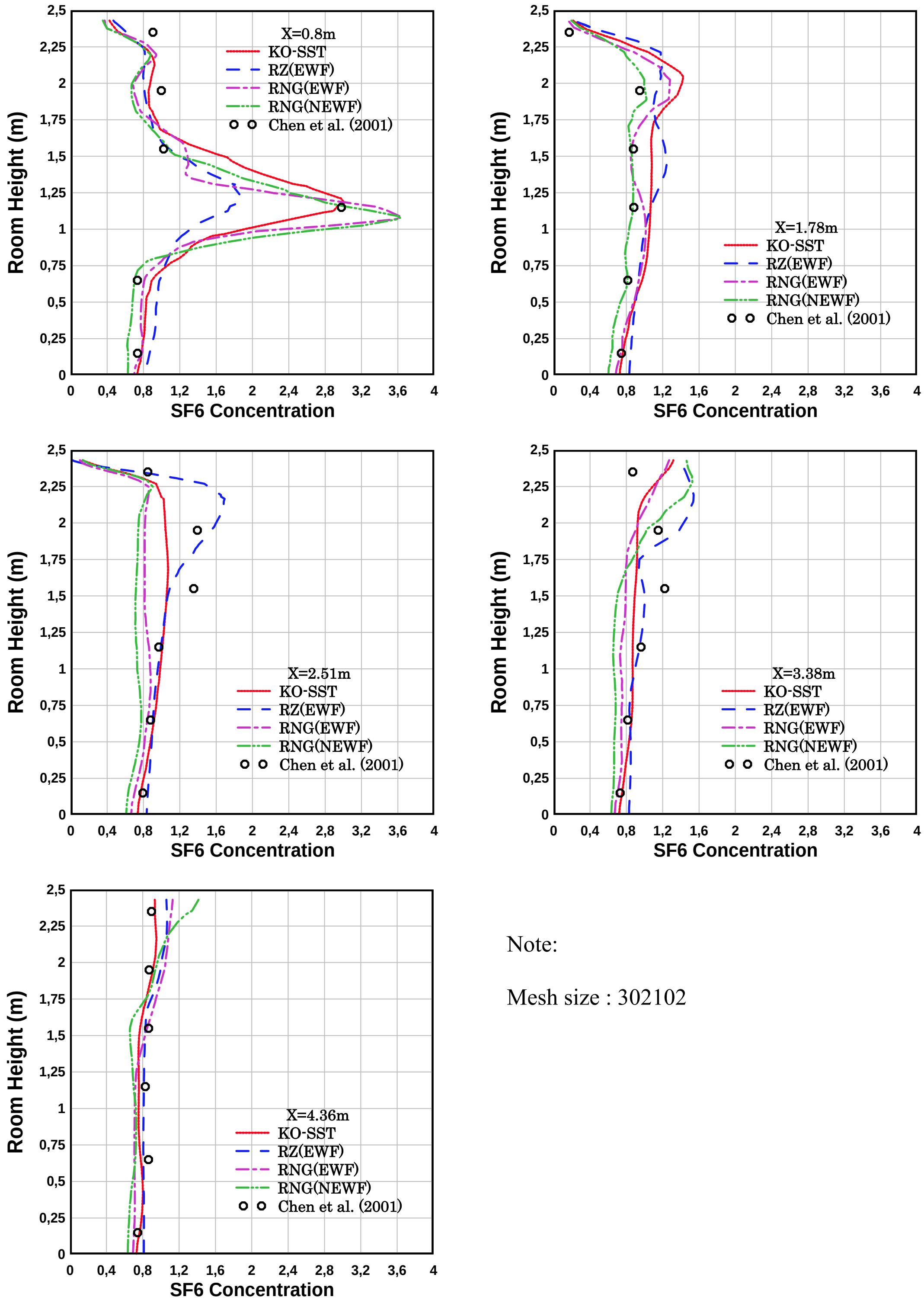

Note:

Mesh size : 302102

Fig. 6.22 Comparison of predicted SF6 concentration profiles using different turbulence models with experiment measurements (Normalized as $C^*=(C-C_{in})/(C_{out}-C_{in})$, C_{in}=0.0327 ppm, C_{out}=0.5546 ppm)

6.3.3 Simulation under normal-g and zero-g conditions

Having validated that the SST k-ω model can yield reasonable prediction for the ceiling slot ventilation test case with a mesh grid of 302102 cells under normal condition, the case is recalculated using the same model and the same mesh under zero-g condition to investigate the influence of gravity on the thermal comfort, the distribution of temperature and SF6 concentration in the room. As discussed in Chapter 2, thermal comfort is a function of a range of environmental and physiological factors which include air velocity and temperature, turbulence intensity, mean radiant temperature, vector radiant temperature, humidity, clothing level, metabolic rate and external activity level etc. (Jones et al. 1992). In this preliminary study, only the draught model developed by Fanger et al. (1988) is used to investigate the influence of zero-g and zero-g conditions on the indoor thermal comfort. The draught model of Fanger et al. (1988) predicts the draught rating (DR), which is the percentage of people dissatisfied due to draught, based on the local air speed, air temperature and turbulence intensity:

$$DR = ((34 - T)(v - 0.05)^{0.62})(0.37 \times v \times (TI + 3.14)) \qquad (6.1)$$

where T is the local air temperature in °C, v is the local air speed in m/s and TI is the local turbulence intensity in percent. The correction formula for the turbulence intensity developed by Koskela et al. (2001) is used to correlate the turbulence intensity reported by CFD software package based on equation 4.9 with that measured using omni-directional anemometers:

$$TI = \sqrt{(1 + 3I_v^2)\frac{V_v^2}{V_o^2} - 1} \qquad (6.2)$$

where I_v, V_v and V_o have the same definitions as in the equations 4.7~4.9.

Figs. 6.23, 6.24, 6.25 and 6.26 give a comparison of the predicted mean air speed, temperature, SF6 concentration and draught rating profiles under zero-g and zero-g conditions, respectively. It can be seen that the gravity doesn't have much influence on the predicted velocity profiles and draught rating profiles at the plane Y=0.85m, this is because in this test case, the ventilation rate is high (9.2 ACH), which is much higher than the normal ventilation requirements (3~4.5 ACH) in an office room, thus the forced convection dominates in the flow. On the other hand, the predicted temperature and SF6 concentration under zero-g are higher than under zero-g in the middle of the room, and the SF6 concentration is much higher near the west and east walls where the SF6 sources are located.

Further investigation reveals that although the predicted velocity and draught rating profiles don't differ much under the two test conditions at the Y=0.85m plane, there are significant differences in the flow pattern, temperature and SF6 distributions in the other parts of the room especially in the regions where the air flow is slow. In Figs. 6.27~6.29, an example of comparison is given for the predicted velocity field, temperature and SF6 distributions under the two conditions at the plane Y=0.275m, respectively. Although this plane is near the supply diffuser and the air flow in the plane is strong enough, the influence of gravity on the air flow pattern is still considerable. From Fig. 6.27a it can be clearly seen that the upward thermal plume created by the thermal buoyancy of the computer changed the air flow pattern, and a recirculation flow formed above the computer. As a result, the SF6 emitted from the human simulator nearby is trapped in the recirculation flow, thus a high SF6 concentration region forms above the computer; this is well illustrated in Fig. 6.29a. At the left side of one of the lamps (left one in Fig. 6.27a), there is another recirculation flow formed by the convective current created by the thermal buoyancy from the lamp, and also the SF6 is trapped in the recirculation flow thus forms another high SF6 concentration region. On the other hand, it can be seen from Fig. 6.27a that because of the recirculation flow above the computer, the air flow at the left side of the computer is very slow, thus the heat transfer by forced convection is small; as a consequence, the temperature at the left surface of the computer attains a high level. Under zero-g condition, there is no convective current created by the thermal buoyancy above the computer, the supplied air first impinges on one of the side walls (west wall) and is then reflected at about 45° angle toward the floor, the air flow passes directly above the computer and impinges on one surface of the cabinet (at left) then turns toward the ceiling. It entrains the SF6 emitted by the human simulator to the ceiling region and a high SF6 concentration region forms at the upper left corner. Because the air flow at the two sides of the computer is very slow, the temperature at the left and right surfaces of the computer attains a very high level.

The predicted temperatures at the surfaces of the computer in Fig. 6.28 may not be correct, because the effect of radiation and conduction is not taken into account which may play an important role when air flow is slow; also it is well known that when the mesh grids adjacent to the surfaces are not fine enough, the wall-function approach will largely under-predict the convective heat transfer coefficient at the surfaces which then will lead to unrealistic high temperatures near surfaces in the prediction, but the predicted positions of the high-temperature zones in Fig. 6.28 are correct because when g=0, the flow field is decoupled from the temperature field, i.e., the temperature gradients don't have influences on the flow field. Thus the predicted high temperatures near the surfaces of the computer do show that there will possibly be problems in these regions if the air flow pattern is not well designed. Thus the numerical simulation can provide valuable information about the possible problem regions (too high temperature and/or contaminant concentration regions) and how we should better design or optimize the air flow pattern in spacecraft cabins. Numerical simulation is especially useful for space ventilation applications because it is almost impossible to optimize the air flow pattern through experimental studies conducted on Earth.

To further illustrate the differences of the predicted air flow patterns, temperature and SF6 concentration distributions under the two test conditions, two more examples are given in Figs. 6.30 and 6.31. The two SF6 concentration peaks under zero-g near the west and east walls as shown in Fig. 6.25 (at X=0.8m and 4.36m) can be clearly seen from Fig. 6.31a.

Remarks

The examples shown in Figs. 6.27~6.31 demonstrate that even at a rather large ventilation rate (9.2 ACH), the air flow pattern and the temperature and SF6 concentration distributions under zero-g and zero-g conditions may still have considerable differences in some parts of the room.

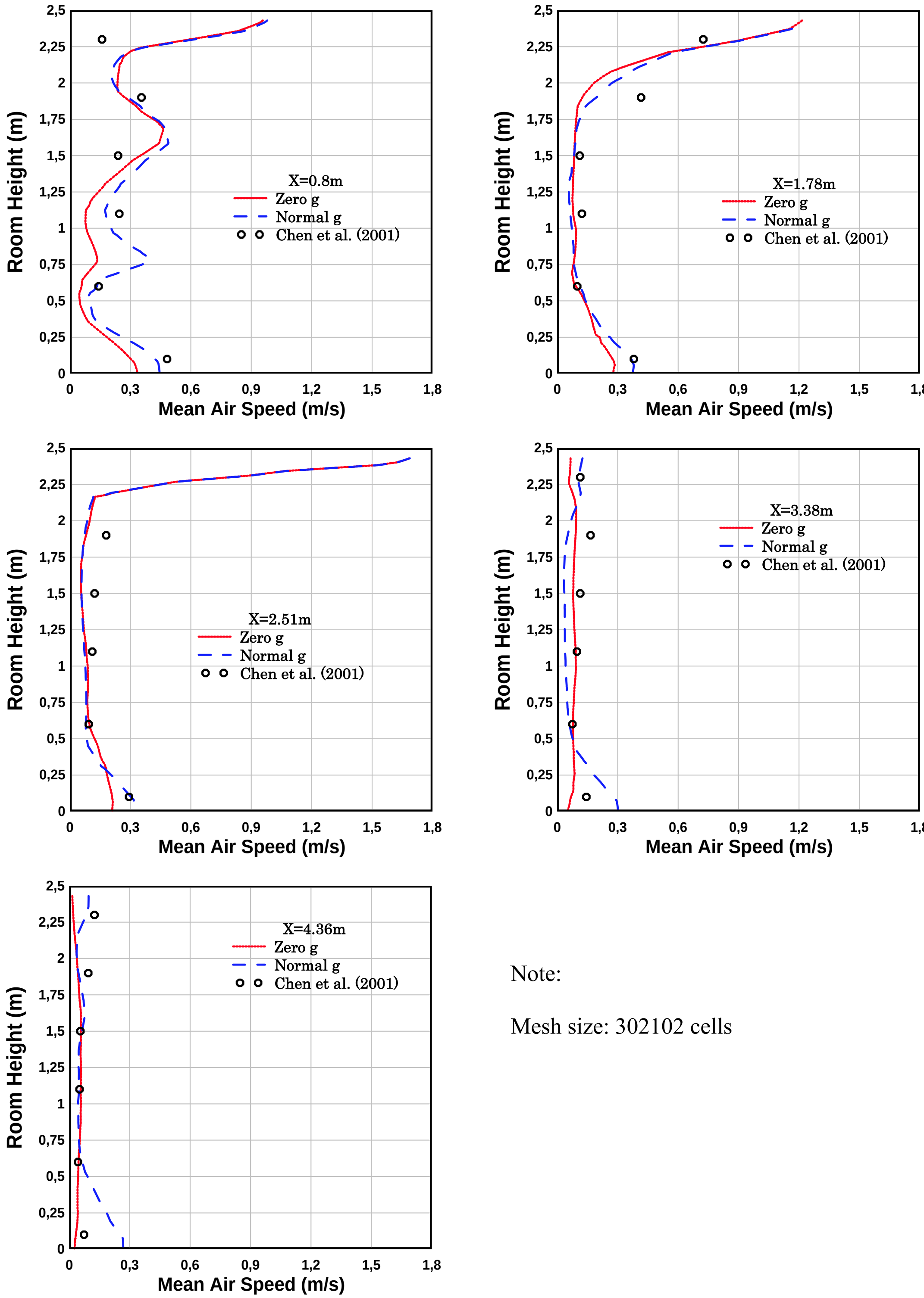

Note:

Mesh size: 302102 cells

Fig. 6.23 Comparison of predicted mean air speed profiles under zero-g and normal-g using SST k-ω model

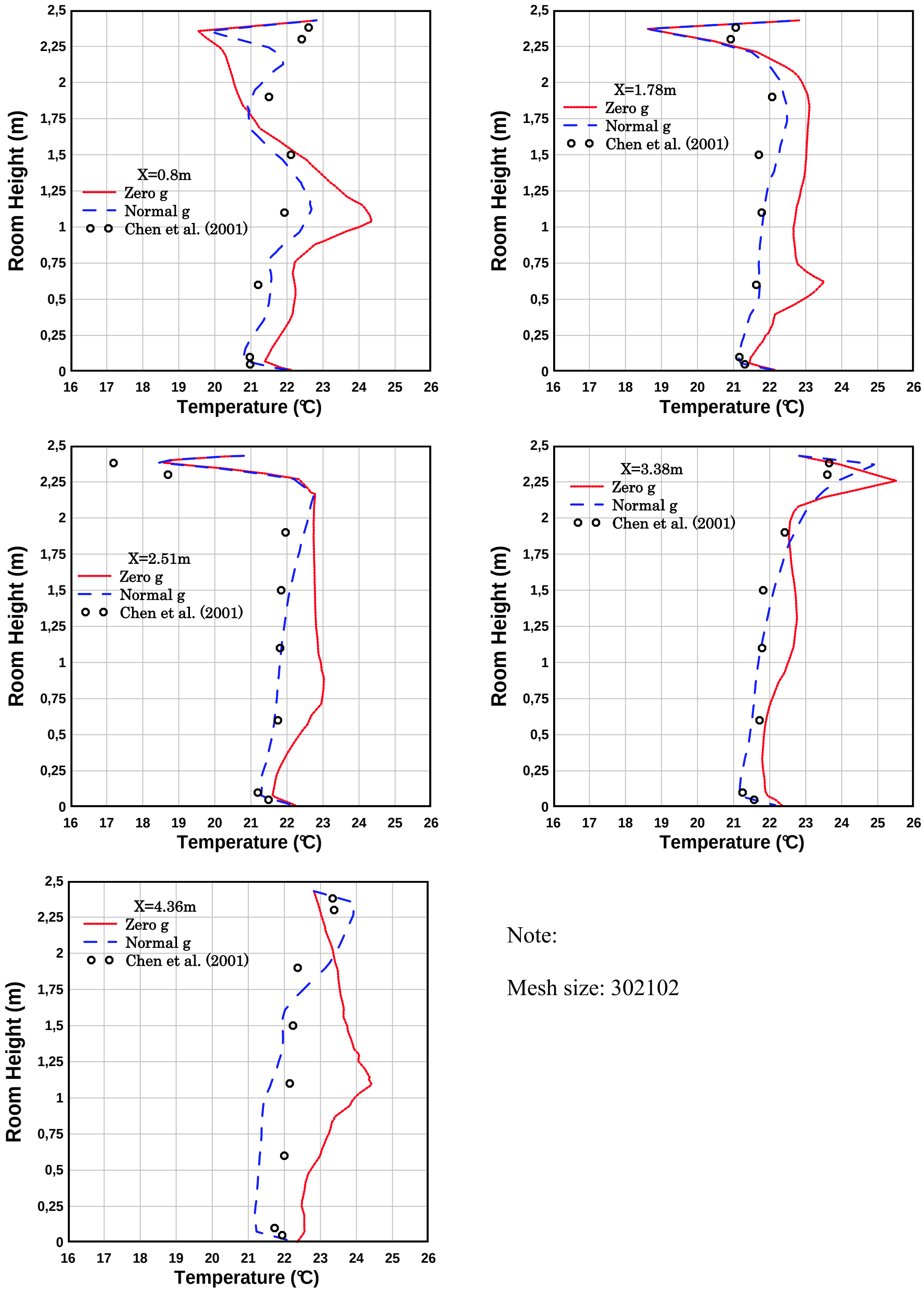

Note:

Mesh size: 302102

Fig. 6.24 Comparison of predicted temperature profiles under zero-g and normal-g using SST k-ω model

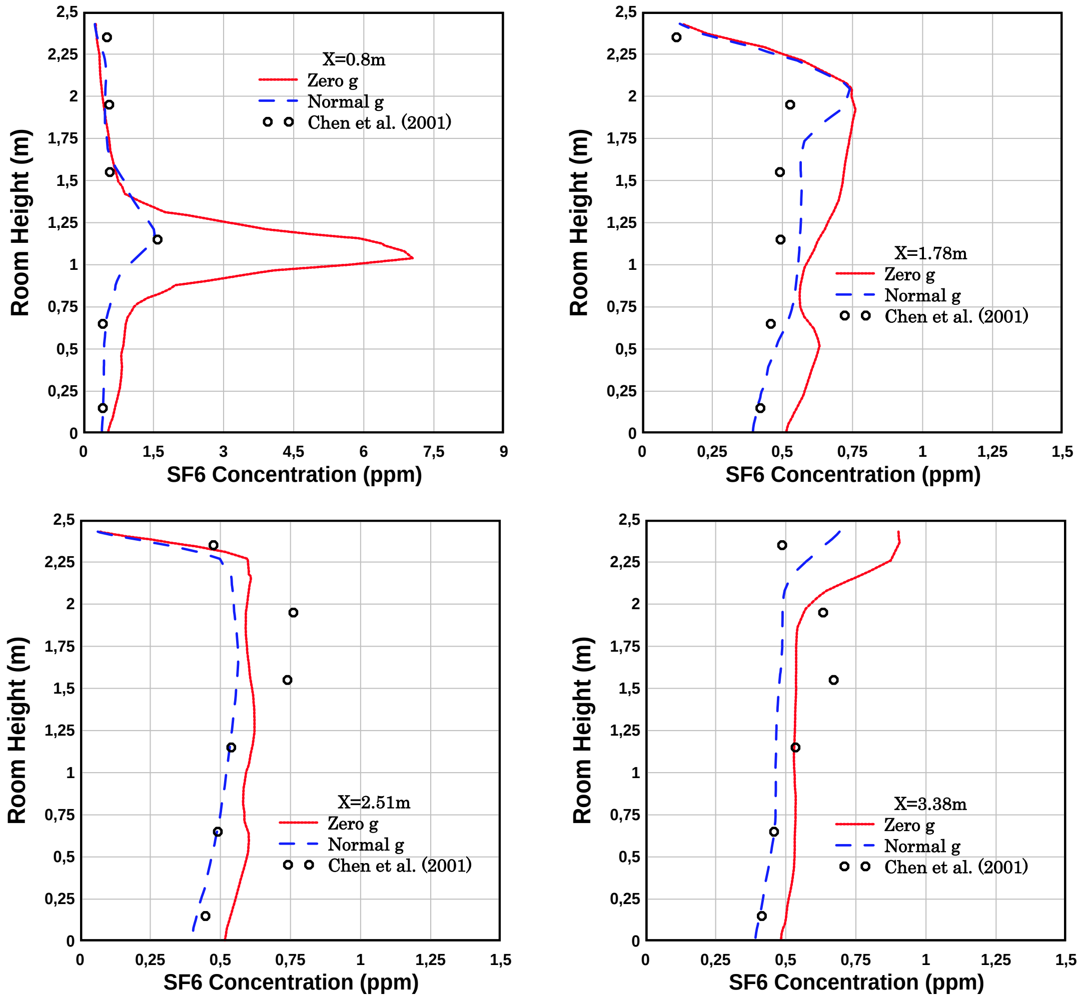

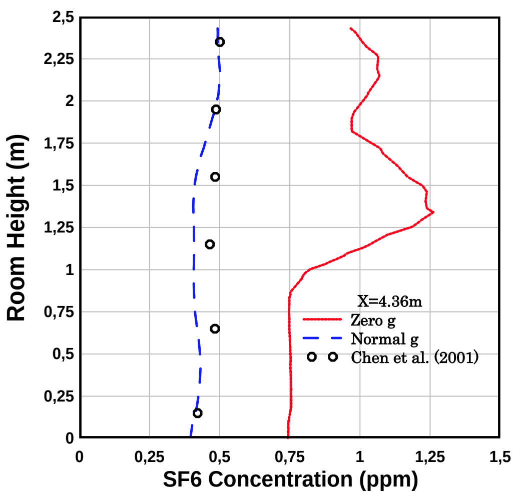

Note:

Mesh size: 302102

Fig. 6.25 Comparison of predicted SF6 concentration profiles under zero-g and normal-g using SST k-ω model

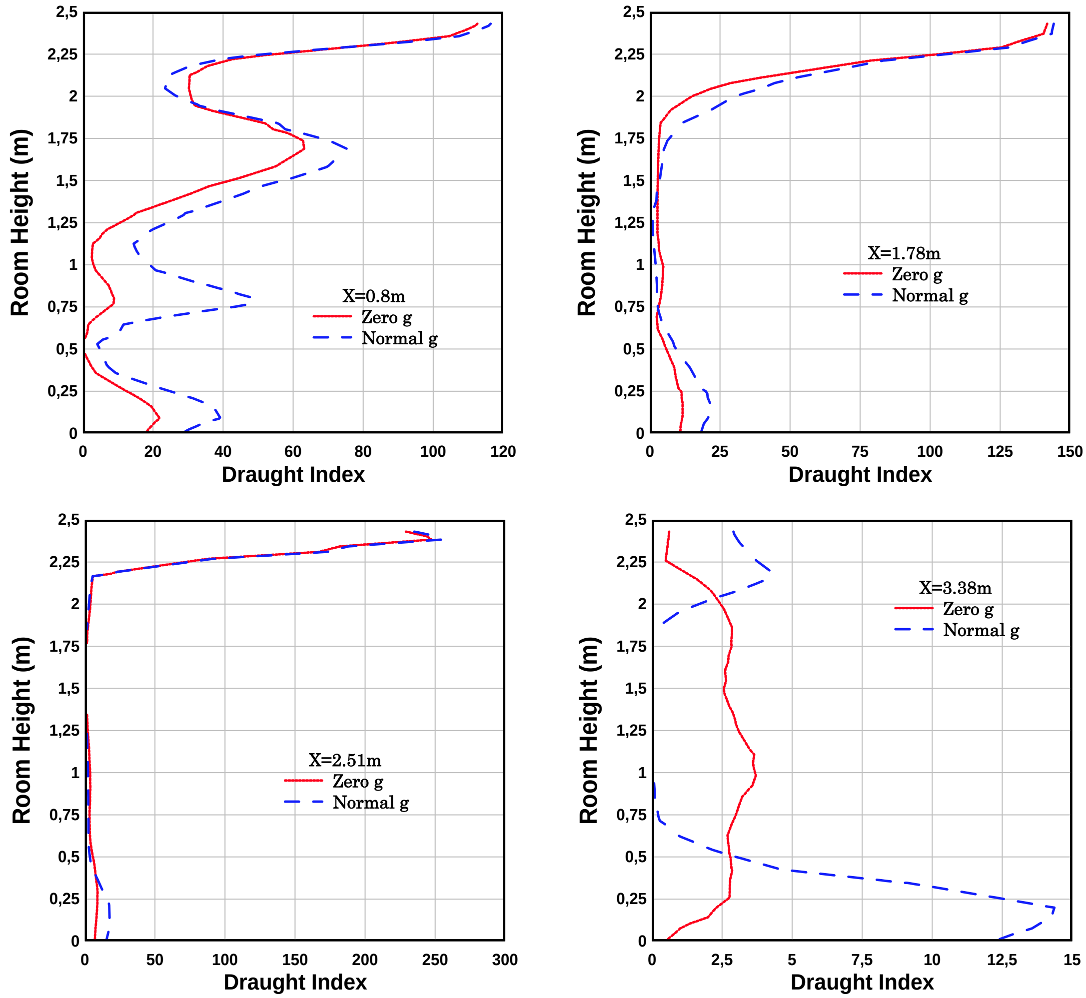

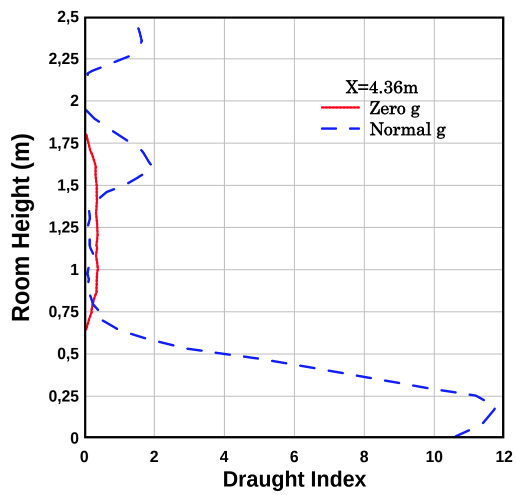

Note:

Mesh size: 302102

Fig. 6.26 Comparison of predicted draught index under zero-g and normal-g using SST k-ω model

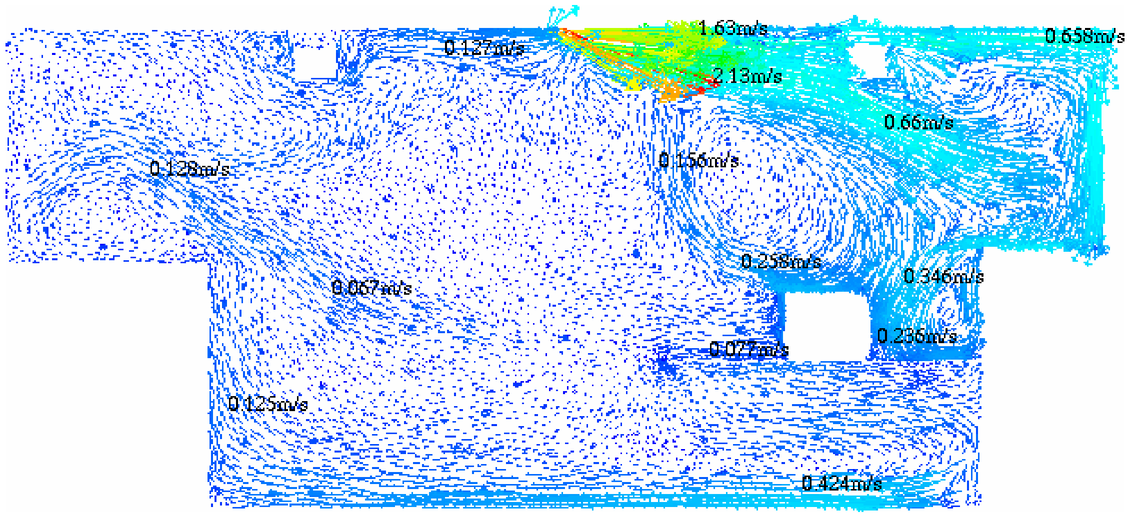

(a) Normal-g

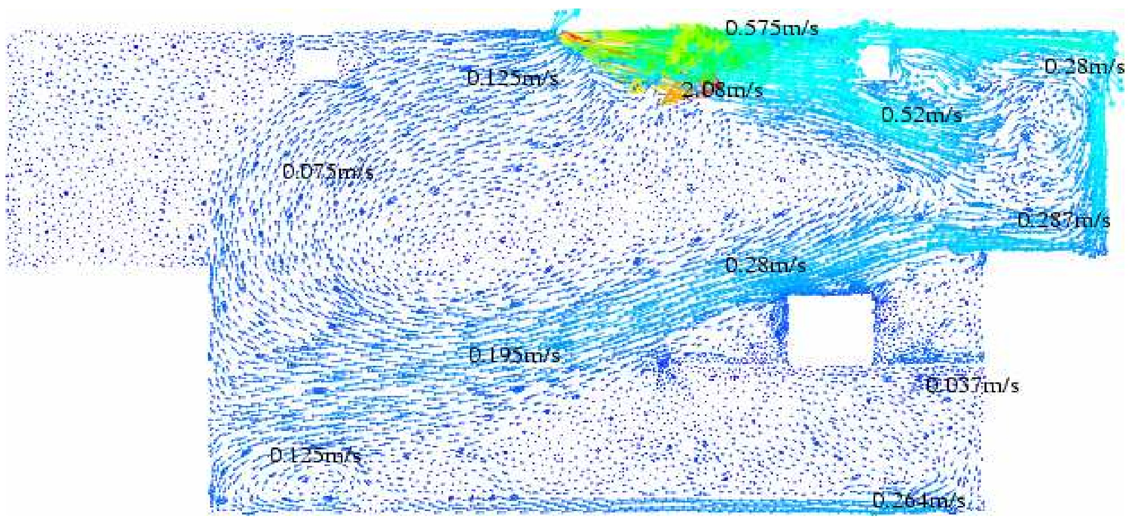

(b) Zero-g

Fig. 6.27 Comparison of the predicted flow fields under normal-g and zero-g conditions at Y=0.275m plane

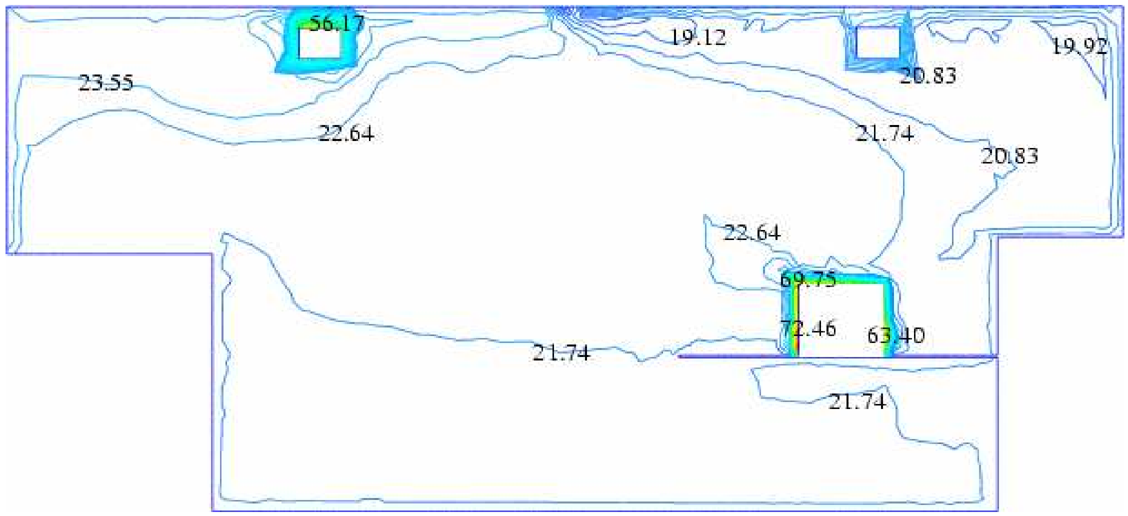

(a) Normal-g (T_{max}=72.46 °C)

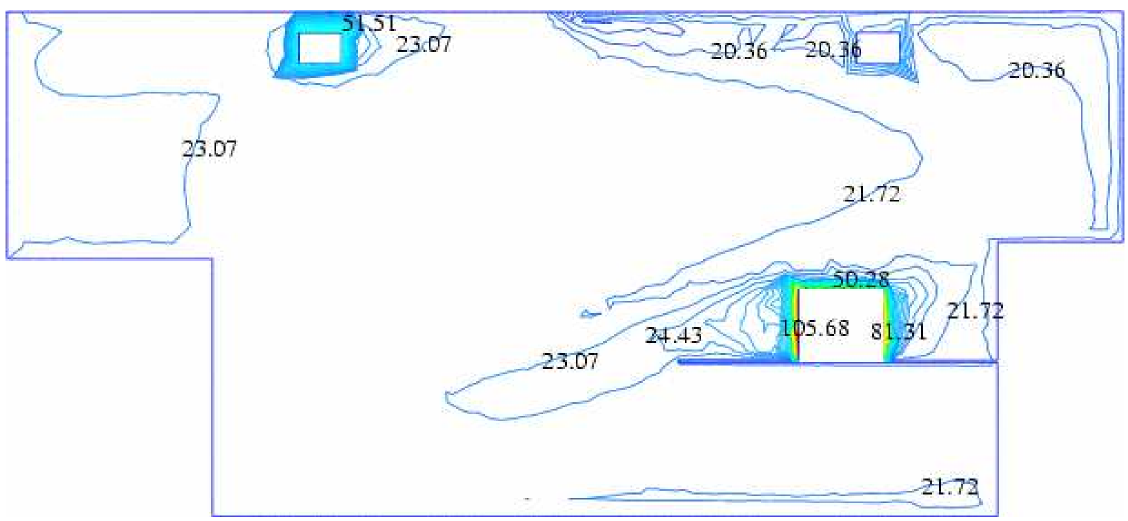

(b) Zero-g (T_{max}=105.68 °C)

Fig. 6.28 Comparison of the predicted temperature distributions under normal-g and zero-g conditions at Y=0.275m plane

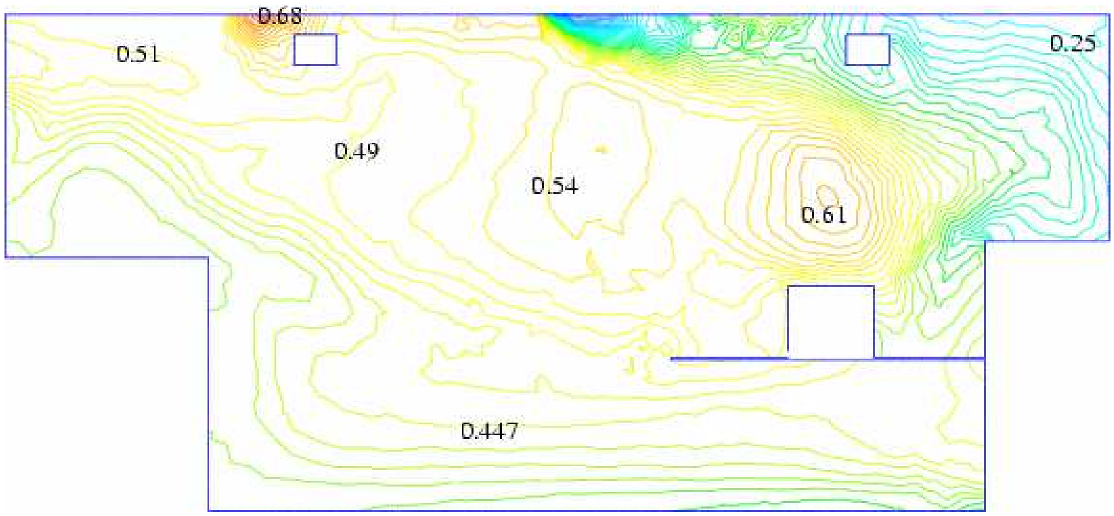

(a) Normal-g (C_{max}=0.68 ppm)

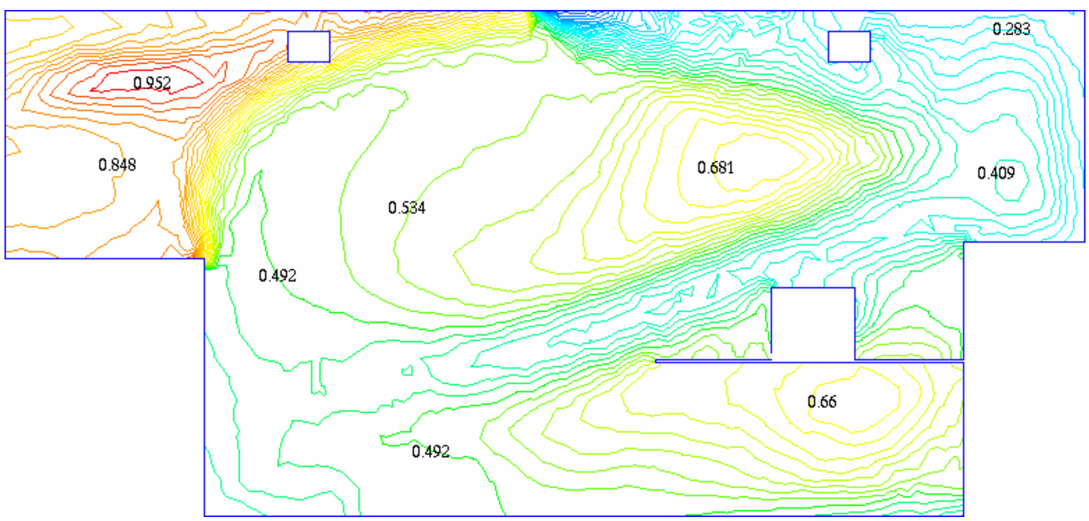

(b) Zero-g (C_{max}=0.952 ppm)

Fig. 6.29 Comparison of the predicted SF6 distributions under normal-g and zero-g conditions at Y=0.275m plane

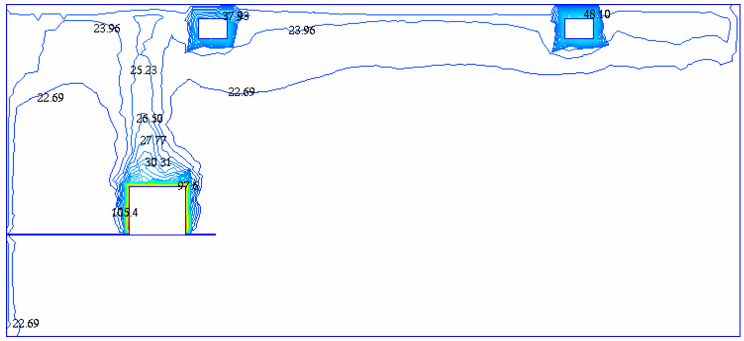

Normal-g (T_{max}=105.4°C)

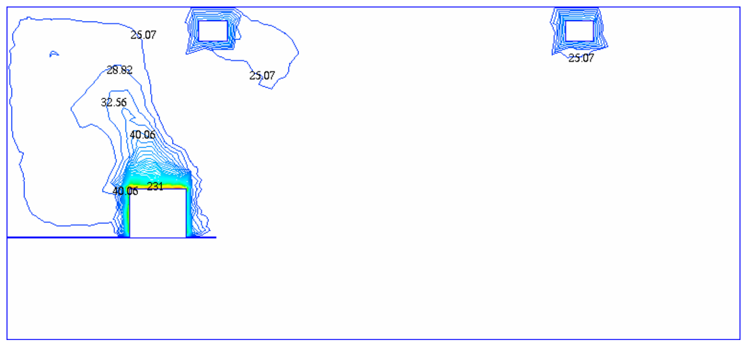

Zero-g (T_{max}=231°C)

(a) Temperature contours at Y=3.375m plane

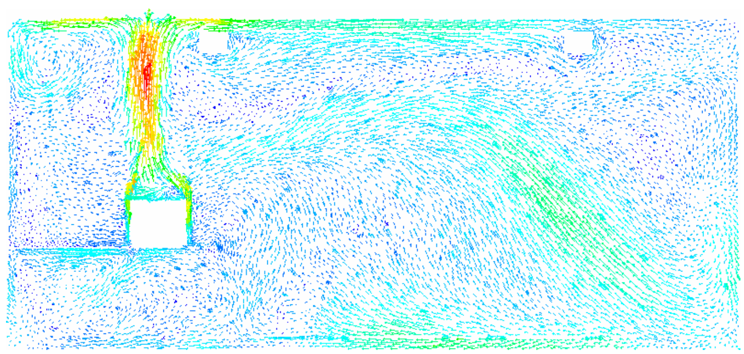
Normal-g

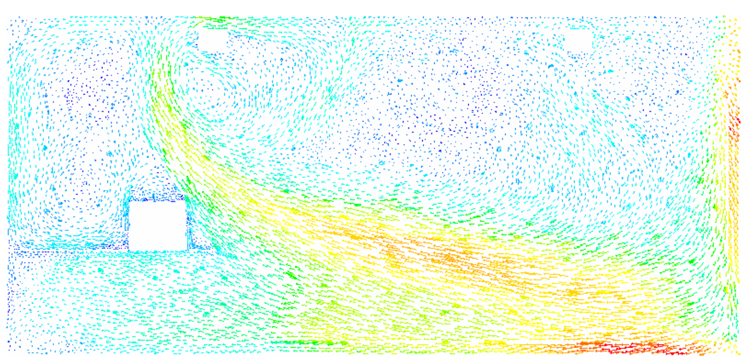
Zero-g

(b) Velocity vectors at Y=3.375m plane

Fig. 6.30 Comparison of the predicted temperature distributions and flow fields under normal-g and zero-g conditions at Y=3.375m plane

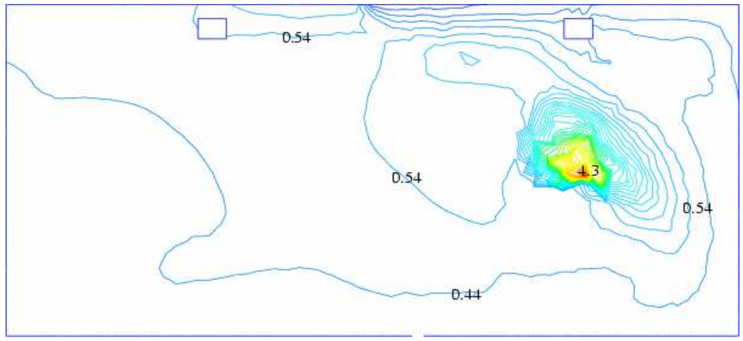

Normal-g (C_{max}=4.3 ppm)

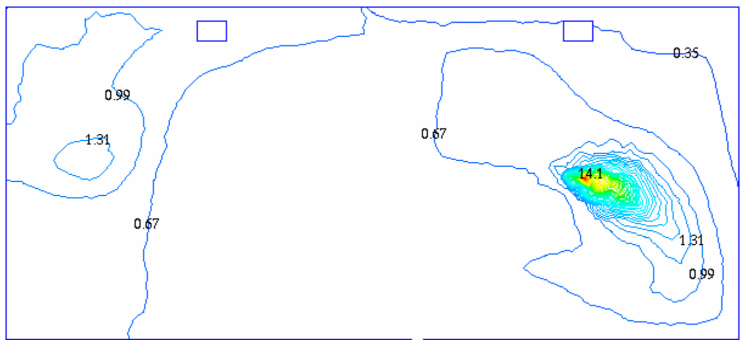

Zero-g (C_{max}=14.1 ppm)

(a) Y=0.85m plane

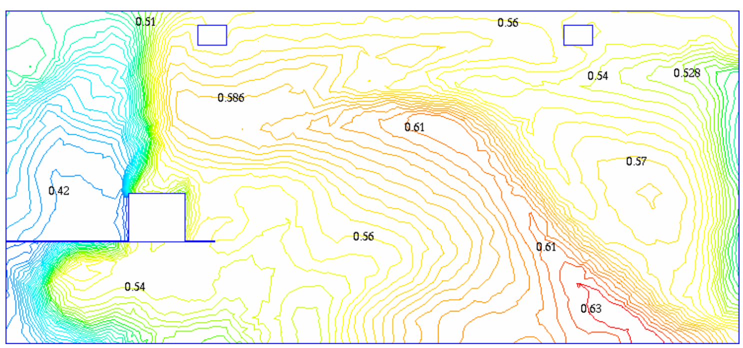

Normal-g (C_{max}=0.63 ppm)

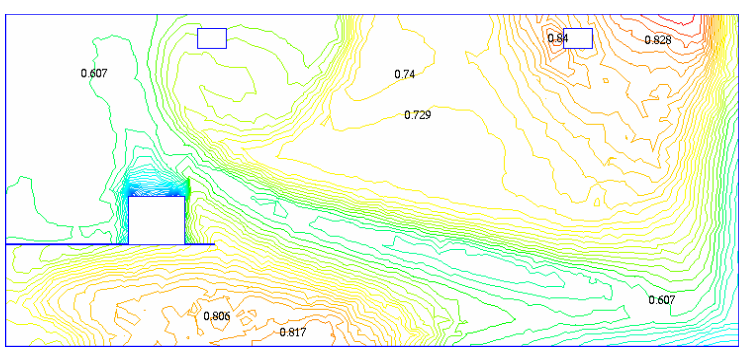

Zero-g (C_{max}=0.828 ppm)

(b) Y=3.375m plane

Fig. 6.31 Comparison of the predicted SF6 distribution under normal-g and zero-g conditions at Y=0.85m and Y=3.375m planes

Chapter 7 General conclusions and perspective for future study

In this chapter general conclusions from this study are summarized.

The long-term objective of the present study is to evaluate the possibility of using numerical simulation by way of Computational Fluid Dynamics (CFD) to investigate the ventilation flows and the associated heat and mass transfer processes inside a spacecraft cabin under microgravity. The study in this thesis focuses mainly on the validation of turbulence models and modeling methods for their capability of correct prediction of some general ventilation flow problems often encountered in ventilated space. Simulations were carried out for the following ventilation flows: (a) ventilation under isothermal and homogeneous conditions; (b) ventilation with internal mass sources (heterogeneous, isothermal) or heat sources (homogeneous, non-isothermal) and (c) ventilation with coupled internal heat and mass sources (heterogeneous and non-isothermal) and the simulation results were validated against experimental data obtained on Earth.

From this study, it can be concluded that numerical simulation can yield reasonable prediction for the above ventilation problems, but model validation is necessary. It can be seen that different models have different performances (advantages and drawbacks) for different problems; a model which works for one case doesn't necessarily mean that it will work for another case, and it is dangerous to validate the models with only 2D cases. More specifically, the following conclusions can be drawn:

- When dealing with practical ventilation flows with coupled heat and mass transfer and with complicated flow configurations, it seems that the SST k-ω model works better than the other two-equation turbulence models, it predicts better the recirculation flow and the flow separation which are often encountered in ventilated rooms with obstacles, although it works badly for the simple 2D case (IEA Annex 20 Test Case 2D). This highlights that the model validation with only 2D test cases is not sufficient for evaluating the performance of a turbulence model for its ability of correctly predicting practical 3D ventilation flows.
- When there are strong recirculations and streamline curvatures in the flows, the RSM model is needed for a better prediction.
- LES with the simple Smagorinsky SGS model is able to predict ventilation flows with complicated flow features like recirculation, separation etc., and it is very useful for studying ventilation flow characteristics. Further tests with non-isothermal cases need to be done to evaluate its performance for the prediction of more practical ventilation flows.
- The correct presentation of the air supply devices in the numerical simulation is of vital importance for the correct prediction of ventilation flows, thus special attention should be paid for the modeling of the air supply devices when carrying out numerical simulation of indoor airflows.
- The near wall treatment method is another very important issue for the correct prediction of indoor airflows; a validation is also needed to verify if the chosen near-wall treatment method is capable of capturing the basic physics of the problem under consideration.
- The microgravity environment has considerable influence on the airflow pattern and air distribution in a habitat. It can be seen that even at a rather large ventilation rate, i.e., with strong forced convection, the predicted air flow pattern, temperature and contaminant distributions still have considerable differences under normal-g and zero-g conditions, especially for the regions where the flow is slow. It has been demonstrated that once a model is validated for the case under consideration, it is very useful to use it to study the airflow and air distribution problems under microgravity, and it can show possible problem regions (over-heating or over-pollution etc.) and provide useful information for the optimization of airflow design which is very difficult to obtain otherwise because in this case a controlled experimental study is very difficult or almost impossible to be carried out on Earth.

Further studies are planned to account for the radiative heat transfer in the CFD predictions to more realistically represent the heat transfer process especially in a microgravity environment.

References

Awbi H. B. 1989. Application of computational fluid dynamics in room ventilation. ***Building and Environment*** 24(1), pp. 73-84.

Bjerg, B. , Svidt, K., Morsing, S. , Zhang, G. and Johnsen, J. O. 1998. Comparison of methods to model a wall inlet in numerical simulation of airflow in livestock rooms, ***EuroAgEng'2000***

Blomqvist, C. 1991a. Measurements of Testcase B (Forced Convection, Isothermal), Research item 1.16, Report No. AN20.1-S-91-SIB1, Working Report, National Swedish Institute for Building Research, May 1991

Blomqvist, C. 1991b. Measurements of Testcase E (Mixed Convection, Summer Cooling). Research Item 1.17, Report No. AN20.1-S-91-SIB2, Working Report, National Swedish Institute for Building Research, March 1991

Buchanan, C. R. 1997. CFD Characterization of a Mechanically Ventilated Office Room: the Effects of Room Design on Ventilation Performance, Ph. D Thesis, University of California

Burgio, F., Gargioli, E., Parodi, P. 1997. Design and development approach for the localized fire detection and suppression function of COLUMBUS APM. 6th European Symposium on Space Environmental Control Systems, Vol.2: 743-754, ESA SP-400, Noordwijk, The Netherlands, 20-22 May 1997

Celik, I. B. 1999. Overview of turbulence modeling for industrial applications, Report No. MAE-IC-99-01, West Virginia University

Chen, Q. 1988. Indoor airflow, air quality and energy consumption of buildings, Ph. D Thesis, Delft University of Technology.

Chen, Q., Moser A. 1991. Simulation of multiple-nozzle diffuser, IEA Annex 20, Research Item 1.20, 12th AIVC Conference, Ottawa, Canada, Sep. 24-27, 1991

Chen, Q. and Jiang, Z. 1992. Significant questions in predicting room air motion. ***ASHRAE Transactions:*** Symposia 98 Part I: 929-939

Chen, Q. 1995. Comparison of different k-ε models for indoor air flow computations. ***Numerical Heat Transfer Part B*** 28: 353-369

Chen, Q. 1996. Prediction of room air motion by Reynolds-stress models. Building and Environment 31(3): 233-244.

Chen, Q. 1997. Computational Fluid Dynamics for HVAC: Successes and Failures***, ASHRAE Transactions*** V. 103, Pt. 1

Chen, Q. and Srebric J. 2001. Simplified diffuser boundary conditions for numerical room airflow models, ***ASHRAE RP-1009***

Davidson, L. and Nielsen, P. V. 1996. Large Eddy Simulation of the Flow in a Three-Dimensional Ventilated Room, ***Proc. of Roomvent'96***, 5th International Conference on Air Distribution in Rooms, Vol. 2, 161-168, July 17-19, Yokohama, Japan

Eckhardt B., Zori, L. 2003. Saving Money and Lives: Simulation and NASA's Lifeboat. (http://www.deskeng.com/articles/03/july/web2/main.htm)

Embacher, E., Huchler, M. 1991. Application of CFD tools in space projects. ***4th European Symposium on Space Environmental Control Systems, Vol. 1***: 529-535, ESA

Emmerich, S. J. 1997. Use of Computational Fluid Dynamics to Analyze Indoor Air Quality Issues, Building and Fire Research Lab., ***NISTIR-5997***

Emmerich, S. J. 1998. Application of a Large Eddy Simulation Model to Study Room Airflow***, ASHRAE Trans., Vol. 104, Part I***

Emvin P. and Davidson L. 1996. A numerical comparison of three inlet approximations of the diffuser in case E1 Annex 20. ***5th Int. Conf. on Air Distributions in Rooms, ROOMVENT'96, Vol. 1***, pp 219-226, 1996.

Ewert, M., Renz, U., Vogl, N. and Zeller, M. 1991. Definition of the flow parameters at the room inlet devices—measurements and calculations, ***Proc. of 12th AIVC Conference***, Ottawa, Canada, Sept. 24-27, 1991

Fanger, P.O., Melikov, A.K., Hanzawa, H. and Ring, R. 1988. Air turbulence and sensation of draught. ***Energy and Buildings*** 12: 21-29.

Fluent Inc. 2001. Fluent 6 User Manual.

Fontaine J. R., Biolley F., Rapp, R., Sérieys J. C. and Cunin J. C. 1994. Analysis of a three dimensional ventilation flow: experimental validation on a waters scale model of numerical simulations. ***Numerical Heat Transfer Part A*** 26: 431-451.

Gan G. 1998. Prediction of turbulent buoyant flow using an RNG k-ε model, ***Numerical Heat Transfer, Part A*** 33: 169-189.

Gibson M. M. and Launder B. E. 1978. Ground Effects on Pressure Fluctuations in the Atmospheric Boundary Layer. ***J. Fluid Mech***. 86:491-511

Gosman, A. D., 1999. Developments in CFD for industrial and environmental applications in wind engineering, ***J. Wind Eng. Ind. Aerodyn***. 81: 21-39

Heikkinen J. 1991a. Modeling of supply air terminal for room air flow simulation. Proc. of 12th AIVC Conference, Ottawa, Canada, Sept. 24-27, 1991.

Heikkinen J. 1991b. Measurement of test case B2, B3, E2 and E3 (isothermal and summer cooling cases), Research item No. 1.16SF and 1.17SF, Report No. AN20.1-SF-91-VTT08, Annex Report, Technical Research Centre of Finland (VTT), 1991.

Heindel, T.J., Ramadhyani, S. and Incropera, F. P. 1994. Assessment of Turbulence Models for Natural Convection in an Enclosure, ***Numerical Heat Transfer, Part B*** 26: 147-172

Heiselberg, P. 1991, Measurements of test case F (Forced convection, isothermal with contaminants***), ISSN 0902-7531 R9132***

Henkes R. A. W. and Hoogendoorn, C. J. 1989. Comparison of turbulent models for the natural convection boundary layer along a heated vertical plate, ***Int. J. Heat mass Transfer*** *32(1): 157-169*

Ideriah, F. J. K. 1980. Prediction of turbulent cavity flow driven by buoyancy and shear. ***J. Mech. Engng Sci.*** 22, 287-295.

Jaw, S. Y., Chen , C. J. 1998a. Present status of second-order closure turbulence models--I. Overview. ***Journal of Engineering Mechanics*** May 1998: 485-501.

Jaw, S. Y., Chen , C. J. 1998b. Present status of second-order closure turbulence models--II. Applications. ***Journal of Engineering Mechanics*** May 1998: 501-512.

Jorgensen, C. A. Ed., International Space Station Evolution Data Book, Volume I. Baseline Design, Revision A, ***NASA/SP-2000-6109/VOL1/REV1***, Oct. 2000

Joubert, P., Sandu, A., Beghein, C. and Allard, F. 1996. Numerical study of the influence of inlet boundary conditions on the air movement in a ventilated room, ***Proc. of ROOMVENT'96, Vol. 1***, pp. 235-242

Kader, B. 1993. Temperature and Concentration Profiles in Fully Turbulent Boundary Layers***, Int. J. Heat Mass Transfer*** 24(9):1541-1544

Koskela H., Heikkinen, J., Niemelä, R., Hautalampi, T. 2001. Turbulence correction for thermal comfort calculation, ***Building and Environment*** 36: 247-255.

Koskela H., Heikkinen, J. 2002. Calculation of thermal comfort from CFD-simulation results, Indoor air 2002, ***9th International Conference on Indoor Air Quality and Climate***, Monterey, CA, 30, June 5 – July 7 2002, Vol. 3: 712-717, 2002

Kovanen, K., Seppänen, O., Siren, K. and Majanen, A. 1987. Air velocity, turbulence intensity and fluctuation frequency in ventilated spaces. ***Proceedings of Roomvent'87***, Stockholm, Sweden

Launder, B. E., Spalding, D. B. 1972. Mathematical models of turbulence. Academic Press, London 1972.

Launder, B. E., Spalding, D. B. 1974. The Numerical Computation of Turbulent Flows. ***Computer Methods in Applied Mechanics and Engineering*** 3:269-289

Launder, B. E., Reece, G. J., and Rodi, W. 1975. Progress in the Development of a Reynolds-Stress Turbulence Closure. ***J. Fluid Mech.*** 68(3):537-566.

Launder, B. E. 2002. Private discussion

Lemaire, A. D. 1993. Annex 20 Air Flow Patterns within Buildings: Room air and contaminant flow, evaluation of computational methods—Subtask-1 Summery Report, TNO Building and Construction Research

Lepers, S., Aude, P. , Depecker, P. and Guarracine, G. 1998. Numerical Prediction of Mixed Turbulent Airflow within a Cavity Using Various Turbulence Models, ***EPIC'98, Vol. 3***, 929-934.

Lin, C. H., Son, C. H., Horstman, R. H. 2000. CFD studies on the ECLSS airflow and CO2 accumulation of the International Space Station, ***SAE 2000-01-2364***

Loomans, M.G. L. C. and Mook, F. J. R. van. 1995. Survey on measuring indoor air flows. FAGO report 95.25.W, Eindhoven University of Technology.

Loomans M. G. L. C. 1998. The Measurement and Simulation of Indoor Air Flow. Ph. D Thesis, Eindhoven University of Technology

Luo, S., Roux B. Modeling of the HESCO nozzle diffuser used in IEA Annex 20 experiment test room, accepted by ***Building and Environment***, 2003

Markatos, N. C., Malin M. R. M. and Cox M. 1982. Mathematical modeling of buoyancy-Induced smoke in enclosures, ***Int. J. Heat Mass Transfer*** 25(1): 63-75

Markatos, N. C. 1987. Computer simulation techniques for turbulent flows. In: Cheremisinoff, N. P. (Ed.) ***Encyclopedia of Fluid Mechanics, Vol. 6*** - Complex Flow Phenomena and Modelling: 1221-1275, Gulf Publishing Co. 1987.

Markus, H., Karl, H. 1992 Analysis of CO2-distribution in the CLUMBUS subfloor area for fire suppression purposes, ***Proc. of 22nd International Conference on Environmental Control Systems***, SAE, Seattle, WA, July 13-16, 1992

McConnaughey, P. 1992. Space Station Flow Analysis. (http://www.nas.nasa.gov/pubs/TechSums/9293/105.html)

Melikov, A.K., Hanzawa, H. and Fanger, P.O. 1988. Airflow characteristics in the occupied zone of heated space without mechanical ventilation. ***ASHRAE Transactions*** 94 Part 1: 52-70.

Melikov, A.K., Langkilde, G. and Derbiszewski, B. 1990. Airflow characteristics in the occupied zone of rooms with mechanical ventilation. ***ASHRAE Transactions*** 96 Part 1: 555-563.

Melikov, A.K., Krüger, U., Zhou, G., Madsen, T.L. and Langkilde, G. 1997. Air temperature fluctuations in rooms, ***Building and Environment*** 32(2): 101-114

Moser, A. 1991. The message of annex 20: air flow patterns within buildings, ***Proc. of 12th AIVC Conference***, Ottawa, Canada, Sept. 24-27, 1991

Murakami S., Kato S. 1989. Numerical and experimental study on room airflow — 3-D predictions using the k-ε turbulence model. ***Building and Environment*** 24(1): 85-97.

Murakami, S., Kato, S., Kobayashi H. and Hanyu, F., 1995. Current Status of CFD Application to Air-Conditioning Engineering. ***Pan Pacific Symposium on Building and Urban Environmental Conditioning in Asia.***, 24 pp.

Murakami, S., Kato, S. and Zang, J. 1998. Numerical Simulation of Contaminant Distribution Around a Modeled Human Body: CFD Studies on Computational Thermal Manikin-Part II, ***ASHRAE Trans.***

Murakami, S. 1999. Current status and future trends in computational wind engineering, ***J. Wind Eng. Ind. Aerodyn.*** 67 & 68, 3-34

NASA-TD9702A, International Space Station Familiarization, Mission Operations Directorate, Space Flight Training Division, Lyndon B. Johnson Space Center, Houston, Texas, Jul 31, 1998

NASA Facts, International Space Station Environmental Control and Life Support System, FS-2002-05-85-MSFC, Marshall Space Flight Center, Alabama, May 2002

Nielsen, P. V. 1974. Flow in Air Conditioned Rooms, Ph. D Thesis, Technical University of Denmark

Nielsen, P. V., Restivo, A. and Whitelaw, J. H. 1978. The velocity characteristics of ventilated rooms, ***J. Fluids Engng.*** 100: 291-298

Nielsen P. V., Restivo, A. and Whitelaw, J. H. 1979. Buoyancy-affected flows in ventilated rooms. ***Numerical Heat Transfer*** 2: 115-127.

Nielsen, P. V. 1990. Specification of a two-dimensional test case Research item No. 1.45, ISSN 0902-7513 R9040, Dept. of Building technology and Structural Engineering, Aalborg University, Danmark

Nielsen, P. V. 1992. Description of supply openings in numerical models for room air distribution, ***ASHRAE Transactions*** 98(1): 963-971.

Nielsen, P. V. 1997. The box method—a practical procedure for introduction of an air supply device in CFD calculation, Institute for Bygningsteknik, Aalborg University

Nielsen, P. V. 1998. The Selection of Turbulence Models for Prediction of Room Airflow***, ASHRAE Transactions, Vol. 104, Part 1B***, 1119-1127

Peng S-H, 1994 Indoor Air Flow and its Simulation: A Review and Evaluation, ***Climate and Buildings*** 2: 5-98

Peng, S-H, 1998. Modelling of Turbulent Flow and Heat Transfer for Building Ventilation, Ph. D Thesis, Chalmers University of Technology

Piomelli, U. 1996. Large-eddy simulation of turbulent flows--Invited poster presented at the ONR 50th Anniversary Symposium, Washington, DC, May 22, 1996.
(http://www.glue.umd.edu/~ugo/research/poster.html)

Piomelli, U. 1999. Large-eddy simulation: achievements and challenges***, Progress in Aerospace Science 35***: 335-362

Restivo, A. 1979. Turbulent Flow in Ventilated Rooms. Ph. D Thesis. Imperial Colledge, London. March 1979.

Rodi, W. 1980. Turbulence models and their application in hydraulics—A state of art review. International Association of Hydraulic Research.

Rodi, W. 2000. Simulation of turbulence in practical flow calculations. ***Proc. of ECOMAS 2000***, Barcelona, 11-14 September 2000.

Roos, A. 1998. On the Effectiveness of Ventilation, Ph. D Thesis, Eindhoven University of Technology

Sandberg, M. 1987. Velocity characteristics in mechanically ventilated office rooms. ***Proceedings of Roomvent'87***, Stockholm, Sweden

Schiestel, R. 1998. Les Écoulements Turbulents--Modélisation et Stimulation. Editions Hermès 1998.

Schild, P. 1997. Accurate prediction of indoor climate in glazed enclosures. Ph. D Thesis, Norwegian Univ. of Science and Technology (NTNU), 1997

Schulte, T. E., Bergstrom, D. J. and Bugg, J. D. 1998. Numerical Simulation of Three-Dimensional Airflow in Unfurnished Rooms, ***ASHRAE Transactions***.

Skovgaard, M. and Nielsen, P. V. 1991a. Simulation of simple test case, case 2D1 (two-dimensional isothermal forced convection). Research Item 1.46dk, ISSN 0902-7513 R9131, Dept. of Building technology and Structural Engineering, Aalborg University, Danmark

Skovgaard, M. and Nielsen, P. V. 1991b. Modeling complex geometries in CFD—applied to air flow in ventilated rooms, ***Proc. of 12th AIVC Conference, Ottawa***, Canada, Sept. 24-27, 1991

Steelant, J., Romera-Pere, J. A., Bouckaert, F., Tamburini, P., Witt, J. 2001. Flow analysis for spacecraft. ***ESA Bulletin 107***: 106-111, August 2001

Terzi, D. A. V. Computing Turbulent Flows, 1996
(http://cfd.ame.arizona.edu/~dominic/RESEARCH/PROJECTS/numerics.html)

Versteeg H. K. and Malalasekera W. 1995. Introduction to computational fluid dynamics. Longman Group Ltd.

Vieser, W., Esch, T., Menter, F. 2002. Heat transfer predictions using advanced two-equation turbulence models. ***CFX-VAL 10/0602***.

Wieland, P. O., Designing for Human Presence in Space: An Introduction to Environmental Control and Life Support Systems, ***NASA RP-1324***, Marshall Space Flight Center, Alabama, 1994

Wieland, P. O., Living together in Space; The Design and Operation of the Life Support Systems on the International Space Station, ***NASA-TM-1998-206956/Vol. 1***, Marshall Space Flight Center, Alabama, Jan. 1998

Wilcox. D. C. 2000. Turbulence Modeling for CFD, DCW Industries, Inc., La Canada, California

Xu, W. 1998. New Turbulence Models for Indoor Airflow Simulation, Ph. D Thesis, Massachusetts Institute of Technology

Zhang G., Morsing S., Bierg B., Svidt, K., Strøm J. S. 2000. Test room for validation of airflow patterns estimated by computational fluid dynamics. ***J. Agric. Engng. Res.*** 76: 141-148.

Appendix

Appendix 1-1 Comparison of predicted mean air speed profiles (RNG k-ε model; full room and half room approach) with measurements at the 6 side planes (Z=±0.6m, ±1.2m, ±1.7m; IEA Annex 20 Test Case B2)

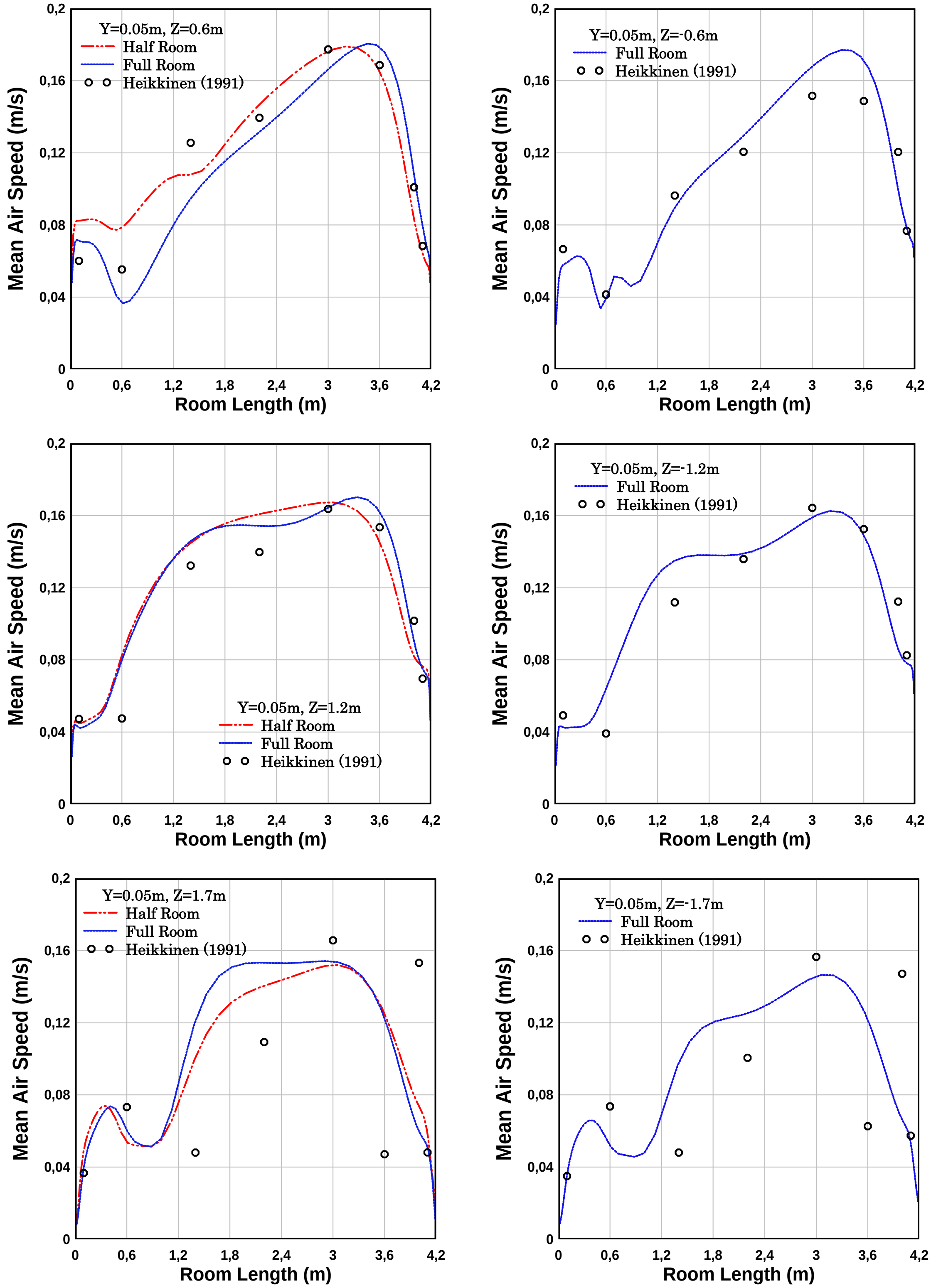

Fig. A-1-1-1 Y=0.05m (Test Case B2)

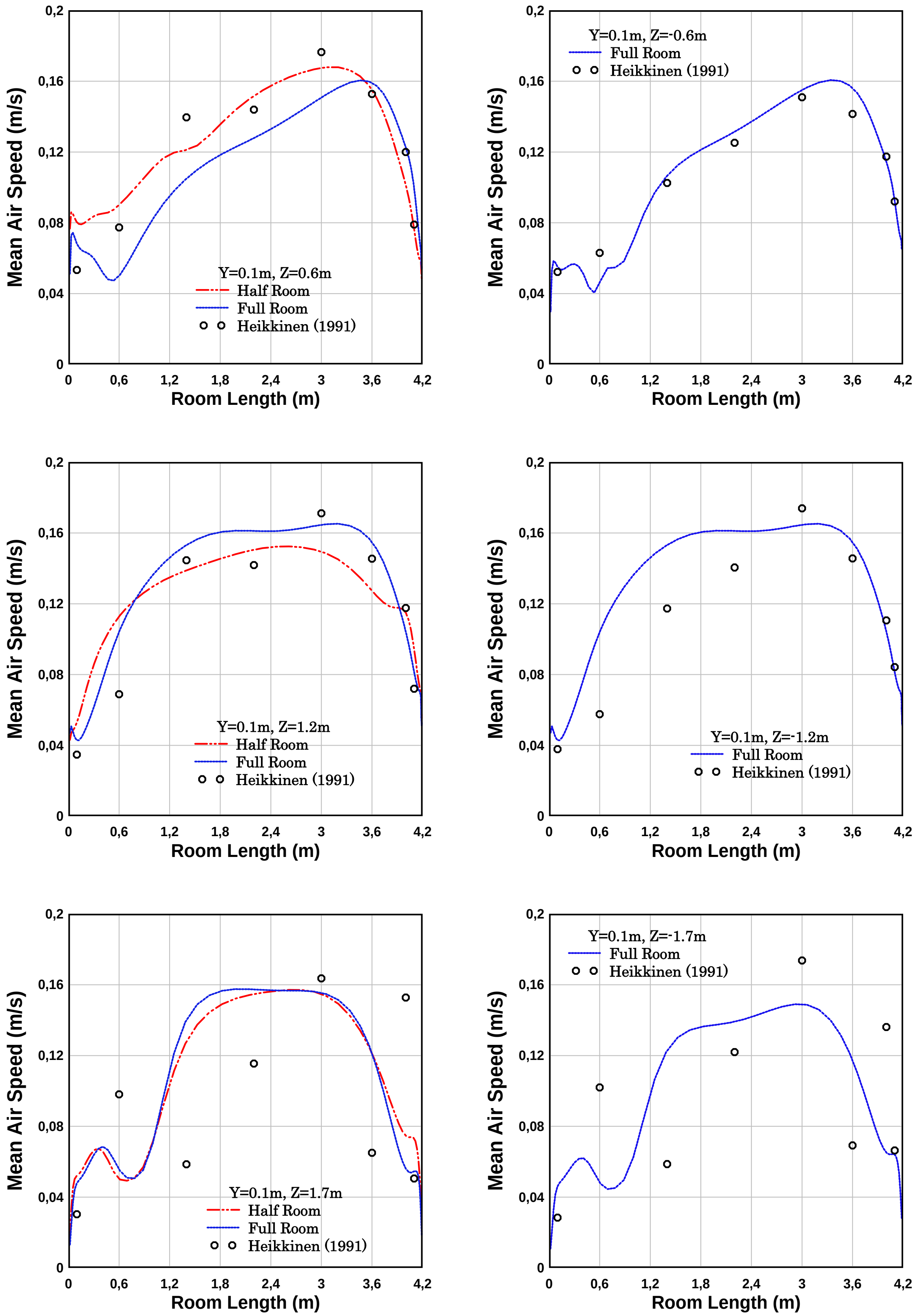

Fig. A-1-1-2 Y=0.1m (Test Case B2)

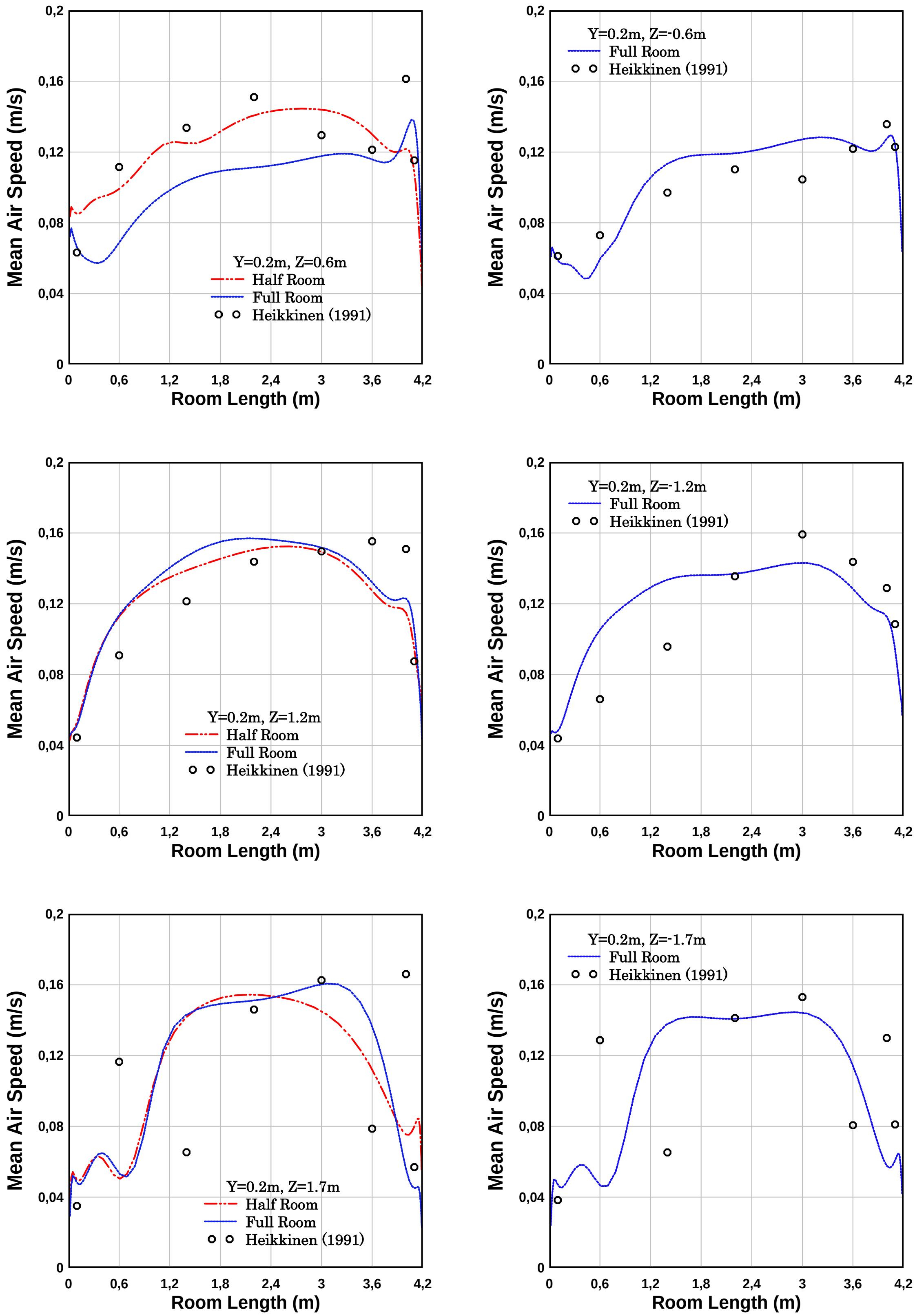

Fig. A-1-1-3 Y=0.2m (Test Case B2)

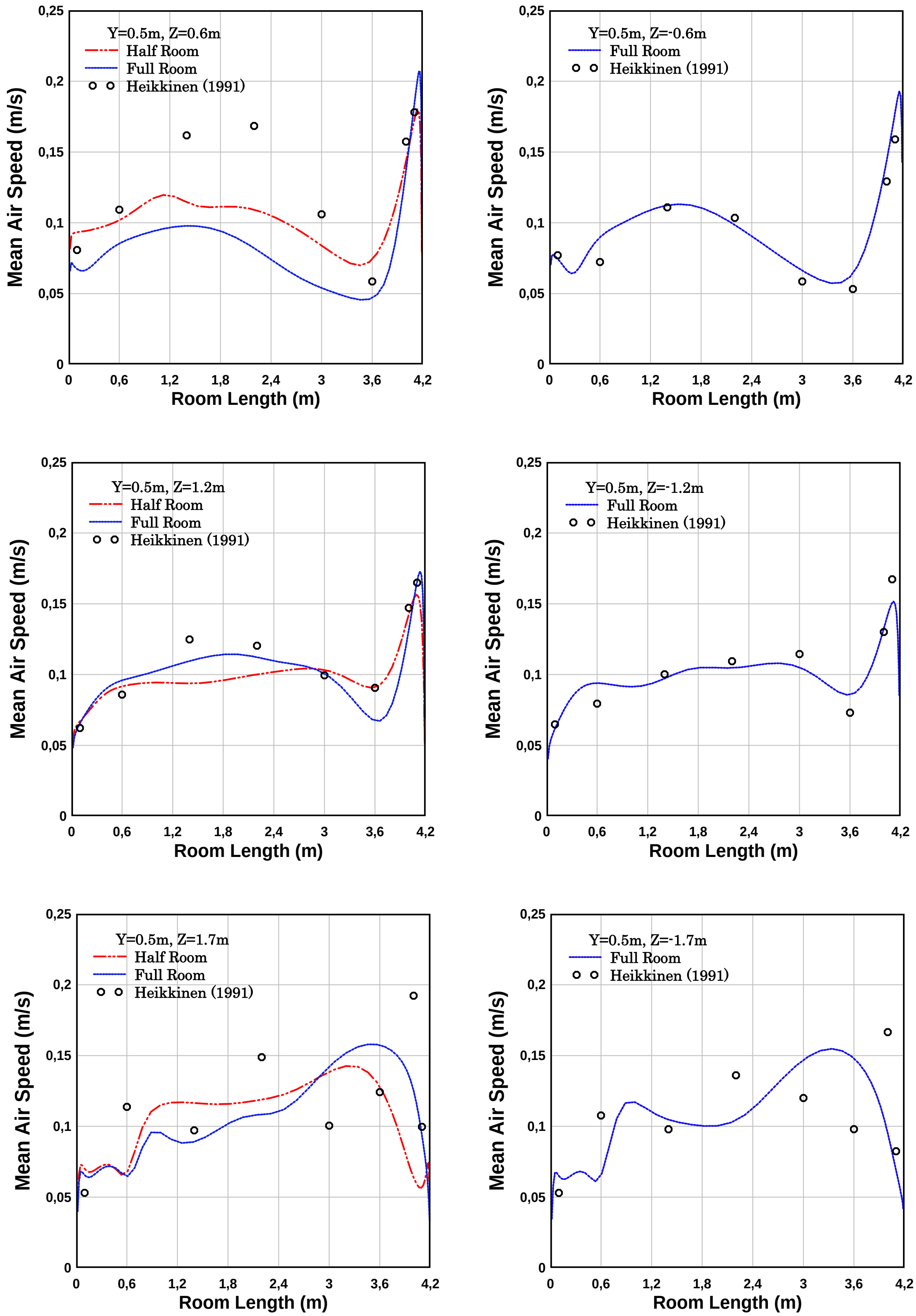

Fig. A-1-1-4 Y=0.5m (Test Case B2)

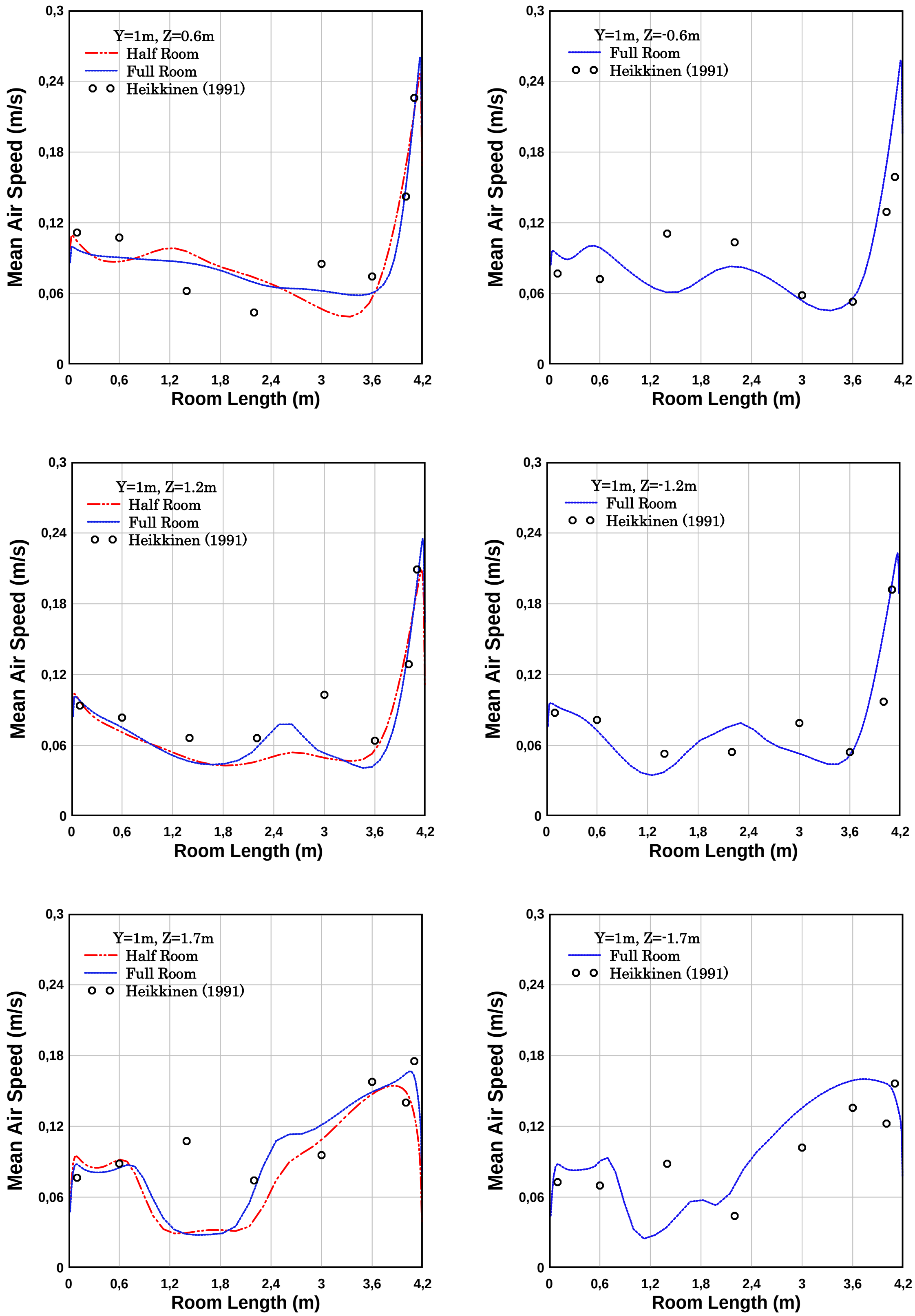

Fig. A-1-1-5 Y=1.0m (Test Case B2)

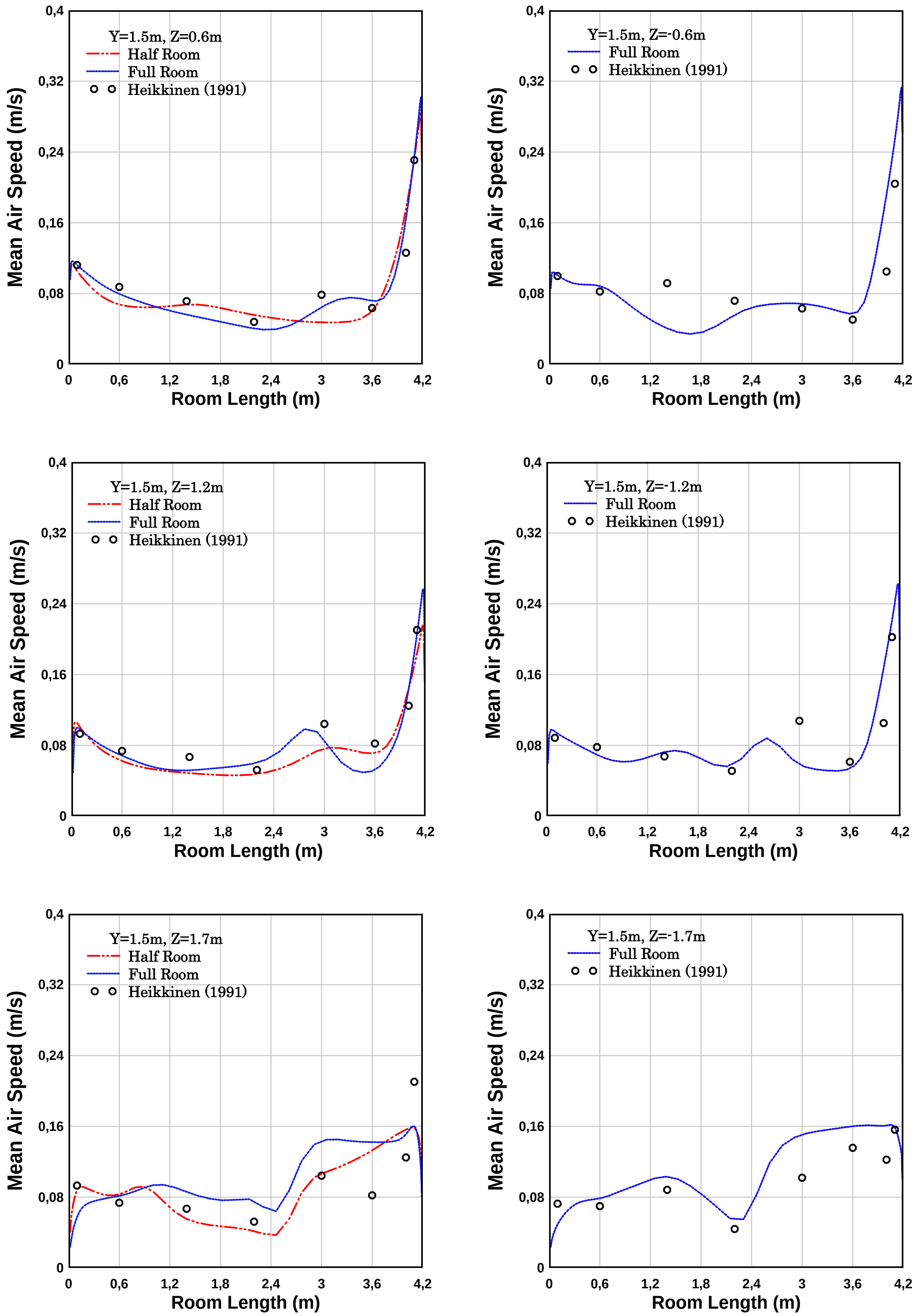

Fig. A-1-1-6 Y=1.5m (Test Case B2)

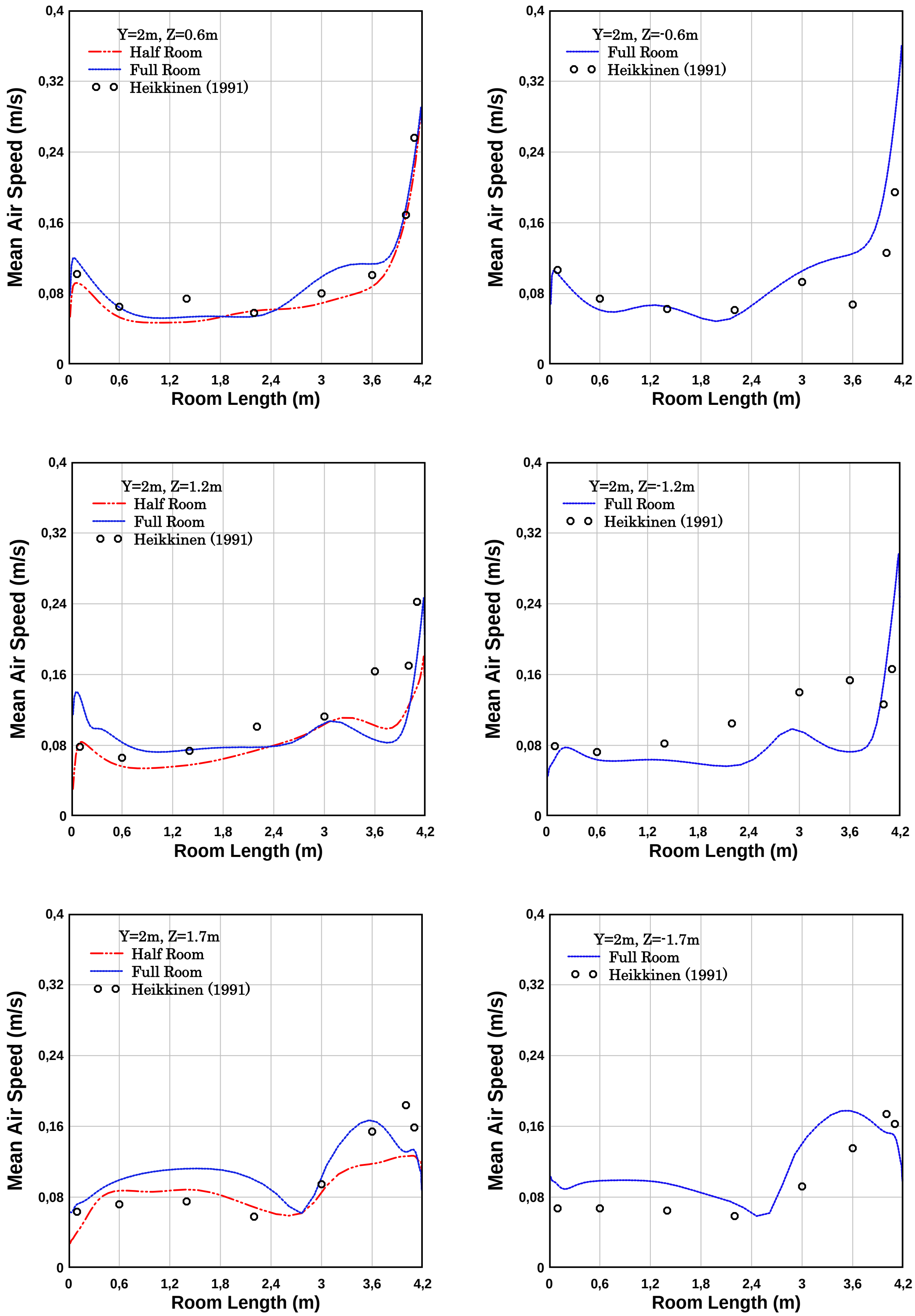

Fig. A-1-1-7 Y=2.0m (Test Case B2)

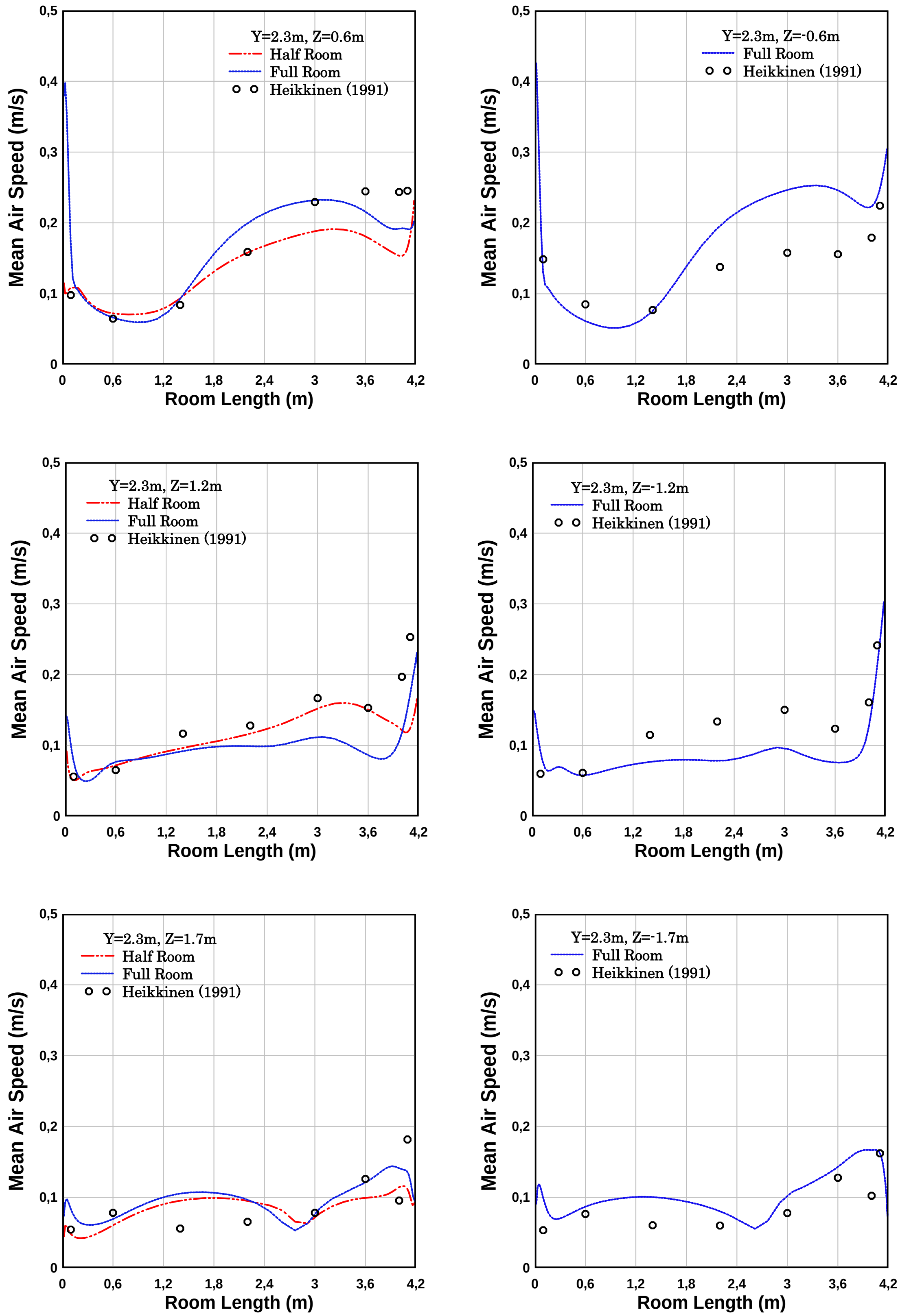

Fig. A-1-1-8 Y=2.3m (Test Case B2)

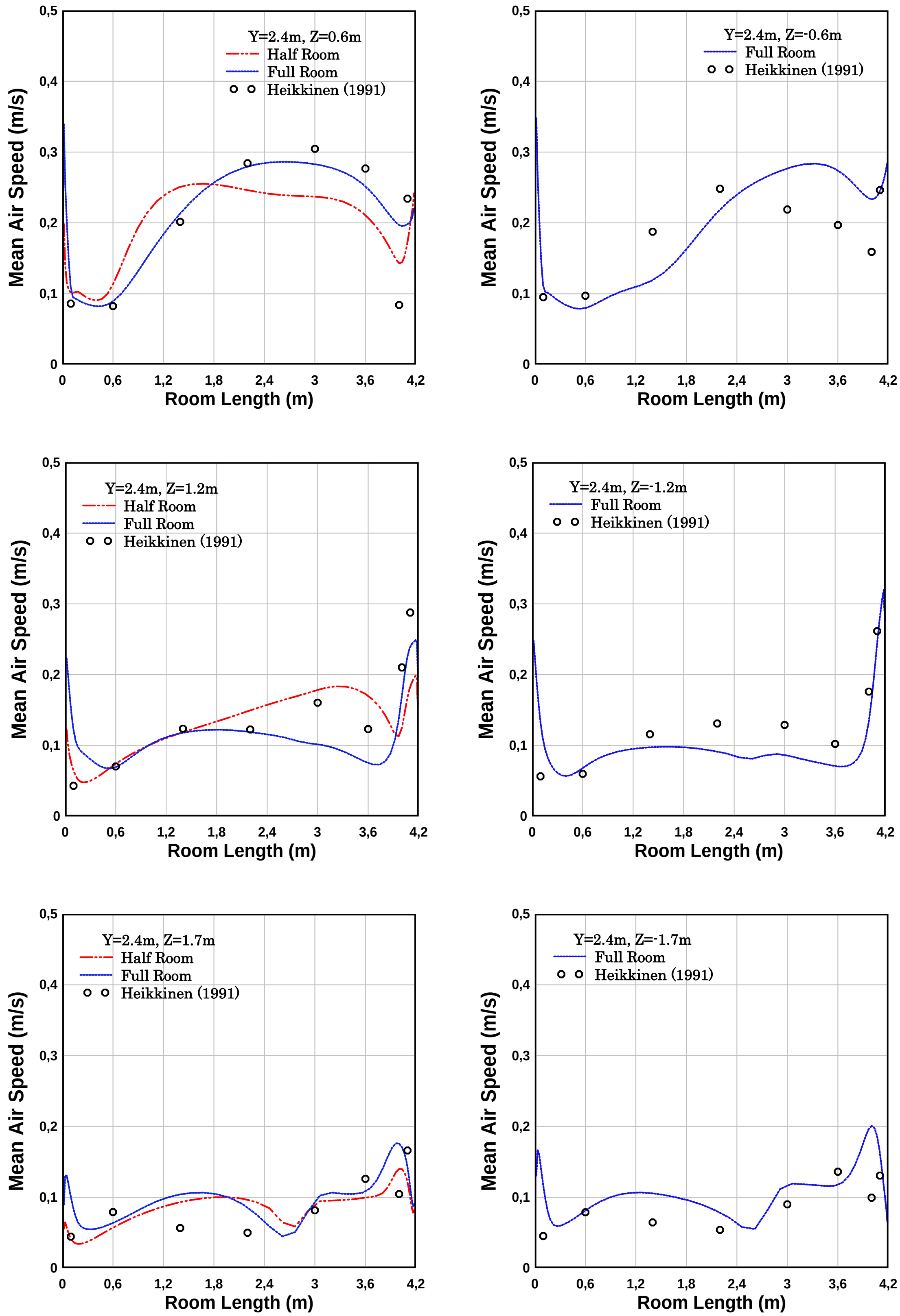

Fig. A-1-1-9 Y=2.4m (Test Case B2)

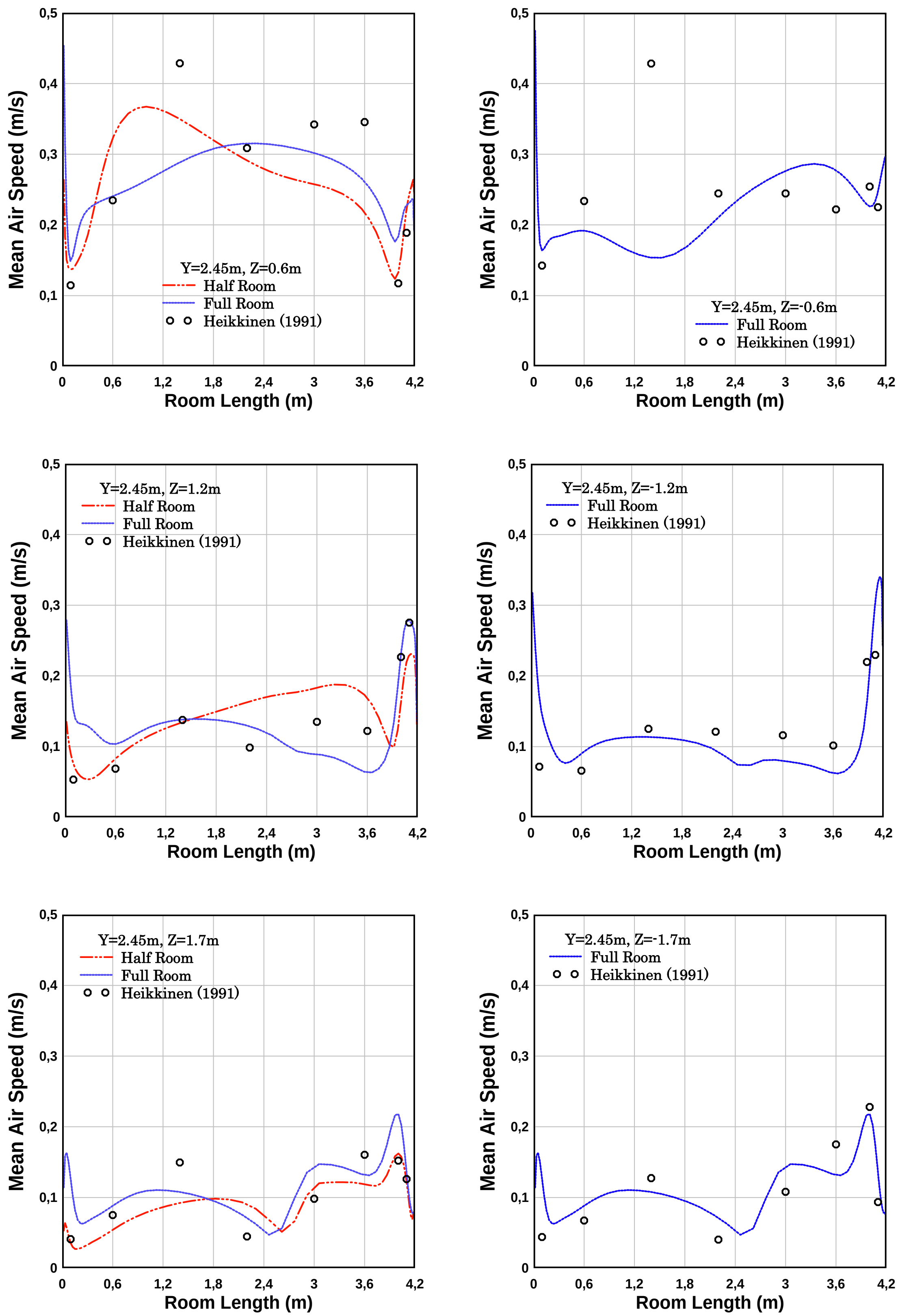

Fig. A-1-1-10 Y=2.45m (Test Case B2)

Appendix 1-2 Comparison of predicted mean air speed profiles (RNG k-ε model; full room and half room approach) with measurements at the 6 side planes (Z=±0.6m, ±1.2m, ±1.7m; IEA Annex 20 Test Case B3)

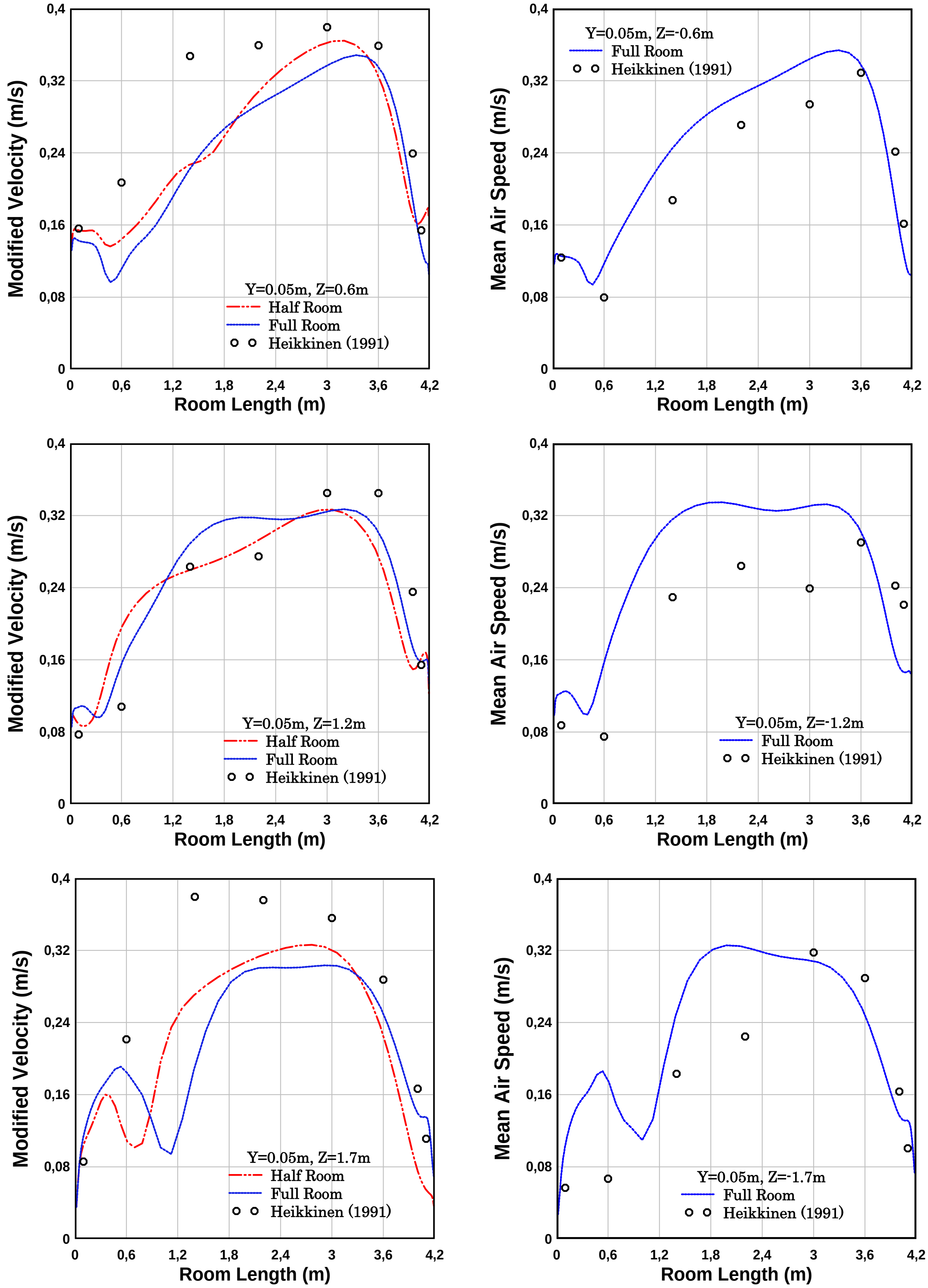

Fig. A-1-2-1 Y=0.05m (Test Case B3)

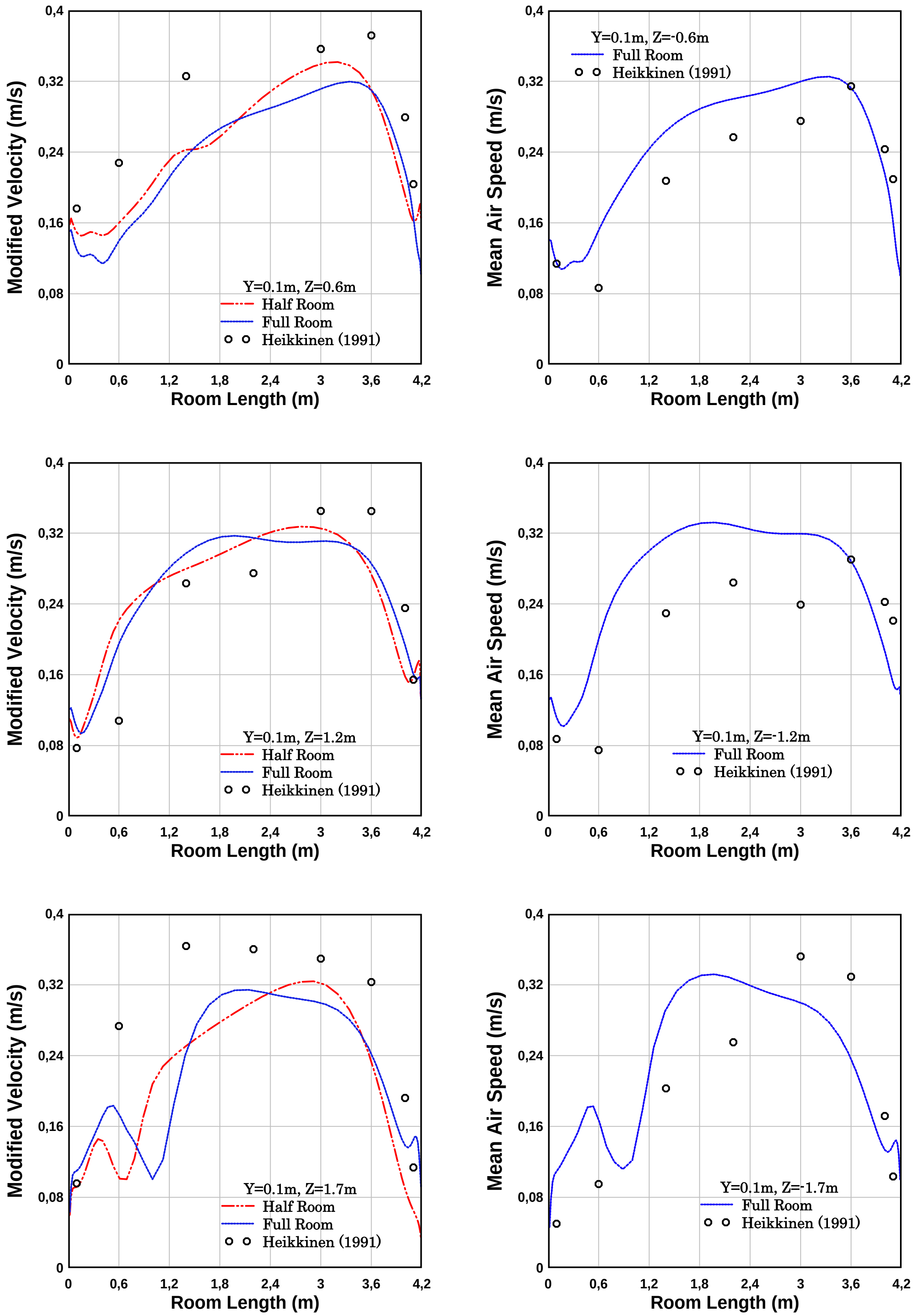

Fig. A-1-2-2 Y=0.1m (Test Case B3)

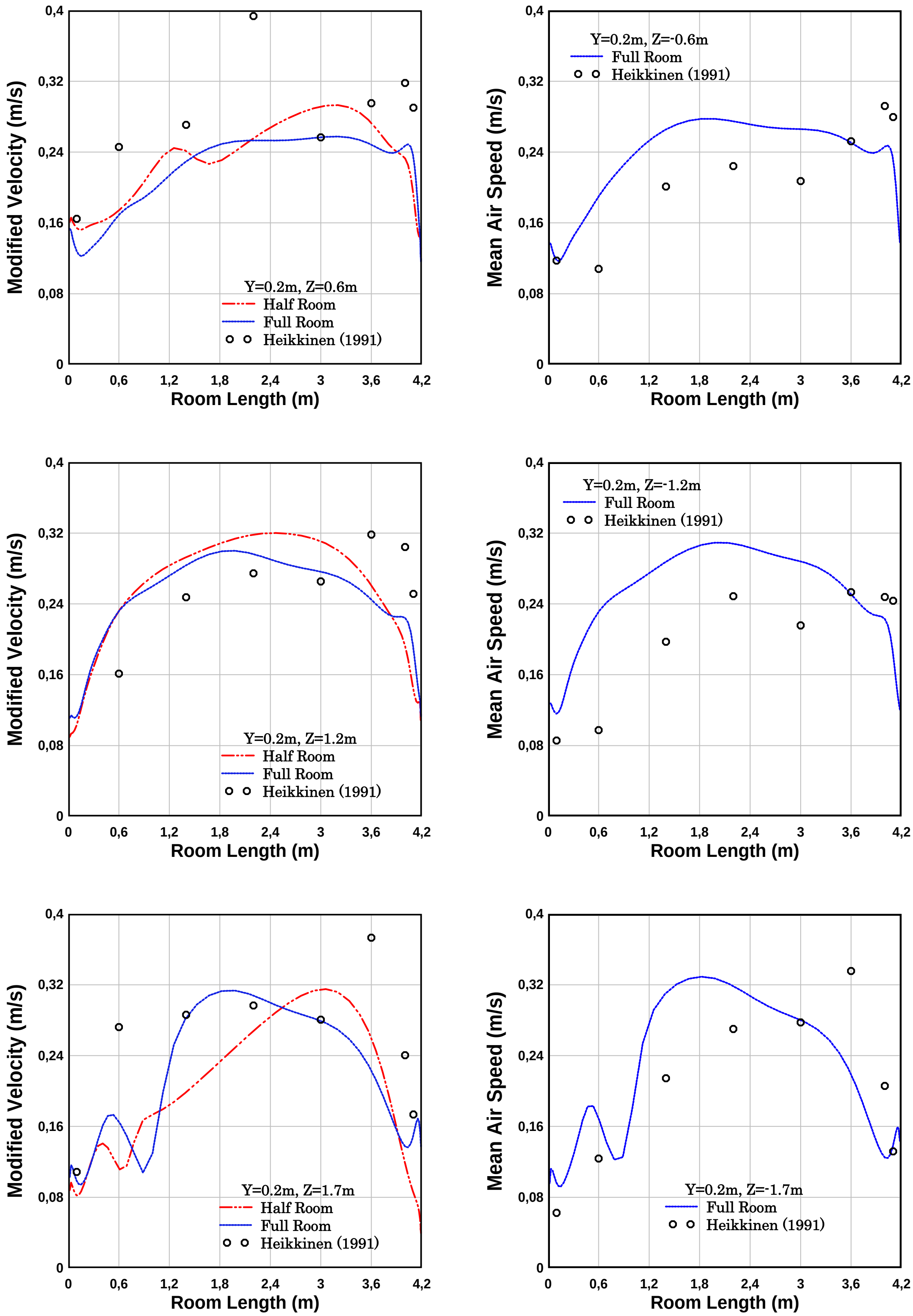

Fig. A-1-2-3 Y=0.2m (Test Case B3)

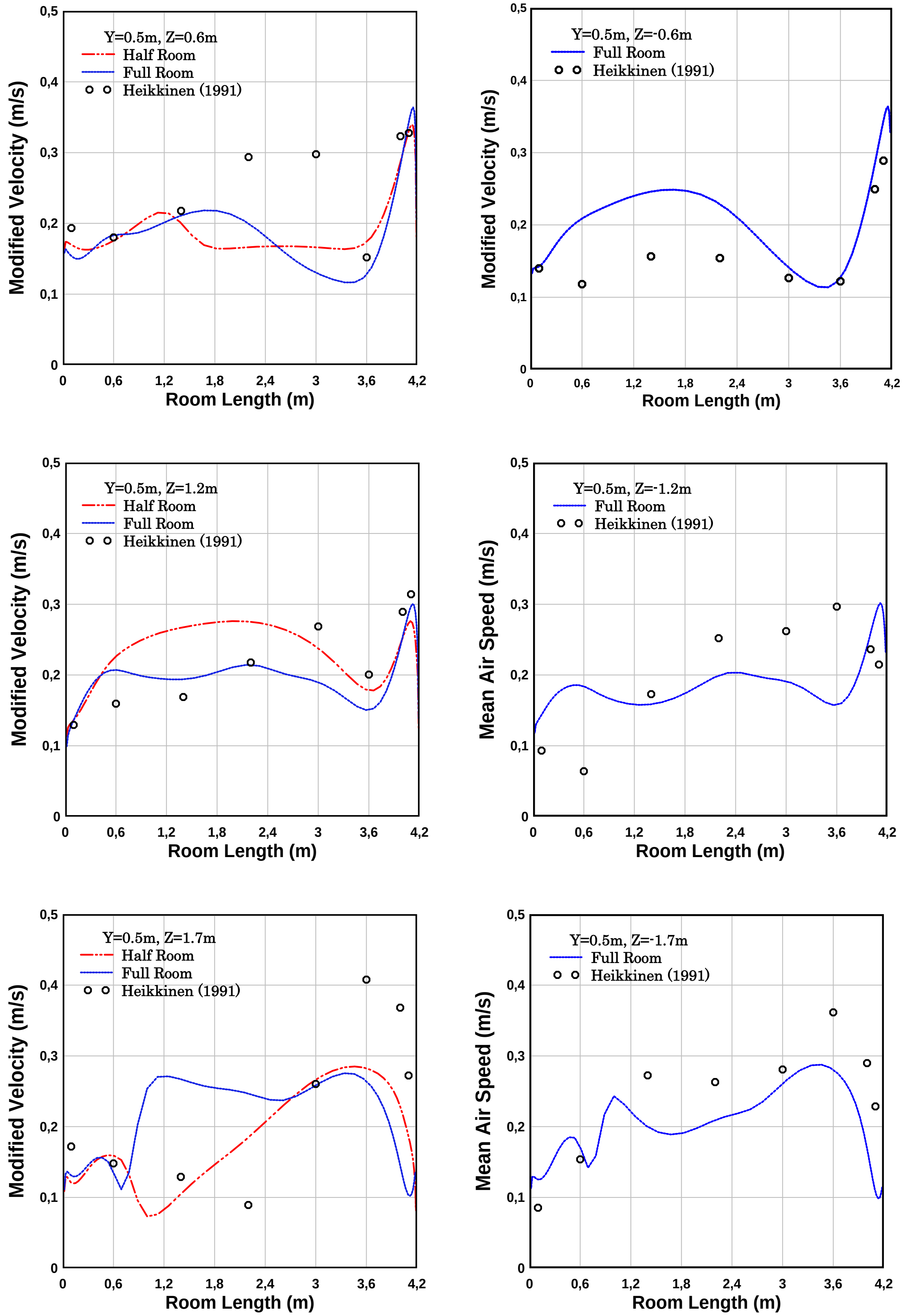

Fig. A-1-2-4 Y=0.5m (Test Case B3)

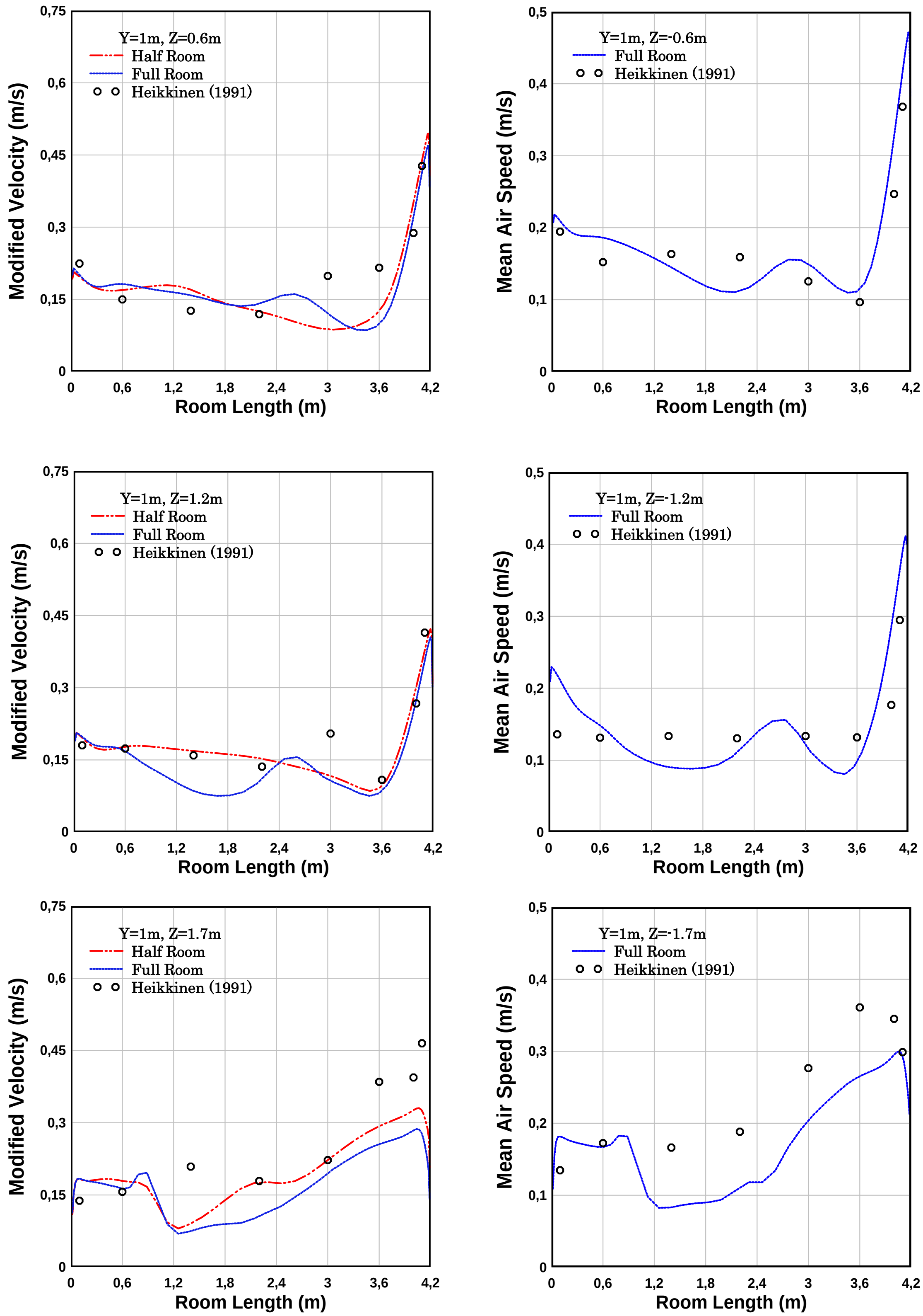

Fig. A-1-2-5 Y=1.0m (Test Case B3)

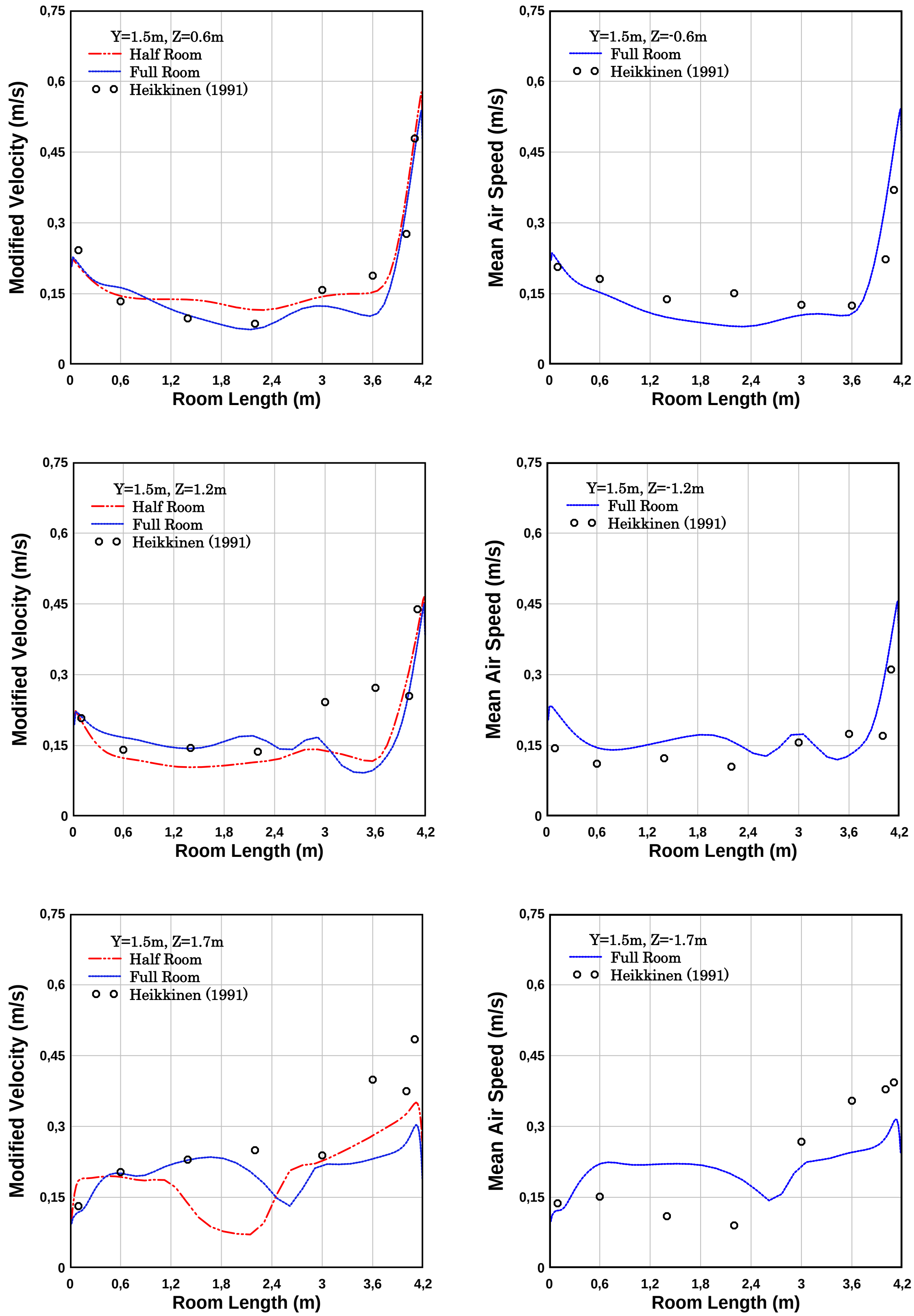

Fig. A-1-2-6 Y=1.5m (Test Case B3)

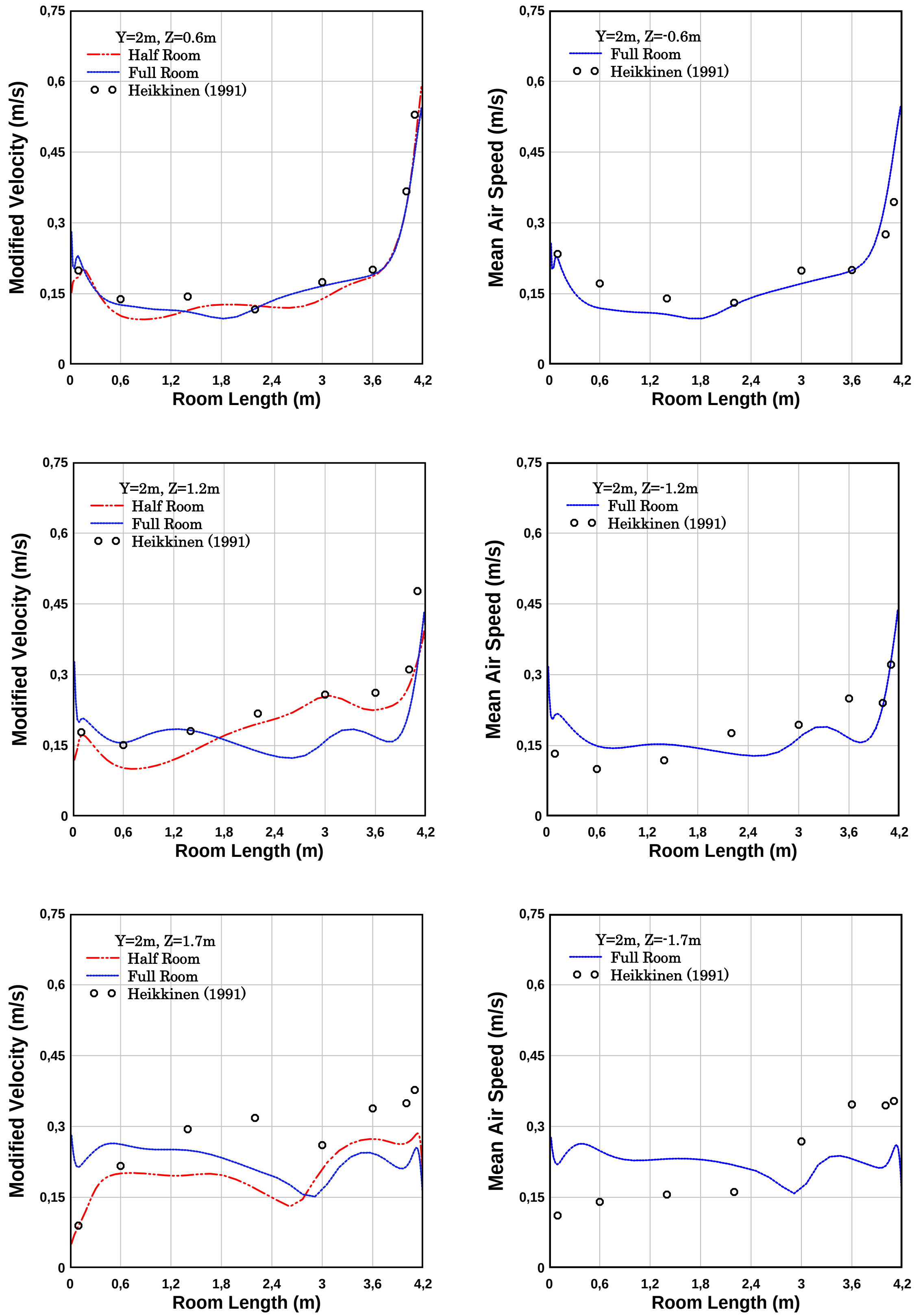

Fig. A-1-2-7 Y=2.0m (Test Case B3)

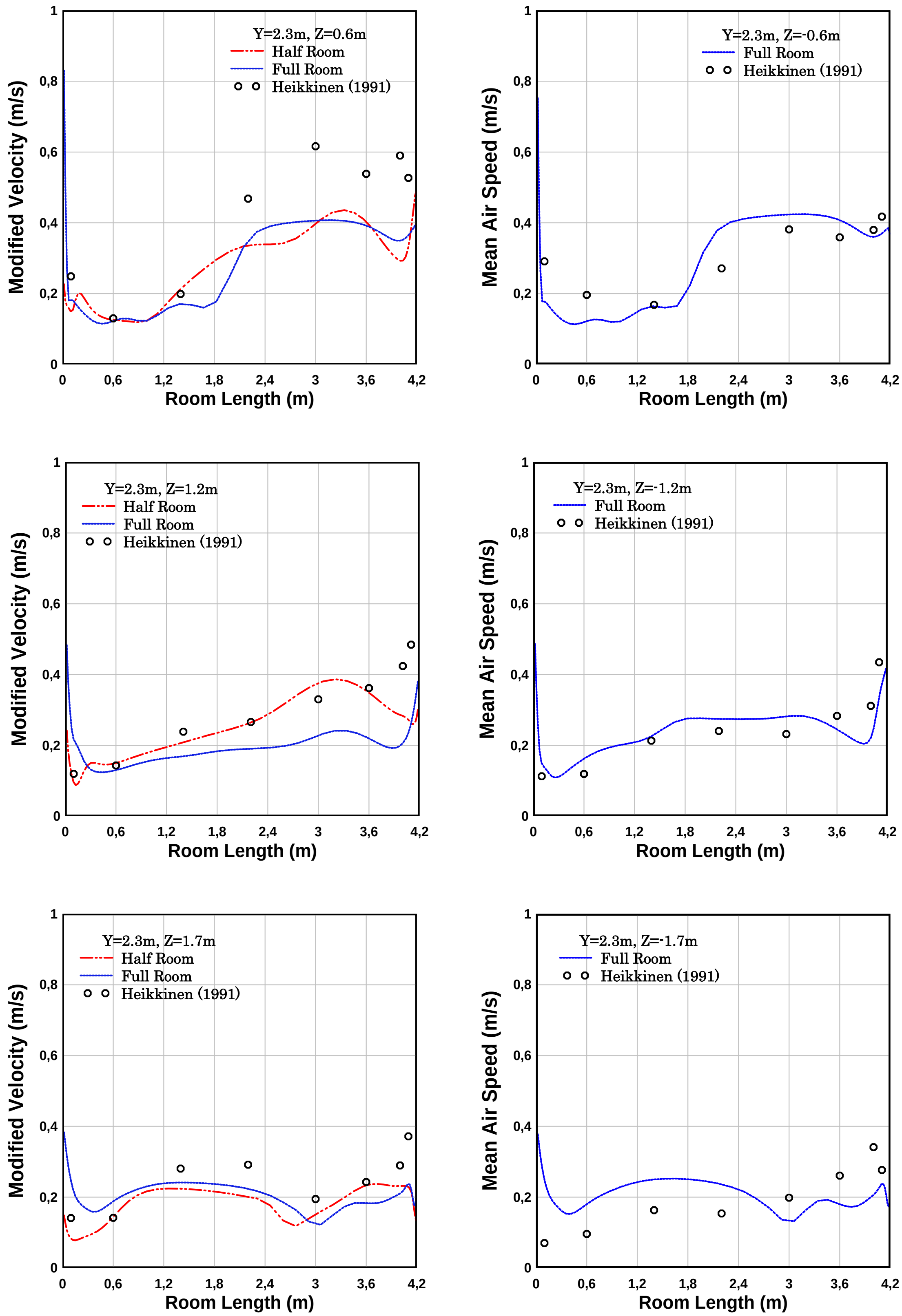

Fig. A-1-2-8 Y=2.3m (Test Case B3)

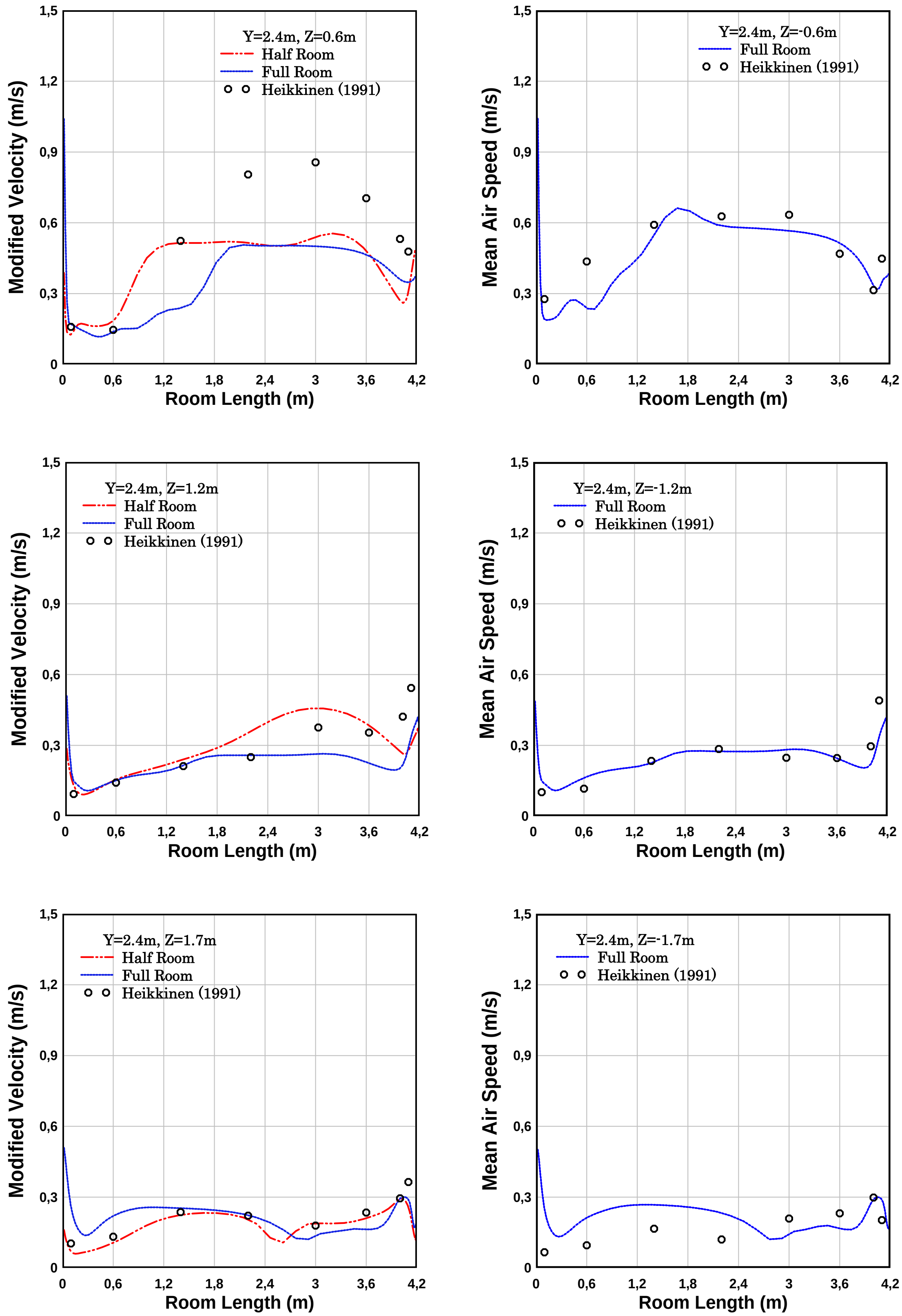

Fig. A-1-2-9 Y=2.4m (Test Case B3)

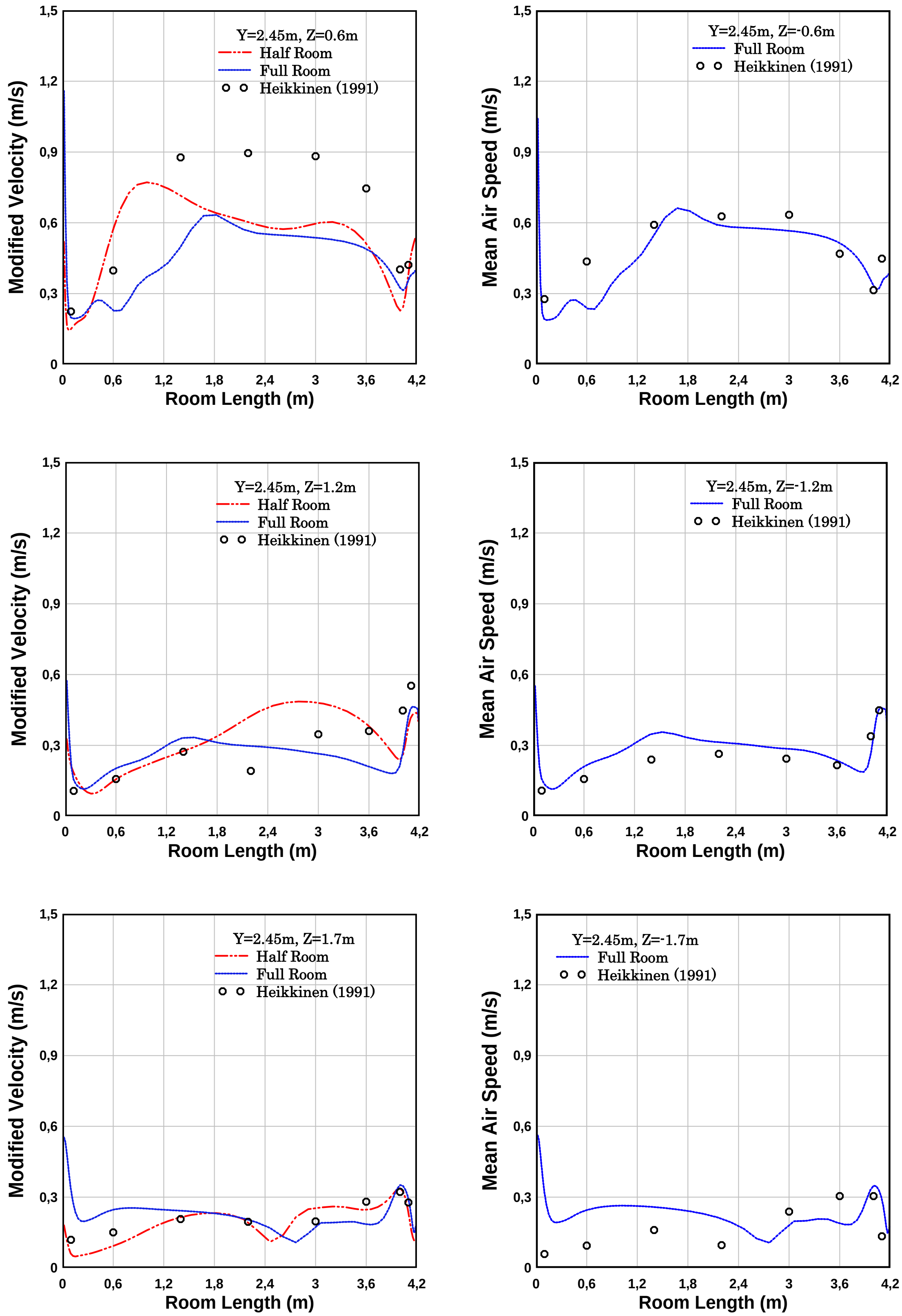

Fig. A-1-2-10 Y=2.45m (Test Case B3)

Appendix 2-1 Comparison of predicted temperature and mean air speed profiles (SST k-ω model; full room and half room approach) with measurements (Z=±0.6m, ±1.2m, ±1.7m; IEA Annex 20 Test Case E2)

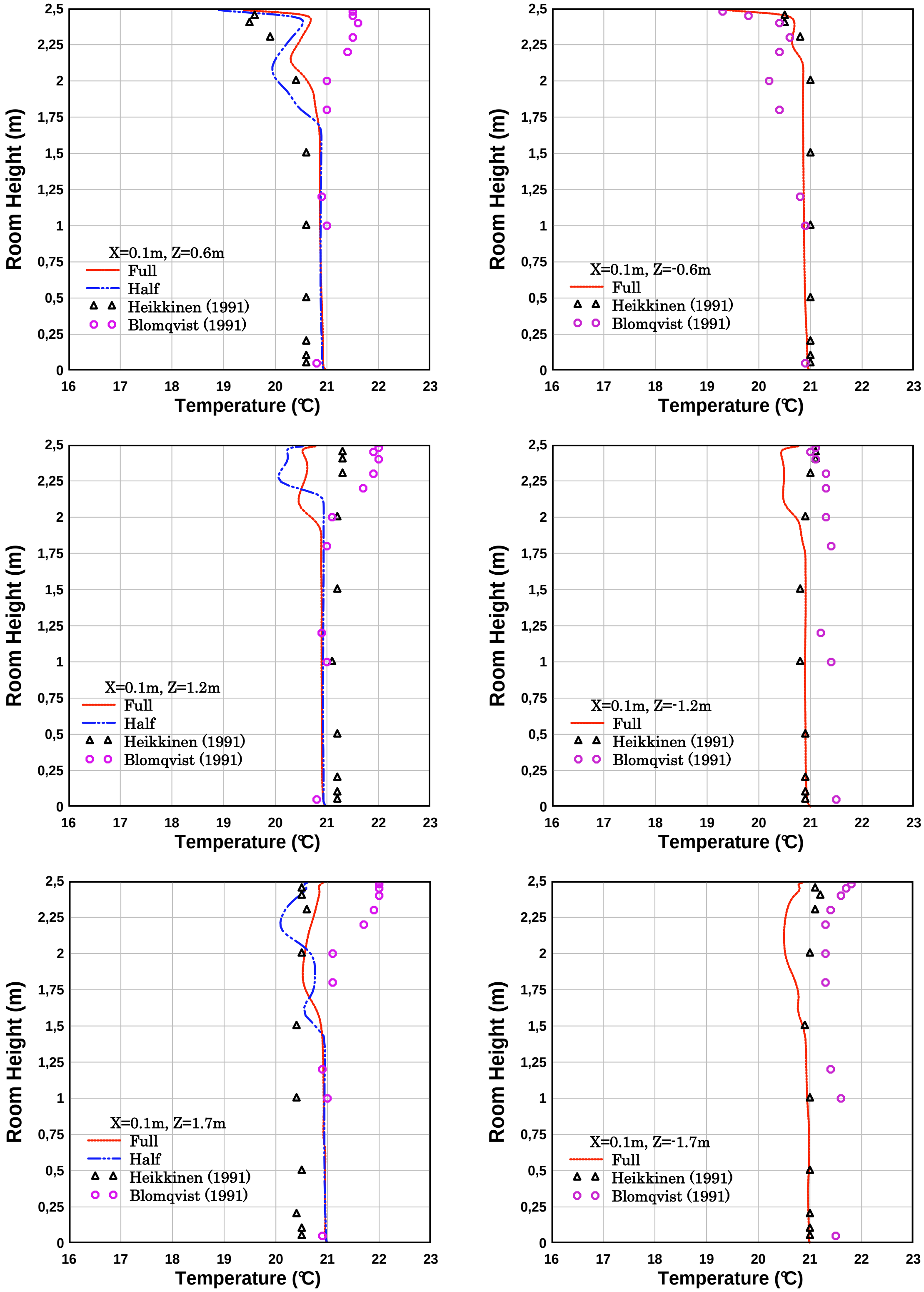

Fig. A-2-1-1 X=0.1m, Temperature

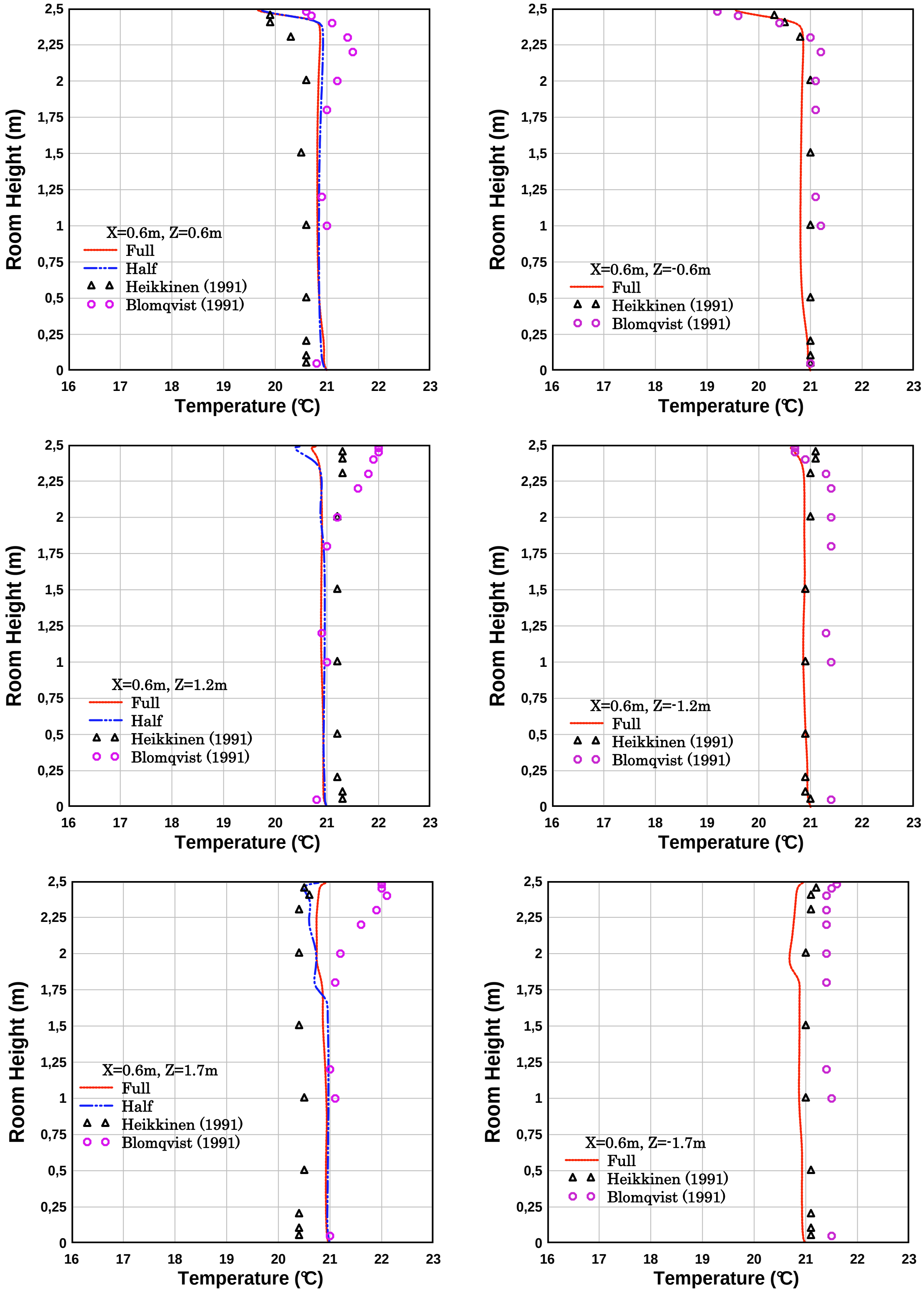

Fig. A-2-1-2 X=0.6m, Temperature

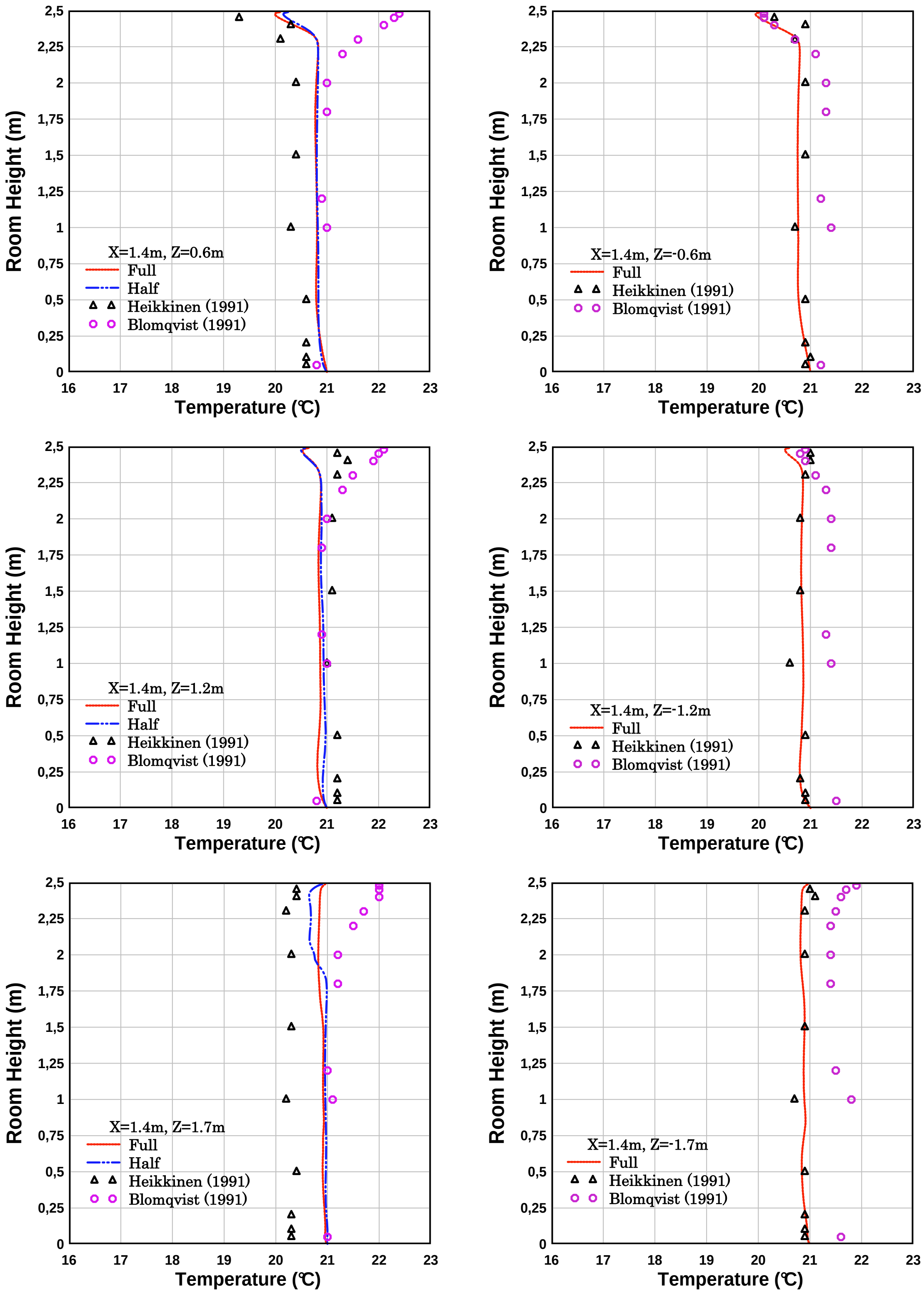

Fig. A-2-1-3 X=1.4m, Temperature

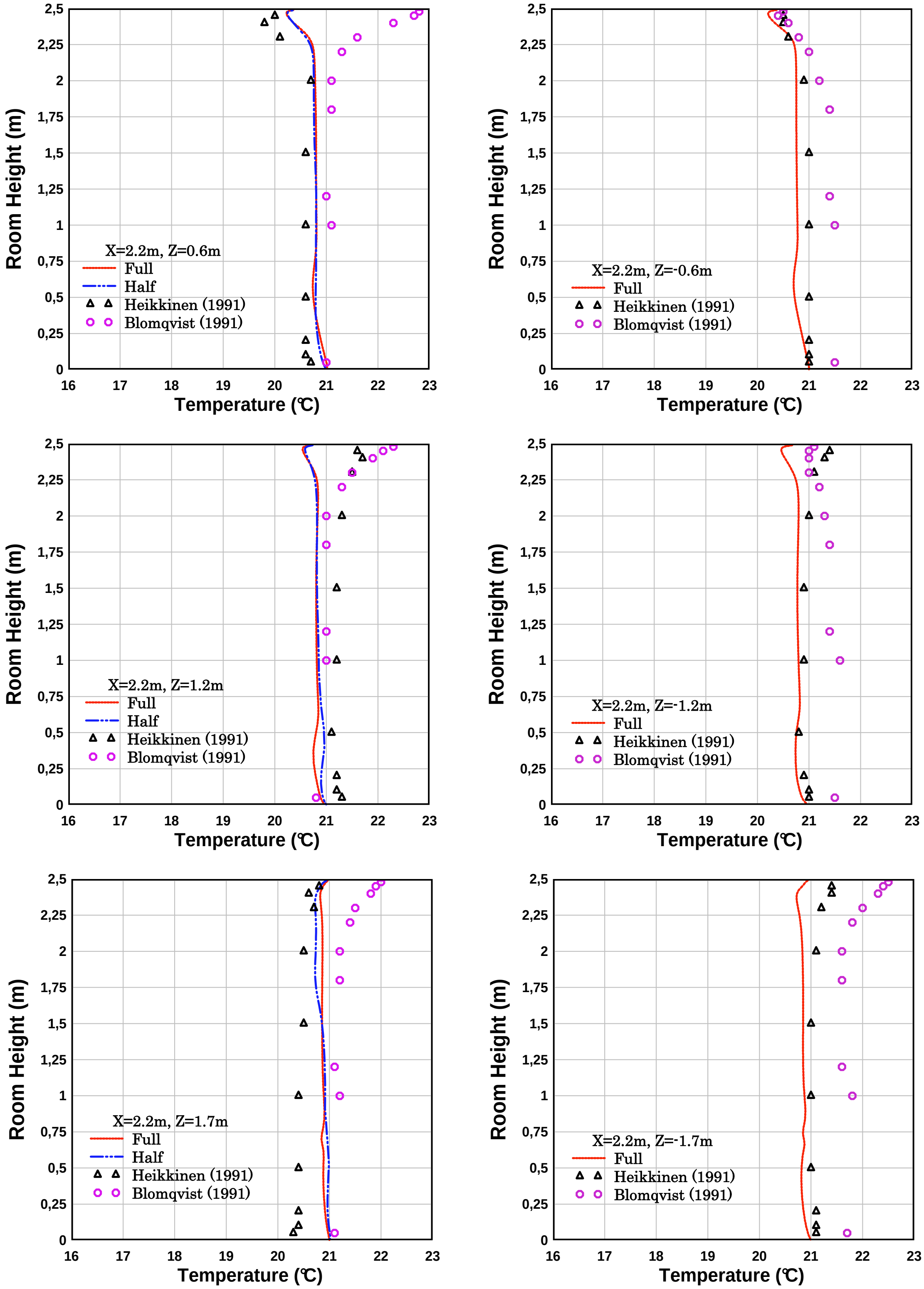

Fig. A-2-1-4 X=2.2m, Temperature

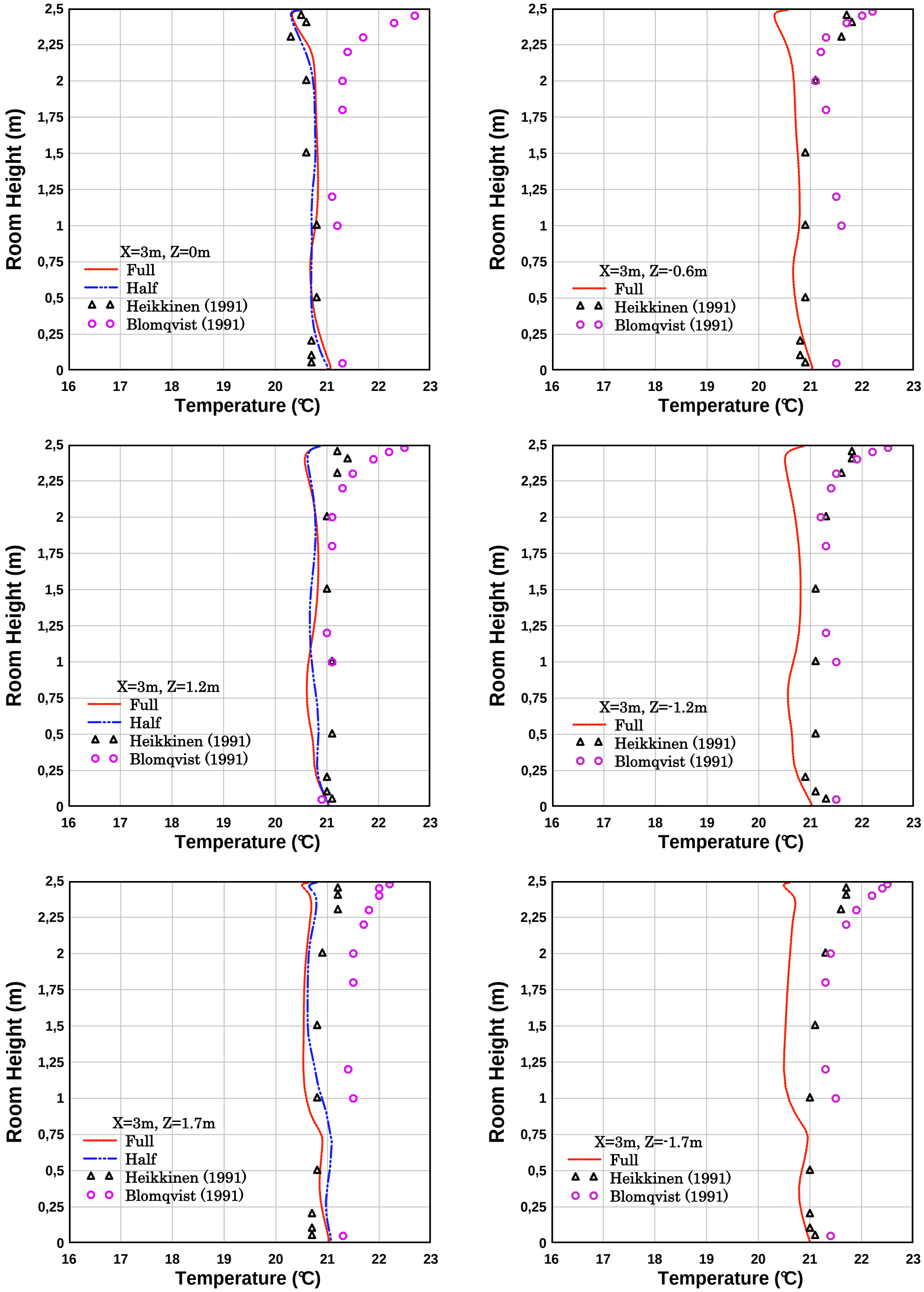

Fig. A-2-1-5 X=3m, Temperature

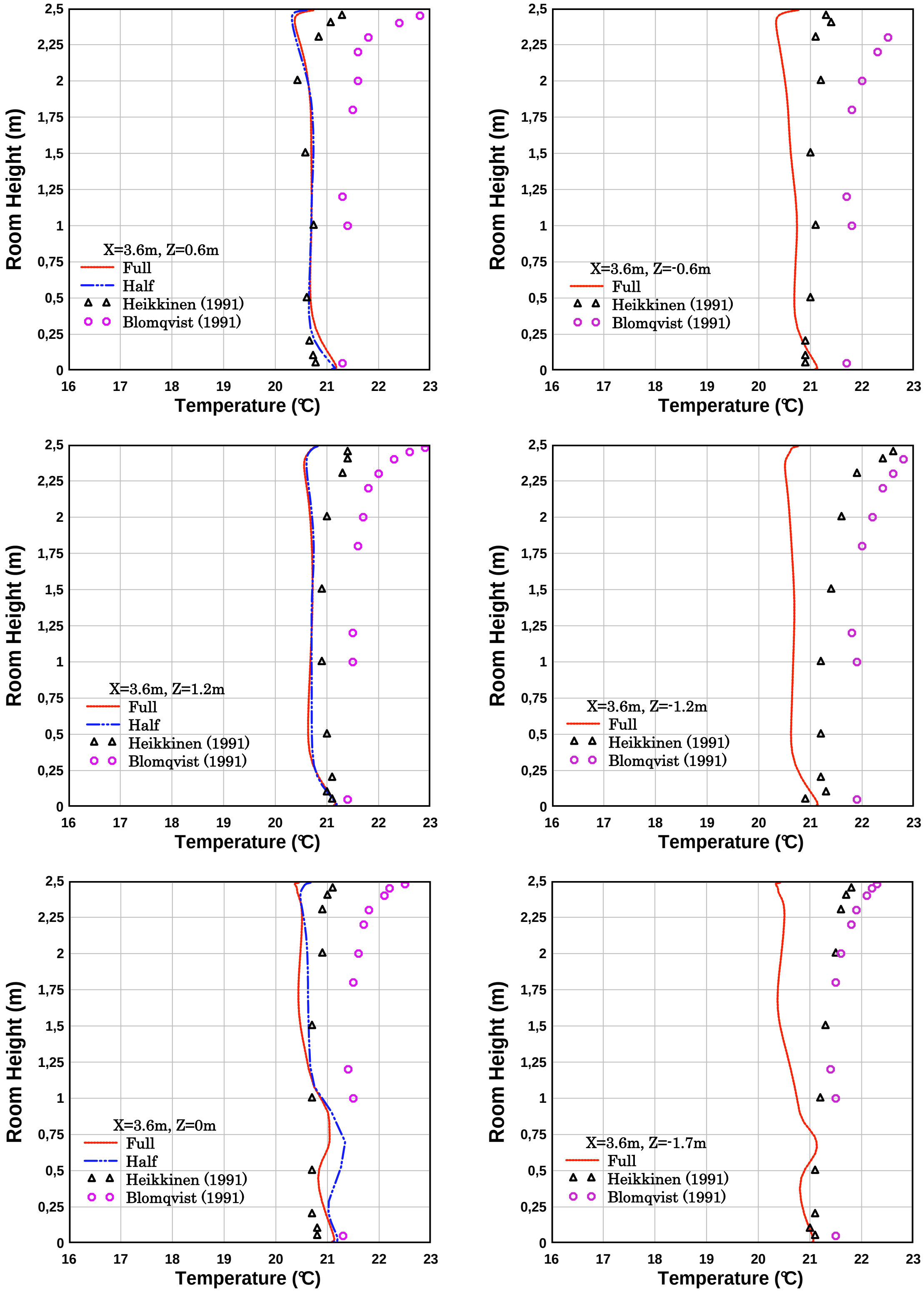

Fig. A-2-1-6 X=3.6m, Temperature

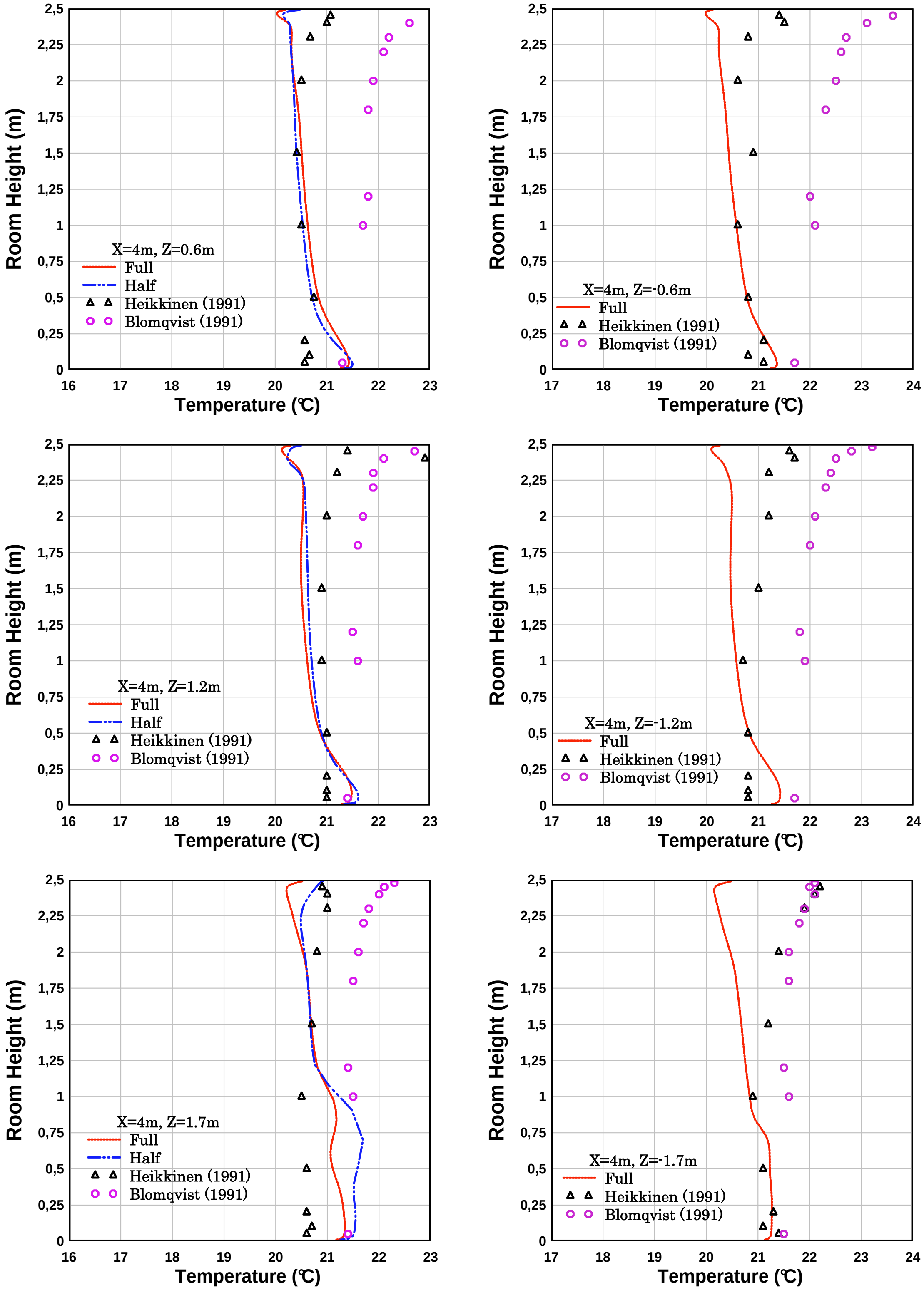

Fig. A-2-1-7 X=0.1m, Temperature

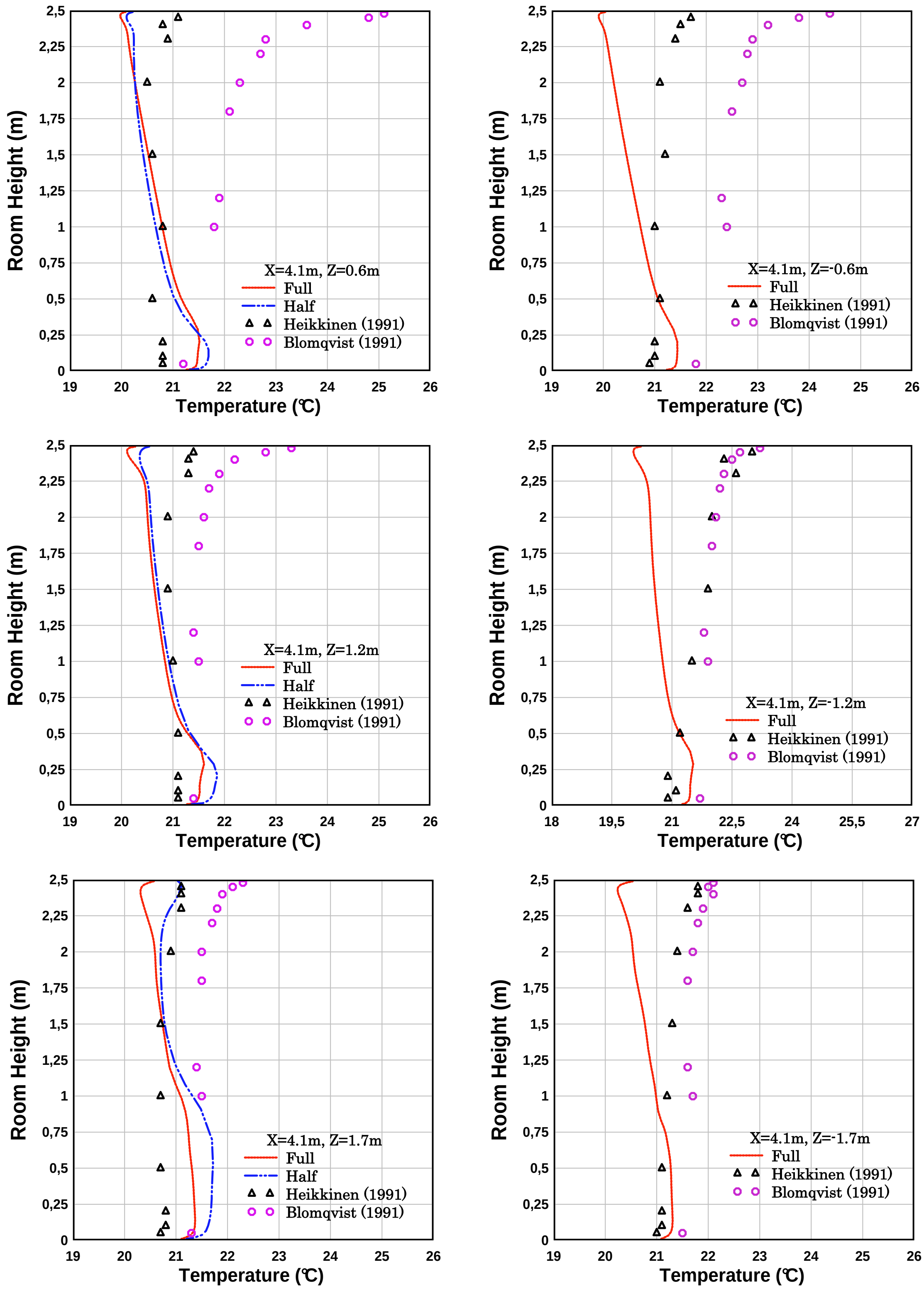

Fig. A-2-1-8 X=4.1m, Temperature

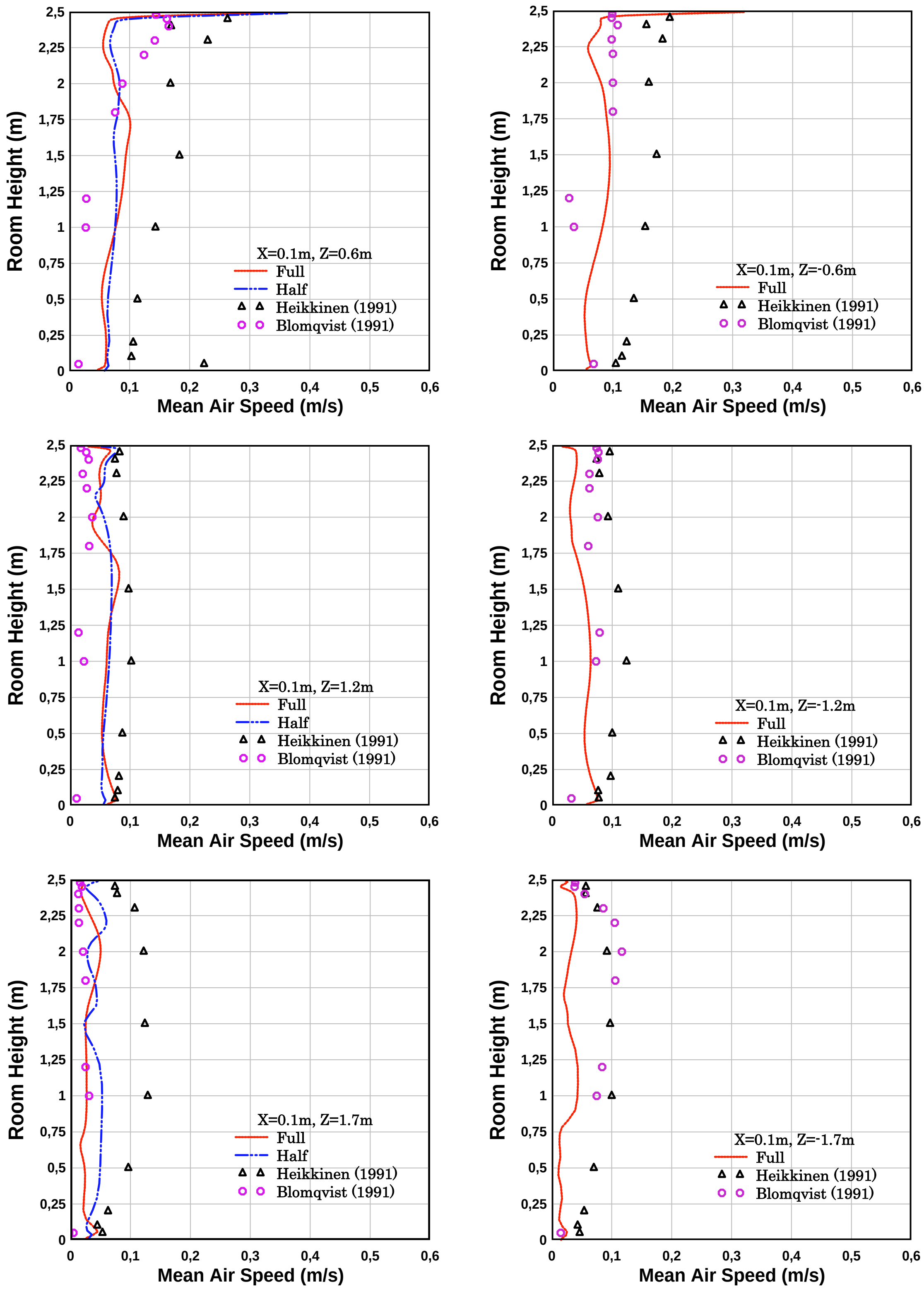

Fig. A-2-1-9 X=0.1m, Mean Air Speed

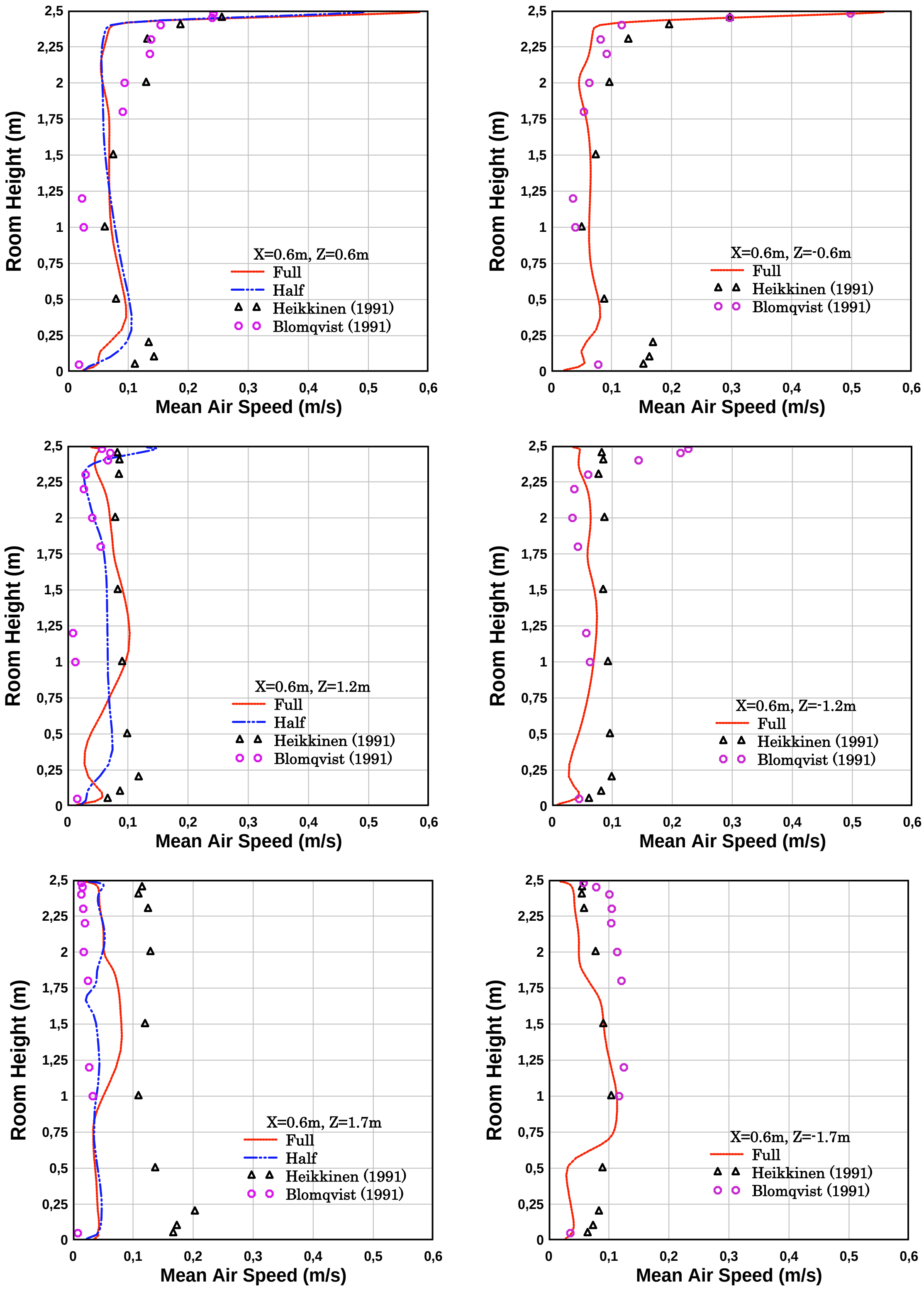

Fig. A-2-1-10 X=0.6m, Mean Air Speed

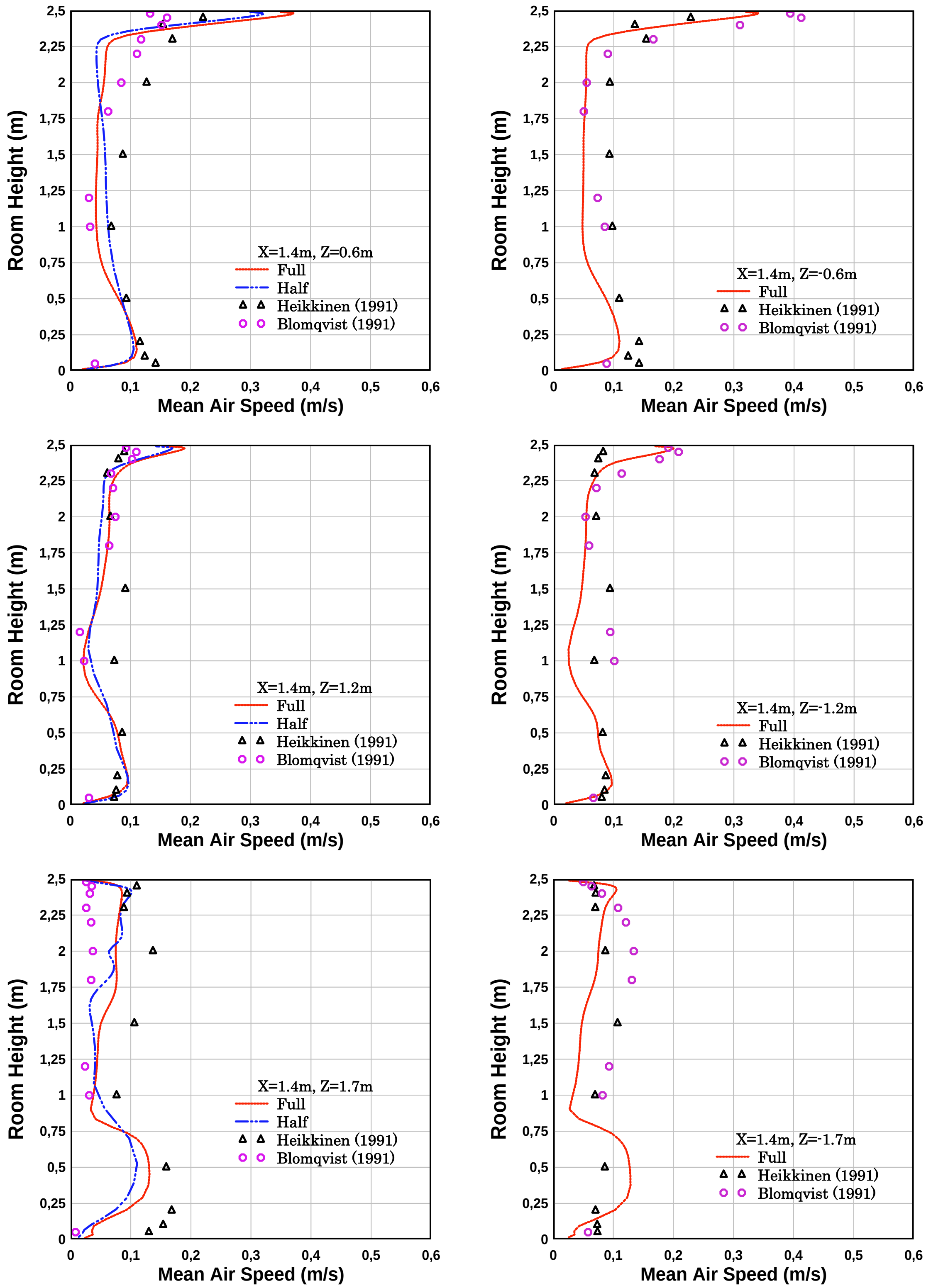

Fig. A-2-1-11 X=1.4m, Mean Air Speed

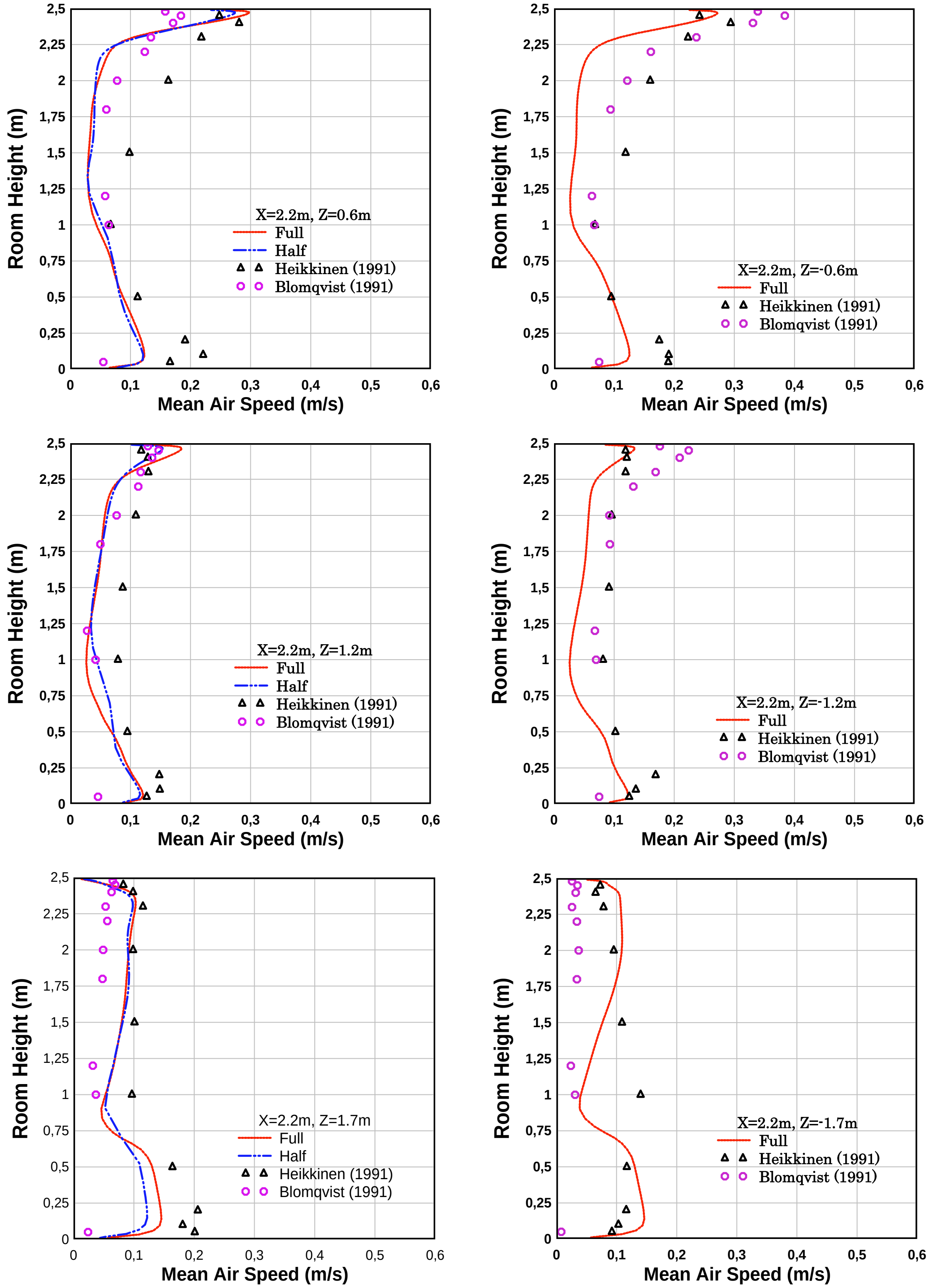

Fig. A-2-1-12 X=2.2m, Mean Air Speed

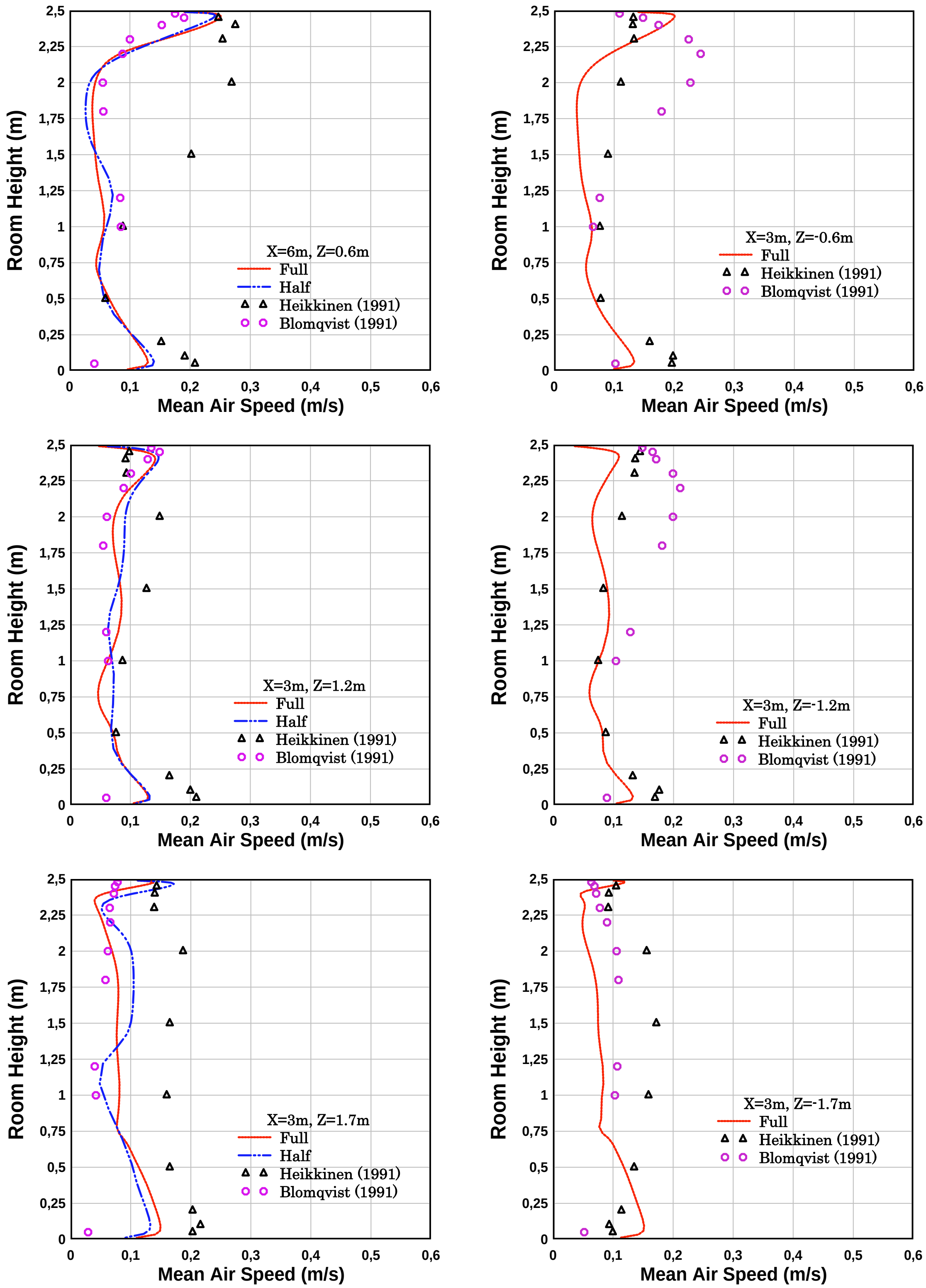

Fig. A-2-1-13 X=3m, Mean Air Speed

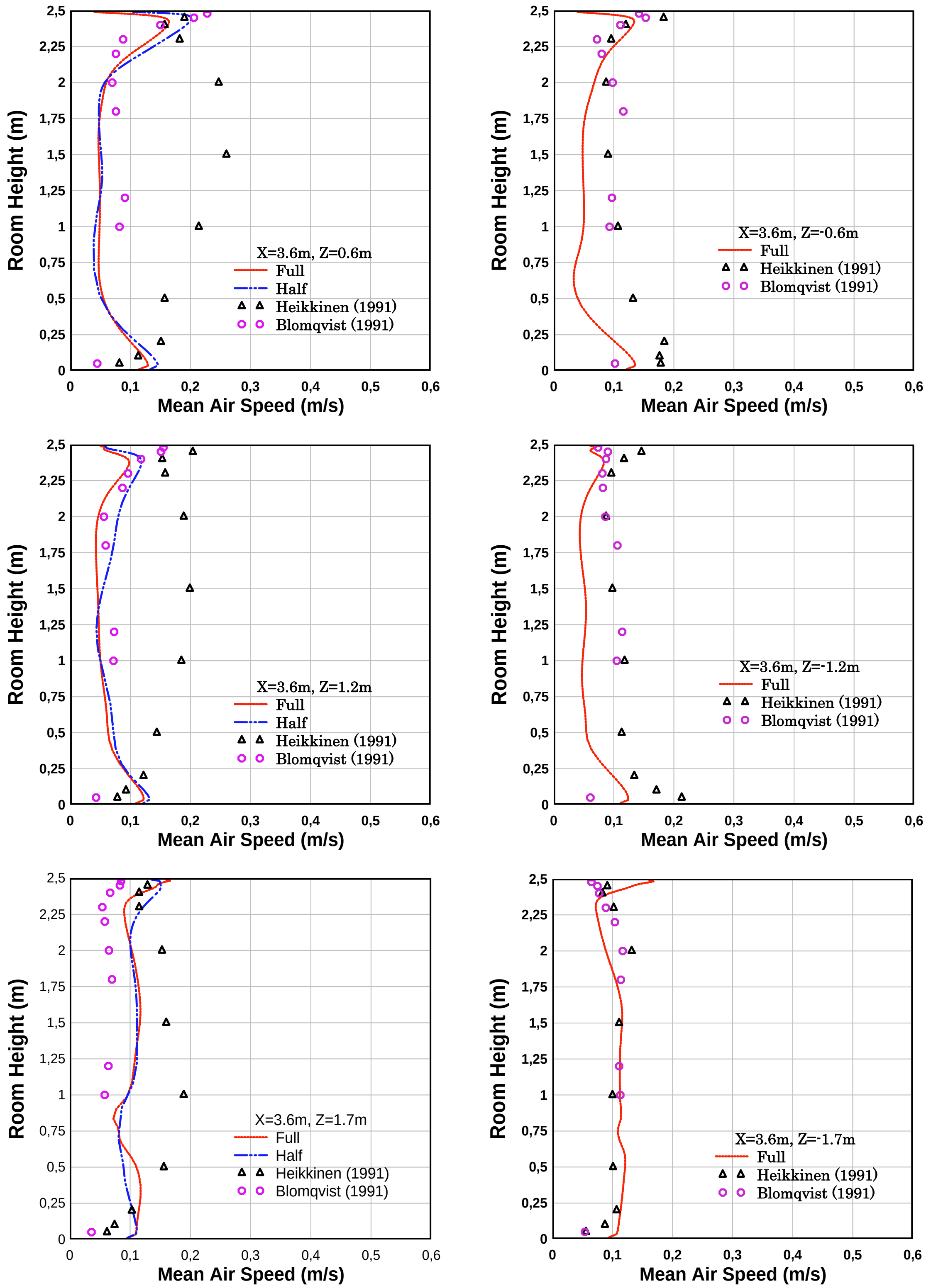

Fig. A-2-1-14 X=3.6m, Mean Air Speed

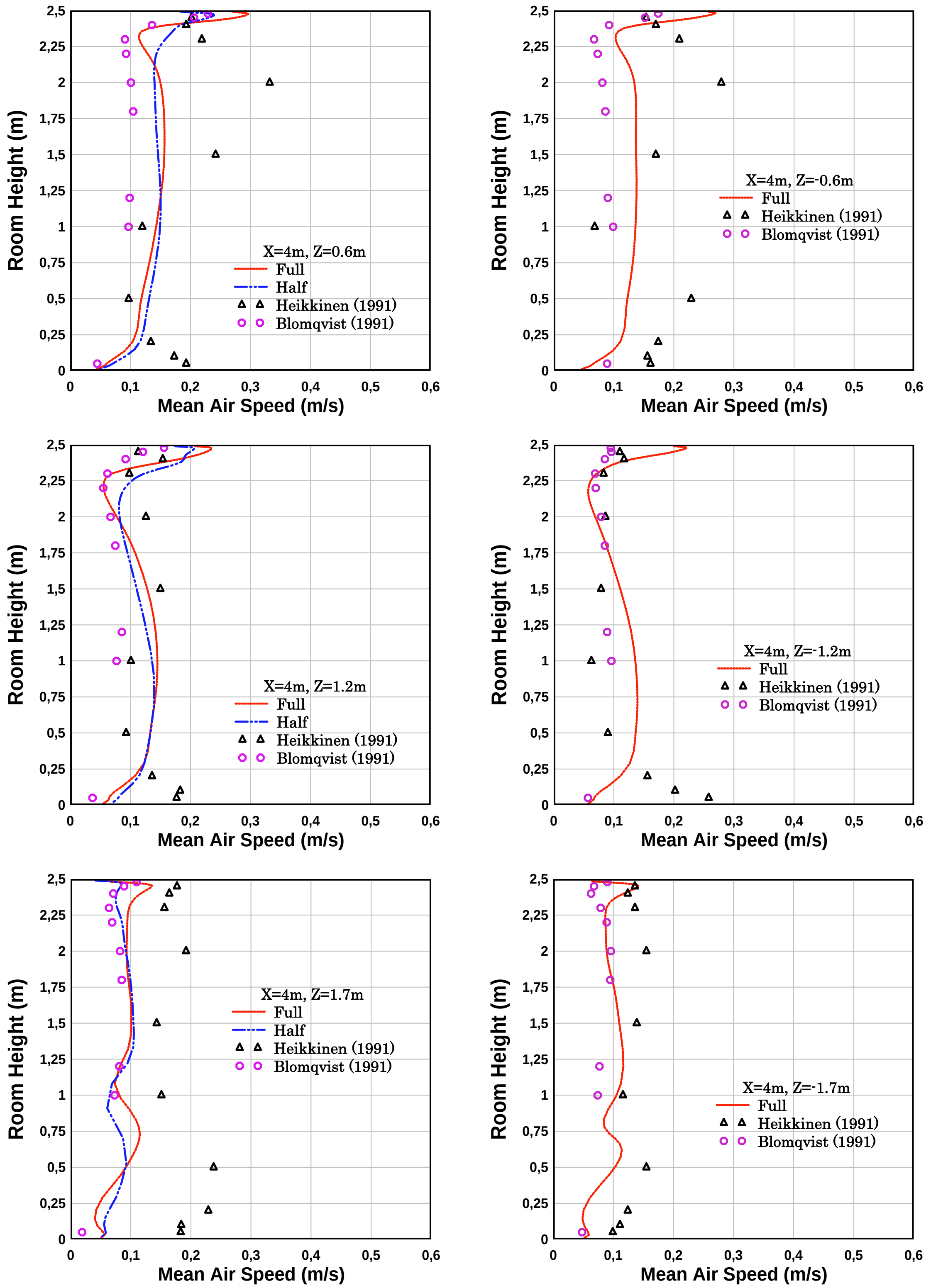

Fig. A-2-1-15 X=4m, Mean Air Speed

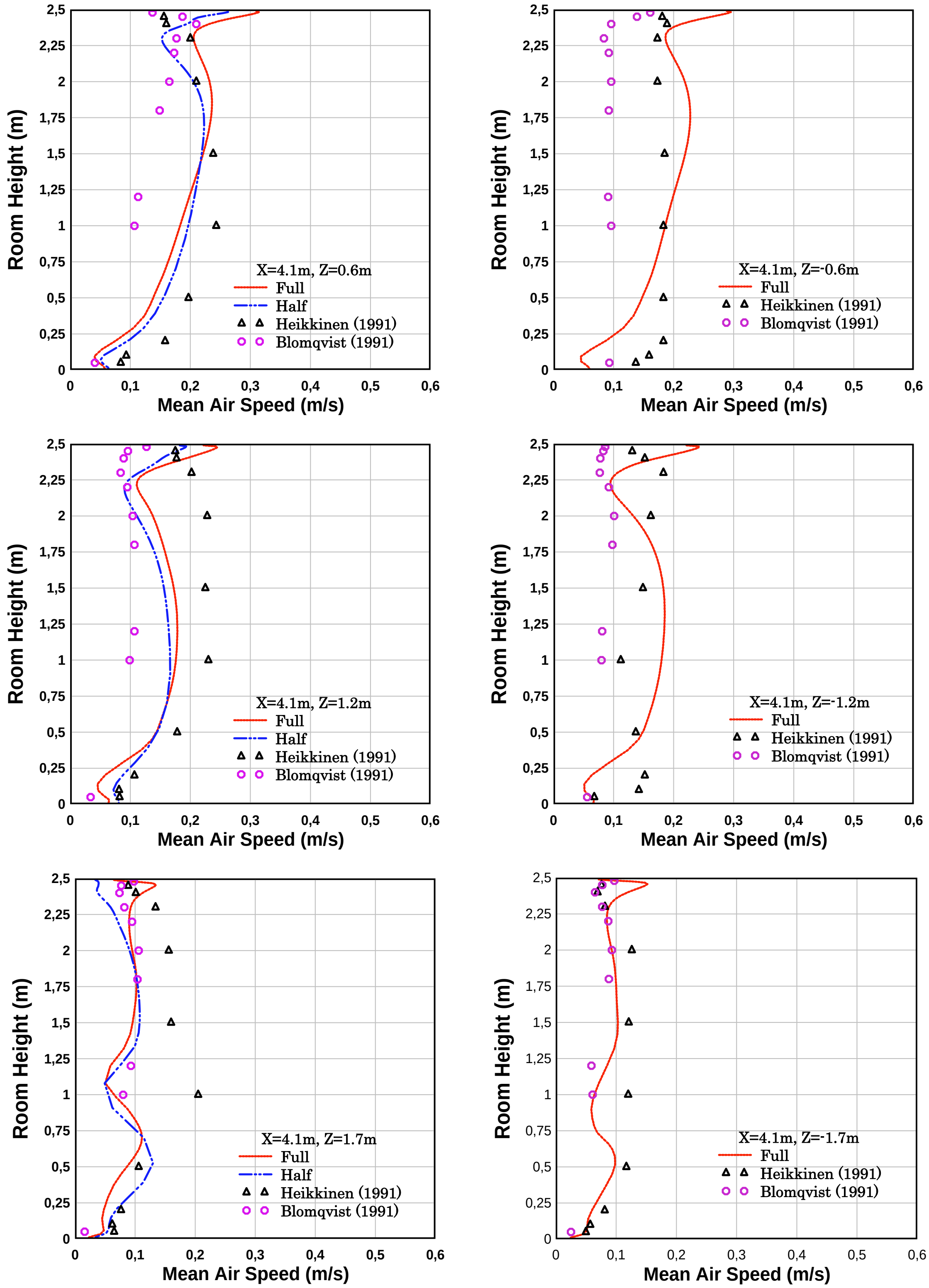

Fig. A-2-1-16 X=4.1m, Mean Air Speed

Appendix 2-2 Comparison of predicted temperature and mean air speed profiles with measurements at the 6 sides planes (Z=±0.6m, ±1.2m, ±1.7m) (Test Case E3, half room)

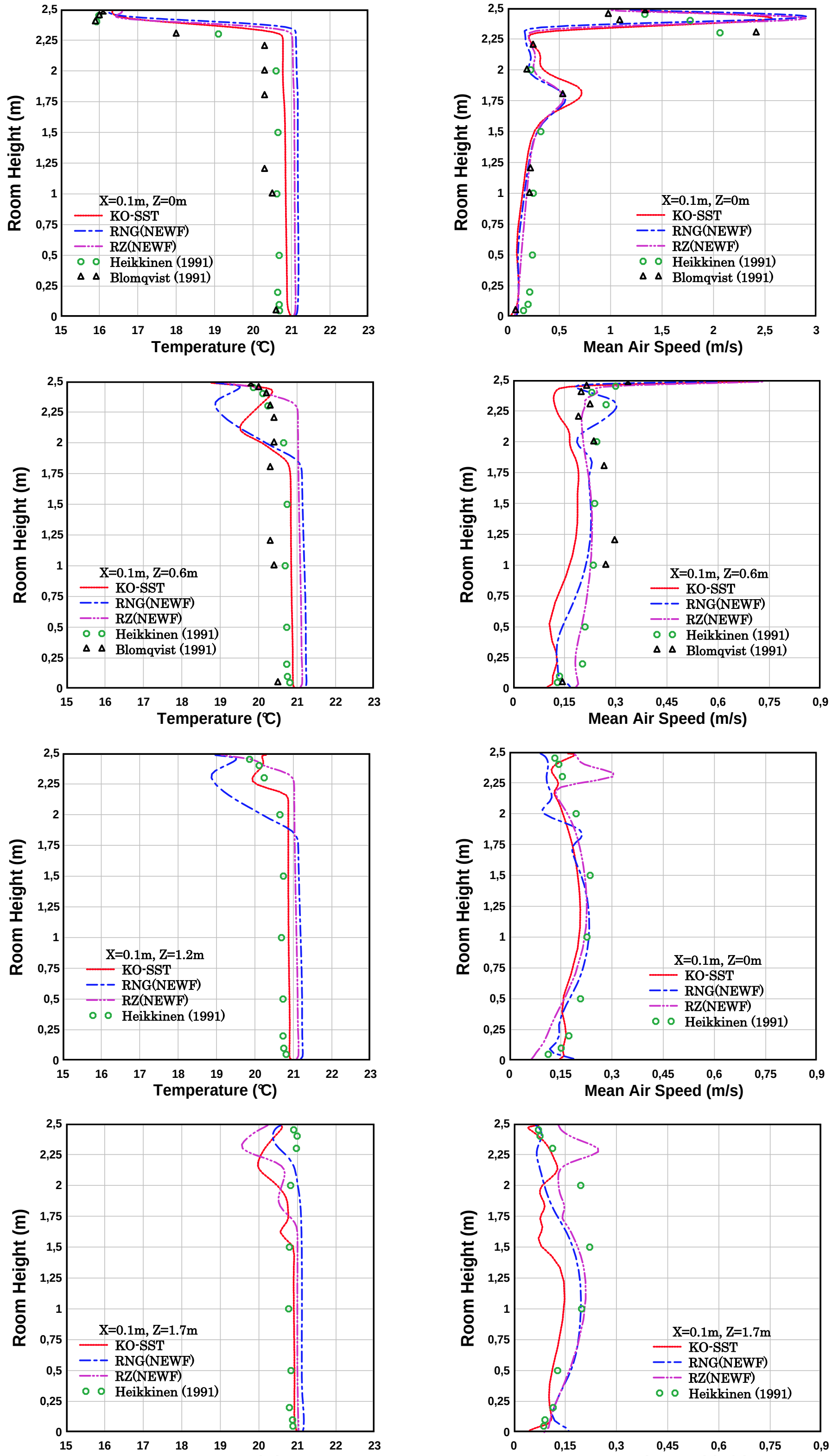

Fig. A-2-2-1 X=0.1m

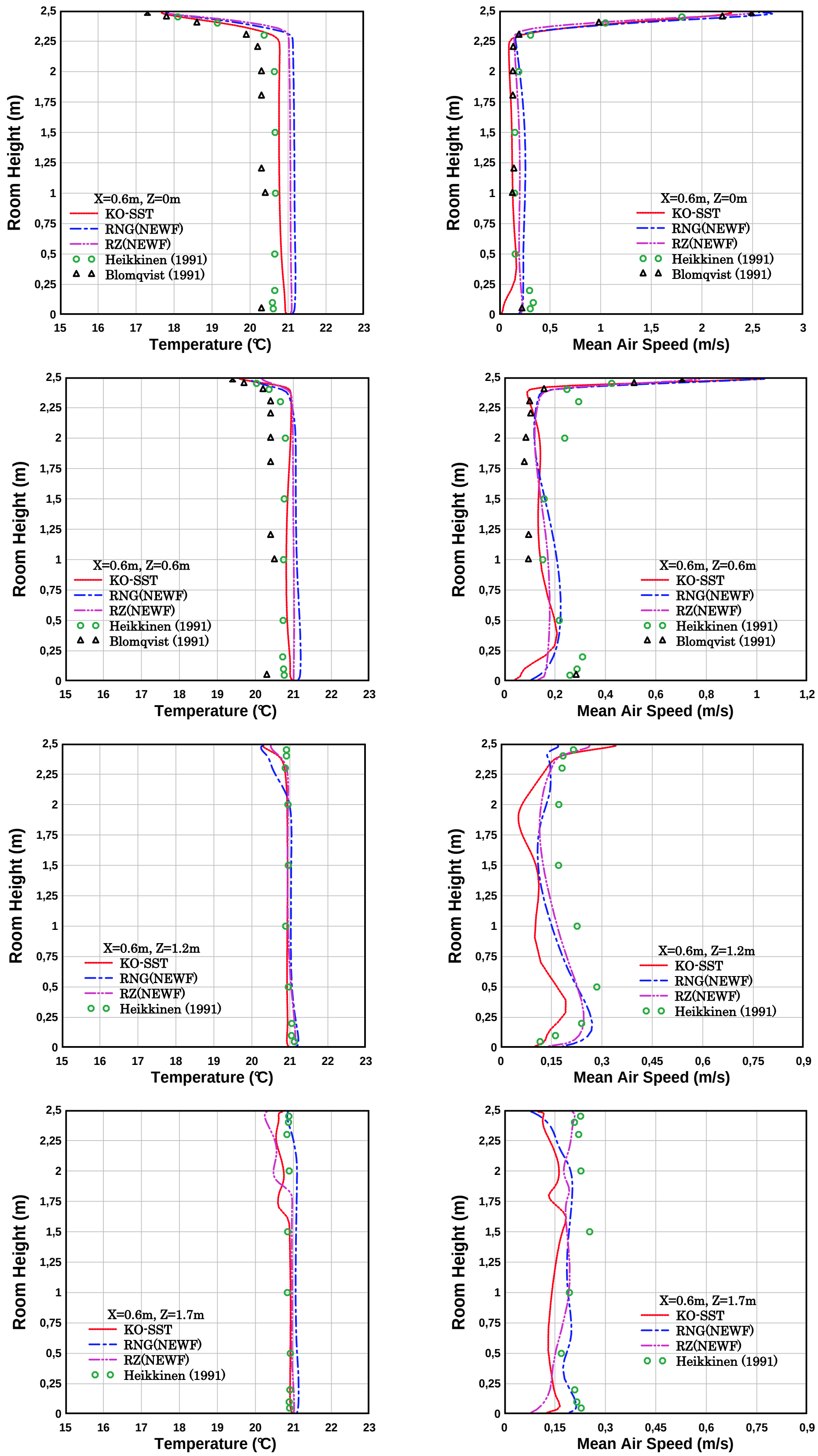

Fig. A-2-2-2 X=0.6m

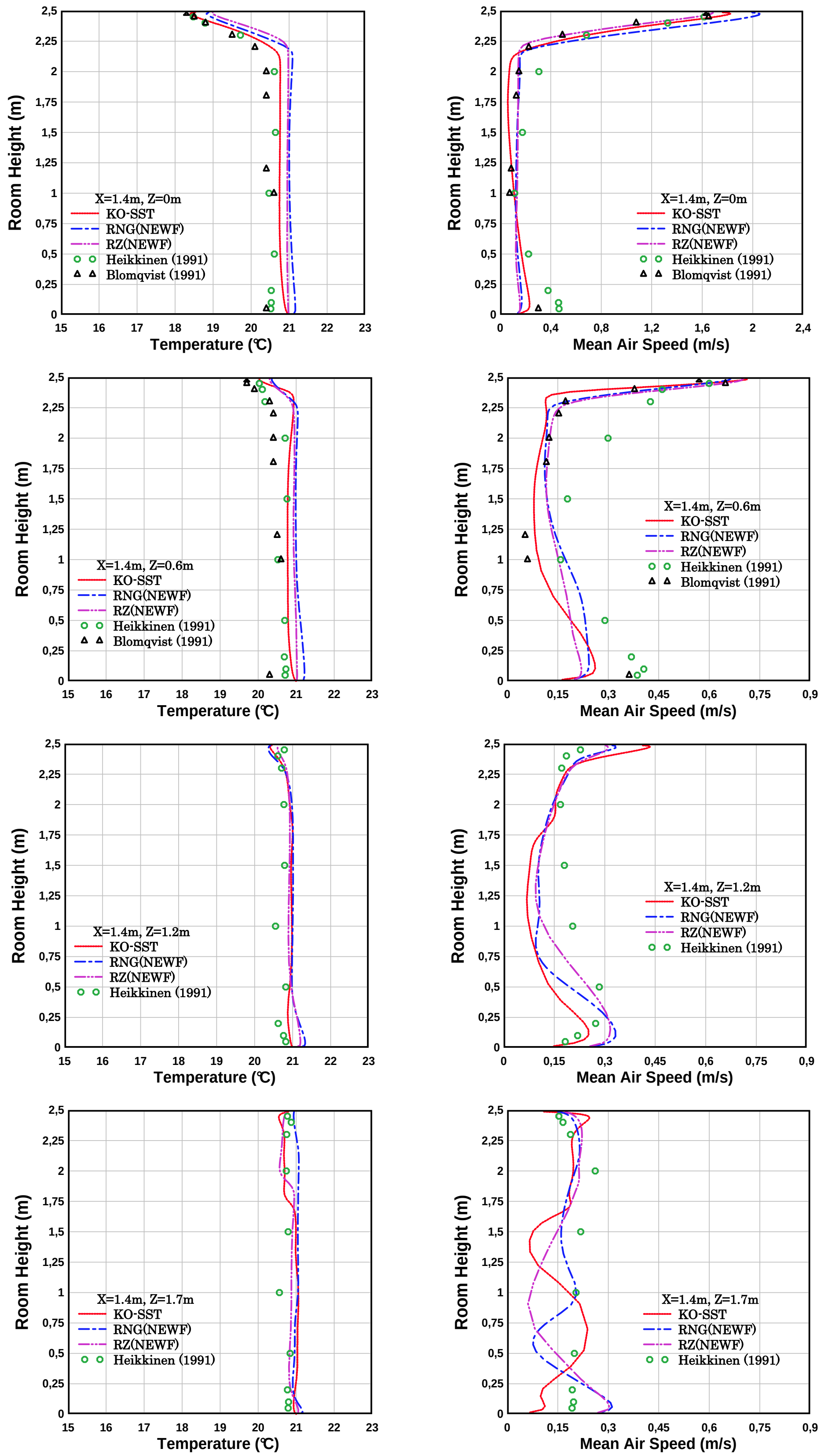

Fig. A-2-2-3 X=1.4m

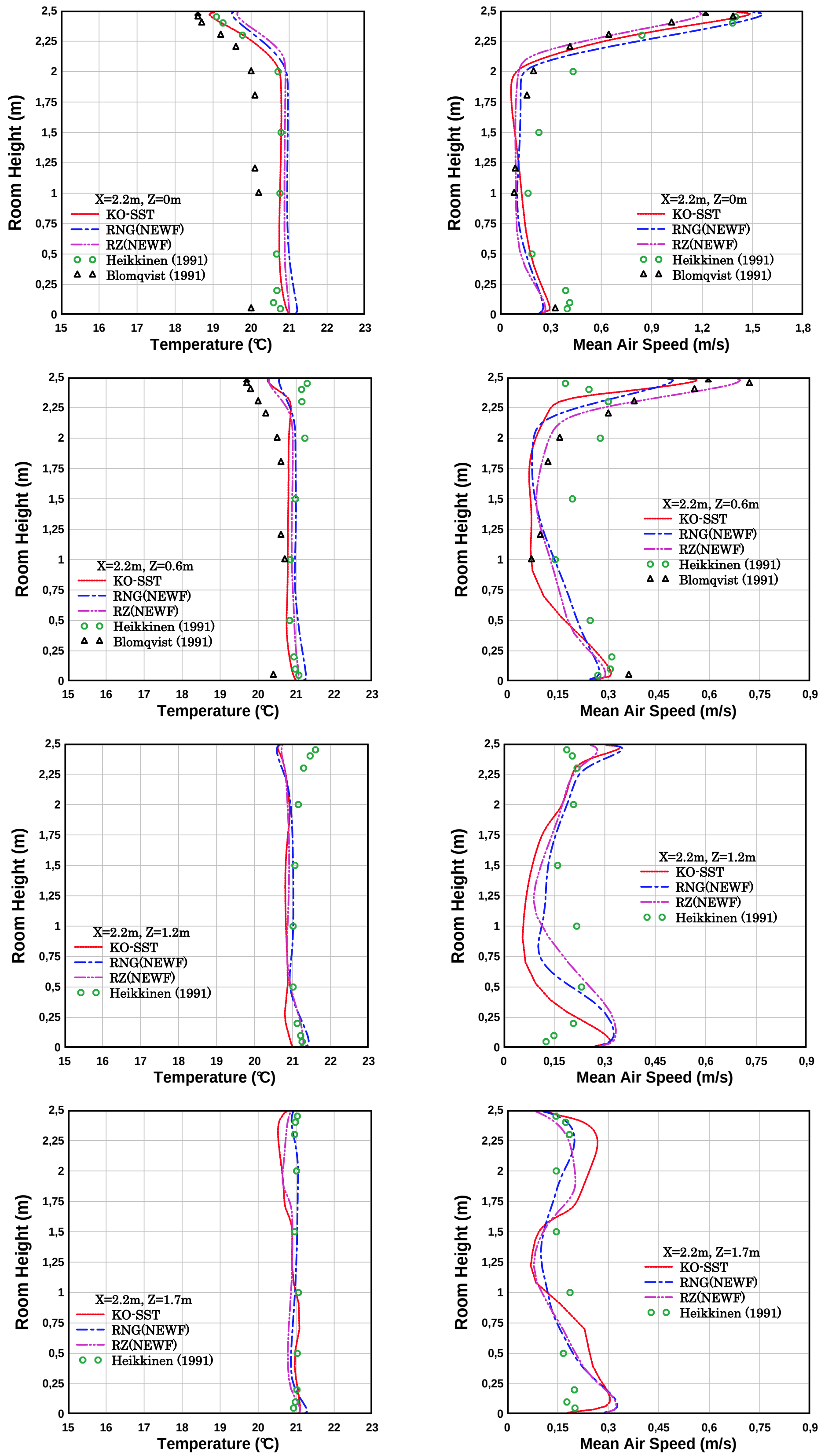

Fig. A-2-2-4 X=2.2m

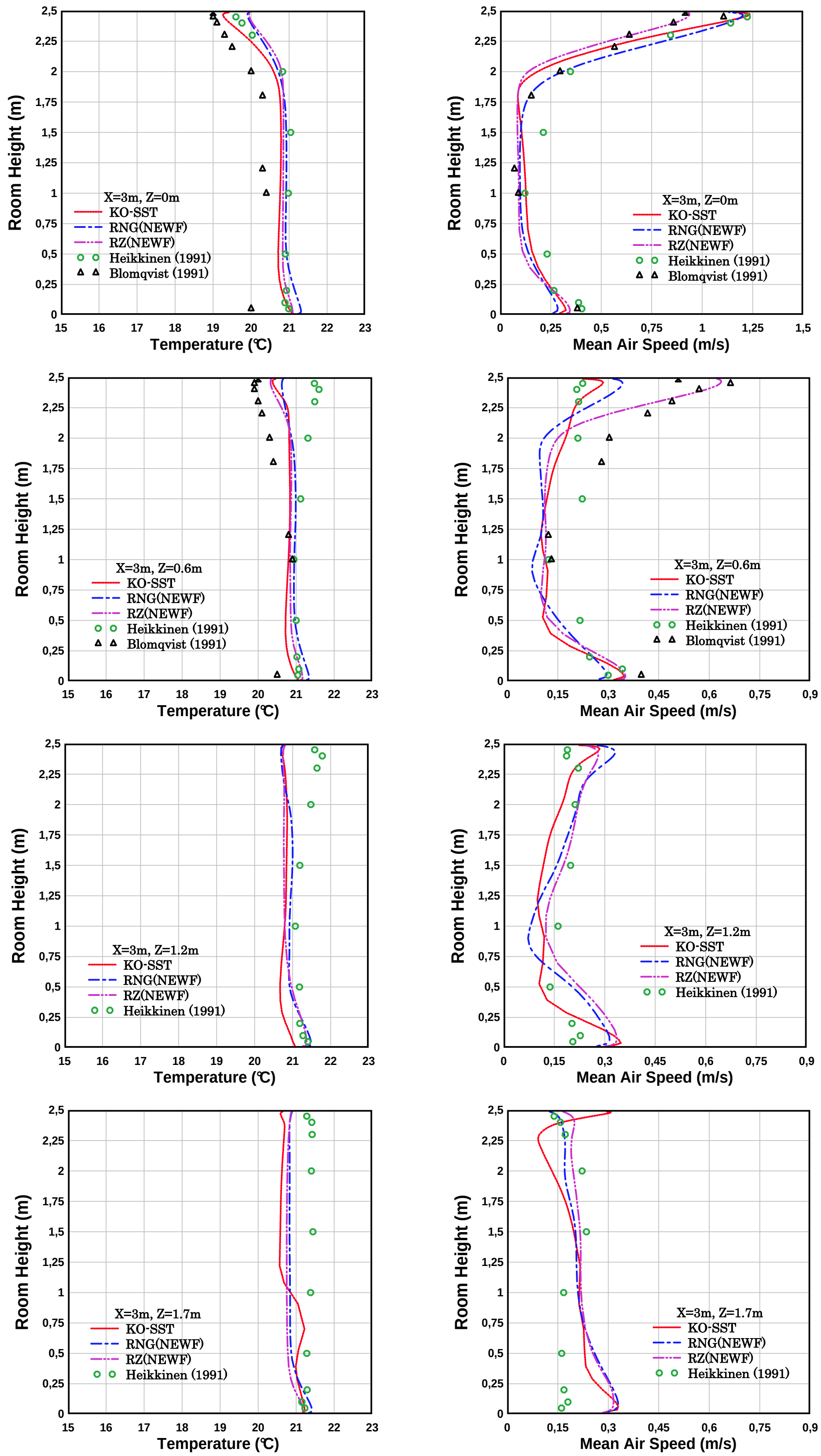
X=3m, Z=0m
KO-SST
RNG(NEWF)
RZ(NEWF)
Heikkinen (1991)
Blomqvist (1991)
Room Height (m)
Temperature (℃)
Mean Air Speed (m/s)
X=3m, Z=0.6m
X=3m, Z=1.2m
X=3m, Z=1.7m

Fig. A-2-2-5 X=3m

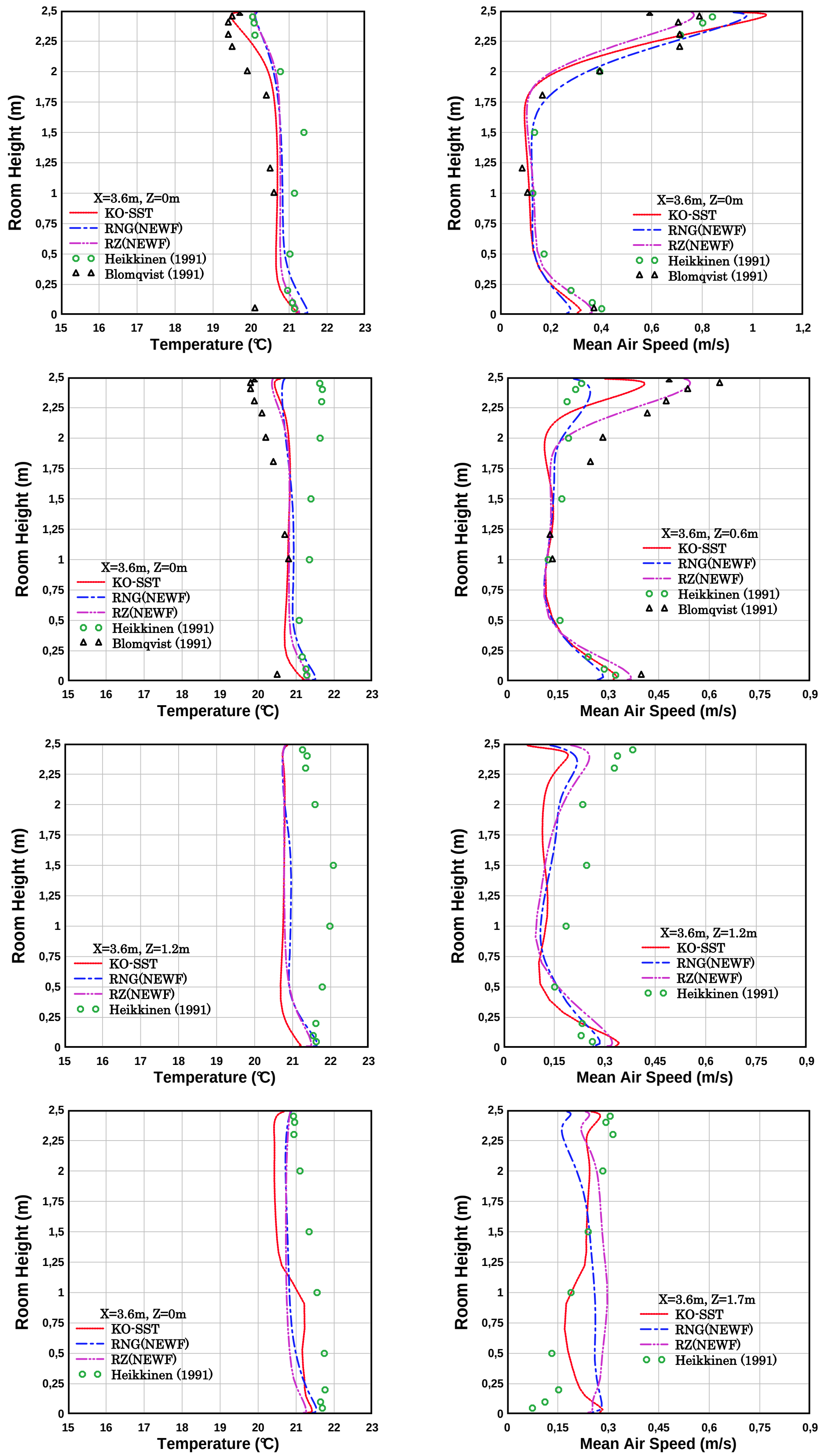

Fig. A-2-2-6 X=3.6m

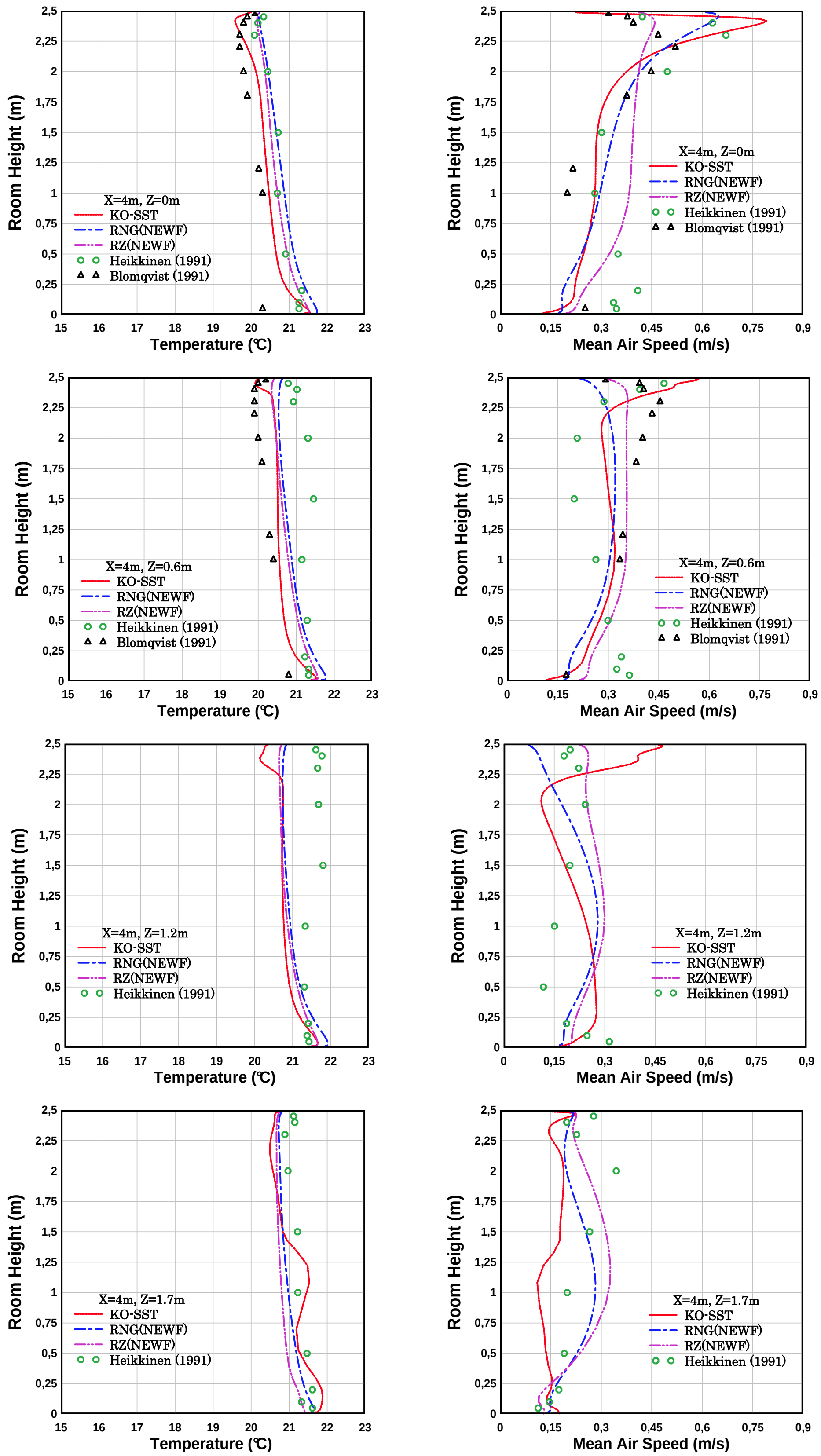
Room Height (m)
Temperature (℃)
Mean Air Speed (m/s)
X=4m, Z=0m
X=4m, Z=0.6m
X=4m, Z=1.2m
X=4m, Z=1.7m
KO-SST
RNG(NEWF)
RZ(NEWF)
Heikkinen (1991)
Blomqvist (1991)

Fig. A-2-2-7 X=4m

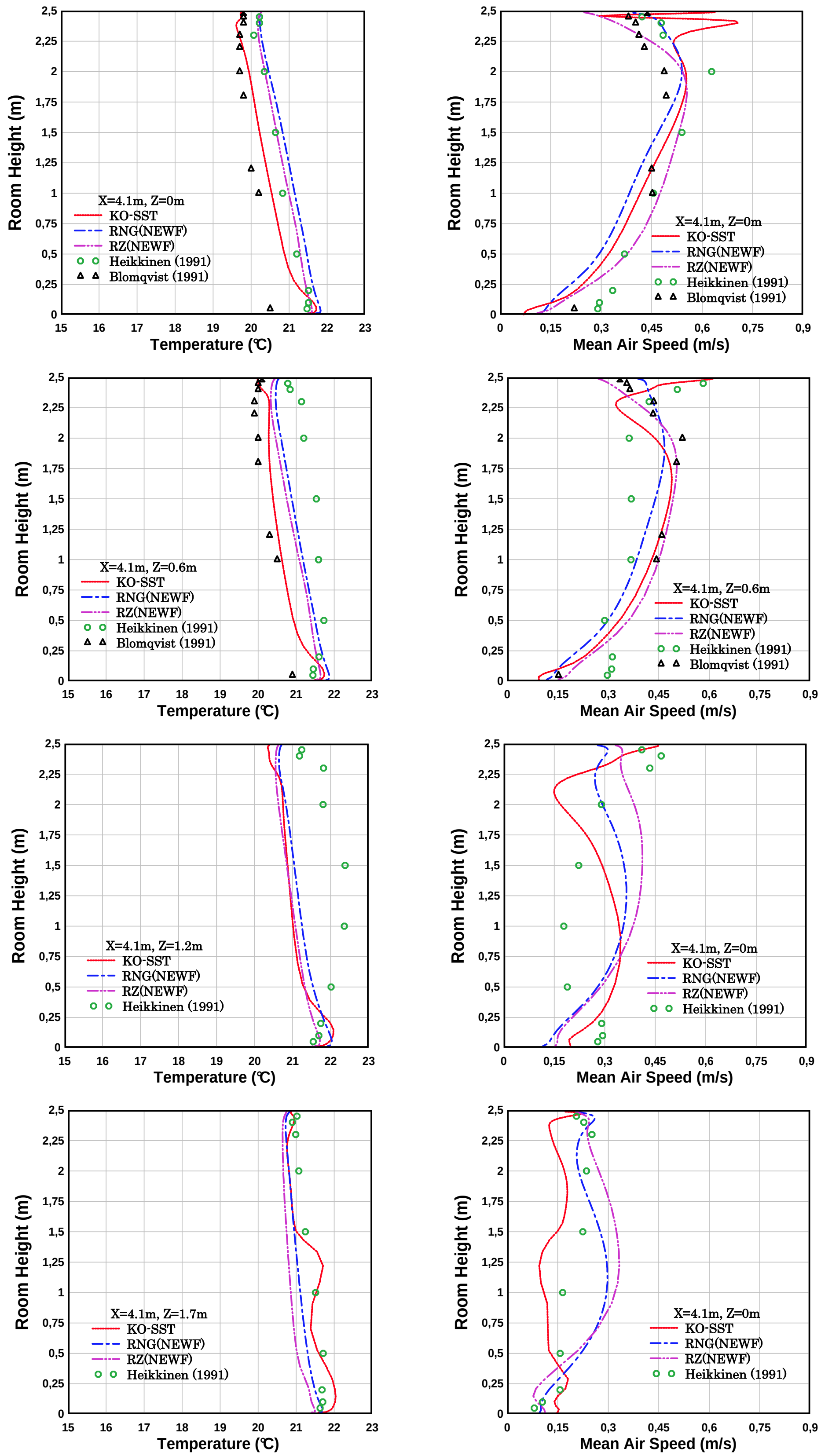

Fig. A-2-2-8 X=4.1m